



Technische Universität München

Lehrstuhl für Anorganische Chemie mit Schwerpunkt Neue Materialien

Investigation of Soluble Mixed Si-Ge Clusters and Sn-Bi Alloys
for the Synthesis of Macroporous Thin Films

Michael Alexander Giebel

Vollständiger Abdruck der von der Fakultät für Chemie der Technischen Universität
München zur Erlangung des akademischen Grades eines

Doktors der Naturwissenschaften (Dr. rer. nat.)

genehmigten Dissertation.

Vorsitzender: Prof. Dr. Tom Nilges

Prüfer der Dissertation:

1. Prof. Dr. Thomas F. Fässler
2. Prof. Dr. Dr. h. c. Bernhard Rieger

Die Dissertation wurde am 05.11.2019 bei der Technischen Universität München eingereicht und durch die Fakultät für Chemie am 27.11.2019 angenommen.

“Do not go where the path may lead, go instead where there is no path and leave a trail.”

- Ralph Waldo Emerson (1803-1882)

Danksagung

Mein besonderer Dank gilt zunächst meinem Doktorvater

Prof. Dr. Thomas F. Fässler

für die Möglichkeit dieses überaus interessante Thema im Lehrstuhl für Anorganische Chemie mit Schwerpunkt neue Materialien zu bearbeiten, für die unentwegte Unterstützung und die vielen hilfreichen Diskussionen im Verlauf der Promotion.

Des Weiteren möchte ich weiteren Personen danken deren tatkräftige Beiträge diese Arbeit vorangebracht haben:

Manuela Donaubauer für die Hilfe bei organisatorischen Problemen aller Art und dafür auch für andere Belange immer ein offenes Ohr zu haben.

Prof. Dr. Peter Müller-Buschbaum, Nuri Hohn und **Christian Weindl** für eine gelungene Kooperation, die über mehrere Jahre diverse neue Verwendungszwecke für unsere Zintl-Precursoren in Kombination mit Diblockcopolymeren hervorgebracht hat. Außerdem danke ich für anregende Gespräche über die Ergebnisse aus diesen Experimenten.

Prof. Dr. Dina Fatthakova-Rohlfing für die Möglichkeit diverse Geräte zur Herstellung des PMMA Templats sowie der Charakterisierung von dünnen Schichten zu verwenden.

Prof. Dr. Frank Hegmann für die Bereitstellung des Terahertz-Messstands sowie für die anregenden Diskussionen, die mich mehr für physikalische Fragestellungen sensibilisiert haben.

Prof. Dr. Eric Rivard für viele anregende Gespräche innerhalb und außerhalb von Gruppenseminaren während meines Kanada Aufenthalts in seinem Arbeitskreis und für die Möglichkeit in seinen Laboren neue Reaktionen auszutesten.

Den **Arbeitskreisen** von **Prof. Dr. Frank Hegmann** und **Prof. Dr. Eric Rivard** die mich während meines Aufenthalts in Kanada sehr unterstützt haben. Besonders danke ich **Naaman Amer**, **Charles Jensen** und **Mary A. Narreto** für die Unterstützung bei der Durchführung der Terahertz-Messungen und die Geduld bei den vielen nötigen Erklärungen. Außerdem danke ich **Jocelyn Sinclair** und **Ian Watson** für die gute Zusammenarbeit und die diversen Aktivitäten außerhalb der Universität, die den Aufenthalt in Kanada sehr angenehm gemacht haben.

Dr. Steffen Schmidt und **Daniel Böhm** für die Durchführung der REM-Messungen und Aufnahme der EDX-Spektren von dünnen Schichten, sowie **Daniel Böhm** für hilfreiche Tipps bei der Synthese des PMMA-Templats und beim PMMA Dip coating.

Maria Müller für die Aufnahme der EDX-Spektren von Pulvern und Einkristallen.

Sebastian Geier und **Christoph Wallach** für die Aufnahme der vielen Raman-Spektren.

Lorenz Schiegerl und **Christina Fischer** für die Aufnahme der ESI-MS-Spektren.

Dr. Wilhelm Klein und **Dr. Viktor Hlukhyy** für die Hilfe bei diversen Problemen bei der Pulver- und Einkristalldiffraktometrie.

Tim Kratky für die Aufnahme und Auswertung der XPS-Spektren.

Ulrike Ammari für die Durchführung der Elementaranalysen.

Meinem Masteranden **Fiorello Buzi** für die gute und produktive Zusammenarbeit im Rahmen des Erasmus Programms.

Meinen Laborkollegen **Sebastian Geier**, **Sabine Frischhut**, **Kerstin Mayer** und **Kevin Frankiewicz** für eine gute Zusammenarbeit, hilfreiche Diskussionen sowie die eine oder andere willkommene Ablenkung vom Laboralltag.

Dem gesamten **Arbeitskreis Prof. Dr. Thomas F. Fässler** für ein angenehmes Arbeitsklima und etliche gemeinsame Unternehmungen, die immer wieder Spaß gemacht haben.

Bei all meinen **Freunden** und **Verwandten**, die mich während der Zeit hier in München bzw. bei Besuchen zu Hause aus dem ein oder anderen Stimmungstief wieder herausziehen konnten und mir gezeigt haben, dass auch noch andere Sachen neben der Arbeit wichtig sind. Besonders möchte ich dabei **Claudia Ott** für die Zeit und die vielen gemeinsamen Unternehmungen in Kanada danken, durch die der Auslandsaufenthalt sich zu einer sehr interessanten Erfahrung entwickelt hat.

Ein besonderer Dank gilt außerdem meinen **Eltern Inge** und **Helmut**, ohne deren konstante Unterstützung während meines gesamten Studiums und der Promotion diese Arbeit sicher nicht möglich gewesen wäre.

Zusammenfassung

Der technische Fortschritt sowie der Klimawandel resultieren darin, dass erneuerbare Energien im Vergleich zu fossilen Brennstoffen immer wichtiger werden. Halbleitende Materialien aus Tetrelementen spielen dabei eine tragende Rolle in neuen Techniken zur Energiegewinnung (Solarzellen) und Energiespeicherung (Batterien). Von besonderem Interesse für diese Anwendungen sind poröse, nanostrukturierte Materialien aufgrund ihrer großen Oberfläche. Intermetallische Verbindungen mit der Zusammensetzung $A_{12}E_{17}$ ($A = \text{Na}-\text{Cs}$; $E = \text{Si}-\text{Pb}$) sowie $A_4\text{Ge}_9$ ($A = \text{K}-\text{Cs}$) beinhalten ZINTL Cluster, die zur Herstellung dieser porösen Materialien eingesetzt werden können.

In dieser Arbeit wurden dünne Germaniumschichten mit inverser Opalstruktur ausgehend von K_4Ge_9 in Ethylendiamin (*en*) hergestellt und deren Ladungsträgermobilitäten mittels Terahertzspektroskopie bestimmt. Die erhaltenen Mobilitäten lagen im Bereich von $\mu_m \approx 200 \frac{\text{cm}^2}{\text{V}\cdot\text{s}}$ und somit im Bereich der für polykristalline Germaniumschichten erhaltenen Werte. Da dünne Germaniumschichten mit inverser Opalstruktur durch eine einfache lösungsmittelbasierte Herstellung gewonnen werden können, bieten sie somit eine vielversprechende Alternative poröser Materialien zur Nutzung in Anwendungen wie etwa Solarzellen.

Außerdem wurden $A_{12}\text{Si}_{17-x}\text{Ge}_x$ - ($A = \text{K}, \text{Rb}$) und $\text{K}_4\text{Si}_{4-x}\text{Ge}_x$ -Phasen hergestellt und durch ihre Löslichkeit in Ethylendiamin (*en*) auf Ihre Eignung als Ausgangsverbindungen für poröse, nanostrukturierte Materialien untersucht. Für $\text{K}_{12}\text{Si}_{17-x}\text{Ge}_x$ -Phasen wurden siliciumhaltige Spezies in Lösung mittels NMR (^1H , ^{29}Si) sowie Abbauprodukte der löslichen Spezies nach Erhitzen mittels Pulverdiffraktometrie, EDX und Raman Spektroskopie bestimmt. Diese Phasen wurden als Ausgangsverbindungen in einem lösungsmittelbasierten Prozess für die Herstellung dünner Silicium-Germanium-Schichten mit inverser Opalstruktur verwendet. Mittels XPS konnte gezeigt werden, dass Germanium größtenteils als $\text{Ge}(0)$ in diesen Schichten vorlag. Silicium hingegen lag als $\text{Si}(+\text{IV})$ vor. Dennoch konnten für dünne Silicium-Germanium-Schichten mit inverser Opalstruktur Ladungsträgermobilitäten erhalten werden, die Werten für polykristalline Siliciumschichten in der Literatur ähneln.

Weiterhin wurden Verfahren zum Einbau von Heteroatomen (Sn, Bi, Se, Te) in dünne Schichten untersucht. Der Versuch Chalkogenide (Se, Te) in dünne Germaniumschichten mit inverser Opalstruktur einzubringen war aufgrund von Löslichkeitsproblemen limitiert. Allerdings war es möglich durch Umsetzung der intermetallischen Ausgangsverbindung K_2SnBi mit $SiCl_4$ dünne metallische Sn/Bi Schichten mit poröser Struktur (große Oberfläche) herzustellen. Eine geordnete inverse Opalstruktur konnte für diese Schichten jedoch nicht erhalten werden. Daher kann die Annahme getroffen werden, dass Cluster als Ausgangsverbindungen nötig sind, um eine solche geordnete Morphologie zu erhalten.

Um die Löslichkeit von $Si_{9-x}Ge_x$ -Clustern von bisher verwendeten polaren Amininen wie *en* auf unpolare Lösungsmittel (Acetonitril, THF, Toluol, Hexan) auszuweiten, wurden Liganden eingeführt und somit gleichzeitig die Ladung der Cluster verringert. Durch Reaktionen von $[Si_{9-x}Ge_x]^{4-}$ mit einem Überschuss an Tris(trimethylsilyl)silan (*hyp*) kam es zur Bildung von silylierten $[E_9(hyp)_3]^-$ Clustern ($E = Si, Ge$), die mittels ESI-MS sowie NMR ($^1H, ^{13}C, ^{29}Si$) untersucht wurden. Aus diesen Verbindungen konnte $K(2.2.2-crypt)[Si_{1.68}Ge_{7.32}(hyp)_3]$ als erster tris-silylierter, siliciumhaltiger Cluster kristallisiert werden. Eine Kombination aus Raman spektroskopischen Untersuchungen und theoretischen Berechnungen bestätigte, dass Si-Si exo Bindungen in diesen Verbindungen gegenüber Ge-Si exo Bindungen bevorzugt werden und somit eine bevorzugte Besetzung der Si/Ge-Clusterpositionen mit exo Bindung durch Si erfolgt. Die Umsetzung von Münzmetall NHC-Verbindungen mit bis-silylierten Clustern führte zur Bildung von ungeladenen $[(NHC_M)_2\{\eta^3-Ge_9(Si(TMS)_3)_2\}]$ Clustern ($M = Cu, Ag, Au$) und erweiterte somit die Löslichkeit in unpolaren Lösungsmitteln, die mittels ESI-MS und NMR Spektroskopie untersucht wurden. Die kupferhaltige Verbindung $[(NHC^{Dipp}Cu)_2\{\eta^3-Ge_9(Si(TMS)_3)_2\}]$ konnte zusätzlich kristallisiert werden. Die breite Löslichkeit von ZINTL Clustern mit unterschiedlicher Ladung könnte neue Möglichkeiten der Herstellung von dünnen Schichten aus Halbleitermaterialien schaffen und daher neue Anwendungen ermöglichen.

Abstract

Technological development as well as the climate change result in renewable energies becoming increasingly important compared to fossil fuels. In this context, semiconducting materials of Group 14 elements play a key role in new technologies for generation (solar cells) and storage (batteries) of energy. Especially porous nanostructured materials have attracted a growing interest due to their high surface area being beneficial for these applications. Intermetallic compounds with the composition $A_{12}E_{17}$ ($A = \text{Na-Cs}$; $E = \text{Si-Pb}$) and $A_4\text{Ge}_9$ ($A = \text{K-Cs}$) contain well-defined ZINTL clusters, representing precursors for the fabrication of such materials.

Within this work, inverse opal structured Ge thin films were synthesized starting with K_4Ge_9 in ethylene diamine (*en*). Charge carrier mobilities within these films were obtained through terahertz spectroscopy. The carrier mobilities obtained were in the range of $\mu_m \approx 200 \frac{\text{cm}^2}{\text{V}\cdot\text{s}}$, challenging high mobility values obtained for bulk polycrystalline germanium materials. Due to inverse opal structured thin films being synthesized through a simple solution-based process, they are promising candidates for macroporous materials in applications like solar cells.

Moreover, $A_{12}\text{Si}_{17-x}\text{Ge}_x$ - ($A = \text{K, Rb}$) and $\text{K}_4\text{Si}_{4-x}\text{Ge}_x$ -phases were evaluated as precursors for porous materials through their solubility in ethylenediamine (*en*). Silicon species in solution (through ^1H and ^{29}Si NMR) as well as annealing products of the soluble species (through powder diffraction, EDX and Raman spectroscopy) of $\text{K}_{12}\text{Si}_{17-x}\text{Ge}_x$ -phases were determined. These phases were used as precursors in a solution-based approach to yield inverse opal structured mixed silicon-germanium thin films. XPS investigations showed that germanium was mostly present as Ge(0) in these films. In contrast, silicon was detected as Si(+IV). Nevertheless, carrier mobilities obtained for inverse opal structured mixed silicon-germanium thin films as well as silicon thin films were in the range of values obtained for polycrystalline silicon materials in the literature.

Furthermore, the introduction of hetero atoms (Sn, Bi, Se, Te) in thin films was investigated. The introduction of Group 16 elements (Se, Te) to inverse opal structured germanium thin films was limited due to solubility issues. However, porous metallic Sn/Bi thin films with a high surface area could be obtained by linking the intermetallic precursor K_2SnBi with SiCl_4 . An ordered, inverse opal structured material could not be

obtained in this case, indicating that well-defined clusters are necessary to achieve this ordered morphology.

To expand the solubility of $\text{Si}_{9-x}\text{Ge}_x$ -clusters from highly polar amines towards less polar solvents (such as acetonitrile, THF, toluene or hexane), ligands were introduced to the clusters, reducing their charge in the process. Reactions of $[\text{Si}_{9-x}\text{Ge}_x]^{4-}$ with an excess of tris(trimethylsilyl)silane (*hyp*) thereby yielded a series of silylated $[\text{E}_9(\text{hyp})_3]^-$ clusters ($E = \text{Si}, \text{Ge}$) which were investigated through ESI-MS and NMR (^1H , ^{13}C , ^{29}Si). These compounds also yielded the first crystals of a tris-silylated siliconoid cluster in form of $\text{K}(2.2.2\text{-crypt})[\text{Si}_{1.68}\text{Ge}_{7.32}(\text{hyp})_3]$. A combination of Raman spectroscopic measurements with theoretical calculations confirmed that Si-Si exo bonds are favored over Ge-Si exo bonds in these compounds, resulting in a Si favored occupation of Si/Ge cluster vertices containing exo bonds. Additional introduction of coinage metal NHC (*N*-heterocyclic carbene) compounds to bis-silylated clusters led to the formation of a series of uncharged $[(\text{NHCM})_2\{\eta^3\text{-Ge}_9(\text{Si}(\text{TMS})_3)_2\}]$ clusters ($M = \text{Cu}, \text{Ag}, \text{Au}$), which were characterized through ESI-MS and NMR. The compound containing copper $[(\text{NHC}^{\text{Dipp}}\text{Cu})_2\{\eta^3\text{-Ge}_9(\text{Si}(\text{TMS})_3)_2\}]$ was also crystallized. The resulting broad range of soluble ZINTL cluster compounds may lead to new reaction paths for solution-based fabrication of thin films of semiconducting materials and therefore enable new applications.

Table of Contents

1	Introduction.....	1
1.1	Energy Reform.....	1
1.2	Flexible Solar Cells – Types and Functionality.....	4
1.2.1	Dye-Sensitized Solar Cell (DSSC).....	4
1.2.2	Perovskite Solar Cell	6
1.2.3	Polymer and Hybrid Solar Cell.....	8
1.3	Inverse Opal Structured Thin Films of Semiconductors	11
1.4	ZINTL clusters – Properties and Reactivity in Solution	13
1.4.1	Deltahedral Group 14 Element Clusters – Structure and Solubility	13
1.4.2	Organo-Functionalization and Silylation of Group 14 Element Clusters ...	15
1.4.3	Reactivity of Silylated Group 14 Element Clusters	16
1.5	Motivation and Scope.....	18
1.6	Outline.....	19
2	Experimental Section.....	20
2.1	Experimental Techniques.....	20
2.1.1	Inert Gas Conditions.....	20
2.1.2	Ball-Milling	20
2.1.3	Solid-State Synthesis	21
2.1.4	Filtration of Solutions	23
2.1.5	Substrate Preparation.....	23
2.1.6	Dip Coating of PMMA Suspensions.....	23
2.1.7	Drop Casting of Precursor Solutions	24
2.1.8	Annealing of Thin Films and Dried Residues.....	24
2.1.9	Reagents	25
2.2	Characterization Methods	27
2.2.1	Scanning Electron Microscopy	27

2.2.2 Energy Disperse X-Ray	27
2.2.3 Powder X-Ray Diffraction	27
2.2.4 Single Crystal X-Ray Diffraction	28
2.2.5 Raman Spectroscopy	28
2.2.6 Nuclear Magnetic Resonance.....	29
2.2.7 Electrospray Ionization Mass Spectrometry	29
2.2.8 Terahertz Spectroscopy	30
2.2.9 Elemental Analysis	31
2.2.10 Profilometry	31
2.2.11 X-Ray Photoelectron Spectroscopy	31
2.2.12 Computational Details	32
2.3 Syntheses	33
2.3.1 Synthesis of $\text{Si}_{17-x}\text{Ge}_x$	33
2.3.2 Synthesis of $\text{K}_{12}\text{Si}_{17-x}\text{Ge}_x$	33
2.3.3 Synthesis of $\text{Rb}_{12}\text{Si}_{17-x}\text{Ge}_x$	34
2.3.4 Synthesis of $\text{K}_4\text{Si}_{4-x}\text{Ge}_x$	34
2.3.5 Synthesis of K_4Ge_9	35
2.3.6 Synthesis of K_2SnBi	35
2.3.7 Synthesis of “ $\text{K}_2\text{Si}_2\text{P}_2$ ” and “ $\text{K}_2\text{Si}_7\text{P}_2$ ”	36
2.3.8 Synthesis of 250 – 270 nm PMMA Beads	36
2.3.9 Preparation of Precursor Solutions.....	37
2.3.10 Preparation of Thin Film Sheets	39
2.3.11 Synthesis of $\text{K}[(\text{Si}_{9-y}\text{Ge}_y)(\text{Si}(\text{TMS})_3)_3]$	40
2.3.12 Synthesis of $(\text{NHC}^{\text{Dipp}}\text{M})_2\{\eta^3\text{-Ge}_9(\text{Si}(\text{TMS})_3)_2\}$ (M = Cu, Ag, Au).....	41
3 Results and Discussion	42
3.1 Inverse Opal Structured Ge Thin Films	42
3.1.1 Synthesis and Characterization of Inverse Opal Structured Ge Thin Films	42

3.1.2 Charge Carrier Mobility in Inverse Opal Structured Ge Thin Films (Terahertz Spectroscopy)	44
3.2 Si/Ge-Clusters as Wet Chemical Precursors for Inverse Opal Structured Thin Films	50
3.2.1 Synthesis and Characterization of $K_{12}Si_{17-x}Ge_x^-$, $Rb_{12}Si_{17-x}Ge_x^-$ and $K_4Si_{4-x}Ge_x^-$ -Phases	50
3.2.2 Solubility of $K_{12}Si_{17-x}Ge_x^-$, $Rb_{12}Si_{17-x}Ge_x^-$ and $K_4Si_{4-x}Ge_x^-$ -Phases in Ethylene Diamine	58
3.2.3 Characterization of Dried Residues ($K_{12}Si_{17-x}Ge_x/en$ Solutions)	60
3.2.4 Characterization of Annealed Residues ($K_{12}Si_{17-x}Ge_x/en$ Solutions).....	63
3.2.5 Characterization of Silicon Species in $K_{12}Si_{17/en}$ Solution.....	66
3.2.6 Synthesis and Characterization of Inverse Opal Structured Mixed Si/Ge as well as Si Thin Films.....	68
3.2.7 Charge Carrier Mobility in Inverse Opal Structured Mixed Si/Ge Thin Films (Terahertz Spectroscopy)	75
3.3 Ge/Se and Ge/Te Thin Films	81
3.4 Sn/Bi Thin Films with High Surface Area	83
3.5 Silylation of Mixed Nine Atomic Si/Ge Clusters.....	88
3.6 Conversion of Silylated Ge-Clusters with Coinage Metal NHC Compounds .	100
4 Summary and Conclusion	108
5 Appendix	112
5.1 Powder Diffraction Patterns and Raman Spectra of Precursor Compounds .	112
5.2 Terahertz Measurements.....	118
5.3 ESI-MS Measurements.....	124
5.4 Crystals.....	128
5.5 Raman Measurements of Crystals.....	131
5.6 NMR Measurements	132
5.7 XPS Investigations – Ge oxidation states	143
5.8 References.....	145

Abbreviations and Symbols

#	number
%	percentage
%at.	atomic percentage
%wt.	weight percentage
°	degree (angle)
°C	degree Celsius (temperature)
2θ	diffraction angle
ϵ_0	vacuum permittivity
λ	wavelength
τ_{DS}	effective scattering time
ω_p	plasma frequency
Å	angstrom
<i>a</i>	amorphous
α	crystalline
a. c.	ambient conditions
approx.	approximately
a. u.	arbitrary unit
BTS	copper oxide catalyst (gas regeneration)
CCD	charge-coupled device
cm	centimeter
cm ⁻¹	reciprocal centimeter (wavenumber)
18-crown-6	crown ether; 1,7,10,13,16-hexaoxacyclooctadecane
2.2.2-crypt	4,7,13,16,21,24-hexaoxa-1,10-diazabicyclo-[8.8.8]hexacosane
cST	centi stokes (viscosity)
d	day(s)

Dipp	di <i>iso</i> -propylphenyl
DLS	dynamic light scattering
DMF	dimethyl formamide
DMSO	dimethyl sulfoxide
E	energy
<i>e</i>	electronic charge
EDX	energy dispersive X-Ray analysis
<i>e. g.</i>	<i>exempli gratia</i> (for example)
<i>en</i>	ethylene diamine
ESI-MS	electron ionization mass spectrometry
<i>et al.</i>	<i>et aliae</i> (and others)
ETM	electron transport material
eV	electron volt
F	fluence
fig.	figure(s)
FTO	flourine doped tin oxide
fwhm	full width at half maximum
g	gram
h	hour(s)
HMBC	heteronuclear multiple bond correlation, 2D NMR method
HTM	hole transport material
<i>hyp</i>	tris(trimethylsilyl)silane (“hypersilyl”-group)
<i>hyp-Cl</i>	chlorotris(trimethylsilyl)silane (“hypersilylchloride”)
<i>i. c.</i>	inert conditions
IG	inverse gated, method for ²⁹ Si NMR
INEPT	intensive nuclei enhancement by polarisation transfer, pulse method for ²⁹ Si NMR enhancing signal intensity if hydrogen is in vicinity
IR	infrared

ITO	indium tin oxide
K	kelvin (temperature)
kV	kilovolt
m^*	effective mass
M	(transition) metal
mbar	millibar
Mes	mesityl
mg	milligram
min	minute(s)
mL	milliliter
mm	millimeter
MMA	methyl methacrylate
mmol	millimole
mW	milliwatt
μ	effective carrier mobility
μ	micro
μL	microliter
μm	micrometer
μmol	micromole
N	carrier density
n. a.	not applicable (undetermined)
NHC	N-heterocyclic carbene
nm	nanometer
NMR	nuclear magnetic resonance spectroscopy
ns	nanosecond
PMMA	poly(methyl methacrylate)
ppm	parts per million

ps	picosecond
PXRD	powder X-ray diffraction
rpm	rounds per minute
SC-XRD	single crystal X-ray diffraction
SDS	sodium dodecyl sulfate
SEM	scanning electron microscopy
t	time
ΔT	difference in temperature
ΔT	difference in transmission (terahertz signals: reference – probe)
T_0	reference transmission (terahertz signal: reference)
TCO	transparent conductive oxide
theo.	theoretically
THF	tetrahydrofuran
THz	terahertz
TMS	trimethylsilyl
TOF	time-of-flight
TSG	trissilylated Ge-Cluster $K[Ge_9(hyp)_3]$
TW	terawatt
UV	ultraviolet
W	watt
XPS	X-ray photoelectron spectroscopy
XRD	X-ray diffraction

Table of Figures

Figure 1.1. World energy consumption in TWh.....	1
Figure 1.2. Total energy gross production by energy source in Germany in 2017.....	2
Figure 1.3. Schematic representation of a DSSC setup.	5
Figure 1.4. a) Molecular structure of $\text{CH}_3\text{NH}_3\text{PbX}_3$ ($X = \text{I}, \text{Br}$ and/or Cl) perovskites ^[62] and b) schematic representation of a perovskite solar cell ^[60]	6
Figure 1.5. Schematic representation of different morphologies of the active layer in polymer solar cells with a regular architecture.....	8
Figure 1.6. Operating mechanism of a polymer solar cell with a regular architecture.	9
Figure 1.7. Structures of common donors (P3HT and PTB7) and acceptor (PC ₆₁ BM) in active layers of polymer solar cells.	10
Figure 1.8. Structures of $[\text{E}_9]^{4-}$ and $[\text{E}_9]^{2-}$ clusters in comparison.....	14
Figure 1.9. Reported tris-silylated $[\text{Ge}_9\text{R}_3]^-$ clusters bearing silyl ligands with different steric demand. ^[163-167]	16
Figure 2.1. Ball-mill (left) and milling jar (right) with safety closure cap and tungsten carbide balls.	21
Figure 2.2. Stainless-steel autoclave (left) and corundum tube with balloon for pressure regulation (right).	22
Figure 2.3. Tantalum ampoule (left) and fused silica tube (right).....	22
Figure 2.4. Schematic display of PMMA dip coating (left) and dip coater setup (right).	24
Figure 3.1. Synthesis of inverse opal structured Ge thin films.	42
Figure 3.2. SEM pictures of germanium thin films.	43
Figure 3.3. Transient photoconductivity $ \Delta T/T_0 $ for germanium thin films.....	45
Figure 3.4. Rise time (a) and signal decay (b) for an inverse opal structured germanium thin film starting from 340 nm PMMA template beads.	46
Figure 3.5. Complex conductivity $\sigma(\omega)$ plots for germanium thin films.....	48
Figure 3.6. a) Powder diffraction patterns of $\text{K}_{12}\text{Si}_{17-x}\text{Ge}_x$ ($x = 0, 5, 9, 12, 17$) compounds. b) highlighted area of the compounds featuring a shift for the main reflex.	51

Figure 3.7. Recorded Raman spectra of $K_{12}Si_{17-x}Ge_x$ ($x = 0, 5, 9, 12, 17$) compounds.	53
Figure 3.8. a) Powder diffraction patterns of $K_4Si_{4-x}Ge_x$ ($x = 0, 1.2, 2.1, 2.8, 4$) compounds. b) highlighted area of the compounds featuring a shift for the main reflex.	54
Figure 3.9. Determined cell volumes for $K_4Si_{4-x}Ge_x$ ($x = 0, 1.2, 2.1, 2.8, 4$) compounds.	55
Figure 3.10. Recorded Raman spectra of $K_4Si_{4-x}Ge_x$ ($x = 0, 1.2, 2.1, 2.8, 4$) compounds.....	57
Figure 3.11. Raman spectra of dried residues from $K_{12}Si_{17-x}Ge_x/en$ solutions.....	61
Figure 3.12. Powder diffraction patterns of dried residues from $K_{12}Si_{17-x}Ge_x/en$ solutions.	62
Figure 3.13. Raman spectra of residues from $K_{12}Si_{17-x}Ge_x/en$ solutions after annealing at 873 K.	64
Figure 3.14. Powder diffraction patterns of residues from $K_{12}Si_{17-x}Ge_x/en$ solutions after annealing at 873 K.....	65
Figure 3.15. Recorded 1H -spectrum of $K_{12}Si_{17}$ in solution.....	66
Figure 3.16. Recorded ^{29}Si -IG spectra of $K_{12}Si_{17}$ in solution.....	67
Figure 3.17. Synthesis of inverse opal structured mixed Si/Ge and silicon thin films.	68
Figure 3.18. SEM pictures of 300 nm sized PMMA beads.....	69
Figure 3.19. SEM pictures of inverse opal structured mixed Si/Ge as well as pure silicon thin films.	70
Figure 3.20. Raman spectra of mixed Si/Ge as well as silicon thin films at varying laser intensities.....	72
Figure 3.21. Ge 2p XPS spectra of inverse opal structured thin films from $K_{12}Si_5Ge_{12}$, $K_{12}Si_8Ge_9$, $K_{12}Si_{12}Ge_5$ and $K_{12}Si_{17}$ a) without and b) after 40 min of Ar^+ sputtering. .	73
Figure 3.22. Si 2p XPS spectra of inverse opal structured thin films from $K_{12}Si_5Ge_{12}$, $K_{12}Si_8Ge_9$, $K_{12}Si_{12}Ge_5$ and $K_{12}Si_{17}$ a) without and b) after 40 min of Ar^+ sputtering. .	73
Figure 3.23. N/Si as well as N/(SiGe) ratio in inverse opal structured thin films.	74
Figure 3.24. Transient photoconductivity $ \Delta T/T_0 $ for an inverse opal structured mixed Si/Ge thin film starting from $K_{12}Si_5Ge_{12}$	75

Figure 3.25. Fluence and temperature dependency of peak signal for transient photoconductivity $ \Delta T/T_0 $ (peak) of inverse opal structured thin films and comparison of $ \Delta T/T_0 $ for different ZINTL precursors.....	76
Figure 3.26. Rise time (a) and signal decay (b) for an inverse opal structured mixed Si/Ge thin film starting from $K_{12}Si_5Ge_{12}$	77
Figure 3.27. Complex conductivity $\sigma(\omega)$ plots for inverse opal structured thin films. 79	
Figure 3.28. Pictures of K_2Te and selenium solutions as well as thin films.....	81
Figure 3.29. Raman spectra (a) and powder diffractograms (b) of different Se:Ge ratios compared to solid K_4Ge_9	82
Figure 3.30. Pictures of K_2SnBi/en solution (a) and Sn/Bi thin film (b).....	83
Figure 3.31. Raman spectra of Sn/Bi thin film at different steps in the synthesis compared to solid K_2SnBi	85
Figure 3.32. Powder diffraction patterns of Sn/Bi thin film at different steps in the synthesis.....	86
Figure 3.33. SEM pictures of Sn/Bi thin films after treatment with various linkers at different concentrations.	87
Figure 3.34. Synthesis of $K[E_9(hyp)_3]$ (E : Si, Ge).....	88
Figure 3.35. ESI-MS spectra of $[E_9(hyp)_3]^-$ (E : Si, Ge) in negative (-) ion mode.....	89
Figure 3.36. Selected high resolution areas of the ESI-MS spectrum of $[E_9(hyp)_3]^-$ (E : Si, Ge) in negative (-) ion mode.....	90
Figure 3.37. 1H -NMR of reaction solution of $K[E_9(hyp)_3]$ (E : Si, Ge) starting from $K_{12}Si_8Ge_9$ as a precursor.	91
Figure 3.38. Detailed view of the $-CH_3$ (TMS) peaks in 1H -NMRs of reaction solutions of $K[E_9(hyp)_3]$ (E : Si, Ge) compounds starting from $K_{12}Si_{17-x}Ge_x$ ($x = 0, 5, 12, 17$) as a precursor.	92
Figure 3.39. ^{13}C -NMR of reaction solution of $K[E_9(hyp)_3]$ (E : Si, Ge) starting from $K_{12}Si_8Ge_9$ as a precursor.	92
Figure 3.40. ^{29}Si -NMR spectra of reaction solution of $K[E_9(hyp)_3]$ (E : Si, Ge) starting from $K_{12}Si_8Ge_9$ as a precursor.....	93
Figure 3.41. Molecular structure of a silylated cluster in $K(2.2.2-crypt)[Si_{1.68(1)}Ge_{7.32(1)}(hyp)_3]$	94

Figure 3.42. a) Front view of the central $[\text{Si}_{1.68(1)}\text{Ge}_{7.32(1)}]$ unit in $\text{K}(2.2.2\text{-crypt})[\text{Si}_{1.68(1)}\text{Ge}_{7.32(1)}(\text{hyp})_3]$ and b) schematic view of the central $[\text{Si}_{1.68(1)}\text{Ge}_{7.32(1)}]$ unit highlighting important parameters for symmetry of the cluster.	96
Figure 3.43. Raman spectra of various $\text{K}(2.2.2\text{-crypt})[\text{E}_9\{\text{Si}(\text{TMS})_3\}_3]$ (E : Si, Ge) compounds.....	98
Figure 3.44. Experimental values for Ge-Si stretching (a), E-Si (E : Si, Ge) bending (b) and Si-Si stretching (c) vibration of the cluster exo bonds in $[\text{E}_9\{\text{Si}(\text{TMS})_3\}_3]^-$ (E : Si, Ge) compared to theoretical values for $[\text{Si}_2\text{Ge}_7\{\text{Si}(\text{SiH}_3)_3\}_3]^-$	99
Figure 3.45. Synthesis of binuclear ZINTL-cluster coinage metal NHC compounds $[(\text{NHCM})_2\{\eta^3, \eta^3\text{-Ge}_9(\text{Si}(\text{TMS})_3)_2\}]$	101
Figure 3.46. $^1\text{H-NMR}$ of $[(\text{NHC}^{\text{Dipp}}\text{Cu})_2\{\eta^3, \eta^3\text{-Ge}_9(\text{Si}(\text{TMS})_3)_2\}]$ in $\text{THF-}d_8$	102
Figure 3.47. $^{13}\text{C-NMR}$ of $[(\text{NHC}^{\text{Dipp}}\text{Cu})_2\{\eta^3, \eta^3\text{-Ge}_9(\text{Si}(\text{TMS})_3)_2\}]$ in $\text{THF-}d_8$	102
Figure 3.48. $^{29}\text{Si-INEPT NMR}$ of $[(\text{NHC}^{\text{Dipp}}\text{Cu})_2\{\eta^3, \eta^3\text{-Ge}_9(\text{Si}(\text{TMS})_3)_2\}]$ in $\text{THF-}d_8$	103
Figure 3.49. Selected high resolution areas of the ESI-MS spectrum of an acetonitrile solution of $[(\text{NHC}^{\text{Dipp}}\text{Cu})_2\{\eta^3, \eta^3\text{-Ge}_9(\text{Si}(\text{TMS})_3)_2\}]$	103
Figure 3.50. Molecular structure of $[(\text{NHC}^{\text{Dipp}}\text{Cu})_2\{\eta^3, \eta^3\text{-Ge}_9(\text{Si}(\text{TMS})_3)_2\}]$	104
Figure 4.1. Schematic display of inverse opal structured thin films and functionalized clusters obtained from reaction of bare $\text{K}_{12}\text{Si}_{17-x}\text{Ge}_x$ clusters ($x = 0, 5, 9, 12, 17$) within this work.	110
Figure 4.2. Schematic display of porous thin films obtained by a wet-chemical process involving $\text{K}_4\text{Ge}_9/\text{en}$ (a) and $\text{K}_2\text{SnBi}/\text{en}$ (b) solutions.....	111
Figure 5.1. a) Powder diffraction patterns of $\text{Rb}_{12}\text{Si}_{17-x}\text{Ge}_x$ ($x = 0, 5, 9, 12, 17$) compounds. b) highlighted area of the compounds featuring a shift for the main reflex.	112
Figure 5.2. Recorded Raman spectra of $\text{Rb}_{12}\text{Si}_{17-x}\text{Ge}_x$ ($x = 0, 5, 9, 12, 17$) compounds.	113
Figure 5.3. Powder diffraction patterns of $\text{Rb}_{12}\text{Si}_{17-x}\text{Ge}_x$ ($x = 0, 12$) compounds at different temperatures.....	114
Figure 5.4. Powder diffraction pattern of K_4Ge_9	114
Figure 5.5. Recorded Raman spectrum of K_4Ge_9	115
Figure 5.6. Powder diffraction pattern of K_2SnBi	115
Figure 5.7. Recorded Raman spectrum of K_2SnBi	116

Figure 5.8. Powder diffraction patterns of “K ₂ Si ₂ P ₂ ” and “K ₂ Si ₇ P ₂ ” .	117
Figure 5.9. Rise time (a) and signal decay (b) for an inverse opal structured mixed Si/Ge thin film starting from K ₁₂ Si ₁₂ Ge ₅ .	118
Figure 5.10. Rise time (a) and signal decay (b) for an inverse opal structured mixed Si/Ge thin film starting from K ₁₂ Si ₁₇ .	118
Figure 5.11. Transient photoconductivity $ \Delta T/T_0 $ for germanium thin films.	122
Figure 5.12. Rise time (a) and signal decay (b) for an unstructured germanium thin film.	122
Figure 5.13. Rise time (a) and signal decay (b) for an inverse opal structured germanium thin film starting from 150 nm PMMA template beads.	123
Figure 5.14. Rise time (a) and signal decay (b) for bulk crystalline germanium.	123
Figure 5.15. Selected high resolution areas of the ESI-MS spectrum of [E ₉ (hyp) ₃] ⁻ (E: Si, Ge) in negative (-) ion mode.	124
Figure 5.16. Selected high resolution areas of the ESI-MS spectrum of [E ₉ (hyp) ₃] ⁻ (E: Si, Ge) in negative (-) ion mode.	124
Figure 5.17. Selected high resolution areas of the ESI-MS spectrum of [E ₉ (hyp) ₃] ⁻ (E: Si, Ge) in negative (-) ion mode.	125
Figure 5.18. Selected high resolution areas of the ESI-MS spectrum of [E ₉ (hyp) ₃] ⁻ (E: Si, Ge) in negative (-) ion mode.	125
Figure 5.19. Selected high resolution areas of the ESI-MS spectrum of [E ₉ (hyp) ₃] ⁻ (E: Si, Ge) in negative (-) ion mode.	126
Figure 5.20. Selected high resolution areas of the ESI-MS spectrum of an acetonitrile solution of [(NHC ^{Dipp} Au) ₂ {η ³ ,η ³ -Ge ₉ (Si(TMS) ₃) ₂ }].	126
Figure 5.21. Selected high resolution areas of the ESI-MS spectrum of an acetonitrile solution of [(NHC ^{Dipp} Ag) ₂ {η ³ ,η ³ -Ge ₉ (Si(TMS) ₃) ₂ }] and [(NHC ^{Mes} Cu) ₂ {η ³ ,η ³ -Ge ₉ (Si(TMS) ₃) ₂ }] in negative (-) ion mode.	127
Figure 5.22. Raman spectra of K(2.2.2-crypt)[Si _{1.68(1)} Ge _{7.32(1)} (hyp) ₃] (red block) compared to orange needle from the same crystallization experiment.	131
Figure 5.23. ¹ H-NMR of K[Ge ₉ (hyp) ₃] (TSG) starting from K ₁₂ Ge ₁₇ as a precursor.	132
Figure 5.24. ¹ H-NMR of K[E ₉ (hyp) ₃] (E: Si, Ge) starting from K ₁₂ Si ₅ Ge ₁₂ as a precursor.	132

Figure 5.25. $^1\text{H-NMR}$ of $\text{K}[\text{E}_9(\text{hyp})_3]$ (E : Si, Ge) starting from $\text{K}_{12}\text{Si}_{12}\text{Ge}_5$ as a precursor.	133
Figure 5.26. $^1\text{H-NMR}$ of $\text{K}[\text{Si}_9(\text{hyp})_3]$ starting from $\text{K}_{12}\text{Si}_{17}$ as a precursor.	133
Figure 5.27. $^{29}\text{Si-INEPT}$ NMR of $\text{K}[\text{Ge}_9(\text{hyp})_3]$ (TSG) starting from $\text{K}_{12}\text{Ge}_{17}$ as a precursor.	134
Figure 5.28. $^{29}\text{Si-INEPT}$ NMR of $\text{K}[\text{E}_9(\text{hyp})_3]$ (E : Si, Ge) starting from $\text{K}_{12}\text{Si}_5\text{Ge}_{12}$ as a precursor.	134
Figure 5.29. $^{29}\text{Si-INEPT}$ NMR of $\text{K}[\text{E}_9(\text{hyp})_3]$ (E : Si, Ge) starting from $\text{K}_{12}\text{Si}_{12}\text{Ge}_5$ as a precursor.	135
Figure 5.30. $^{29}\text{Si-INEPT}$ NMR of $\text{K}[\text{Si}_9(\text{hyp})_3]$ starting from $\text{K}_{12}\text{Si}_{17}$ as a precursor.	135
Figure 5.31. $^{29}\text{Si-IG}$ NMR of $\text{K}[\text{E}_9(\text{hyp})_3]$ (E : Si, Ge) starting from $\text{K}_{12}\text{Si}_{12}\text{Ge}_5$ as a precursor.	136
Figure 5.32. $^{29}\text{Si-IG}$ NMR of $\text{K}[\text{Si}_9(\text{hyp})_3]$ starting from $\text{K}_{12}\text{Si}_{17}$ as a precursor.	136
Figure 5.33. $^1\text{H-NMR}$ of $[(\text{NHC}^{\text{Dipp}}\text{Ag})_2\{\eta^3, \eta^3\text{-Ge}_9(\text{Si}(\text{TMS})_3)_2\}]$ in $\text{THF-}d_8$	137
Figure 5.34. $^{13}\text{C-NMR}$ of $[(\text{NHC}^{\text{Dipp}}\text{Ag})_2\{\eta^3, \eta^3\text{-Ge}_9(\text{Si}(\text{TMS})_3)_2\}]$ in $\text{THF-}d_8$	137
Figure 5.35. $^{29}\text{Si-INEPT}$ NMR of $[(\text{NHC}^{\text{Dipp}}\text{Ag})_2\{\eta^3, \eta^3\text{-Ge}_9(\text{Si}(\text{TMS})_3)_2\}]$ in $\text{THF-}d_8$	138
Figure 5.36. $^1\text{H-NMR}$ of $[(\text{NHC}^{\text{Dipp}}\text{Au})_2\{\eta^3, \eta^3\text{-Ge}_9(\text{Si}(\text{TMS})_3)_2\}]$ in C_6D_6	138
Figure 5.37. $^{13}\text{C-NMR}$ of $[(\text{NHC}^{\text{Dipp}}\text{Au})_2\{\eta^3, \eta^3\text{-Ge}_9(\text{Si}(\text{TMS})_3)_2\}]$ in C_6D_6	139
Figure 5.38. $^{29}\text{Si-INEPT}$ NMR of $[(\text{NHC}^{\text{Dipp}}\text{Au})_2\{\eta^3, \eta^3\text{-Ge}_9(\text{Si}(\text{TMS})_3)_2\}]$ in C_6D_6	139
Figure 5.39. $^1\text{H-NMR}$ of $[(\text{NHC}^{\text{Mes}}\text{Cu})_2\{\eta^3, \eta^3\text{-Ge}_9(\text{Si}(\text{TMS})_3)_2\}]$ in $\text{THF-}d_8$	140
Figure 5.40. $^{13}\text{C-NMR}$ of $[(\text{NHC}^{\text{Mes}}\text{Cu})_2\{\eta^3, \eta^3\text{-Ge}_9(\text{Si}(\text{TMS})_3)_2\}]$ in $\text{THF-}d_8$	140
Figure 5.41. $^{29}\text{Si-INEPT}$ NMR of $[(\text{NHC}^{\text{Mes}}\text{Cu})_2\{\eta^3, \eta^3\text{-Ge}_9(\text{Si}(\text{TMS})_3)_2\}]$ in $\text{THF-}d_8$	141
Figure 5.42. Comparison of $^1\text{H-NMRs}$ of silylation product of $\text{K}_{12}\text{Ge}_{17}$ with <i>hyp</i> -Cl (6 eq., blue line/top) and $[\text{Ge}_9\{\text{Si}(\text{TMS})_3\}_2]^{2-}$ (red line/bottom) in $\text{THF-}d_8$	141
Figure 5.43. Comparison of $^{29}\text{Si-INEPT}$ NMRs of silylation product of $\text{K}_{12}\text{Ge}_{17}$ with <i>hyp</i> -Cl (6 eq., blue line/top) and $[\text{Ge}_9\{\text{Si}(\text{TMS})_3\}_2]^{2-}$ (red line/bottom) in $\text{THF-}d_8$	142
Figure 5.44. Ge 3d XPS spectra of inverse opal structured thin films from $\text{K}_{12}\text{Si}_5\text{Ge}_{12}$, $\text{K}_{12}\text{Si}_8\text{Ge}_9$, $\text{K}_{12}\text{Si}_{12}\text{Ge}_5$ and $\text{K}_{12}\text{Si}_{17}$ a) without and b) after 40 min of Ar^+ sputtering.	143

List of Tables

Table 2.1. List of reagents used within this thesis.	25
Table 2.2. Net weights for synthesis of $K_{12}Si_{17-x}Ge_x$ compounds.....	33
Table 2.3. Net weights for synthesis of $Rb_{12}Si_{17-x}Ge_x$ compounds.	34
Table 2.4. Net weights for synthesis of $K_4Si_{4-x}Ge_x$ compounds.	35
Table 3.1. Parameters obtained from complex conductivity of germanium thin films using the Drude-Smith model (equation 1) at room temperature (295 K).....	48
Table 3.2. Solubility of $K_{12}Si_{17-x}Ge_x$ -phases ($x = 0, 5, 9, 12, 17$) in <i>en</i>	58
Table 3.3. Solubility of $K_4Si_{4-x}Ge_x$ -phases ($x = 0, 1.2, 2.1, 2.8, 4$) in <i>en</i>	59
Table 3.4. Elemental composition of dried residues from $K_{12}Si_{17-x}Ge_x/en$ solutions.	60
Table 3.5. Elemental composition of annealed residues from $K_{12}Si_{17-x}Ge_x/en$ solutions.	63
Table 3.6. Elemental composition (EDX) and size distribution of the empty spheres in inverse opal structured thin films from $K_{12}Si_{17-x}Ge_x$	70
Table 3.7. Parameters obtained from complex conductivity $\sigma(\omega)$ plots of inverse opal structured thin films using the Drude-Smith model (equation 1) at room temperature (295 K).....	79
Table 3.8. Elemental composition (EDX) of dried $Se/K_4Ge_9/en$ mixtures.	83
Table 3.9. Elemental composition (EDX) of Sn/Bi thin films after treatment with various linkers at different concentrations.	86
Table 3.10. Crystallographic data of $K(2.2.2-crypt)[Si_{1.68(1)}Ge_{7.32(1)}(hyp)_3]$	95
Table 3.11. Comparison of the ZINTL cluster shape in $K(2.2.2-crypt)[Si_{1.68(1)}Ge_{7.32(1)}(hyp)_3]$ with literature known compound $K(2.2.2-crypt)[Ge_9(hyp)_3]$ [162]	96
Table 3.12. Elemental composition (EDX) of $K(2.2.2-crypt)[Si_{1.68(1)}Ge_{7.32(1)}(hyp)_3]$ (red blocks) compared to the values obtained for orange needles found in the same crystallization experiment.	97
Table 3.13. Crystallographic data of $[(NHC^{Dipp}Cu)_2\{\eta^3, \eta^3-Ge_9(Si(TMS)_3)_2\}]$	105

Table 3.14. Comparison of the ZINTL cluster shape in $[(\text{NHC}^{\text{Dipp}}\text{Cu})_2\{\eta^3, \eta^3\text{-Ge}_9(\text{Si}(\text{TMS})_3)_2\}]$ with literature known compounds $[(\text{NHC}^{\text{Dipp}}\text{Cu})\{\eta^3\text{-Ge}_9(\text{Si}(\text{R})_3)_3\}]$ (R = TMS ^[269] , ^t Bu ^[163]).	106
Table 3.15. Selected distances and angles in $[(\text{NHC}^{\text{Dipp}}\text{Cu})_2\{\eta^3, \eta^3\text{-Ge}_9(\text{Si}(\text{TMS})_3)_2\}]$	107
Table 5.1. Values for bi-exponential signal decay in fluence dependent measurements of an inverse opal structured thin film from $\text{K}_{12}\text{Si}_5\text{Ge}_{12}$ at room temperature (295 K).	119
Table 5.2. Values for bi-exponential signal decay in temperature dependent measurements of an inverse opal structured thin film from $\text{K}_{12}\text{Si}_5\text{Ge}_{12}$ at $F = 810 \mu\text{J}/\text{cm}^2$	119
Table 5.3. Values for single exponential signal decay in fluence dependent measurements of an inverse opal structured thin film from $\text{K}_{12}\text{Si}_{12}\text{Ge}_5$ at room temperature (295 K).	119
Table 5.4. Values for single exponential signal decay in temperature dependent measurements of an inverse opal structured thin film from $\text{K}_{12}\text{Si}_{12}\text{Ge}_5$ at $F = 810 \mu\text{J}/\text{cm}^2$	120
Table 5.5. Values for single exponential signal decay in fluence dependent measurements of an inverse opal structured thin film from $\text{K}_{12}\text{Si}_{17}$ at room temperature (295 K).	120
Table 5.6. Parameters obtained from complex conductivity of an inverse opal structured thin from $\text{K}_{12}\text{Si}_5\text{Ge}_{12}$ using the Drude-Smith model at room temperature (295 K).	120
Table 5.7. Parameters obtained from complex conductivity of an inverse opal structured thin from $\text{K}_{12}\text{Si}_5\text{Ge}_{12}$ using the Drude-Smith model at $F = 810 \mu\text{J}/\text{cm}^2$	120
Table 5.8. Parameters obtained from complex conductivity of an inverse opal structured thin from $\text{K}_{12}\text{Si}_{12}\text{Ge}_5$ using the Drude-Smith model at room temperature (295 K).	121
Table 5.9. Parameters obtained from complex conductivity of an inverse opal structured thin from $\text{K}_{12}\text{Si}_{12}\text{Ge}_5$ using the Drude-Smith model at $F = 810 \mu\text{J}/\text{cm}^2$	121

Table 5.10. Parameters obtained from complex conductivity of an inverse opal structured thin film from $K_{12}Si_{17}$ using the Drude-Smith model at room temperature (295 K).	121
Table 5.11. Fractional site occupation of cluster atoms in $K(2.2.2\text{-crypt})[Si_{1.68}Ge_{7.32}(hyp)_3]$	128
Table 5.12. Selected bond lengths in $K(2.2.2\text{-crypt})[Si_{1.68}Ge_{7.32}(hyp)_3]$	128
Table 5.13. Selected bond lengths and angles in $[(NHC^{Dipp}Cu)_2\{\eta^3\text{-Ge}_9(\text{Si}(\text{TMS})_3)_2\}]$	129
Table 5.14. Originally obtained and shifted theoretical values for cluster exo bond vibrations in $[Si_2Ge_7\{Si(\text{SiH}_3)_3\}_3]^-$	131
Table 5.15. Relative occupancy of Ge oxidation states on the surface of inverse opal structured thin films (without sputtering) for Ge 2p.	143
Table 5.16. Relative occupancy of Ge oxidation states in the inner structure of inverse opal structured thin films (after 40 min of Ar^+ sputtering) for Ge 2p.	143
Table 5.17. Relative occupancy of Ge oxidation states on the surface of inverse opal structured thin films (without sputtering) for Ge 3d.	144
Table 5.18. Relative occupancy of Ge oxidation states in the inner structure of inverse opal structured thin films (after 40 min of Ar^+ sputtering) for Ge 3d.	144

1 Introduction

1.1 Energy Reform

Global energy consumption is at an all-time high and is projected to rise even further.^[1] However, the role of nuclear energy is frequently questioned for safety reasons of active power plants (e. g. accident in the Fukushima nuclear power plant in 2011) and impact of long-term storage of nuclear waste.^[2-4] Fossil fuels like natural gas, coal and petroleum are projected to be depleted within the next century and are a main source of the anthropogenic climate change through emission of CO₂.^[5-7] The climate change is one of the most discussed topics nowadays as it is responsible for the melting of glaciers and polar ice caps^[8], acidification of oceans^[9] and the increasing number of extreme weather events^[10]. Therefore, renewable sources like wind energy, tidal and geothermal power as well as solar energy are projected to become increasingly important (see Figure 1.1).^[1] Renewable energy technologies benefit from an overall low impact on CO₂ emission based on their lifecycle (g CO₂/kWh) when compared to fossil fuels.^[6]

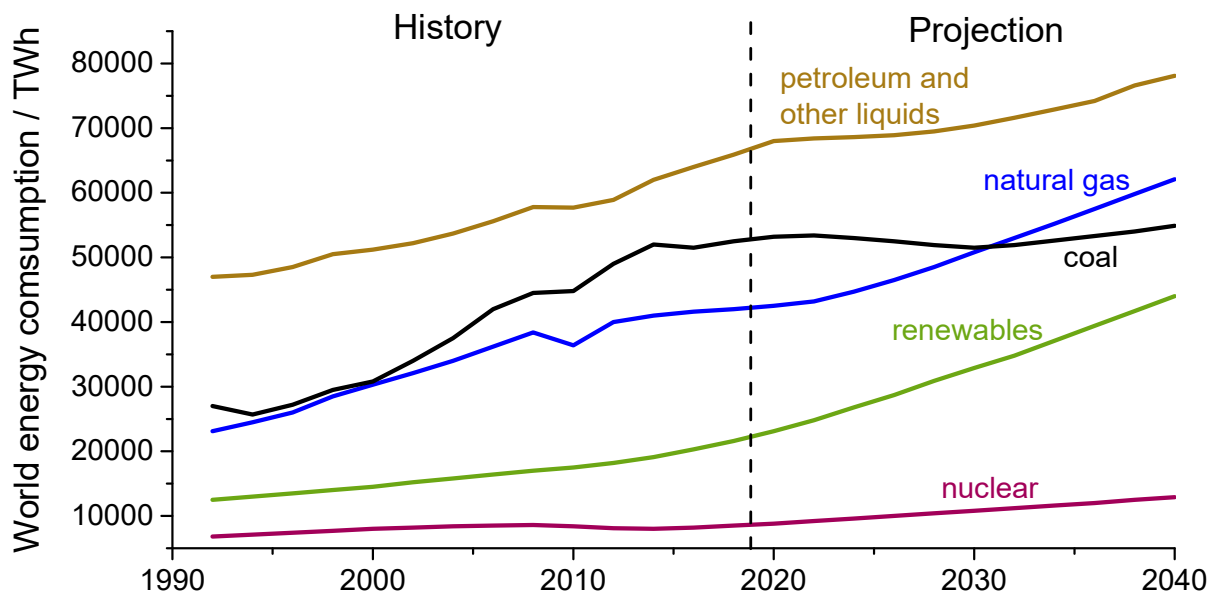


Figure 1.1. World energy consumption in TWh. Historical data since 1992 and projected data until 2040 are displayed.^[1]

However, the amount of renewable energy in global energy consumption is still low (12% in 2015).^[11] In Germany, the transition of energy consumption towards renewables was accelerated after the accident in the Fukushima nuclear power plant in 2011 and includes the goal of reduction of greenhouse gases by at least 80-95% by

Introduction

the year 2050.^[12] The value of renewable energy in Germany drastically increased since the year 2000 (6% of total energy production) and reached 33.3% by 2017 (see Figure 1.2).^[13] This value is supposed to reach 40-45% by the year 2025 as defined in the renewable energy law revised in 2014 (“Erneuerbare-Energien-Gesetz”, EEG).^[13] As renewable energies often require special environmental conditions (e. g. wind energy or solar energy), energy storage systems gain importance as well. To balance supply and demand of energy, large sodium sulfur and lithium ion battery parks with energy storage capabilities similar to those of pumped hydro facilities were built recently.^[14-16]

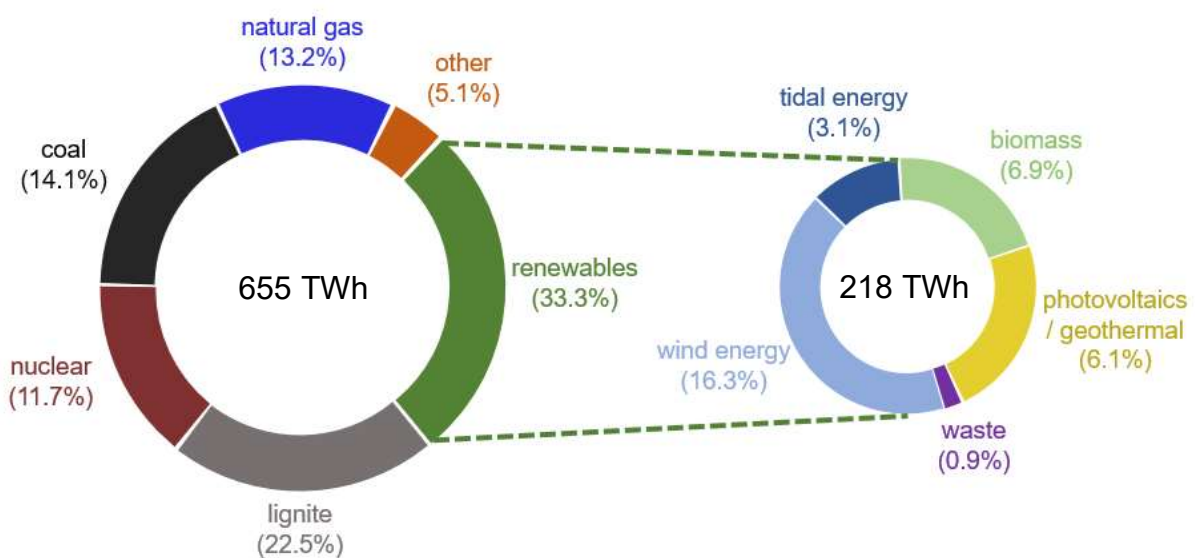


Figure 1.2. Total energy gross production by energy source in Germany in 2017.^[13] Geothermal energy is included in photovoltaics due to its low value.

In means of energy production, solar energy remains the renewable energy source with the highest untapped value. The sun represents an effectively unlimited energy supply at no cost and the surface of the earth receives about 100.000 TW of solar power every hour, which is nearly enough power to supply the global energy need for a year. When coupled with effective energy storage facilities to balance supply and demand, solar energy can be the most promising carbon-free technology.^[17] However, long-term stability issues still limit the use of most promising solar cell types (see chapter 1.2). Solar cells converting solar into electric energy were first established for satellites like Vanguard 1 (1959) by the NASA (National Aeronautics and Space Administration, USA) in which crystalline silicon cells producing about 1 W with an efficiency of 10% were used.^[18, 19] Since then, a variety of different modules have been developed. However, most commercially available modules are still confined to

polycrystalline or monocrystalline silicon due to its natural abundance in earth's crust (27.72%, mostly in form of silicates)^[20] and therefore comparably low production cost. Modern undoped crystalline silicon modules are approaching the theoretical efficiency limit of 29.43%.^[21] Recently, an efficiency of 26.63% was achieved in an amorphous silicon/crystalline silicon heterojunction cell with interdigitated back contacts (both positive and negative contacts on the back of the cell).^[22] This value can be boosted by application of multijunction solar cells introducing multiple layers of different semiconducting materials. Values beyond the theoretical efficiency limit for pure silicon solar cells can be achieved by direct wafer bonding of thin films of multiple III-V semiconductors such as Ga-In-P and Al-Ga-As in combination with silicon, boosting light absorption in the visible light and near ultraviolet (UV) region.^[23, 24] The recent maximum efficiency for such a monolithic multiple junction solar cell involving silicon is 34.1%.^[23] However, commercially available silicon solar cells only produce efficiencies of 15-18% (polycrystalline silicon cells) to values just beyond 20% (monocrystalline silicon cells).^[25]

In comparison, germanium is quite uncommon in the earth's crust (natural abundance: 0.0004%)^[20] and is industrially obtained as a by-product from processing zinc ores.^[26] However, germanium exhibits a higher charge carrier mobility^[27, 28] and shows better optoelectronic properties^[29, 30] than silicon. Therefore, an increasing amount of germanium has been used in solar cells^[31-33] and as anodes in lithium ion batteries^[34-37] recently. Efforts also include alloying silicon with germanium for use in solar cells or using both semiconductors in multiple junction solar cells to enhance efficiency (e. g. by tailoring the band gap of the semiconducting material).^[38-41] Germanium was also introduced in bottom-up approaches using Ge₉ clusters in solution as a basis for unstructured^[42] or inverse opal structured^[43, 44] thin films for application in hybrid solar cells as well as anodes in lithium ion batteries.

1.2 Flexible Solar Cells – Types and Functionality

As described in chapter 1.1, most commercial solar cells consist of polycrystalline or monocrystalline silicon. However, a new generation of solar cells is on the rise due to several advantages in comparison to common silicon solar cells. Dye-sensitized solar cells (DSSCs), perovskite solar cells and polymer solar cells can be synthesized *via* solution-based methods like spin-coating, spray-coating or printing, enabling device fabrication on a large scale at ambient temperatures.^[45, 46] Additionally, such solar cells produce lower processing costs and have less environmental impact.^[46-48] However, their greatest advantage over common silicon solar cells is that their lightweight, flexibility and transparency due to their plastic casing. In contrast to common silicon solar cells, portable, wearable^[49] and even window tinting^[50] applications can be realized.^[51] The following chapters describe the functionality of these solar cells types.

1.2.1 Dye-Sensitized Solar Cell (DSSC)

DSSCs are comprised of five different layers (see Figure 1.3). A transparent anode is created by treating a plastic or glass substrate with a transparent conductive oxide (TCO) like indium tin oxide (ITO) or fluorine doped tin oxide (FTO).^[46, 52, 53] The anode is followed by a layer of mesoporous oxide (usually TiO₂ in anatase structure) with a high surface area to improve electronic conduction. A monolayer of charge transfer dye (traditionally Ru complexes^[54], in recent cells also perovskites^[55]) is covalently attached to the surface of this mesoporous oxide to enhance light absorption. The dye is in direct contact with an electrolyte (usually acetonitrile) containing a redox mediator (usually I⁻/I₃⁻) to improve regeneration of the dye by electron transport through the electrolyte solution. The back side of the device is closed by another transparent conductive oxide on a plastic or glass substrate. However, this cathode side is coated with a catalyst (usually gold or platinum) to facilitate electron collection.^[46, 52, 53]

When the dye is photo-excited and oxidized by exposure to sunlight, in turn it oxidizes the redox mediator. The electrons move to the conduction band of the mesoporous TiO₂ film, diffuse to the anode (see Figure 1.3) and are transported to the cathode through an external current. The dye cycle is then completed by the redox mediator (I⁻/I₃⁻) being regenerated at the cathode by these electrons. The porosity and morphology and therefore the surface area of the mesoporous TiO₂ layer is regulating

1.2 Flexible Solar Cells – Types and Functionality

the amount of dye molecules adsorbed and as a result the amount of incident light collected. Therefore, the mesoporous TiO_2 layer is important for both exciton separation and electron transfer processes in the device.^[46, 53]

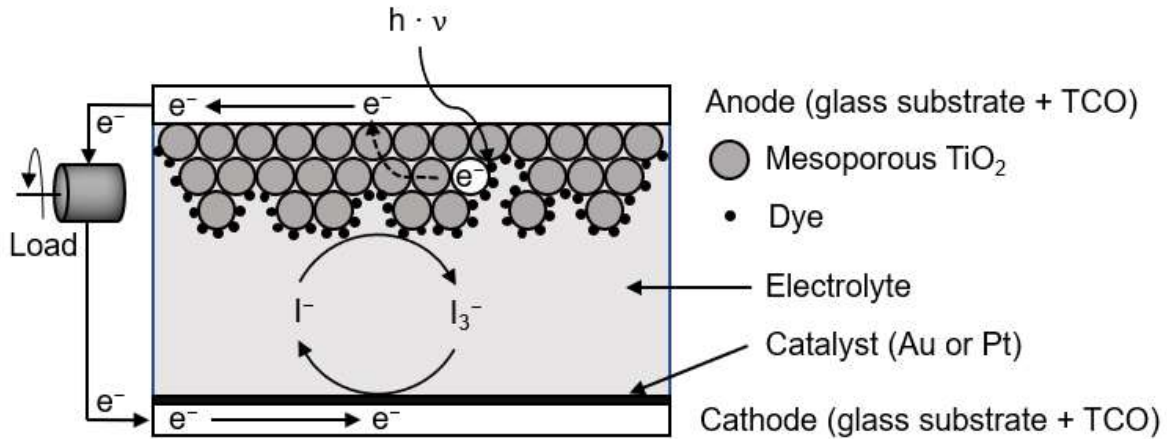


Figure 1.3. Schematic representation of a DSSC setup.^[52] Electrons from the photo-excited dye diffuse to the anode and are then transported to the cathode through an external current. The redox mediator (I^-/I_3^-) is oxidized by the dye completes the cycle by being regenerated by the electrons at the cathode. TCO: transparent conductive oxide.

Next to the general advantages of flexible solar cells, DSSC also work under comparably low-light conditions, hence being able to work under indirect sunlight and cloudy skies. Also, DSSCs show a better internal heat management than common silicon solar cells as thin plastic substrates allow for a fast heat dissipation. In contrast to silicon solar cells, higher temperatures also result in a higher efficiency for DSSCs. Remaining challenges of DSSCs are mainly associated with the liquid electrolyte and redox mediator being used. The liquid solvent is prone to expand or contract depending on the temperature, hence damaging the cell. This can result in leakage of toxic organic compounds and is preventing large-scale outdoor applications to date. Experiments replacing the electrolyte by a solid resulted in a higher degree of degradation operating the cell and therefore loss of long-term stability.^[46] DSSCs using traditional Ru-complex dyes achieved efficiencies of up to 11.2% in laboratory experiments.^[56] Other setups with high efficiency involved a combination of a porphyrin metal complex dye with an organic dye (12.3%^[57]) and perovskite dyes (15.0%^[55]). Therefore, efficiencies for DSSCs are still lower than values achieved for commercial solar cells, but their advantages could lead to commercial applications if the long-term stability of such devices is improved.

1.2.2 Perovskite Solar Cell

The perovskite structure ABX_3 ($CaTiO_3$ structure type) consists of corner-linked octahedrons of the X-anions with the A-cation occupying the center of the octahedrons (see Figure 1.4a). The B-cation meanwhile is occupying the center of a cuboctahedral coordination polyhedron with twelve X-anions in the coordination sphere.^[58] The perovskite structure has been known for many years, but the first incorporation into a solar cell was reported in 2009 with a efficiency of only 3.8%.^[59] However, the efficiency boost achieved for perovskite solar cells since then has been the fastest of all solar cell types with modern cells already challenging the best value found for a single junction silicon solar cell (26.7%^[22]).^[46, 60] Early reports on perovskite solar cells were based on a DSSC solar cell setup using perovskites as dyes. This setup was already able to produce decent efficiencies of up to 15.0%^[55]. However, it still suffered from common disadvantages of DSSCs emerging from the liquid electrolyte and redox mediator. Therefore, experiments were carried out using only solid components in perovskite solar cells. Fortunately, in 2012 the solid organic hole transport material (HTM) *spiro-OMeTAD* was introduced as a substitution for liquid electrolytes, improving the stability of the perovskite significantly and reached an efficiency of up to 9.7%.^[61]

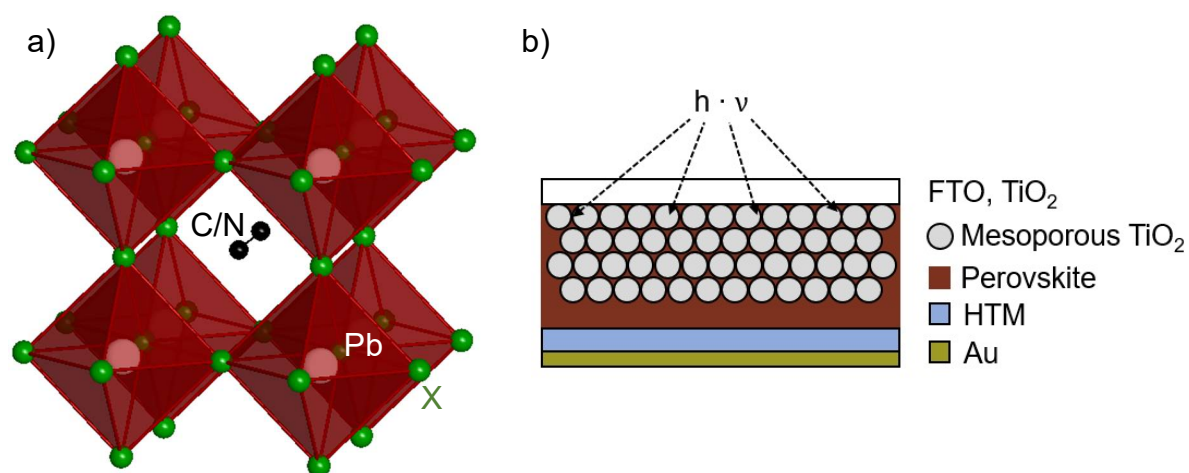


Figure 1.4. a) Molecular structure of $CH_3NH_3PbX_3$ ($X = I, Br$ and/or Cl) perovskites^[62] and b) schematic representation of a perovskite solar cell^[60]. Protons in the structure of a) are omitted due to clarity reasons. FTO: fluorine doped tin oxide, HTM: hole transport material.

Nowadays, perovskite solar cells usually are comprised of a FTO and TiO_2 layer on the front side of the device followed by either a mesoporous TiO_2 layer with perovskite or just a thin perovskite film (see Figure 1.4b). The perovskite material as the light-

1.2 Flexible Solar Cells – Types and Functionality

harvesting layer usually is lead or tin halide based ($\text{CH}_3\text{NH}_3\text{EX}_3$ with $E = \text{Pb}, \text{Sn}$; $X = \text{I}, \text{Br}$ and/or Cl). The perovskite is placed in between an electron transport material (ETM, usually mesoporous and/or flat TiO_2 on the front side of the device) and a hole transport material (HTM). For the latter, solid films of several organic molecules have been established. The electrode on the back side of the cell usually is a thermally evaporated gold layer.^[46, 63]

Perovskite solar cells utilize a donor-acceptor setup like polymer solar cells.^[46] However, in case of perovskite cells charge carrier generation occurs by photo-excitation of electrons to the LUMO (lowest unoccupied molecular orbital) of the perovskite. Electrons are transported through the TiO_2 conduction band to the FTO-layer. Meanwhile, the holes are transported through the HOMO (highest occupied molecular orbital) of the hole transport material to the gold electrode. Electron and hole transport layers in these cells are boosting the charge carrier mobility (free carriers) and therefore result in a low recombination rate.^[46, 64] This advantage lead to a fast rise in efficiencies since the development of solid hole transport materials. It was also found that a mixture of halides as well as mixed cations in the perovskite structure has a positive influence on the stability as well as the performance of the cell.^[65, 66] For example, the highest value for a single-junction perovskite solar cell was reported for a mixture of Br and I perovskite at 22.1%.^[65] However, tandem solar cell combining perovskite with silicon are able to reach even higher values. Recently, such a tandem solar cell achieved a 27.3% conversion efficiency, exceeding the current record for single-junction silicon solar cells.^[67]

The greatest challenge for perovskite solar cells is their short-term and long-term stability. This instability is attributed to degradation by environmental conditions like moisture^[68], oxygen^[69] and light (visible and UV)^[69, 70] as well as thermal^[70, 71] degradation. To overcome these mechanisms, several encapsulation techniques for the active materials were tested.^[72] For example, exchanging the hole transport material with a composite of carbon nanotubes (CNTs) in an inert polymer matrix proved to result in a decent resistance for thermal degradation as well as degradation by moisture and air.^[73] However, next to environmental conditions perovskite solar cells also face mechanical degradation of the active layers.^[74] So far, the highest efficiency achieved in long-term stability experiments of large scale (10 x 10 cm) perovskite solar cells is 11.2%.^[75] Therefore, stability issues are still limiting the commercial application of perovskite solar cells.

1.2.3 Polymer and Hybrid Solar Cell

Polymer solar cells utilize a donor-acceptor setup between organic polymers or small organic molecules for light absorption and charge transport. Instead of free carriers, excitons (bound state of an electron and an electron hole by electrostatic interactions) are generated by photo-excitation through solar radiation.^[46] Polymer solar cells can roughly be classified in three different architectures.^[64, 76] In a regular architecture, a transparent anode comprised of ITO glass is followed by a hole transporting material (usually PEDOT:PSS, a mixture of poly[3,4-ethylenedioxy-thiophene] and polystyrene sulfonate).^[76] The active layer is comprised of a donor and acceptor material (see Figure 1.5) followed by a low work-function reflective metal cathode (usually Al or Ca) on the back side of the device.^[46, 76] However, there are also inverted architectures where the transparent and light receiving side of the device is the cathode. In these cases, the cathode is comprised of ITO glass and the reflective anode on the back side of the device is a high work-function metal electrode (usually Ag or Au).^[46, 76] Another possibility is a tandem architecture using several active layers.^[76] Next to various architectures of the cell, the morphology and content of the active layer is important. Historically, polymer solar cells were comprised of only a single layer of active material in form of small organic molecules or polymers. However, these devices only yielded up to 0.3% efficiency due to high recombination rates of excitons through insufficient separation of electrons and holes.^[77] Nowadays, active layers in polymer solar cells are either comprised of a thin planar bilayer (see Figure 1.5a) or controlled growth as well as bulk heterojunction (see Figure 1.5b) setup of a donor and an acceptor.^[78]

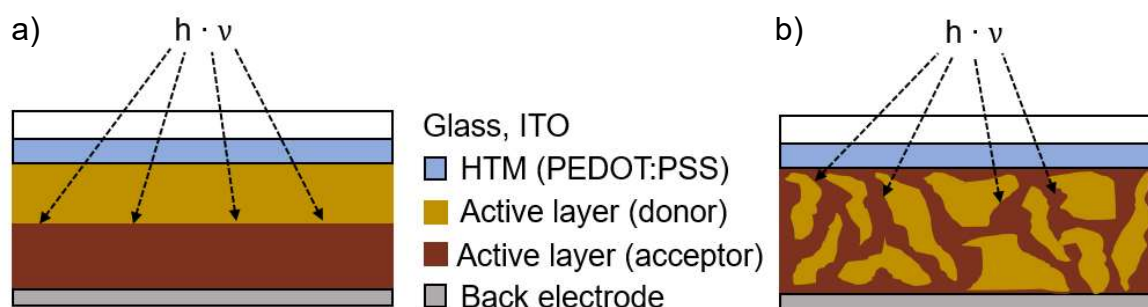


Figure 1.5. Schematic representation of different morphologies of the active layer in polymer solar cells with a regular architecture. a) planar bilayer and b) bulk heterojunction setup.^[64, 76] Charge separation of excitons created at the donor/acceptor interface: electrons are transported by the acceptor to the back electrode (cathode) and holes diffuse through a hole transport material (HTM, usually PEDOT:PSS) to the anode (indium tin oxide, ITO). Inverted architectures for both setups are also known.

1.2 Flexible Solar Cells – Types and Functionality

Charge separation of excitons into free electron/hole pairs at the donor-acceptor interface of these cells is depicted in Figure 1.6. The band gap of donor and acceptor materials is therefore defined as the gap between HOMO and LUMO level in these materials.^[46] The open circuit voltage V_{oc} of the cell is defined as the difference between the HOMO of the donor material and the LUMO of the acceptor material and is the driving force for charge separation.^[46, 78] When electrons are photo-excited at the donor/acceptor interface of a polymer solar cell with a regular architecture, the resulting excitons are charge separated by the electron diffusing through the acceptor towards the cathode. Meanwhile the electron holes are diffusing through the donor material and the hole transport material (HTM, usually PEDOT:PSS) to the indium tin oxide (ITO) anode. Donor and acceptor domains in bulk heterojunction materials should be around twice the size of exciton diffusion length (≈ 10 nm), allowing excitons to reach the donor-acceptor interface before recombination.^[78]

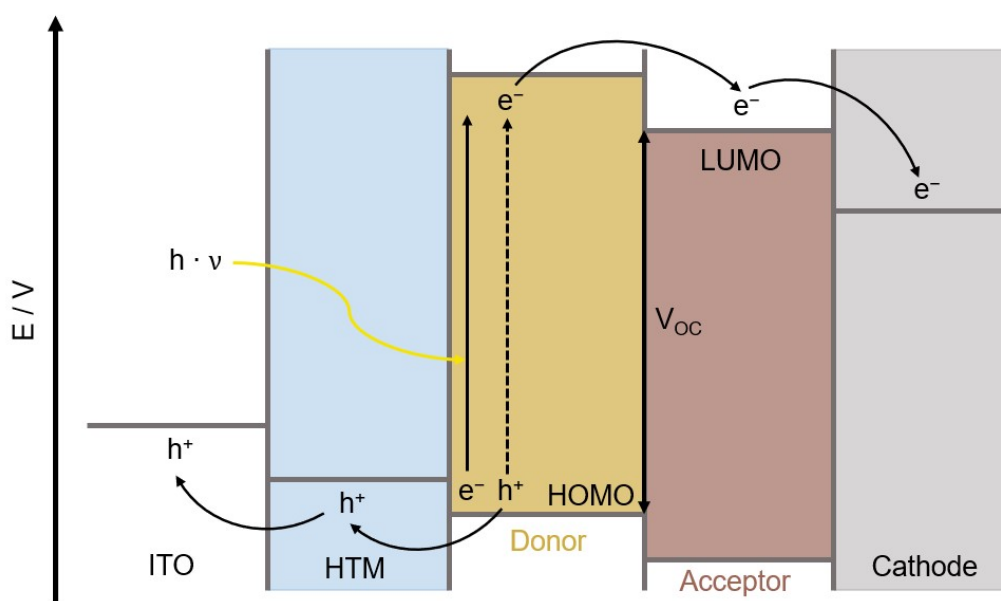


Figure 1.6. Operating mechanism of a polymer solar cell with a regular architecture.^[64, 78] Charge separation of excitons into free electron/hole pairs is achieved at the donor-acceptor interface in the active layer of the cell.

A wide range of compounds has been tested as donors and acceptors in polymer solar cells. Conjugated carbon-carbon double bonds are common to all of them as they are responsible for electronic properties and low-energy optical transitions.^[46] Most polymer solar cells consist of a polymer donor which is responsible for light absorption and a fullerene acceptor (weak absorber of visible and near-infrared light).^[76]

Introduction

Traditionally, the most common donor was P3HT (poly[3-hexylthiophene-2,5-diyl], see Figure 1.7) due to its wide band gap of ≈ 2.1 eV, good solubility in organic solvents and ability to self-assemble.^[46, 76] However, research has been focused to new donors with a smaller optical bandgap to broaden absorption range into the infrared (IR) while still exhibiting suitable LUMO levels for efficient electron transfer to the fullerene moiety. Suitable copolymers like PTB7 (poly[[4,8-bis[(2-ethylhexyl)oxy]benzo[1,2-b:4,5-b']-dithiophene-2,6-diyl][3-fluoro-2-[(2-ethylhexyl)carbonyl]thieno[3-b]thiophenediyl]]) were developed as a result.^[76] Fullerenes were introduced as acceptors in 1992 by application of the Buckminsterfullerene C_{60} in a polymer solar cell.^[79] However, the low solubility of C_{60} in common solvents soon led to the functionalization of C_{60} and C_{70} as a common practice to improve solubility. Therefore, $PC_{61}BM$ ^[80, 81] (see Figure 1.7) and its analogue $PC_{71}BM$ ^[82] soon emerged as the most common acceptors in polymer solar cells.

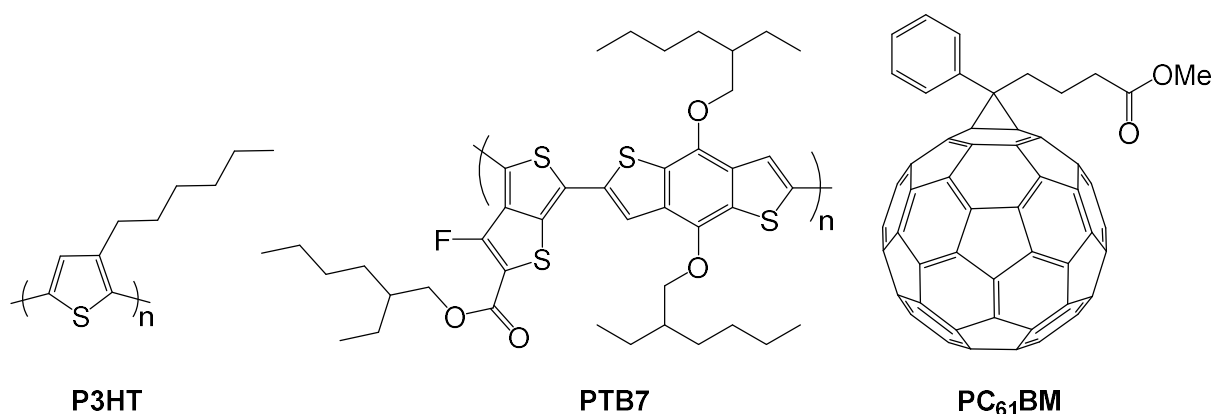


Figure 1.7. Structures of common donors (P3HT and PTB7) and acceptor ($PC_{61}BM$) in active layers of polymer solar cells.

However, commercialization of polymer solar cells wasn't successful so far. Despite their advantages in means of flexibility, processability and low cost, they face similar stability issues as other flexible solar cells. Instability against oxidative and reductive conditions as well as temperature variation leads to degradation of the solar cells. This occurs to different degrees when using different donors and acceptors in the active layer.^[46] Also, exciton diffusion length and therefore recombination rate as well as charge separation issues limit the efficiencies achieved to date. Therefore, efficiencies for polymer solar cells with binary active layers have been limited to about 10%.^[46] Slightly higher values were achieved by adding another component to the active layer. These ternary active layers achieved up to 11.2%^[83] efficiency for fullerene based and 13.7%^[84] in non-fullerene based devices so far. Recently, by addition of an electron

transport material (ETM) in form of perylene diimides^[85], an efficiency of 15.7% was achieved in a device containing an organic dye as acceptor.^[86] For tandem cells using multiple active layers, an efficiency of 17.3%^[87] was achieved recently. To address some of these issues, hybrid solar cells combining advantages of both organic and inorganic semiconductors have attracted considerable interest.^[88] Typically, inorganic materials in these hybrid cells are used as the acceptor and electron transport material.^[89] The active layer in these cells usually is comprised of a bulk heterojunction setup with a high surface area to achieve decent efficiencies.^[90, 91]

1.3 Inverse Opal Structured Thin Films of Semiconductors

One way to achieve an inorganic semiconductor structure with high surface area as desired for hybrid solar cells is using polymer template beads. Polymer template beads of poly(methyl methacrylate) or polystyrene (PMMA^[92, 93] or PS^[94]) can be synthesized with a narrow size distribution. When dispersed in water they can be used in various coating processes onto a broad range of substrates to form highly regular opal structured thin films.^[93-95] Inverse opal structured films can be prepared by chemical vapor deposition (CVD) of hydrides (e. g. Ge₂H₆) onto opal structured templates.^[96] Another approach is the electrodeposition of semiconducting materials in Teflon coated cells to avoid reaction with the reactants.^[97] An indium tin oxide (ITO) working electrode is thereby coated with the template and halides of semiconducting materials (e. g. ECl₄ for E = Si^[98, 99], Ge^[97-99]) as well as mixtures with AlCl₃^[99] are deposited by applying a constant potential. In these cells, a Pt-wire is used as a counter electrode and an Ag wire is used as a quasi-reference electrode. These reactions usually take place in ionic liquids due to common organic solvents producing hydrogen instead of facilitating the deposition of the halides.^[97] After removal of the template, inverse opal structured thin films of Ge or bilayer films of Ge/Si or Ge/Al are obtained.^[97] However, N. Chandrasekharan and S. C. Sevov also showed that anodic electrodeposition of thin germanium films using the ZINTL phase K₄Ge₉ in ethylene diamine (*en*) as a precursor is possible in a Teflon cuvette under nitrogen atmosphere.^[42] Deposition of [Ge₉]⁴⁻ clusters occurred on a B-doped silicon wafer as the anode while a Cu-wire was used as the counter electrode.^[42]

Introduction

ZINTL ions of group 14-16 elements in solution were widely investigated for their ability to form nanostructures with tunable composition and electronic properties. For example, adamantane structured $[E_4Q_{10}]^{4-}$ clusters (with $E = \text{Ge, Sn}$ and $Q = \text{S, Se, Te}$)^[100, 101] as well as $[\text{SnSe}_4]^{4-}$ ^[101, 102] and $[\text{Sn}_2\text{Se}_6]^{4-}$ ^[101] were linked by a broad range of (transition) metal salts in the presence of the surfactant cetylpyridinium bromide (CPBr) acting as a template. However, the resulting periodic nanostructured semiconductors contained high values of organic material from the surfactant.^[100, 102] Additional surfactant-templated nanostructured semiconductors were found by the self-assembly of $[\text{EQ}_4]^{4-}$ (with $E = \text{Ge, Sn}$ and $Q = \text{Se, Te}$) as well as $[\text{E}_4\text{Se}_{10}]^{4-}$ (with $E = \text{Ge, Sn}$) clusters linked by Pt, Rh, Ir and Ni salts in the presence of cetyltriethylammonium bromide (CTEABr) as the surfactant.^[103-105]

Recently, a wet-chemical approach by Bentlohner *et al.* utilized the ZINTL phase K_4Ge_9 in solution yielding inverse opal structured germanium.^[43] PMMA beads dispersed in water were dip coated onto various substrates (Si, SiO_2 , Al_2O_3 , ITO or FTO). A solution of K_4Ge_9 in *en* was drop casted onto the PMMA coated substrates and residual solvent removed under ambient conditions. GeCl_4 was used as a linker to obtain inverse opal structured thin germanium films after annealing. Depending on the annealing temperature and time, either amorphous or crystalline thin germanium films could be obtained.^[43] These inverse opal structured films were tested as anodes in lithium batteries (using Cu substrates) and yielded a high capacity retention (good long-term stability).^[44]

Inverse opal structured films of group 14 elements like germanium provide a high surface area (due to their porosity) and mechanical stability, making them potential candidates for several applications. Therefore, a focus of this work was to broaden the range of precursor materials to yield tunable conditions for these structured films with high surface area while investigating properties like carrier behavior to evaluate potential applications.

1.4 ZINTL clusters – Properties and Reactivity in Solution

Polyanions of main group elements were first observed by A. Joannis in 1891.^[106] The reaction of Pb and Na in liquid ammonia led to the formation of a green colored solution, which was later determined as the formation of $[\text{Pb}_9]^{4-}$ and was the starting point for deltahedral anions.^[107] Successive research in this area was carried out by Smyth^[108], Kraus^[109-112] and Zintl^[113-117]. The term ZINTL phase (where these polyanions can be derived from) was posthumously introduced by F. Laves in 1941 in recognition of Eduard Zintl's work in the area.^[118] The molecular structure of Group 14 element polyanions was verified by crystal structure determination of $[\text{Sn}_9]^{4-}$.^[119, 120] A significant breakthrough in the crystallization of these ZINTL clusters was achieved by addition of sequestering agents like 2.2.2-crypt (4,7,13,16,21,24-hexaoxa-1,10-diazabicyclo-[8.8.8]hexacosane) or 18-crown-6 (1,7,10,13,16-hexaoxacyclooctadecane) which facilitate crystal growth.^[121-124]

1.4.1 Deltahedral Group 14 Element Clusters – Structure and Solubility

ZINTL phases are salt-like compounds consisting of an alkali metal or alkaline earth element (Group 1 or 2) and a post transition p-block (semi)metal (Group 13-16). The Zintl-Klemm concept states that valence electrons of the Group 1 or 2 metal are formally transferred to the polyanionic substructure, thus following the $(8-N)$ rule.^[107] As a result, polyanions can be formed as one-dimensional chains, two- or three-dimensional networks or clusters with oxidation states in these structures ranging from 0 to -1 . For Group 14 elements, the smallest deltahedral clusters $[\text{E}_4]^{4-}$ ($\text{E} = \text{Si-Pb}$, tetrahedrons) were first observed as binary compounds with alkali metals ($\text{A} = \text{Na-Cs}$) in a 1:1 ratio (A_4E_4 phases).^[125-128] D_{3h} symmetric bipyramidal $[\text{E}_5]^{2-}$ clusters ($\text{E} = \text{Ge-Pb}$) were obtained from ethylenediamine (*en*) solutions of A-E alloys with various ratios by addition of 2.2.2-crypt.^[129, 130] The corresponding $[\text{Si}_5]^{2-}$ cluster was synthesized by extraction of $\text{K}_6\text{Rb}_6\text{Si}_{17}$ with liquid ammonia in the presence of 2.2.2-crypt.^[131] These intermetallic $\text{A}_{12}\text{E}_{17}$ compounds ($\text{A} = \text{Na-Cs}$; $\text{E} = \text{Si-Pb}$) contain tetrahedral $[\text{E}_4]^{4-}$ as well as $[\text{E}_9]^{4-}$ clusters in a 2:1 ratio.^[132, 133] Except for silicon, the corresponding A_4E_9 ($\text{A} = \text{K-Cs}$; $\text{E} = \text{Ge-Pb}$) phases only containing $[\text{E}_9]^{4-}$ clusters could also be synthesized by alloying stoichiometric amounts of the elements.^[132, 133] The largest homoatomic Group 14 element clusters are $[\text{E}_{10}]^{2-}$ clusters ($\text{E} = \text{Ge, Pb}$; bi-capped square antiprisms) which were crystallized from *en* solutions in the presence

Introduction

of 2.2.2-crypt.^[134, 135] In contrast to other elements (e. g. Group 13 ^[122]), no homoatomic, ligand-free clusters of Group 14 elements with six, seven, eight or more than ten vertices have been detected in solution so far. The structures of tetrahedral $[E_4]^{4-}$, trigonal bipyramidal $[E_5]^{2-}$ and bi-capped square antiprismatic $[E_{10}]^{2-}$ clusters follow Wade's rule developed for deltahedral boranes and correspond to a *nido* cluster with 12 skeletal electrons ($[E_4]^{4-}$), *closo* cluster with 12 skeletal electrons ($[E_5]^{2-}$) and *closo* cluster with 22 skeletal electrons ($[E_{10}]^{2-}$).^[136, 137] These clusters are thereby depicted as delocalized and electron deficient systems with each vertex (n) contributing two electrons to bond within the cluster. However, nine atomic clusters of Group 14 elements display structural flexibility (see Figure 1.8). $[E_9]^{4-}$ clusters can be described as C_{4v} symmetric mono-capped square antiprisms with 22 skeletal electrons and are thereby classified as *nido* clusters ($2n+4$ skeletal electrons with n = number of vertices plus fourfold negative charge).^[136, 137] Although, $[E_9]^{4-}$ clusters often appear in distorted structures. Through this structural flexibility, other charges can be adopted by the polyanions ($[E_9]^{3-}$ and $[E_9]^{2-}$). $[E_9]^{2-}$ clusters can also be described as D_{3h} symmetric tri-capped trigonal prisms with 20 skeletal electrons and are thereby classified as *closo* clusters ($2n+2$ skeletal electrons).^[136, 137]

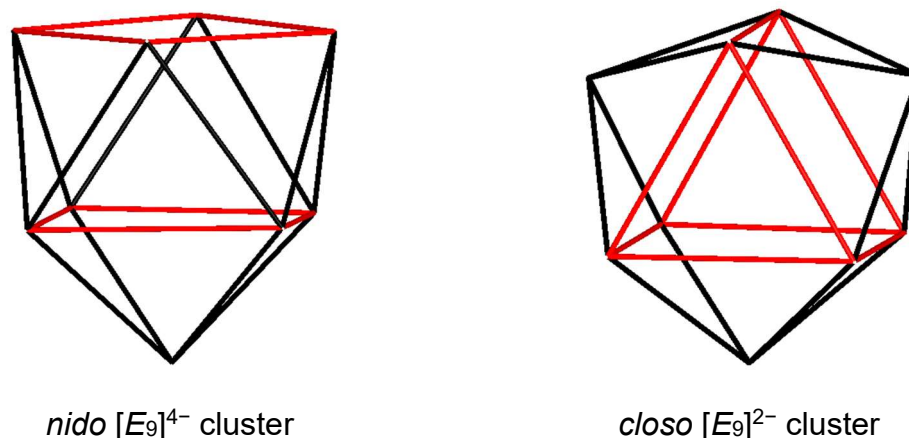


Figure 1.8. Structures of $[E_9]^{4-}$ and $[E_9]^{2-}$ clusters in comparison. C_{4v} symmetric mono-capped square antiprism of *nido* $[E_9]^{4-}$ cluster (left) and D_{3h} symmetric tri-capped trigonal prism of *closo* $[E_9]^{2-}$ cluster (right). E = Si–Pb. Square planes (left) and trigonal prism (right) are highlighted in red.

ZINTL phases of Group 14 elements are at least partially soluble in highly polar solvents such as liquid ammonia^[108-110, 113-115, 138-140], *en*^[119, 120] or DMF (dimethyl formamide)^[141]. Additional solvents such as pyridine can be used after prior activation of ZINTL phases in liquid ammonia.^[142] ZINTL clusters are retained in solution and are therefore accessible for further reactions.^[143]

1.4.2 Organo-Functionalization and Silylation of Group 14 Element Clusters

Solubility of bare Si/Ge clusters is heavily limited to a few highly polar solvents due to their high charge. Therefore, a growing interest has been placed in lowering the charge of clusters by attaching substituents to them, achieving a shift in polarity. Prominent examples feature organo-functionalization with bis(trimethylsilyl)acetylene, yielding vinylated $[E_9(\text{CH}=\text{CH}_2)]^{3-}$ ($E = \text{Ge}^{[144, 145]}$, $\text{Sn}^{[146]}$), $[\text{Ge}_9(\text{CH}=\text{CH}_2)_2]^{2-}$ ^[144, 145, 147, 148] or $[\text{CH}_2=\text{CH}-\text{Ge}_9-\text{Ge}_9-\text{CH}=\text{CH}_2]^{4-}$ ^[149] clusters. Other acetylene derivatives ^[146, 148, 150, 151], alkyl ^[146, 150, 152] and aryl ^[145] substituents were introduced to $[E_9]^{4-}$ clusters ($E = \text{Ge}, \text{Sn}$) via single exo bonds as well. Recently, an extension of the conjugated electron system of $[\text{Ge}_9]^{4-}$ clusters was achieved by linking two clusters with conjugated organic building blocks, resulting in the isolation of $[\text{R}-\text{Ge}_9-\text{CH}=\text{CH}-\text{CH}=\text{CH}-\text{Ge}_9-\text{R}]^{4-}$ ($\text{R} = -\text{CH}=\text{CH}_2$ ^[153], $-\text{C}(\text{CH}_3)=\text{CH}-\text{CH}=\text{N}(\text{CH}_2)\text{NH}_2$ ^[153-155]).

Next to organo-functionalization, reactions with heavier main-group elements ($\text{In}^{[156]}$, $\text{Ge}^{[157]}$, $\text{Sn}^{[150, 157, 158]}$, $\text{Sb}^{[159]}$ and $\text{Bi}^{[160]}$) were discovered. However, since the synthesis of $[\text{Ge}_9\{\text{Si}(\text{TMS})_3\}_3]^-$, silylation reactions attracted a growing amount of attention. ^[161, 162] $[\text{Ge}_9\{\text{Si}(\text{TMS})_3\}_3]^-$ benefits from increased stability compared to bare $[\text{Ge}_9]^{4-}$ clusters and is soluble in common laboratory solvents such as acetonitrile (MeCN) and THF. ^[161, 162] $[\text{Ge}_9\{\text{Si}(\text{TMS})_3\}_3]^-$ was originally obtained by reactions of Ge(I)-halides with $\text{Li}\{\text{Si}(\text{TMS})_3\}_3$. ^[161] Subsequently, the simple one-step heterogenous reaction of K_4Ge_9 with $\{\text{Si}(\text{TMS})_3\}_3\text{SiCl}$ in acetonitrile was found to result in decent yields. ^[162] Reactions involving derivatives of the tris(trimethylsilyl)silane $-\text{Si}\{\text{Si}(\text{TMS})_3\}_3$ group (“hypersilyl group”, *hyp*) since resulted in the formation of a series of tris-silylated $[\text{Ge}_9\text{R}_3]^-$ clusters ($\text{R} = \text{SiEt}_3$ ^[163], Si^iPr_3 ^[163], Si^iBu_3 ^[163], SiPh_3 ^[164], $\text{Si}(\text{TMS})_2(\text{SiPh}_3)$ ^[165, 166], SiH^tBu_2 ^[166], $\text{Si}(\text{TMS})_2(\text{Si}^i\text{Pr}_3)$ ^[166], $\text{Si}(\text{SiPh}_2-\text{CH}=\text{CH}_2)_3$ ^[167], $\text{Si}(\text{SiPh}_2-(\text{CH}_2)_3\text{CH}=\text{CH}_2)_3$ ^[167], $\text{Si}(\text{TMS})_2(\text{SiPh}_2-\text{CH}=\text{CH}_2)$ ^[167], $\text{Si}(\text{TMS})_2(\text{SiPh}_2-(\text{CH}_2)_3\text{CH}=\text{CH}_2)$ ^[167]; see Figure 1.9). Moreover, a synthesis of the bis-silylated cluster $[\text{Ge}_9\{\text{Si}(\text{TMS})_3\}_2]^{2-}$ was reported with reasonable yield. ^[168] This enabled the synthesis of tris-silylated clusters bearing two silyl group with different steric demand ^[165, 167] and allowed for the introduction of other main-group element substituents ^[169, 170]. However, corresponding silylated silicon clusters are scarce. Recently, bis-silylated $[\text{Si}_9\{\text{Si}^t\text{Bu}_2\text{H}\}_2]^{2-}$ ^[171] and $[\text{Si}_9\{\text{Si}(\text{TMS})_3\}_2]^{2-}$ ^[172] clusters were crystallized. Evidence

1.4 ZINTL clusters – Properties and Reactivity in Solution

formation of $[\text{Ge}_9\{\text{Si}(\text{TMS})_3\}_2\text{Et}]^-$ which loses one silyl group upon crystallization, yielding the mono-silylated species $[\text{Ge}_9\{\text{Si}(\text{TMS})_3\}\text{Et}]^{2-}$.^[177] Additionally, functional organic groups could be introduced to $[\text{Ge}_9\{\text{Si}(\text{TMS})_3\}_3]^-$ by reaction with alkenyl halides resulting in the formation of neutral $[\text{Ge}_9\{\text{Si}(\text{TMS})_3\}_3\text{R}]$ clusters ($\text{R} = \text{CH}_2\text{-CH=CH}_2, (\text{CH}_2)_3\text{CH=CH}_2$).^[178] Moreover, neutral $[\text{Ge}_9\{\text{Si}(\text{TMS})_3\}_3\text{C}(\text{O})\text{R}]$ clusters ($\text{R} = \text{Me}, ^i\text{Pr}, ^t\text{Bu}, \text{Ph}, \text{Bz}, \text{cyclopropylmethyl}, \text{phenethyl}, 4\text{-vinylphenyl}$) were formed by reaction with acylchlorides.^[179] However, for $[\text{Ge}_9\{\text{Si}(\text{TMS})_3\}_3\text{C}(\text{O})^t\text{Bu}]$ a subsequent decarbonylation occurred, yielding $[\text{Ge}_9\{\text{Si}(\text{TMS})_3\}_3^t\text{Bu}]$.^[179]

The most common reaction types of silylated clusters involve transition metals though. The tris-silylated cluster $[\text{Ge}_9\{\text{Si}(\text{TMS})_3\}_3]^-$ can thereby be reacted with transition metal halides or transition metal complexes bearing labile ligands, leading to bridged $[\text{Ge}_9]$ dimer compounds $[\text{M}(\eta^3\text{-Ge}_9\{\text{Si}(\text{TMS})_3\}_3)_2]^{n-}$ ($\text{M} = \text{Mn}^{[180]}, \text{Pd}^{[181]}, \text{Cu-Au}^{[182, 183]}, \text{Zn-Hg}^{[184]}$; $n = 0\text{-}2$). A similar reaction involving dppe [1,2-bis(diphenylphosphino)ethane] stabilized transition metals yielded neutral $[(\text{dppe})_2\text{M}][\text{Ge}_9\{\text{Si}(\text{TMS})_3\}_3]$ ($\text{M} = \text{Fe}, \text{Co}$) and $[(\text{dppe})\text{Ni}(\eta^3\text{-Ge}_9\{\text{Si}(\text{TMS})_3\}_3)]$ compounds as well as the cationic species $\{[(\text{dppe})\text{Ni}]_2(\eta^3, \eta^3\text{-Ge}_9\{\text{Si}(\text{TMS})_3\}_3)\}^+$.^[180] Investigations involving Cu^+ -phosphine complexes resulted in the formation of $[\text{CuP}^i\text{Pr}_3(\eta^3\text{-Ge}_9\{\text{Si}(\text{TMS})_3\}_3)]$ ^[164], $[(\text{CuP}^i\text{Pr}_3)_4\{\eta^3\text{-Ge}_9(\text{SiPh}_3)_2\}_2]$ ^[164] and $[\text{Cu}(\eta^3\text{-Ge}_9\{\text{Si}(\text{TMS})_3\}_3)_2\text{-Cu-PPh}_3]$ ^[181]. Reaction of $[\text{Ge}_9\{\text{Si}(\text{TMS})_3\}_3]^-$ with $\text{Cr}(\text{CO})_5(\text{coe})$ ($\text{coe} = \text{cyclooctene}$) yielded $[(\text{CO})_5\text{Cr}(\eta^1\text{-Ge}_9\{\text{Si}(\text{TMS})_3\}_3)]^-$ compounds in which Cr interacts with a single vertex of the cluster.^[185] In contrast, reactions with $\text{M}(\text{CO})_3(\text{MeCN})_3$ compounds ($\text{M} = \text{Cr}, \text{Wo}, \text{W}$) led to the formation of $[(\text{CO})_3\text{M}(\eta^5\text{-Ge}_9\{\text{Si}(\text{TMS})_3\}_3)]^-$ in which the transition metal M interacts with five Ge atoms, posing as an additional cluster vertex.^[185, 186] Further investigations involving Cp-stabilized transition metals yielded $[\text{Cp}^*\text{Zn}(\eta^3\text{-Ge}_9\{\text{Si}(\text{TMS})_3\}_3)]$ ^[164], $[\text{Cp}_2\text{Ti}(\eta^1\text{-Ge}_9\{\text{Si}(\text{TMS})_3\}_3)]$ ^[187] as well as $\text{K}_3[\text{Cp}_2\text{Ti}(\eta^1\text{-Ge}_9\{\text{Si}(\text{TMS})_3\}_2)_2]$ ^[187] compounds.

Moreover, reactions of silylated $[\text{Ge}_9]$ clusters involving NHC-stabilized coinage metal halides $\text{NHC}^{\text{Dipp}}\text{MCl}$ ($\text{M} = \text{Cu}, \text{Ag}, \text{Au}$) led to the formation of $[(\text{NHC}^{\text{Dipp}}\text{M})_2(\eta^3, \eta^3\text{-Ge}_9\{\text{Si}(\text{TMS})_3\}_2)]$ ^[188] ($\text{M} = \text{Cu}, \text{Ag}, \text{Au}$; see chapter 3.6), $[\text{NHC}^{\text{Dipp}}\text{Cu}\{\eta^3\text{-Ge}_9(\text{SiR}_3)_3\}]$ ($\text{R} = ^i\text{Pr}^{[188]}, ^t\text{Bu}^{[163]}$) and $[\text{NHC}^{\text{Dipp}}\text{M}(\eta^3\text{-Ge}_9\{\text{Si}(\text{TMS})_3\}_3)]$ ^[189] ($\text{M} = \text{Cu}, \text{Ag}, \text{Au}$) compounds. The reactivity of a tris-silylated $[\text{Ge}_9]$ cluster bearing smaller silyl groups $[\text{Ge}_9(\text{Si}^i\text{Bu}_3)_3]^-$ was further investigated yielding the dimeric Au^+ bridged species $[\text{Au}\{\eta^3\text{-Ge}_9(\text{Si}^i\text{Bu}_3)_3\}_2]^-$.^[163] In contrast, the reaction of $[\text{Ge}_9(\text{Si}^i\text{Pr}_3)_3]^-$ with $\text{Pd}(\text{PPh}_3)_4$ yielded the Pd_3 bridged dimeric compound $[\text{Pd}_3\{\text{Ge}_9(\text{Si}^i\text{Pr}_3)_3\}_2]^{2-}$.^[190]

1.5 Motivation and Scope

Renewable energy sources as well as energy storage are projected to play an increasingly important role within the years to come.^[1] Therefore, semiconducting Group 14 materials are of interest due to their broad range of applications in solar cells^[22, 25, 40, 46, 76, 78], optoelectronics^[29, 30] and as anodes in lithium ion batteries^[34-36, 44]. Nanostructured materials of these semiconductors can provide unique morphologies and tunability of the materials properties (e. g. band gap).^[38-41] Especially a bottom-up approach using Group 14 ZINTL clusters in solution as a basis for such structured materials was of interest for this work. ZINTL phases with the composition A_4E_9 ($A = K-Cs$; $E = Ge-Pb$) and $A_{12}E_{17}$ ($A = Na-Cs$; $E = Si-Pb$) contain well-defined nine-atomic $[E_9]^{4-}$ ZINTL clusters and are easily accessible from the elements *via* a one-step solid state reaction.^[132, 133, 139, 140] These intermetallic ZINTL phases represent precursors for solution-based fabrication of unstructured and structured porous thin filmed semiconducting materials.^[42-44, 95] However, investigations using this solution-based process were confined to Ge and Sn thin films as well as Ge/Sn, Ge/P, Sn/Se, Sn/Te and Sn/P mixtures so far.^[43, 44, 95] In case of inverse opal structured Ge thin films, their morphology and composition have already been investigated.^[43] They have also been investigated as potential anode materials in Li ion batteries.^[95] However, charge carrier mobilities within these films remain unknown so far.

This work aimed to deepen the understanding of inverse opal structured Ge thin films established by Bentlohner *et al.*^[43] by investigation of carrier mobilities in Ge thin films with different morphologies. Furthermore, the fabrication of thin films was aimed to be expanded to silicon as well as Si/Ge mixtures to combine advantages of both materials and tailor properties of the resulting semiconducting films (e. g. band gap). Other goals involved the introduction of hetero atoms (Sn, Bi, Se, Te) to porous thin films (e. g. fabrication of metallic films).

To overcome the limited solubility of bare Si/Ge ZINTL clusters in highly polar amines, this work aimed to introduce ligands (silyl groups and coinage metal NHC complexes) to the clusters, thereby effectively lowering their charge. The resulting new compounds (soluble in less polar solvents) were aimed to enable additional approaches to the solution-based fabrication of Si/Ge thin films.

1.6 Outline

Chapter 2 is focused on experimental techniques (**chapter 2.1**), characterization techniques (**chapter 2.2**) and syntheses (**chapter 2.3**) used within this work.

In **chapter 3.1**, inverse opal structured Ge thin films are presented. Thereby, **chapter 3.1.1** highlights the synthesis and characterization of inverse opal structured Ge thin films (as previously reported by Bentlohner et al.^[43]) and compares them to unstructured Ge thin films synthesized from K_4Ge_9 in solution. Meanwhile, **chapter 3.1.2** presents charge carrier mobilities within these films obtained through terahertz spectroscopy.

In **chapter 3.2**, inverse opal structured Si/Ge thin films are presented as new materials for several applications. **Chapter 3.2.1** is focused on the synthesis and characterization of $A_{12}Si_{17-x}Ge_x$ - ($A = K, Rb$; $x = 0, 5, 9, 12, 17$) and $K_4Si_{4-x}Ge_x$ -phases ($x = 0, 1.2, 2.1, 2.8, 4$) while **chapter 3.2.2** evaluates them as starting materials for the solution-based fabrication of thin films through their solubility in *en*. **Chapter 3.2.3** and **chapter 3.2.4** characterize dried and annealed residues of the soluble part of $K_{12}Si_{17-x}Ge_x$ -phases. Meanwhile, **chapter 3.2.5** highlights silicon species in solution while using ZINTL clusters containing silicon. In **chapter 3.2.6**, fabrication and characterization of inverse opal structured Si/Ge as well as Si thin films is discussed. The carrier mobility within these films is investigated in **chapter 3.2.7**.

Chapter 3.3 describes the fabrication of Ge/Se and Ge/Te mixed thin films while **chapter 3.4** is focused on porous metallic Sn/Bi thin films with a high surface area.

In contrast, **chapter 3.5** discusses the silylation of bare mixed Si/Ge clusters in order to broaden the solubility of precursor materials for thin film production. Thereby, the synthesis of a series of $[E_9(hyp)_3]^-$ clusters ($E = Si/Ge$ in various ratios) is discussed through a reaction with tris(trimethylsilyl)silane (*hyp*). Silylated clusters are subsequently treated with coinage metal NHC compounds to yield neutral $[(NHCM)_2\{\eta^3-Ge_9(Si(TMS)_3)_2\}]$ compounds ($M = Cu, Ag, Au$) in **chapter 3.6**.

2 Experimental Section

2.1 Experimental Techniques

2.1.1 Inert Gas Conditions

Almost all the precursors as well as the products were highly sensitive towards moisture or at least prone to oxidation. Therefore, all synthesis and characterization methods were carried out in inert gas atmosphere. Experiments were performed using standard SCHLENK techniques. All glass equipment was cleaned using an isopropanol/potassium hydroxide bath, washed with deionized water and stored in an oven at 393 K prior to use. Additionally, glassware was heated in fine vacuum (vacuum pump, PFEIFFER Duo 3 M, $< 10^{-3}$ mbar) then purging with argon (argon 4.8, WESTFALEN, 99.998% purity) for three times. The argon was further purified by a BTS catalyst, molecular sieve 4 Å and P₄O₁₀ before usage. The pressure was measured using a Pirani pressure sensor (PFEIFFER Single Gauche TPG 361). Sample preparation was carried out in a glovebox (MBRAUN, O₂ < 0.1 ppm, H₂O < 0.1 ppm) under argon. The glovebox was equipped with a BTS catalyst, molecular sieve and an activated carbon filter to purify the argon. The catalyst was periodically regenerated by forming gas (WESTFALEN, 95% Ar, 5% H₂).

2.1.2 Ball-Milling

Silicon and germanium do not melt at the temperatures used in solid state reactions within this work (< 1175 K). Therefore, it was necessary to ball-mill silicon, germanium and mixtures upfront solid-state reactions to increase the surface area and thereby reactivity. The starting materials were placed within a tungsten carbide milling jar (see Figure 2.1) under inert gas atmosphere. The milling jar was equipped with a safety closing cap and three tungsten carbide balls (1.5 cm diameter). Afterwards, the milling jar was fixated in the ball-mill (RETSCH PM 100, Figure 2.1).



Figure 2.1. Ball-mill (left) and milling jar (right) with safety closure cap and tungsten carbide balls.

After removal of the products, the milling jar was cleaned by a mixture of sand and either deionized water or isopropanol and placed in the ball mill again. It was running at 400 rpm for 30 min changing rotational direction every 2 min with a resting period of 1 min. Finally, the milling jar was cleaned with deionized water then isopropanol and put into an oven at 393 K for at least 2 h prior to use.

2.1.3 Solid-State Synthesis

The binary phase K_4Ge_9 was synthesized in stainless-steel autoclaves (see Figure 2.2, inner tube: 1.5 cm diameter, 7.5 cm length; outer tube: 2.5 cm diameter, 10.5 cm length) under argon atmosphere. Before usage, the containers were cleaned with deionized water and stored in an oven at 393 K overnight. The containers were filled and sealed in a glovebox and placed inside a corundum tube equipped with a balloon for pressure regulation (Figure 2.2). The corundum tube was vertically inserted into a tubular furnace (HTM REETZ GMBH) that was attached to a temperature controlling unit (EUROTHERM DEUTSCHLAND GMBH).

Experimental Section

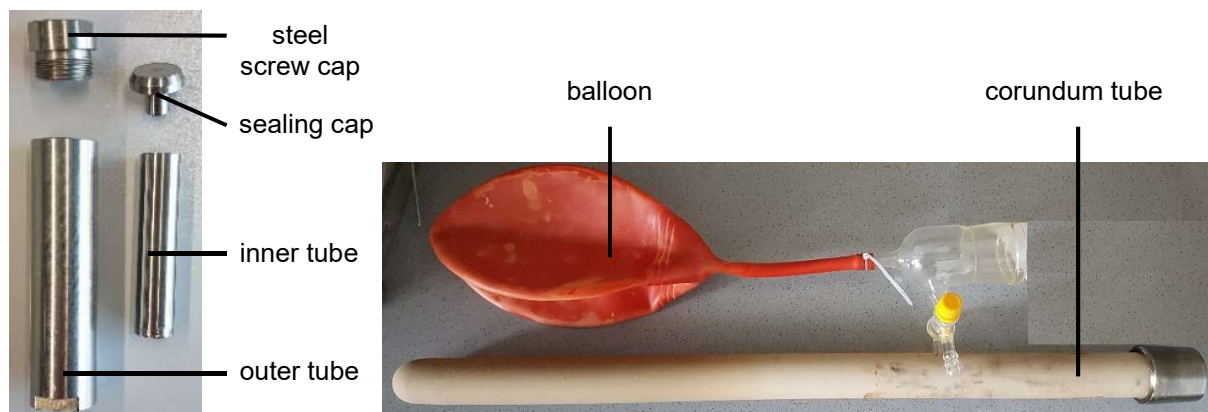


Figure 2.2. Stainless-steel autoclave (left) and corundum tube with balloon for pressure regulation (right).

All other precursor phases were synthesized in tantalum ampoules (see Figure 2.3) in argon atmosphere. To make these ampoules, a tantalum tube was cut into pieces (1 cm diameter, 5 cm length). Afterwards, one side of the ampoule was sealed using an arc furnace (EDMUND BÜHLER, MAM 1). The ampoules were cleaned by ultrasonication for 15 min in acetic acid, water and acetone. Prior to use, they were stored in an oven at 393 K. The ampoules were filled within a glovebox and sealed using an arc furnace again. Afterwards, they were placed inside a fused silica tube under vacuum and purged with argon three times (Figure 2.3). The fused silica tube was vertically inserted into a tubular furnace (HTM REETZ GMBH) that was attached to a temperature controlling unit (EUROTHERM DEUTSCHLAND GMBH).

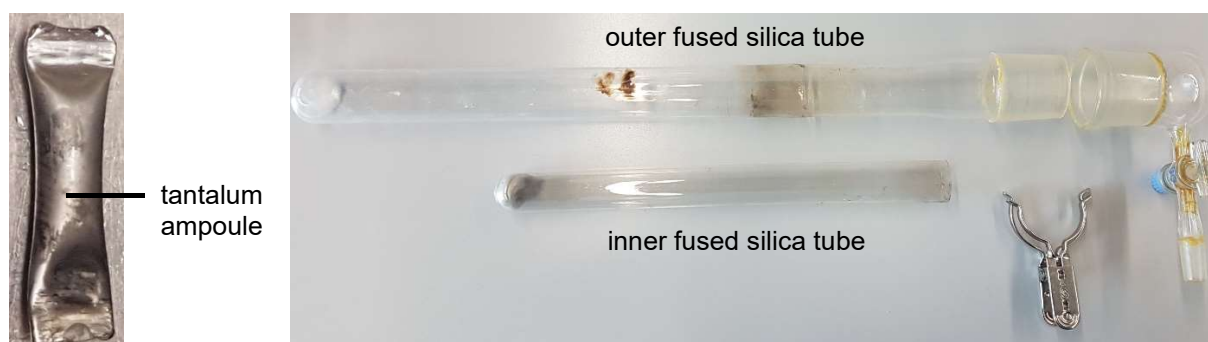


Figure 2.3. Tantalum ampoule (left) and fused silica tube (right).

2.1.4 Filtration of Solutions

Reaction solutions were filtered through a glass fiber filter (Pall Corporation, pore size: 1 μm) to remove any precipitates. Parts of a filter were stuffed into a glass pipette and stored in an oven at 393 K for at least 2 h before usage. Solutions were pressed through the filter by applying pressure to the top of the pipette. Filtrations were performed into either a baked out SCHLENK tube or vial inside a glovebox.

2.1.5 Substrate Preparation

Silicon (SIEGERT WAFER), quartz and sapphire substrates (approx. 1.0 x 1.5 cm) were cleaned by ultrasonication in Extran[®] solution (MERCK MILLIPORE), water and acetone for 15 min each. Afterwards, the substrates were placed in an O₂-plasma oven (ELECTRONIC DIENER, Femto) at 50% intensity for 10 min. The cleaned substrates were either dip coated with a PMMA suspension (see chapter 2.1.6) or stored in a glovebox until further processing.

Copper substrates (1 cm diameter) were punched out of a copper foil (0.2 mm thickness, ADVENT, 99.9%). To achieve a good coverage of PMMA on the surface they had to be treated further.^[95] The substrates were ultrasonicated first in an ammoniacal hydrogen peroxide solution (H₂O₂ (30%) + NH₃ (25%) in H₂O (1.3 : 2.2 : 100 %wt.)) then in a diluted solution of hydrochloric acid (HCl in H₂O (1 : 100 %wt.)). The substrates were cleaned with water and dip coated with a PMMA suspension (see chapter 2.1.6) or stored in a glovebox until further processing.

2.1.6 Dip Coating of PMMA Suspensions

PMMA (poly(methyl methacrylate)) suspensions consisting of PMMA beads (15 %wt., typically around 250-300 nm size; for synthesis see chapter 2.3.8) in water were dip coated onto various substrates. To avoid agglomeration of PMMA beads, the suspensions were stirred at 400-500 rpm when not being used. Prior to use, the suspensions were ultrasonicated (EMMI 120 HC, EMAG) for at least a day. Clean substrates were attached to a movable sample holder in an electronic dip coater setup (see Figure 2.4). The speed of the sample holder could be controlled at any point to achieve a homogeneous distribution of PMMA onto the substrate. Usually, a consistent

Experimental Section

high speed yielded the best homogeneity. Afterwards, the coated substrates were dried at 373 K in vacuum for 4 h and stored in a glovebox under argon.

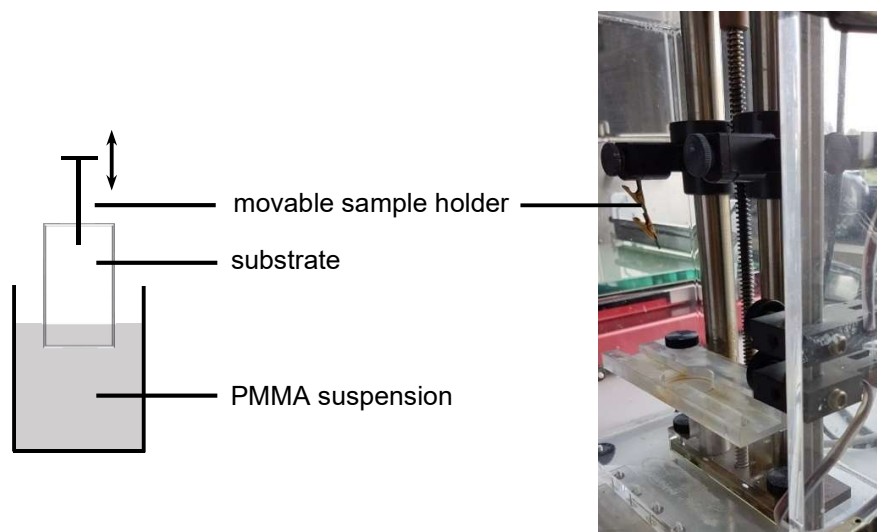


Figure 2.4. Schematic display of PMMA dip coating (left) and dip coater setup (right).

2.1.7 Drop Casting of Precursor Solutions

Precursor solutions (see chapter 2.3.10) were drop casted onto either blank or PMMA coated substrates (silicon, quartz, etc.; see chapter 2.1.5). After depositing one drop of a precursor solution, the substrate was tilted using a pair of tweezers to guarantee a homogenous distribution of the solution throughout the substrate without creating spots of higher concentration.

2.1.8 Annealing of Thin Films and Dried Residues

Thin films as well as dried residues (solvent removed from filtered precursor solutions) were placed in a SCHLENK flask and inserted into a tube furnace (HTM REETZ GMBH, Losa 600-40-180) at temperatures between 373 K and 873 K. Annealing experiments were either carried out in fine vacuum ($< 10^{-3}$ mbar) or under argon. In case of annealing under argon, the SCHLENK flask was connected to a relief valve to ensure ambient pressure in the flask

2.1.9 Reagents

The reagents used within this work are listed in Table 2.1. Solvents were either dried using a solvent purification system (MBRAUN SPS) or under reflux conditions over calcium hydride and stored in a glovebox over previously dried molecular sieve (3 Å or 4 Å). Deuterated NMR solvents were stored over molecular sieve (3 Å or 4 Å) in a glovebox as well. Ethylene diamine (*en*) was dried and checked for residual water content using the method established by Bentlohner *et al.*^[43] using a NMR (nuclear magnetic resonance) probe on the reaction of 1,4-Bis(trimethylsilyl)-butadiyne in *en*. Syntheses of other reactants used are described in chapter 2.3.

Table 2.1. List of reagents used within this thesis. a. c.: ambient conditions (storage on bench), i. c.: inert conditions (storage in glovebox or SCHLENK tube)

Compound	Phase	Supplier / Producer	Purity	Storage
Acetone	Liquid	VWR	Synthesis grade	a. c.
Acetonitrile	Liquid	VWR	SPS	i. c.
Acetonitrile-d ₃	Liquid	DEUTERO	99.8%	i. c.
Benzene-d ₆	Liquid	DEUTERO	99.5%	i. c.
Bismuth	Solid	CHEMPUR	99.999%	i. c.
1,4-Bis(trimethylsilyl)-butadiyne	Solid	ALFA AESAR	98%	i. c.
Calcium hydride	Solid	MERCK	Synthesis grade	a. c.
Chloroform-d ₁	Liquid	DEUTERO	99.8%	i. c.
Chlorotri(<i>iso</i> -butyl)-silane	Liquid	SIGMA-ALDRICH	99%	i. c.
Chlorotris-(trimethylsilyl)silane	Solid	TCI	>95%	i. c.
[2.2.2]-Cryptand	Solid	MERCK	Synthesis grade	i. c.
Dimethyl sulfoxide	Liquid	SIGMA-ALDRICH	>99.9%	i. c.
Ethylene diamine	Liquid	MERCK	Stored over CaH ₂	i. c.
Ethanol	Liquid	VWR	Synthesis grade	a. c.

Experimental Section

Extran®	Liquid	MERCK	-	a. c.
Fluorobenzene	Liquid	SIGMA-ALDRICH	Mole sieve 4 Å	i. c.
Germanium	Solid	EVOCHEM	99.999%	i. c.
Germanium tetrachloride	Liquid	SIGMA-ALDRICH	99.9%	i. c.
Hexane	Liquid	VWR	SPS	i. c.
Hydrochloric acid	Liquid	MERCK	-	a. c.
Hydrogen peroxide	Liquid	MERCK	-	a. c.
Methyl methacrylate	Solid	VWR	>99.5%	a. c.
Potassium	Solid	ALFA AESAR	>98%	i. c.
PMMA beads (150 nm) in water	Suspension	K. PETERS (LMU)	-	a. c.
PMMA beads (300 nm) in water	Suspension	D. BÖHM (LMU)	-	a. c.
Perfluoroalkyl ether	Liquid	ABCR	-	i. c.
Perfluoro hexane	Liquid	ALFA AESAR	>98%	i. c.
Pyridine-d ₅	Liquid	DEUTERO	99.5%	i. c.
Rubidium	Solid	LAB INVENTORY	Liquated	i. c.
Selenium	Solid	CHEMPUR	99.999%	i. c.
Silicon	Solid	CHEMPUR	99.99%	i. c.
Silicon tetrachloride	Liquid	MERCK	>99%	i. c.
Tellurium	Solid	ABCR	99.999%	i. c.
Tetrahydrofuran	Liquid	VWR	SPS	i. c.
Tetrahydrofuran-d ₈	Liquid	DEUTERO	99.5%	i. c.
Tin	Solid	ALFA AESAR	99.8%	i. c.
Tin tetrachloride	Liquid	ACROS ORGANICS	99%	i. c.
Toluene	Liquid	VWR	SPS	i. c.
Toluene-d ₈	Liquid	DEUTERO	99.5%	i. c.

2.2 Characterization Methods

2.2.1 Scanning Electron Microscopy

Scanning electron microscopy (SEM) measurements were carried out using a FEI Helios NanoLab G3 UC scanning electron microscope equipped with a field emission gun operated at 3 – 20 kV. Usually, 3 – 5 kV was used to analyze morphology whereas 20 kV was used in an energy disperse X-ray (EDX) setup. Substrates were mounted onto a conductive carbon tape on an aluminum sample holder. Afterwards, they were coated with silver conducting lacquer (PLANO GMBH, ACHSEON 1415) and carbon to enhance conductivity. Measurements were carried out by either Daniel Böhm or Steffen Schmidt (Bein group, LMU).

2.2.2 Energy Disperse X-Ray

Energy disperse X-ray (EDX) measurements on thin films were performed at 20 kV using a X-Max^N Silicon Drift Detector (OXFORD INSTRUMENTS) with 80 mm² detector area. Data evaluation was achieved with the AZTec acquisition software (OXFORD INSTRUMENTS). Measurements were carried out by either Daniel Böhm or Steffen Schmidt (Bein group, LMU). Measurements on single crystals and powders were performed using a Hitachi TM-1000 tabletop microscope device. Data acquisition was achieved using the SWIFT-ED-TM program (OXFORD INSTRUMENTS: INCA System Software). Measurements were carried out by Maria Müller (Fässler group, TUM).

2.2.3 Powder X-Ray Diffraction

Powder X-ray diffraction (PXRD) was carried out on a STOE Stadi P (Cu-K_{α1} radiation, $\lambda = 1.54056 \text{ \AA}$, Ge monochromator) diffractometer equipped with a DECTRIS Mythen 1k detector. Due to air and moisture sensitivity, samples were finely ground and filled into glass capillaries (HILGENBERG, 0.3 or 0.5 mm diameter, 0.01 mm wall thickness) inside a glovebox. The capillaries were sealed with a drop of wax. Measurements were conducted in the DEBYE-SCHERRER geometry. The acquired powder diffraction patterns were compared to theoretical ones derived from single crystal data using the WinXPOW program package.^[191] Data was plotted using the program OriginPro 2016G (ORIGINLAB).^[192]

2.2.4 Single Crystal X-Ray Diffraction

Single crystal X-ray diffraction (SC-XRD) data collection was performed at a STOE StadiVari diffractometer equipped with a DECTRIS PILATUS 300K detector or a BRUKER AXS D8 equipped with an APEX II detector (both Mo-K α radiation, $\lambda = 0.71073 \text{ \AA}$). Data processing was handled with the X-Area^[193] or APEX^[194] software package. Crystal structures were solved with direct methods (SHELXS) and refined with full-matrix least-squares calculations on F^2 (SHELXL).^[195] The positions of hydrogen atoms were calculated and refined using a riding model. In case of strongly disordered solvent molecules, their electron density was treated with the squeeze function of the program PLATON.^[196, 197]

Due to air and moisture sensitivity, all crystals were prepared for measurement under inert gas atmosphere. Crystals that grew at room temperature were removed from their mother liquor and transferred into a perfluoroalkyl ether (ABCR GMBH, viscosity 1800 cSt) inside a glovebox. Single crystals were separated under a microscope, transferred onto the top of a glass fiber and mounted inside a cold N₂ stream (100 – 150 K, OXFORD CRYOSYSTEMS) in the diffractometer. Crystals that grew inside a fridge at 241 K were removed from their mother liquor and transferred into a perfluorinated ether (Galden[®], SOLVAY SOLEXIS) that was cooled from below by a dewar filled with liquid nitrogen and from above by a cold N₂ stream. Single crystals were separated under a microscope, transferred onto a capillary loop and mounted inside a cold N₂ stream in the diffractometer.

2.2.5 Raman Spectroscopy

Raman spectroscopy was carried out on a RENISHAW inVia Raman microscope equipped with a CCD detector. Three different lasers ($\lambda = 532 \text{ nm}$, 633 nm and 785 nm) could be used at a maximum power of 500 mW. Data collection on the device was conducted using the WiRe 4.2 software (RENISHAW, build 5037). Due to air and moisture sensitivity, powder and single crystal samples were filled into glass capillaries (HILGENBERG, 0.3 or 0.5 mm diameter, 0.01 mm wall thickness) inside a glovebox. The capillaries were sealed with a drop of wax. Measurements on thin films were performed directly on the respective films. Measurements were carried out by either Sebastian Geier or Christoph Wallach (Fässler group, TUM). Data was plotted using the program OriginPro 2016G (ORIGINLAB).^[192]

2.2.6 Nuclear Magnetic Resonance

Nuclear magnetic resonance (NMR) spectra were procured from a BRUKER Avance Ultrashield 400 MHz spectrometer equipped with an auto sampler. Chemical shifts are reported in parts per million (ppm) relative to tetramethylsilane (SiMe_4) with deuterated solvent peaks serving as an internal reference.^[198] For or *in situ* measurements, the signal of the non-deuterated solvent ethylene diamine (*en*) at $\delta = 2.645$ ppm (s, $-\text{CH}_2$) served as a reference. Abbreviations for signal multiplicities are: s (singlet), d (doublet), t (triplet), m (multiplet). Data processing was conducted with the program MestReNova.^[199]

Due to air and moisture sensitivity, experiments were performed in J Young NMR tubes (DEUTERO). Approximately 10 mg residue of a given product was dissolved in 0.6 mL of deuterated solvent.

For *in situ* experiments carried out in non-deuterated solvents (e.g. *en*), approximately 200 μL of the reaction solution was filled into a Norell[®] NMR tube (DEUTERO, 3 mm diameter, 0.3 mm wall thickness). This tube was sealed with a cap and placed in a common NMR tube (DEUTERO, 5 mm diameter, 0.43 mm wall thickness). Then, 0.3 mL deuterated Chloroform ($\text{CDCl}_3\text{-d}_1$) was added to the outer NMR tube and sealed with a cap as well. This way the deuterated solvent can be locked onto and can act as an external reference.

2.2.7 Electrospray Ionization Mass Spectrometry

Electron ionization mass spectrometry (ESI-MS) was performed on a BRUKER Daltronic HCT mass spectrometer. The samples were diluted with acetonitrile or THF to approx. $2\text{-}5 \cdot 10^{-4}$ mmol/mL and injected into the device with a speed of 240 $\mu\text{L}/\text{h}$. Depending on the sample, spectra were measured in the positive (+) or negative (-) ion mode with changing capillary voltages. Measurements were carried out by either Lorenz Schiegerl or Christina Fischer (Fässler group, TUM). Data evaluation was achieved with the program BRUKER Compass Data Analysis 4.0 SP 5. Spectra were plotted using the program OriginPro 2016G (ORIGINLAB).^[192]

2.2.8 Terahertz Spectroscopy

Terahertz (THz) measurements were performed at a THz setup in the laboratories of Prof. Hegmann (physics department, University of Alberta (UofA), Edmonton, Canada). Measurements were partly carried out by Mary A. Narreto, Naaman Amer and Charles Jensen (Hegmann group, UofA). A 1.53 eV (800 nm) laser pulse (SPECTRA PHYSICS, Millennia) was amplified (QUANTRONIX, Odin) and split into a pump beam and probe beam by a beam splitter. The probe beam was then converted into THz pulses by a ZnTe crystal. Both beams were redirected and focused onto the sample (aperture 1.5 mm diameter) by mirrors. The power of the laser was adjusted between 40 and 100 mW prior to entering the sample chamber. The sample holder could be cooled down using a cold finger cryostat, allowing temperature-resolved measurements. The setup was equipped with a ZnTe detector as well as two balanced photodetectors. All samples were measured on silica substrates which are transparent above 180 nm.

The setup was also equipped with two movable stages. The distances within these stages could be adjusted during the experiment. This way, a time-resolved measurement (delay between pump pulse and probe pulse) could be achieved. In such a time resolved THz (TRTS) experiment, the transmitted THz electric field was measured both in time and frequency domain. A 100 fs pump pulse was able to momentarily excite charge carriers within thin films measured. The changes in THz amplitudes between transmission through an unexcited sample (T_0 , reference, without optical pump) and time-delayed (Δt) reduced transmission immediately after the excitation ($-\Delta T$, pumped), provided the measurement of the transient and complex conductivities. For the transient photoconductivity, the peak amplitude of the reference (T_0) is used to check the rise and decay of the photo-excited carriers.

If the relative change in the THz electric field amplitude peak, $|\Delta T/T_0|$ (peak), and the phase shift are small, then $|\Delta T/T_0|$ yields a good measure of the conductivity $\sigma = N e \mu$, where N is the carrier density, e is the electronic charge, and μ is the effective carrier mobility.^[200] Therefore, the development of $|\Delta T/T_0|$ as a function of time provides a good indication of the dynamics of the photoexcited carriers in sub-picosecond scale time resolution.

2.2.9 Elemental Analysis

Elemental analyses were performed in the microanalytical laboratory at the chemistry department of the Technical University Munich. Analyses of C, H and N were carried out in a combustion analyzer (BRUKER, elemental vario EL). Measurements were performed by Ulrike Ammari (TUM).

2.2.10 Profilometry

The thickness of all thin films was determined using a VEECO Dektak 150 profilometer. Small linear cracks were introduced to the thin films using a razorblade. The tip of the profilometer was then placed orthogonal to the cracks so that at least the height of two cracks were measured in a row. At least three of these measurements were conducted at different spots of the cracks to get a good estimate of the overall thickness of the films. The sample stage could be tilted to guarantee a flat surface of the substrate beneath the thin films.

2.2.11 X-Ray Photoelectron Spectroscopy

X-ray photoelectron spectroscopy (XPS) measurements were carried out on a LEYBOLD-HERAEUS LHS 10 spectrometer using a non-monochromatized Al-K α source (1486.7 eV). Thin filmed samples on copper substrates (1.0 cm diameter) were fixed on a sample holder with a screw. The analyzer was operated at a constant pass energy of 100 eV resulting in an energy resolution with a full width at half maximum (fwhm) of around 1.2 eV. The energy scale of the spectra was corrected for sample charging by using the C 1s main signal (284.5 eV). The oxidation stated of germanium and silicon were determined by the Auger parameter ($a' = E_{\text{kin}}(\text{L}_3\text{M}_{45}\text{M}_{45}) + E_{\text{b}}(3\text{d}) = 1174.5 \text{ eV}$ or $a' = E_{\text{kin}}(\text{L}_3\text{M}_{45}\text{M}_{45}) + E_{\text{b}}(2\text{p}_{3/2}) = 2362.4 \text{ eV}$ for Ge(0)^[201]). All measurements were carried out in an ultra-high vacuum chamber at a pressure below $5 \cdot 10^{-8}$ mbar. Core level spectra were deconvoluted using Voigt functions and linear background subtraction.

The oxidation states of Ge were identified by deconvolution of the Ge 2p_{3/2} and the Ge 3d peak. Quantification was accomplished by comparison of the peak areas of the respective deconvoluted Ge species. The derived peak area fractions depend sensitively on the energy reference (Auger parameter relating to Ge(0)). The precision

Experimental Section

of the energy referencing of ± 0.1 eV influences the outcome of the peak deconvolution and thus, introduces errors of about 7% for each Ge fraction.

2.2.12 Computational Details

The silylated mixed cluster $[\text{Si}_{1.68}\text{Ge}_{7.32}\{\text{Si}(\text{TMS})_3\}_3]^-$ was investigated by computational analysis using the Turbomole V7.3 program package^[202], with exchange correlation hybrid functional after Perdew, Burke and Ernzerhof (PBE0)^[203, 204] and a def2-TZVP basis set for all considered elements Si, Ge and H^[205, 206]. The ligand $\{\text{Si}(\text{TMS})_3\}$ of the cluster $[\text{Si}_{1.68}\text{Ge}_{7.32}\{\text{Si}(\text{TMS})_3\}_3]^-$ was shortened due to computational resources. Therefore $\{\text{Si}(\text{SiH}_3)_3\}$ was used as ligand instead of $\{\text{Si}(\text{TMS})_3\}$ and additionally the ratio of Si to Ge was set to 2:7 in the cluster resulting in a $[\text{Si}_2\text{Ge}_7\{\text{Si}(\text{SiH}_3)_3\}_3]^-$ cluster anion (Figure SI). Multipole-accelerated resolution-of-the-identity technique^[207-209] was used to speed up the calculations and a continuum solvation model (conductor-like screening model, COSMO)^[210] was applied for compensation of the negative charge. Jmol^[211] and TmoleX^[212] were used for data processing. The structure was optimized and the character of a stationary point was investigated with harmonic frequency calculations. No imaginary frequency was found and a HOMO-LUMO gap of 3.84 eV was obtained. Raman intensities were calculated for a wave length of $\lambda = 532$ nm. The wave numbers obtained were shifted by of factor of 1.04 due to numerical derivation.^[213] For comparison of original and shifted data see Table 5.14 in the appendix.

2.3 Syntheses

2.3.1 Synthesis of $\text{Si}_{17-x}\text{Ge}_x$

5.0 g of a mixture of Ge and Si in the desired molar ratio ($x = 0, 5, 9, 12, 17$) were placed in a 50 mL tungsten carbide milling jar equipped with three tungsten carbide balls (15 mm diameter) under argon atmosphere (see chapter 2.1.2). The milling jar was closed with a safety closure cap inside a glovebox to prevent oxygen contamination. The milling jar was placed inside a ball mill and the mixture was grinded into a fine powder at 400 rpm for 20 – 22 h changing rotational direction every 10 min with a resting period of 5 min. The fine $\text{Si}_{17-x}\text{Ge}_x$ powder was stored inside a glovebox for further solid states syntheses (see chapter 2.3.2 – 2.3.5).

2.3.2 Synthesis of $\text{K}_{12}\text{Si}_{17-x}\text{Ge}_x$

Synthesis of $\text{K}_{12}\text{Si}_{17-x}\text{Ge}_x$ was performed with a variation to the procedure reported by Waibel *et al.*^[214] Elemental potassium was formed into little balls and filled into a tantalum ampoule (see chapter 2.1.3). Afterwards, the desired $\text{Si}_{17-x}\text{Ge}_x$ powder was added to yield about 0.9 to 1.1 g of product. Detailed weights for different mixtures are shown in Table 2.2. The ampoule was sealed with an arc furnace and placed in a tube furnace inside a fused silica tube under vacuum. The mixture was heated to 1073 K at a heating rate of 2 K/min, annealed at 1073 K for 15 h before slowly being cooled down to room temperature at a rate of 0.3 K/min. Detailed powder X-ray diffractograms and Raman spectra of the compounds are shown in the appendix (Figure 3.6 and Figure 3.7).

Table 2.2. Net weights for synthesis of $\text{K}_{12}\text{Si}_{17-x}\text{Ge}_x$ compounds.

Ratio (x)	Potassium / mg	Silicon / mg	Germanium / mg
0	516	525	-
5	469	700 ($\text{Si}_{12}\text{Ge}_5$ powder)	
9	382	715 (Si_8Ge_9 powder)	
12	340	734 ($\text{Si}_5\text{Ge}_{12}$ powder)	
17	297	-	781

2.3.3 Synthesis of $\text{Rb}_{12}\text{Si}_{17-x}\text{Ge}_x$

Synthesis of $\text{Rb}_{12}\text{Si}_{17-x}\text{Ge}_x$ was carried out with a variation to the procedure reported by Waibel *et al.*^[214, 215] Elemental rubidium was formed into little balls and filled into a tantalum ampoule (see chapter 2.1.3). Afterwards, the desired $\text{Si}_{17-x}\text{Ge}_x$ powder was added to yield about 0.9 to 1.0 g of product. Detailed weights for different mixtures are shown in Table 2.3. The ampoule was sealed with an arc furnace and placed in a tube furnace inside a fused silica tube under vacuum. The mixture was heated to a temperature between 1073 K and 1173 K at a heating rate of 2 K/min, depending on the composition of the desired phase. The mixture was annealed at peak temperature for 15 h (in case of 1073 K), 12.5 h (in case of 1123 K) or 10 h (in case of 1173 K) before slowly being cooled down to room temperature at a rate of 0.3 K/min. Detailed powder X-ray diffractograms and Raman data of the compounds are shown in the appendix (Figure 5.1 and Figure 5.2).

Table 2.3. Net weights for synthesis of $\text{Rb}_{12}\text{Si}_{17-x}\text{Ge}_x$ compounds.

Ratio (x)	Temperature / K	Rubidium / mg	Silicon / mg	Germanium / mg
0	1173	641	299	-
5	1173	573	391 ($\text{Si}_{12}\text{Ge}_5$ powder)	
9	1123	530	432 (Si_8Ge_9 powder)	
12	1073	496	489 ($\text{Si}_5\text{Ge}_{12}$ powder)	
17	1073	427	-	515

2.3.4 Synthesis of $\text{K}_4\text{Si}_{4-x}\text{Ge}_x$

Synthesis of $\text{K}_{12}\text{Si}_{17-x}\text{Ge}_x$ was performed according to the procedure reported by Waibel *et al.*^[215] Elemental potassium was formed into little balls and filled into a tantalum ampoule (see chapter 2.1.3). Afterwards, the desired $\text{Si}_{17-x}\text{Ge}_x$ powder was added to yield about 1.0 g of product. Detailed weights for different mixtures are shown in Table 2.4. The ampoule was sealed with an arc furnace and placed in a tube furnace inside a fused silica tube under vacuum. The mixture was heated to 873 K at a heating rate of 2 K/min, annealed at 873 K for 10 h before slowly being cooled down to room temperature at a rate of 0.2 K/min. Detailed powder X-ray diffractograms, cell volume

determination and Raman spectra of the compounds are shown in the appendix (Figure 3.8 – Figure 3.10).

Table 2.4. Net weights for synthesis of $K_4Si_{4-x}Ge_x$ compounds.

Ratio (x)	Potassium / mg	Silicon / mg	Germanium / mg
0	508	365	-
1.2	471	497 (Si ₁₂ Ge ₅ powder)	
2.1	430	568 (Si ₈ Ge ₉ powder)	
2.8	391	596 (Si ₅ Ge ₁₂ powder)	
4	352	-	653

2.3.5 Synthesis of K_4Ge_9

Synthesis of K_4Ge_9 was carried out with a variation to the procedure reported by Hoch *et al.*^[132] 1.07 g (27.4 mmol) elemental potassium was formed into little balls and filled into a stainless-steel autoclave (see chapter 2.1.3). Afterwards, 4.03 g (55.5 mmol) ball-milled germanium was added and the autoclave sealed with the screw cap. The autoclave was placed in a tube furnace inside a corundum tube which was filled with argon. The mixture was heated to 923 K at a heating rate of 2 K/min, annealed at 923 K for 46 h before being cooled down to room temperature at a rate of 1 K/min. A detailed powder X-ray diffractogram and Raman spectrum of the compound are shown in the appendix (Figure 5.4 and Figure 5.5).

2.3.6 Synthesis of K_2SnBi

Synthesis of K_2SnBi was performed using a variation to the procedure reported by Asbrand *et al.*^[216] 154 mg (3.94 mmol) elemental potassium was formed into little balls and filled into a tantalum ampoule (see chapter 2.1.3). Afterwards, 234 mg (1.97 mmol) tin and 412 mg (1.97 mmol) bismuth powder were added and the tantalum ampoule sealed using an arc furnace. The ampoule was placed in a tube furnace inside a fused silica tube under vacuum. The mixture was heated to 723 K at a heating rate of 2 K/min, annealed at 723 K for 72 h before slowly being cooled down to room

Experimental Section

temperature at a rate of 0.3 K/min. A detailed powder X-ray diffractogram and Raman spectrum of the compound are shown in the appendix (Figure 5.6 and Figure 5.7).

2.3.7 Synthesis of “K₂Si₂P₂” and “K₂Si₇P₂”

156 mg (4.00 mmol) elemental potassium was formed into little balls and filled into a tantalum ampoule (see chapter 2.1.3). Afterwards, 112 mg (4.00 mmol) or 393 mg (14.00 mmol) ball-milled silicon and 124 mg (4.00 mmol) red phosphorous were added and the tantalum ampoule sealed using an arc furnace. The ampoule was placed in a tube furnace inside a fused silica tube under vacuum. The mixture was heated to 873 K at a heating rate of 2 K/min, annealed at 873 K for 36 h before being cooled down to room temperature at a rate of 1 K/min. Detailed powder X-ray diffractograms of the resulting compounds are shown in the appendix (Figure 5.8).

2.3.8 Synthesis of 250 – 270 nm PMMA Beads

Synthesis of PMMA beads was performed according to the procedure reported by Wang *et al.*^[92, 93] 35.5 g (355 mmol) methyl methacrylate (MMA) and varying amounts of sodium dodecyl sulphate (SDS) were added to deionized water (98 mL) under stirring. Particle size of the resulting PMMA beads could be controlled by the amount of SDS surfactant, lowering sphere sizes with increasing SDS amount used. For a typical size of PMMA beads in the range of 250 – 270 nm, 5.0 mg (17.3 μmol) SDS was added. The deionized water and MMA used had been bubbled with nitrogen for 30 min upfront. After stirring the reaction mixture at 363 K for 1 h, 56.0 mg (207 μmol) potassium persulfate initiator in deionized water (2 mL) was added. The resulting mixture was stirred for another 2.5 h, quenched by cooling with ice and stirred at room temperature overnight. The PMMA beads were separated by centrifugation, filtered and re-dispersed several times to remove any residual side products. PMMA beads were partly obtained from either Daniel Böhm or Kristina Peters (Bein group and Fattakhova-Rohlfing group, LMU).

2.3.9 Preparation of Precursor Solutions

Due to air and moisture sensitivity of the compounds, all precursor solutions were prepared in a SCHLENK tube inside a glovebox. SCHLENK tubes had been cleaned using a KOH/isopropanol bath and were stored inside an oven at 393 K prior to use. For methods of removing residual water from the solvents used see Table 2.1 in chapter 2.1.9. Various concentrations of precursor compounds in solution were tested. Best performing concentrations for the compounds used are listed below.

Preparation of K_4Ge_9 solutions in *en*

0.06 mmol (50 mg) K_4Ge_9 was filled into a SCHLENK tube inside a glovebox. Afterwards, 1 mL *en* was added and the mixture stirred for 2 – 3 h at room temperature. The result was a red solution without any residual solid side products.

Preparation of $K_{12}Si_{17-x}Ge_x$ ($x = 0, 5, 9, 12, 17$) solutions in *en* (+ 2.2.2-crypt)

0.12 mmol (114 – 204 mg) of $K_{12}Si_{17-x}Ge_x$ was filled into a SCHLENK tube inside a glovebox. 2 mL *en* was added and the mixture stirred for 3 d at room temperature. $K_{12}Ge_{17}$ yielded a green colored solution without any residual solid side products. Mixed Si/Ge compounds ($x = 5, 9, 12$) yielded reddish-brown solutions with some residual black solids that were filtered off. The amount of leftover black solid increased with silicon content of the precursor, with a maximum for $K_{12}Si_{17}$ as a precursor showing a yellow-green solution. Addition of 0.48 mmol (180 mg, 4 eq) 2.2.2-crypt increased intensity of the colors for mixed Si/Ge compounds as well as the amount of material dissolved after 3 d. However, for $K_{12}Si_{17}$ this did not improve solubility significantly.

To determine the amount of material dissolved, solutions were filtered into a vial (prior weight determination). This vial was placed into a Schlenk and the solvent removed *in vacuo*. Subsequently, the vial was weighted again to determine the amount of dissolved material from the weight difference. In case of 2.2.2-crypt addition, the combined weight of the precursor phase and 2.2.2-crypt was used as a reference.

Experimental Section

Preparation of $\text{Rb}_{12}\text{Si}_{17-x}\text{Ge}_x$ ($x = 0, 5, 9, 12, 17$) and $\text{K}_4\text{Si}_{4-x}\text{Ge}_x$ ($x = 0, 1.2, 2.1, 2.8, 4$) solutions in *en* (+ 2.2.2-crypt)

0.12 mmol $\text{Rb}_{12}\text{Si}_{17-x}\text{Ge}_x$ or $\text{K}_4\text{Si}_{4-x}\text{Ge}_x$ was filled into a SCHLENK tube inside a glovebox. Then, 2 mL *en* was added and the mixture stirred for 3 d at room temperature. Colors, remaining residual solids and behavior with addition of 2.2.2-crypt were as described for the corresponding $\text{K}_{12}\text{Si}_{17-x}\text{Ge}_x$ -phases in solution. However, solubility of $\text{K}_4\text{Si}_{4-x}\text{Ge}_x$ -phases was significantly lowered compared to $\text{K}_{12}\text{Si}_{17-x}\text{Ge}_x$ -phases. Overall values dissolved in case of $\text{K}_4\text{Si}_{4-x}\text{Ge}_x$ -phases were approximated through the amount of residue remaining after filtration of the solutions.

Preparation of K_2SnBi solutions in *en*

0.96 mmol (195 mg) K_2SnBi was filled into a SCHLENK tube inside a glovebox and 0.5 mL *en* was added. The mixture was stirred for 16 h at room temperature and yielded a red solution and some residual black solids after filtration.

Preparation of K_2SiP_2 solutions in *en* + 2.2.2-crypt

0.18 mmol (30 mg) K_2SiP_2 was filled into a SCHLENK tube inside a glovebox. 1 mL *en* was added and the mixture stirred for 3 d at room temperature. However, the solution did not show any coloring, meaning the compound did not dissolve at all. Therefore, 0.18 mmol (68 mg) 2.2.2-crypt was added and the solution stirred for 3 d, yielding an orange solution and residual brown solids after filtration.

Preparation of K_4Ge_9 + Se solutions in *en*

Upfront, 0.36 mmol (29 mg) selenium was dissolved in 2 mL *en* after stirring for 1 d yielding a dark green solution. 0.2 mL of that solution was then added to 0.07 mmol (60 mg) of K_4Ge_9 dissolved in 1.2 mL *en*.

Preparation of K_2Te solutions in *en*

1.0 mmol (39 mg) potassium and 0.5 mmol (63 mg) tellurium were filled into a SCHLENK tube inside a glovebox. 4 mL *en* was added and the mixture stirred for 7 d at room temperature, yielding a blue-purple solution and some residual black solids after filtration.

Preparation of K_4Ge_9 + K_2Te solutions in *en*

0.12 mmol (100 mg) K_4Ge_9 was filled into a SCHLENK tube inside a glovebox and 2 mL *en* was added. The mixture stirred for 2 h at room temperature before adding 0.2 to 0.9 mL of a K_2Te solution in *en*.

2.3.10 Preparation of Thin Film Sheets

Due to air and moisture sensibility, all preparations took place inside a SCHLENK tube or glovebox. If not stated otherwise in the respective chapters, all syntheses were carried out using PMMA spheres with a size of 250 – 300 nm. Prior to use, substrates were cleaned and coated with PMMA (see chapter 2.1.6).

Preparation of inverse opal structured Si/Ge and Si thin films

A solution of 0.06 mmol (57 – 89 mg) $K_{12}Si_{17-x}Ge_x$ ($x = 5, 9, 12, 17$) in 1 mL *en* was prepared as described in chapter 2.2.9. One drop of this solution was drop coated onto a PMMA covered substrate. Depending on the analysis method, silicon, fused silica, sapphire or copper foil were used as substrates. After the precursor solution had dried, each of the thin films was placed inside vial in a SCHLENK tube. Then, about 25 μ L of a cross-linker ($SiCl_4$ for silicon sheets, $GeCl_4$ for mixed silicon and germanium thin films) per thin film was added to another vial in that SCHLENK tube, avoiding direct contact to the films. The Schlenk tube was stored in a vertical position overnight, creating a saturated $SiCl_4$ or $GeCl_4$ atmosphere within. Afterwards, the substrates were transferred to another SCHLENK tube, that was inserted into a tube furnace (see chapter 2.1.8). Substrates were dried at 373 K for 1 h under dynamic vacuum, before being annealing at 773 K for 5 min either under dynamic vacuum or argon atmosphere. Additionally, crystallization of the material could be achieved by subsequent annealing of the thin films at 873 K for 1 h. Finally, the thin films were placed in a vial inside a glovebox and washed with DMSO then THF for 30 min each and dried under dynamic vacuum.

Preparation of inverse opal structured Ge thin films

Ge thin films were prepared analogous to Si and Si/Ge mixed films using 0.06 mmol (50 mg) K_4Ge_9 in 1 mL *en* as a precursor solution. $GeCl_4$ was used as the cross-linker in this case.

Preparation of inverse opal structured Ge/Se and Ge/Te thin films

Mixed Ge/Se and Ge/Te thin films were prepared analogous to Si and Si/Ge mixed films using the respective *Se/en* or *K₂Te/en* solution in combination with a solution of K_4Ge_9 in *en* as mentioned in chapter 2.3.9. For this, no cross-linker was used. Films were only annealed for 1 h at 373 K in dynamic vacuum.

Preparation of structured Sn/Bi thin films

Mixed Sn/Bi thin films were prepared analogous to Si and Si/Ge mixed films using 0.96 mmol (195 mg) K_2SnBi in 0.5 mL *en* as a precursor solution. As cross-linkers either $SiCl_4$ or $SnCl_4$ were used. In case of the latter, an excess of 0.1 mL was used per thin film. Additionally, a static vacuum of around $1 \cdot 10^{-1}$ mbar was applied to the SCHLENK tube to address the lower vapor pressure of $SnCl_4$. Also, the annealing temperatures had to be adjusted for these thin films. Films were annealed for 20 min at either 373 K or 423 K in dynamic vacuum.

2.3.11 Synthesis of $K[(Si_{9-y}Ge_y)(Si(TMS)_3)_3]$

For the synthesis of $K[(Si_{9-y}Ge_y)(Si(TMS)_3)_3]$, 0.18 mmol (171 – 247 mg) $K_{12}Si_{17-x}Ge_x$ ($x = 5, 9, 12, 17$) was filled into a SCHLENK tube inside a glovebox. 2.16 mmol (612 mg, 12 eq) chlorotris(trimethylsilyl)silane (*hyp*-Cl) and 3 mL acetonitrile were added and the mixture stirred for 3 d at room temperature. After filtration, an orange (high Ge content) to pale yellow (only Si) solution was obtained. The solid residue was then extracted with more acetonitrile till the filtrate was colorless (typically another 3 mL were used). Afterwards, the solvent was removed in dynamic vacuum and the residue re-dissolved in 1.0 - 1.5 mL toluene (or hexane). For crystallization, 0.18 mmol (68 mg, 1 eq) 2.2.2-crypt was added and the solution stored in a fridge at 241 K. After 2 d, thin

orange to yellow needles formed (30 – 60 mg, 12 – 20 %). In case of high Ge content, after 3 months dark red cubes formed.

2.3.12 Synthesis of $(\text{NHC}^{\text{Dipp}}\text{M})_2\{\eta^3\text{-Ge}_9(\text{Si}(\text{TMS})_3)_2\}$ (M = Cu, Ag, Au)

The synthesis of $(\text{NHC}^{\text{Dipp}}\text{M})_2\{\eta^3\text{-Ge}_9(\text{Si}(\text{TMS})_3)_2\}$ (M = Cu, Ag, Au) could be achieved through two different methods.^[188]

Method A:

0.12 mmol (205 mg) $\text{K}_{12}\text{Ge}_{17}$ was filled into a SCHLENK tube inside a glovebox. 0.72 mmol (408 mg, 6 eq) *hyp*-Cl and 2 mL acetonitrile were added and the mixture stirred for 16 h at room temperature. After filtration, a deep red solution was obtained and a solution of 0.24 mmol (117 – 149 mg) $\text{NHC}^{\text{Dipp}}\text{MCl}$ (M = Cu, Ag, Au) in 2 mL acetonitrile was added, immediately leading to the formation of a brown precipitate. The mixture was stirred for another 15 min at room temperature to ensure complete conversion of the reactants. Then, the deep red supernatant solution was removed and the precipitate dried in dynamic vacuum. The brown solid was re-dissolved in 3 mL toluene and filtered again. For crystallization, the solution was concentrated to about half of its original volume and stored in a freezer at 233 K. After 7 d, red plate-shaped crystals formed (74 mg, 30% for M = Cu; 51 mg, 20% for M = Ag; 83 mg, 30% for M = Au).

Method B:

0.075 mmol (92 mg) $\text{K}_2[\text{Ge}_9(\text{Si}(\text{TMS})_3)_2]$ was filled into a SCHLENK tube inside a glovebox and 1 mL acetonitrile was added. To the solution, 0.15 mmol (73 – 93 mg) $\text{NHC}^{\text{Dipp}}\text{MCl}$ (M = Cu, Ag, Au) in 1.5 mL acetonitrile was added, immediately leading to the formation of a brown precipitate. This precipitate was then further treated as described in Method A, yielding red plate-shaped crystals after 7 d at 233 K in a freezer (60 mg, 45% for M = Cu; 40 mg, 25% for M = Ag; 52 mg, 30% for M = Au).

3 Results and Discussion

3.1 Inverse Opal Structured Ge Thin Films

3.1.1 Synthesis and Characterization of Inverse Opal Structured Ge Thin Films

$A_4\text{Ge}_9$ ($A = \text{K}-\text{Cs}$) phases contain well-defined $[\text{Ge}_9]^{4-}$ clusters and can be synthesized by alloying stoichiometric amounts of the elements.^[133] Due to its solubility in highly polar solvents such as ethylene diamine (*en*), the ZINTL-phase K_4Ge_9 was utilized as a precursor for the synthesis of inverse opal structured germanium thin films by Bentlohner *et al.*^[43] Morphology and composition of the thin films have been investigated in detail.^[43] Subsequently, Geier *et al.* proved successful application of these Ge films as anode materials in Li ion batteries.^[95] However, charge carrier mobilities within these films were not determined so far.

Within this work, charge carrier mobilities within Ge thin films as well as the influence of the morphology of the material on these mobilities are determined. Inverse opal structured germanium thin films were synthesized according to the method established by Bentlohner *et al.*^[43] 0.06 mmol (50 mg) K_4Ge_9 was dissolved in 1 mL *en* (for details on the synthesis see chapter 2.3.10) and drop-casted onto a substrate covered with PMMA beads in different sizes to yield inverse opal structured thin films (see Figure 3.1i). Alternatively, the solution of K_4Ge_9 in *en* was drop-casted onto blank substrates to yield unstructured germanium films. The solvent (*en*) was removed by evaporation and GeCl_4 was added as a cross-linker *via* vapor deposition (see Figure 3.1ii and iii). The samples were annealed at 373 K for 1 h followed by 773 K for 5 min to remove the PMMA beads (see Figure 3.1iv). Finally, the thin films were washed with DMSO followed by THF for 30 min each (see Figure 3.1v and vi).

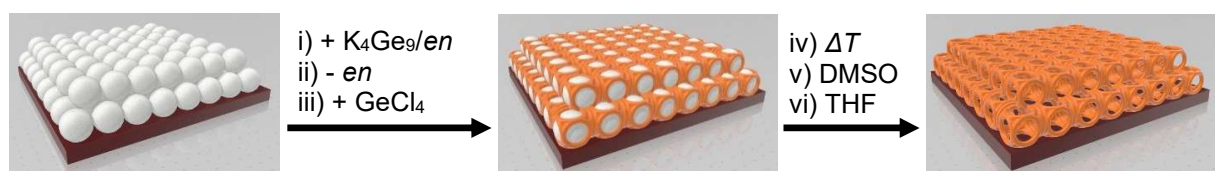


Figure 3.1. Synthesis of inverse opal structured Ge thin films.^[43] i) Infiltration of PMMA beads with a K_4Ge_9 /*en* solution, ii) removal of *en* *via* evaporation, iii) addition of GeCl_4 as a linker, iv) removal of PMMA beads by annealing (ΔT), v) + vi) removal of residual KCl and left-over degradation products from PMMA beads by washing with DMSO and THF.

3.1 Inverse Opal Structured Ge Thin Films

This way, any KCl originating from a reaction of the cross-linker GeCl_4 with the precursor K_4Ge_9 as well as left-over decomposition products from the PMMA beads were removed. The material was then dried in dynamic vacuum to yield Ge thin films.

For inverse opal structured thin films, PMMA template beads were dip-coated onto the substrate prior to the addition of the K_4Ge_9 precursor (for details see chapter 2.1.6). The size distribution of the PMMA beads could be controlled by varying the amount of SDS in the synthesis, with an increased amount resulting in smaller PMMA beads (for details on the synthesis see chapter 2.3.8). However, PMMA beads with a diameter of 100 nm or smaller could not be isolated by centrifugation. Usually, PMMA beads with a size of 250 – 300 nm resulted in the best homogeneity of the inverse opal structured thin films. In order to determine if the morphology of the material is influencing the resulting charge carrier mobilities, homogenous thin films (from 340 nm PMMA) were compared to less homogenous films (from 150 nm PMMA) as well as unstructured films (without PMMA beads).

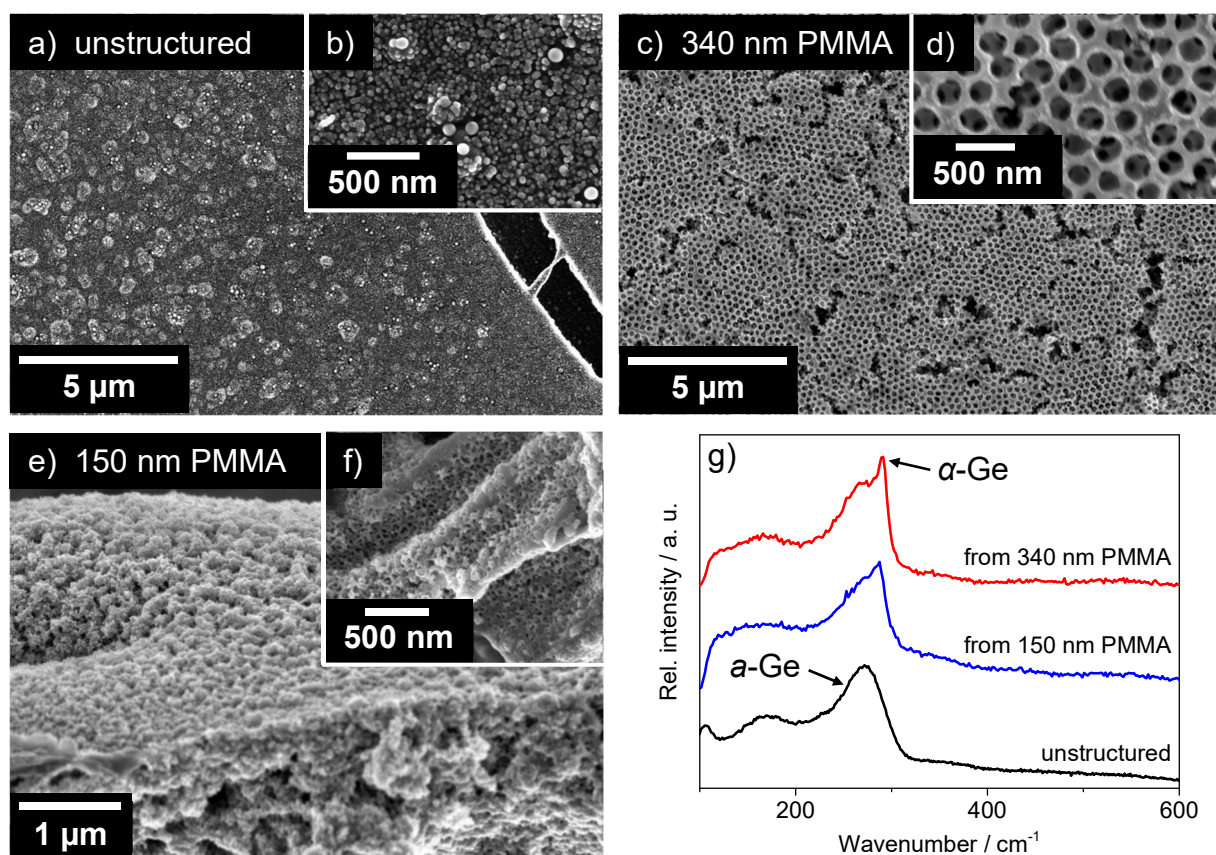


Figure 3.2. SEM pictures of germanium thin films. a) 10.000x and b) 100.000x magnification of unstructured thin film, c) 10.000x and d) 100.000x magnification of inverse opal structured thin film using 340 nm PMMA template beads, e) 35.000x and f) 100.000x magnification of inverse opal structured thin film using 150 nm PMMA template beads, g) Raman spectra ($\lambda = 532$ nm) of germanium thin films.

Results and Discussion

In an unstructured germanium thin film, large cracks (Figure 3.2a) and small spots of agglomerated material (Figure 3.2b) are present due to the annealing process. In a germanium thin film using 340 nm PMMA template beads, inverse opal structured material is detected throughout a large area (Figure 3.2c and d). The inverse opal structure features vacancies with a diameter of 245 ± 24 nm and a pore wall thickness of 90 ± 18 nm. Using significant smaller 150 nm PMMA template beads results in a more irregular structure with a rough surface and only small areas of inverse opal structured material (Figure 3.2e and f). The inverse opal structured part of the material features vacancies with a diameter of 52 ± 9 nm and a pore wall thickness of 24 ± 3 nm. A band located at $270 - 275$ cm^{-1} representing amorphous germanium (*a*-Ge) is detected in Raman spectra of all thin films (Figure 3.2g). However, for inverse opal structured thin film a slight sharp band representing crystalline germanium (α -Ge, 290 cm^{-1}) is detected as well.

3.1.2 Charge Carrier Mobility in Inverse Opal Structured Ge Thin Films (Terahertz Spectroscopy)

Carrier mobility within these inverse opal structured germanium thin films was determined using time resolved terahertz spectroscopy (TRTS).^[217] Fluence and temperature dependent measurements were carried out as described in chapter 2.2.8. The transient photoconductivity $|\Delta T/T_0|$ did not change drastically in temperature dependent measurements. However, in fluence dependent measurements the value of $|\Delta T/T_0|$ (peak) steadily increased alongside an increase in initial laser power for all germanium thin films (see Figure 3.3a for inverse opal structured sample from 340 nm PMMA template beads as well as Figure 5.11 in the appendix for other samples). The value of $|\Delta T/T_0|$ (peak) represents the maximum in reduction of THz transmission. This value is drastically decreased for an inverse opal structured thin film compared to unstructured material due to a reduced density of photoexcited carriers (Figure 3.3b). The value of $|\Delta T/T_0|$ (peak) changes almost linearly with the fluence indicating that quantum efficiency approaches 100% especially at lower fluences.

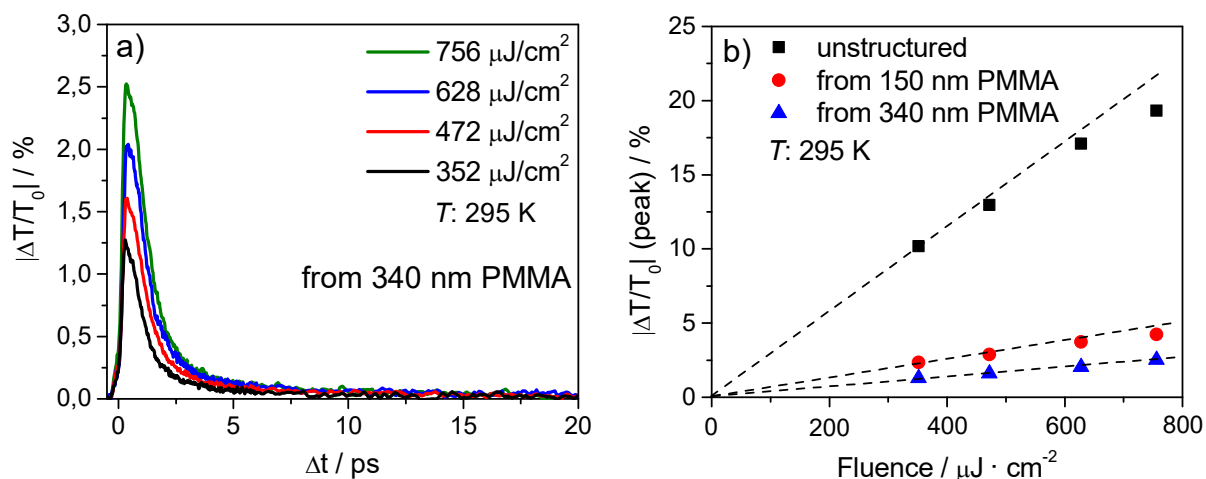


Figure 3.3. Transient photoconductivity $|\Delta T/T_0|$ for germanium thin films. a) Fluence dependency at room temperature (295 K) for an inverse opal structured thin film using 340 nm PMMA template beads, b) comparison of fluence dependency at room temperature (295 K) of all germanium thin films.

The transient photoconductivity $|\Delta T/T_0|$ has a fast rise time in the range of the minimum response time of the THz pulse detection setup used, indicating a fast photoexcitation of mobile carriers for all thin films.^[200] The rise time found for inverse opal structured thin films (≈ 0.35 ps, see Figure 3.4a as well as Figure 5.12a in the appendix) is faster by about 33% than the value found for an unstructured thin film (≈ 0.5 ps, see Figure 5.13a in the appendix). These free carriers could lead to the formation of polarons, decreasing carrier mobility due to an increase in effective mass,^[218] which has been described for a variety of disordered amorphous semiconductors.^[219] The fast rise times also propose that mainly intraband relaxation of carriers occurs.^[220] In contrast, bulk crystalline germanium shows a slow rise time (≈ 3.5 ps, see Figure 5.14a in the appendix) due to phonon-assisted scattering to the low mobility satellite valleys.^[221]

After the transient photoconductivity reached its peak, the decay mechanism can be deduced while the transmission recovers. Compared to bulk crystalline germanium, in which mobile carrier lifetimes last up to microseconds (see Figure 5.14b in the appendix), all thin films show a fast decay time. As expected for amorphous materials, the lack of long-range order inhibits carrier migration, resulting in the short photoconductivity due to localization of charge carriers. For the unstructured amorphous Ge thin film, this results in a photoconductivity of less than 100 ps (see Figure 5.12b in the appendix). In inverse opal structured thin films, the transient photoconductivity is shortened even further. Transient photoconductivity of less than 40 ps for an inverse opal structured thin film starting with 150 nm PMMA template beads (see Figure 5.13b in the appendix) and less than 30 ps for a thin film starting

Results and Discussion

with 340 nm PMMA beads (see Figure 3.4b) is detected. However, this is still significantly longer than the transient photoconductivity found in inverse opal structured mixed Si/Ge and silicon thin films (see chapter 3.2.7).

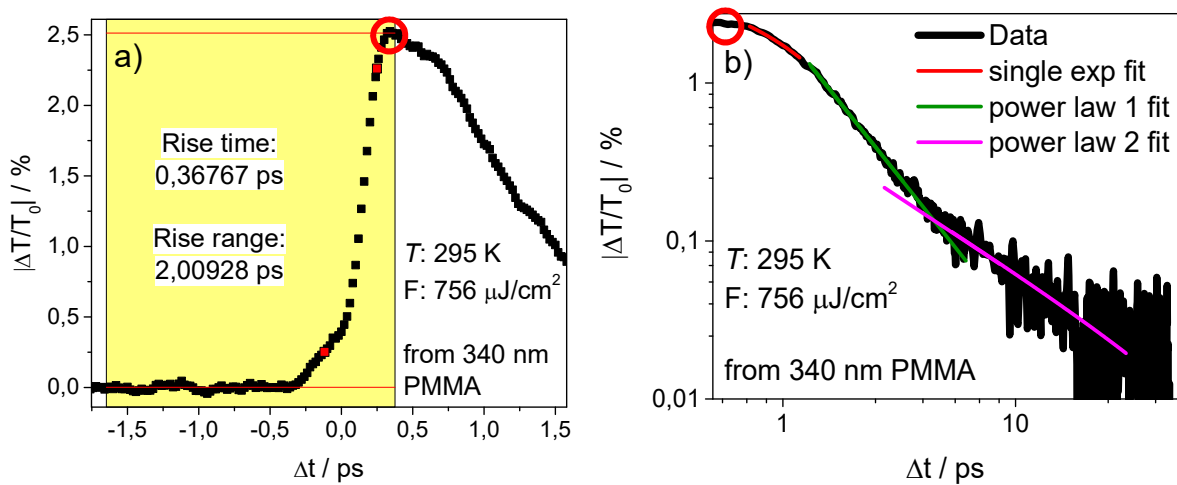


Figure 3.4. Rise time (a) and signal decay (b) for an inverse opal structured germanium thin film starting from 340 nm PMMA template beads. Starting point for signal decay plot is the peak signal for transient photoconductivity (red circle in both graphs). Signal decay plot (b) is depicted in logarithmic scale to highlight power law dependency.

The ultrafast carrier dynamics within these thin films can be described by a fit of the transient photoconductivity with three decay components. Firstly, the signal follows a single exponential decay (see Figure 3.4b, red fit). The tail of $|\Delta T/T_0|$ can be fitted to two power law decays: $y = B \cdot x^{-\beta_1} + y_0$ and $y = C \cdot x^{-\beta_2} + y_0$ with pre-factors B and C as well as power law exponents β_1 and β_2 . This remains unchanged for various fluences (carrier densities). Photo-excited carriers undergoing a rapid exponential decay (40 – 55% of integrated value) are immediately trapped into defects on the surface or into grain boundaries, resulting in a fast decay time of $t_1 \approx 2.3 - 2.5$ ps for the unstructured Ge thin film and even faster decay times of $t_1 \approx 0.6 - 1.0$ ps for inverse opal structured films. The decay time of a 150 nm PMMA based inverse opal film is 10 – 20% faster than that of a 340 nm PMMA based film, indicating a higher population of surface states. At lower temperatures, carriers drift at a faster rate, decreasing the decay time even further. Long-lived carriers follow power law decay dynamics, typically observed in amorphous semiconductors, migrating between localized states *via* multiple trapping.^[200, 222, 223] The mechanism behind multiple trapping of carriers within bands has been explained in time-of-flight (TOF) transient photocurrent measurements.^[200, 222]

3.1 Inverse Opal Structured Ge Thin Films

The frequency-resolved complex conductivity σ was deduced from the THz transmission at a fixed delay time (Δt). This fixed optical pump – THz probe delay was set to a value where dispersive transport occurs ($\Delta t = 6.75$ ps for unstructured Ge thin films and $\Delta t = 2.35$ ps for inverse opal structured Ge films). For all Ge thin films, $\sigma(\omega)$ is approximated by a Drude-Smith model of carrier localization (equation 1), in which ω_p is the plasma frequency, ϵ_0 is the vacuum permittivity, τ_{DS} is the effective scattering time in which the mobility μ can be derived as $\mu = e\tau_{DS}/m^*$.

$$\sigma(\omega) = \frac{\omega_p^2 \epsilon_0 \tau_{DS}}{1 - i\omega\tau_{DS}} \left[1 + \frac{c}{(1 - i\omega\tau_{DS})} \right], \text{ with } 0 \leq c \leq -1, \quad (1)$$

The effective mass of an electron in the thin films was set as $m^* = 0.12 m_e^*/m_0$, providing a close estimate for the mobility in bulk germanium. Beyond the Drude model of free-electron gas^[224], equation (1) describes suppressed long-range transport of carriers in materials due to disorder.^[218, 223] The velocity parameter c thereby provides a good estimate of the carrier backscattering within the material due to structural confinement, with c in between 0 (free carriers, restoring the Drude model) and -1 (complete backscattering of carriers). In contrast, bulk crystalline germanium follows the Drude model of free-electron gas^[224] which can be recovered when c is 0.

The frequency-resolved complex conductivity was extracted at 0.5 ps after the peak of $|\Delta T/T_0|$ ($\Delta t = 6.75$ ps after inducing the photoexcitation for the unstructured thin film and $\Delta t = 2.35$ ps for the inverse opal structured films). Both imaginary ($\sigma_i < 0$) and real part ($\sigma_r > 0$) were fitted applying the Drude-Smith model which fits quite well (see Figure 3.5). The parameters extracted from these fits are listed in Table 3.1. The c values were found to be -0.78 for the unstructured thin film and around -0.73 for the inverse opal structured films (INOPs). This indicates that not all carriers backscatter and thereby 20 – 30% are able to drift across the intergranular boundaries. In SEM pictures of inverse opal structured thin films more intergranular connections within the pore wall are detected than in pictures of an unstructured film (see Figure 3.2). Less carrier localization observed in inverse opal structured Ge films (higher c values) compared to the unstructured Ge film may indicate an increased amount of crystalline material as detected in their Raman spectra (see Figure 3.2g in chapter 3.1.1). The fast scattering time τ_{DS} of ≈ 50 fs implies a reduced carrier mean free path compared to bulk crystalline germanium^[225], but is still higher than scattering times found for mixed Si/Ge as well as silicon thin films (see chapter 3.2.7).

Results and Discussion

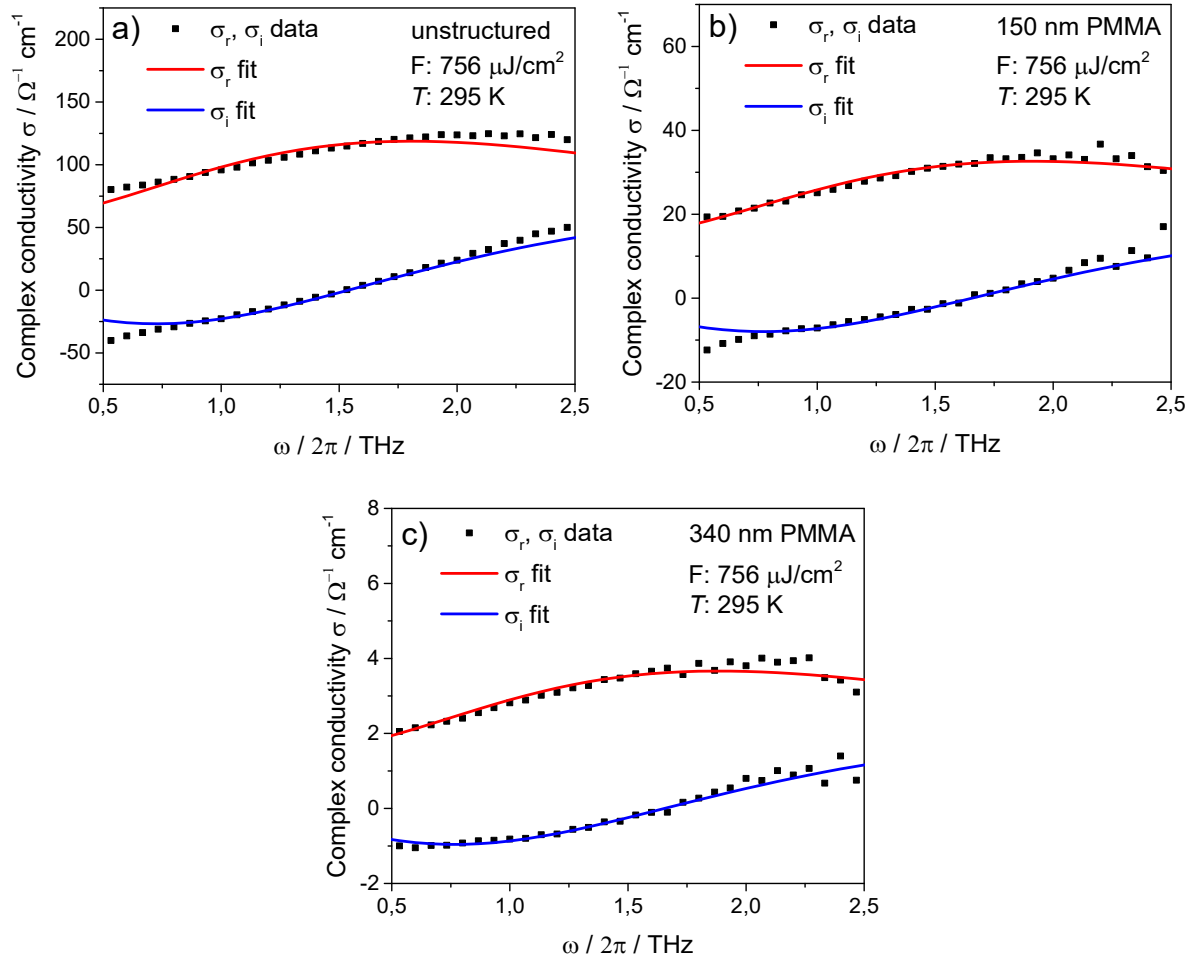


Figure 3.5. Complex conductivity $\sigma(\omega)$ plots for germanium thin films. a) unstructured material, b) starting from 150 nm PMMA beads, c) starting from 340 nm PMMA beads. Both imaginary (σ_i , blue line) and real part (σ_r , red line) were fitted applying the Drude-Smith model.

Table 3.1. Parameters obtained from complex conductivity of germanium thin films using the Drude-Smith model (equation 1) at room temperature (295 K).

Fluence / $\mu\text{J} \cdot \text{cm}^{-2}$	Material	$\tau_{\text{DS}} / \text{fs}$	c	$\mu_m / \text{cm}^2 \text{ V}^{-1} \text{ s}^{-1}$
756	unstructured	61 ± 1	-0.78 ± 0.01	199 ± 6
756	INOP - from 150 nm PMMA	47 ± 3	-0.73 ± 0.01	190 ± 13
756	INOP - from 340 nm PMMA	48 ± 4	-0.72 ± 0.02	190 ± 11

The macroscopic mobility $\mu_m = (1 + c)\mu$, was calculated from the values for c and τ_{DS} . The macroscopic mobility values do not change with the carrier density indicating multiple trapping events rather than an electron-hole recombination process as

3.1 Inverse Opal Structured Ge Thin Films

observed in polycrystalline silicon.^[225] The values of $\mu_m \approx 200 \frac{\text{cm}^2}{\text{V}\cdot\text{s}}$ are similar for all germanium thin films tested, demonstrating that introduction of inverse opal structure does not compromise the electrical properties of *a*-Ge thin films. Moreover, c and τ_{DS} values for both inverse opal structured films are almost identical, indicating that they have similar particle topology. Instead of the size of the empty spheres in the inverse opal structure, the morphology of the germanium framework is responsible for the confinement of carriers.

Exceptionally, these carrier mobility values are exceeding the value reported for amorphous silicon (*a*-Si) of $\mu_0 < 13 \frac{\text{cm}^2}{\text{V}\cdot\text{s}}$ ^[222] (electron-drift mobility using a SCHOTTKY-diode circuit) by far. The mean free path for a purely amorphous semiconductor with a free-electron mass would be around 10^{-6} cm, resulting in the highest possible mobility value of $< 100 \frac{\text{cm}^2}{\text{V}\cdot\text{s}}$ ^[226] for amorphous germanium. The slight crystallinity detected in bands in the Raman spectra of inverse opal structured Ge films (see Figure 3.2g in chapter 3.1.1) is therefore responsible for the high carrier mobility which is close to values found for polycrystalline germanium ($200 - 350 \frac{\text{cm}^2}{\text{V}\cdot\text{s}}$).^[227-229] High mobility values for polycrystalline germanium were achieved through pulsed laser annealing^[227] or fabrication on insulating substrates^[229] at temperatures below 900 °C so far. However, inverse opal structured Ge thin films are available through wet-chemical synthesis and do not undergo long annealing processes at high temperatures. Therefore, the carrier mobilities of $\mu_m \approx 190 \frac{\text{cm}^2}{\text{V}\cdot\text{s}}$ derived for inverse opal structured Ge thin films are exceptional, making these films competitive candidates for macroporous materials in emerging applications in optoelectronics.

3.2 Si/Ge-Clusters as Wet Chemical Precursors for Inverse Opal Structured Thin Films

3.2.1 Synthesis and Characterization of $K_{12}Si_{17-x}Ge_x$ -, $Rb_{12}Si_{17-x}Ge_x$ - and $K_4Si_{4-x}Ge_x$ -Phases

Binary compounds involving tetrahedral $[E_4]^{4-}$ clusters ($E = Si, Ge$) with alkali metals ($A = Na-Cs$) in a 1:1 ratio (A_4E_4 phases) have been known for more than 50 years.^[126] For Germanium, A_4Ge_9 ($A = K-Cs$) phases containing $[Ge_9]^{4-}$ clusters could also be synthesized by alloying stoichiometric amounts of the elements.^[133] However, for silicon a corresponding A_4Si_9 phase could not be obtained so far. Instead, intermetallic $A_{12}E_{17}$ compounds ($A = Na-Cs$; $E = Si, Ge$) containing tetrahedral $[E_4]^{4-}$ as well as $[E_9]^{4-}$ clusters in a 2:1 ratio were synthesized.^[132] Ternary Si/Ge phases were introduced by M. Waibel in the form of $K_{12}Si_{17-x}Ge_x$ -, $Rb_{12}Si_{17-x}Ge_x$ - ($x = 5, 9, 12$) and $K_4Si_{4-x}Ge_x$ ($K_4Si_2Ge_2$) phases.^[140, 230] However, the synthesis of $K_{12}Si_{17-x}Ge_x$ - and $Rb_{12}Si_{17-x}Ge_x$ - phases from the elements often results in to the formation of $A_4Si_{4-x}Ge_x$ ($A = K, Rb$) as side phases.^[231] Therefore, the synthesis was refined by ball milling mixtures of silicon and germanium to fine $Si_{17-x}Ge_x$ powders prior to solid state synthesis by reaction with alkali metals.^[231, 232] These $Si_{17-x}Ge_x$ powders showed no distinct reflexes representing elemental silicon or germanium anymore. Instead, broad reflexes with values in between the values for elemental silicon and germanium were detected.^[232]

This method was applied to the synthesis of $K_{12}Si_{17-x}Ge_x$ -, $Rb_{12}Si_{17-x}Ge_x$ - ($x = 0, 5, 9, 12, 17$) and $K_4Si_{4-x}Ge_x$ -phases ($x = 0, 1.2, 2.1, 2.8, 4$) within this work (for details on the synthesis see chapter 2.3.2, 2.3.3 and 2.3.4, respectively). For $K_{12}Si_{17-x}Ge_x$ - and $Rb_{12}Si_{17-x}Ge_x$ -phases ($x = 0, 5, 9, 12, 17$), their corresponding A_4E_4 ($A = K, Rb$; $E = Si, Ge$) phases frequently appear as side products when synthesized at 1173 K as in earlier works.^[140, 231] Therefore, the temperature for the synthesis of these phases was lowered to 1073 K in most cases within this work. The powder diffraction patterns obtained for $K_{12}Si_{17-x}Ge_x$ - and $Rb_{12}Si_{17-x}Ge_x$ -phases show no reflexes that could be attributed to A_4E_4 phases (see Figure 3.6a for $K_{12}Si_{17-x}Ge_x$ -phases; additionally see Figure 5.1a in the appendix for $Rb_{12}Si_{17-x}Ge_x$ -phases) or left-over starting material (elemental silicon or germanium).

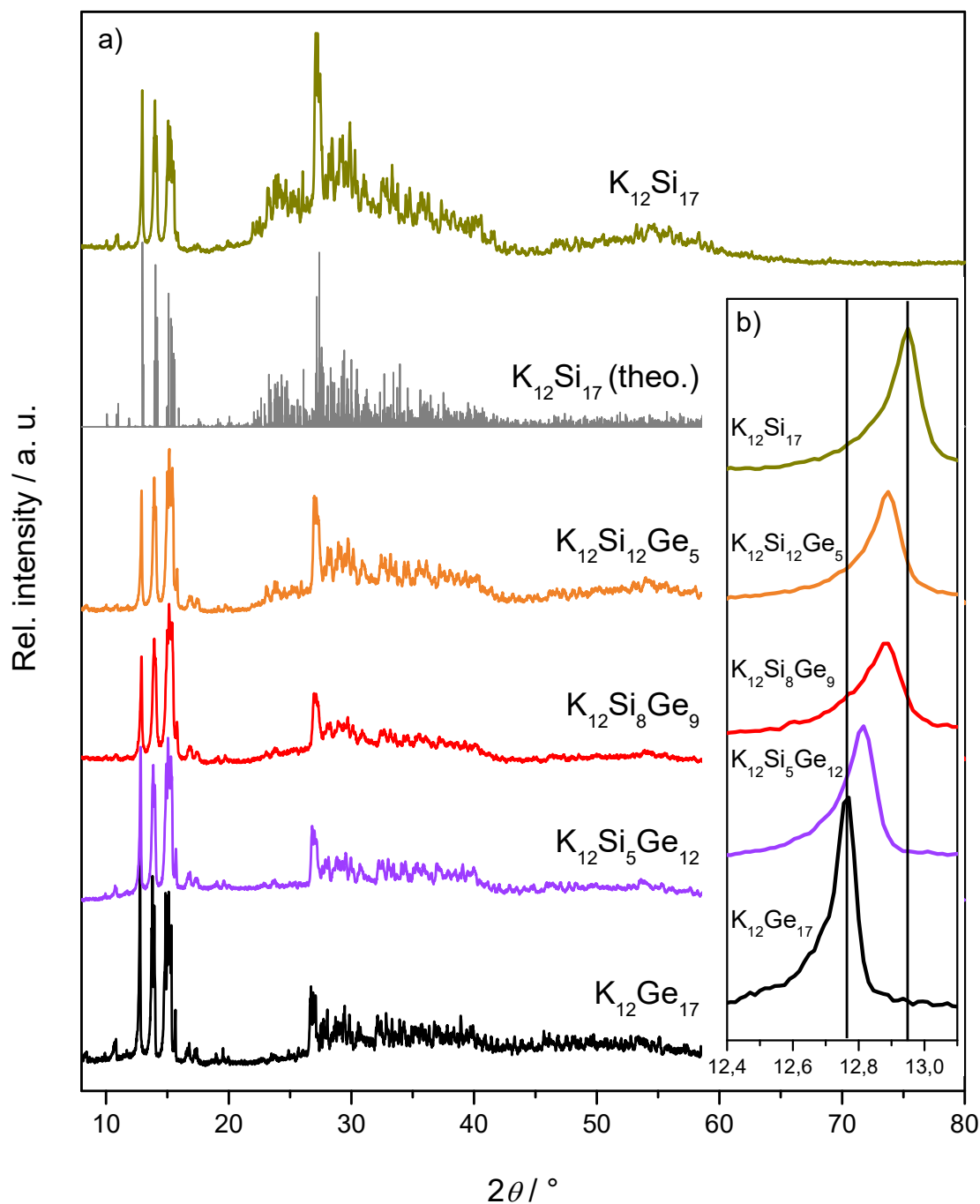


Figure 3.6. a) Powder diffraction patterns of $K_{12}Si_{17-x}Ge_x$ ($x = 0, 5, 9, 12, 17$) compounds. b) highlighted area of the compounds featuring a shift for the main reflex. Powder diffraction patterns were obtained using Cu- $K\alpha_1$ radiation, $\lambda = 1.54056 \text{ \AA}$. No side phases are detected. Also, the diffraction pattern obtained for $K_{12}Si_{17}$ is in good accordance with a theoretical powder diffraction pattern obtained from crystal data available in literature^[132], indicating that the compounds are phase pure.

The powder diffraction patterns obtained for $K_{12}Si_{17}$ and $Rb_{12}Si_{17}$ are also in good accordance with theoretical data obtained from crystal data available in the literature^[132, 233], indicating that the precursor materials are phase pure. Additionally, the detected reflexes shift to higher angles alongside an increasing silicon content in

Results and Discussion

the phase (see Figure 3.6b for $K_{12}Si_{17-x}Ge_x$ -phases; additionally see Figure 5.1b in the appendix for $Rb_{12}Si_{17-x}Ge_x$ -phases). This can be explained through decreasing unit cell parameters due to the lowered space requirements of silicon in comparison to germanium. This shift supports the successful synthesis of mixed $K_{12}Si_{17-x}Ge_x$ - and $Rb_{12}Si_{17-x}Ge_x$ -phases even though the high number of reflexes with low intensity prevents an evaluation through determination of the unit cell volumes of the phases.

Raman spectroscopy was conducted to further assess the composition of $K_{12}Si_{17-x}Ge_x$ - and $Rb_{12}Si_{17-x}Ge_x$ -phases ($x = 0, 5, 9, 12, 17$). The spectra of these compounds feature characteristic bands that can be assigned to specific clusters (see Figure 3.7 for $K_{12}Si_{17-x}Ge_x$ -phases; additionally see Figure 5.2 in the appendix for $Rb_{12}Si_{17-x}Ge_x$ -phases). Raman spectra obtained for binary $A_{12}Si_{17}$ and $A_{12}Ge_{17}$ ($A = K, Rb$) phases are in good accordance with data available in the literature.^[132, 133, 142, 234] For these binary phases, one band representing $[E_9]^{4-}$ ($E = Si, Ge$) clusters as well as three bands representing $[E_4]^{4-}$ clusters are detected. In case of $K_{12}Ge_{17}$, the band at 224 cm^{-1} was described to represent a $[Ge_9]^{4-}$ cluster vibration whereas the bands at $160, 198$ and 277 cm^{-1} were described as $[Ge_4]^{4-}$ cluster vibrations.^[133] For $K_{12}Si_{17}$, the band at 390 cm^{-1} was described to represent a $[Si_9]^{4-}$ cluster vibration whereas the bands at $282, 355$ and 484 cm^{-1} were described as $[Si_4]^{4-}$ cluster vibrations.^[234] For $Rb_{12}Ge_{17}$ and $Rb_{12}Si_{17}$, the same bands are detected with small shifts to the values found for their corresponding potassium phases. Additional bands at 322 cm^{-1} for $K_{12}Ge_{17}$ and 567 cm^{-1} for $K_{12}Si_{17}$ have not been described yet and therefore cannot be assigned to a specific vibration. For the bands at $\approx 124\text{ cm}^{-1}$ in $K_{12}Si_{17-x}Ge_x$ -phases and $\approx 82\text{ cm}^{-1}$ in $Rb_{12}Si_{17-x}Ge_x$ -phases, external lattice vibrations or the libration of the $[E_4]^{4-}$ clusters were suggested in the literature.^[232, 235]

In the Raman spectra of ternary $K_{12}Si_{17-x}Ge_x$ - and $Rb_{12}Si_{17-x}Ge_x$ -phases ($x = 5, 9, 12$), many bands are detected with low intensities (see Figure 3.7 for $K_{12}Si_{17-x}Ge_x$ -phases; additionally see Figure 5.2 in the appendix for $Rb_{12}Si_{17-x}Ge_x$ -phases). This is to be expected due to vibrations originating from different Si-Ge ratios in the clusters and is in good accordance with values found in a recent work by T. Henneberger.^[232] The intensity of the main bands representing $[Ge_4]^{4-}$ (160 cm^{-1}) and $[Ge_9]^{4-}$ (224 cm^{-1}) clusters are detected for all mixed Si/Ge phases and are weakened for an increasing amount of silicon in the precursor as expected. For the main bands representing $[Si_4]^{4-}$ (282 cm^{-1}) and $[Si_9]^{4-}$ (390 cm^{-1}) clusters, an opposing trend is evident. The intensity of both peaks is reduced for an increasing amount of germanium in the precursor.

3.2 Si/Ge-Clusters as Wet Chemical Precursors for Inverse Opal Structured Thin Films

However, in this case the reduction in intensity is even more evident for the peak representing $[\text{Si}_9]^{4-}$ clusters as it is barely recognizable in $\text{K}_{12}\text{Si}_8\text{Ge}_9$ and missing in the Raman spectrum of $\text{K}_{12}\text{Si}_8\text{Ge}_9$. Additional bands with low intensity cannot be matched to bare silicon or germanium clusters and therefore most likely represent vibrations originating from mixed Si-Ge clusters.

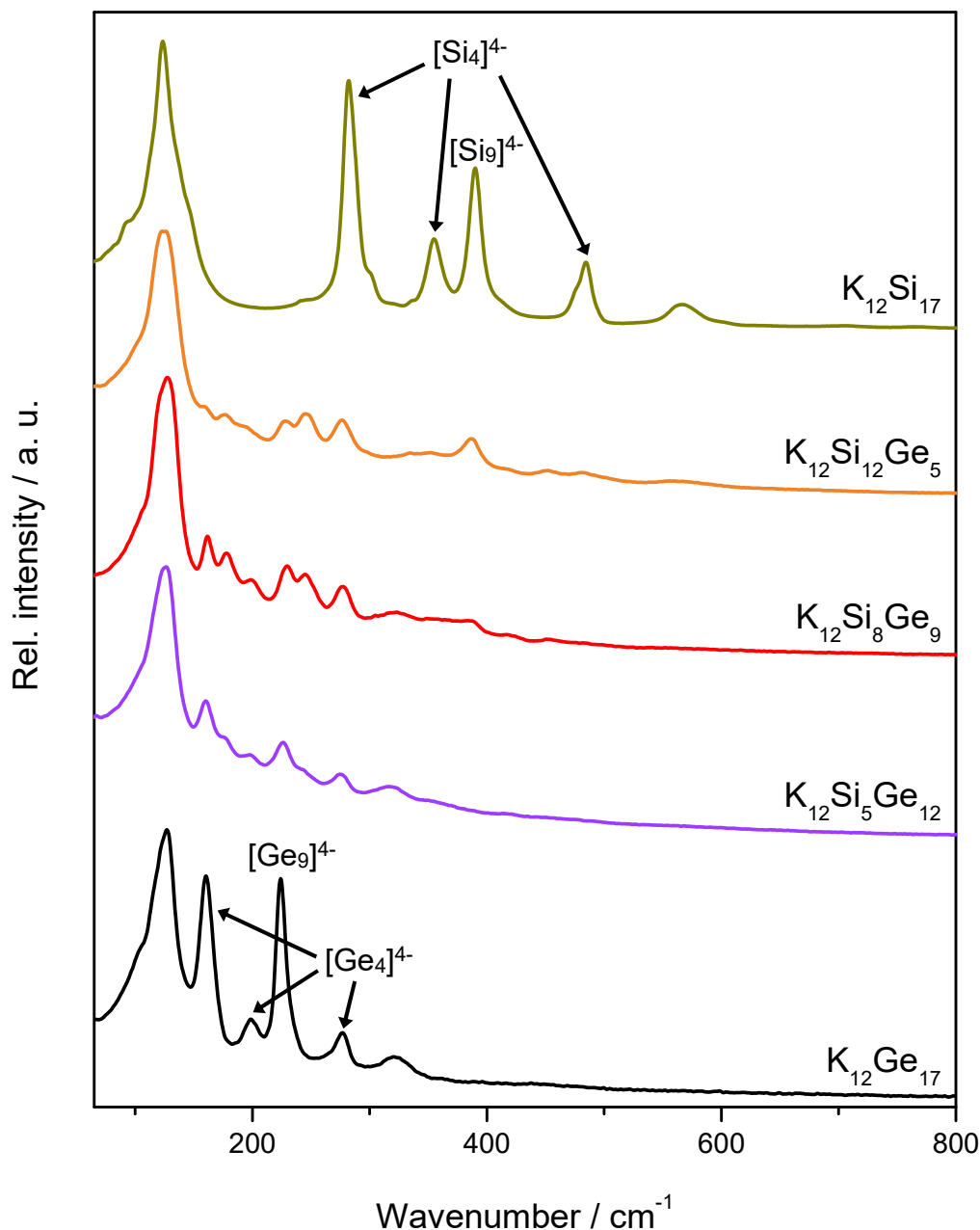


Figure 3.7. Recorded Raman spectra of $\text{K}_{12}\text{Si}_{17-x}\text{Ge}_x$ ($x = 0, 5, 9, 12, 17$) compounds. The location of the bands found in $\text{K}_{12}\text{Si}_{17}$ resemble those found for $[\text{Si}_4]^{4-}$ and $[\text{Si}_9]^{4-}$ in the literature.^[132, 142, 234] $[\text{Si}_4]^{4-}$ (lit., $\text{Rb}_6\text{K}_6\text{Si}_{17}$): 282.6, 355.9 and 479.3 cm^{-1} ; (exp.): 282, 355 and 484 cm^{-1} ; $[\text{Si}_9]^{4-}$ (lit., $\text{Rb}_6\text{K}_6\text{Si}_{17}$): 391.6 cm^{-1} ; (exp.): 390 cm^{-1} . The location of the bands found in $\text{K}_{12}\text{Ge}_{17}$ also resemble those found in the literature.^[133] $[\text{Ge}_4]^{4-}$ (lit.): 160, 199, 278 cm^{-1} ; (exp.): 160, 198, 277 cm^{-1} ; $[\text{Ge}_9]^{4-}$ (lit.): 224 cm^{-1} ; (exp.): 224 cm^{-1} . Spectra were measured at $\lambda = 532 \text{ nm}$.

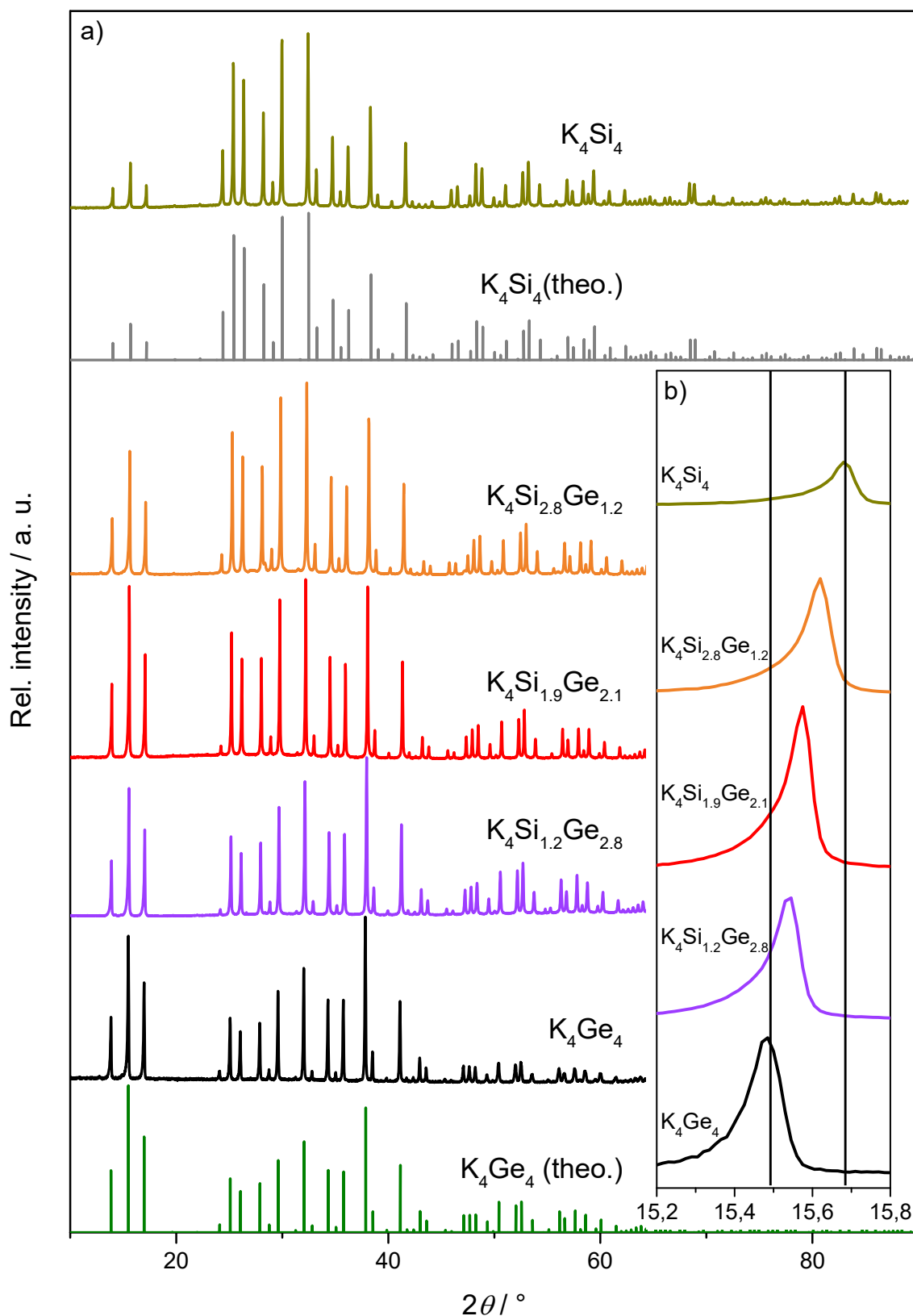


Figure 3.8. a) Powder diffraction patterns of $K_4Si_{4-x}Ge_x$ ($x = 0, 1.2, 2.1, 2.8, 4$) compounds. b) highlighted area of the compounds featuring a shift for the main reflex. Powder diffraction patterns were obtained using Cu- $K\alpha_1$ radiation, $\lambda = 1.54056 \text{ \AA}$. The diffraction patterns obtained for K_4Si_4 and K_4Ge_4 are in good accordance with their theoretical powder diffraction patterns obtained from crystal data available in literature^[126, 127], indicating that the compounds are phase pure.

3.2 Si/Ge-Clusters as Wet Chemical Precursors for Inverse Opal Structured Thin Films

In comparison to $K_{12}Si_{17-x}Ge_x$ -phases ($x = 0, 5, 9, 12, 17$), their corresponding $K_4Si_{4-x}Ge_x$ -phases ($x = 0, 1.2, 2.1, 2.8, 4$) are already accessible at a lower temperature of 873 K (for details on the synthesis see chapter 2.3.4). The powder diffraction patterns obtained for $K_4Si_{4-x}Ge_x$ phases show no side phases or left-over starting material (elemental silicon or germanium). The patterns of K_4Ge_4 and K_4Si_4 are in good accordance with theoretical data obtained from crystal data available in the literature^[126, 127], indicating that the compounds are phase pure (see Figure 3.8a). The detected reflexes shift to higher angles alongside an increasing silicon content in the phase (see Figure 3.8b), due to decreasing unit cell parameters. Contrary to $K_{12}Si_{17-x}Ge_x$ -phases, the diffraction patterns of $K_4Si_{4-x}Ge_x$ -phases feature sharp peaks, allowing for determination of their unit cell volumes. The volumes obtained follow VEGARD's law^[236] (linear dependence of volume with the amount of Ge), as expected for mixing two elements with isotypic crystal structures (see Figure 3.9). The unit cell volumes obtained for K_4Ge_4 and K_4Si_4 are also in good accordance with theoretical values derived from crystal data available in the literature.^[126, 127] Therefore, the linear dependence proves successful mixing of silicon and germanium close to the targeted ratios of $K_4Si_{4-x}Ge_x$ ($x = 1.2, 2.1, 2.8$).

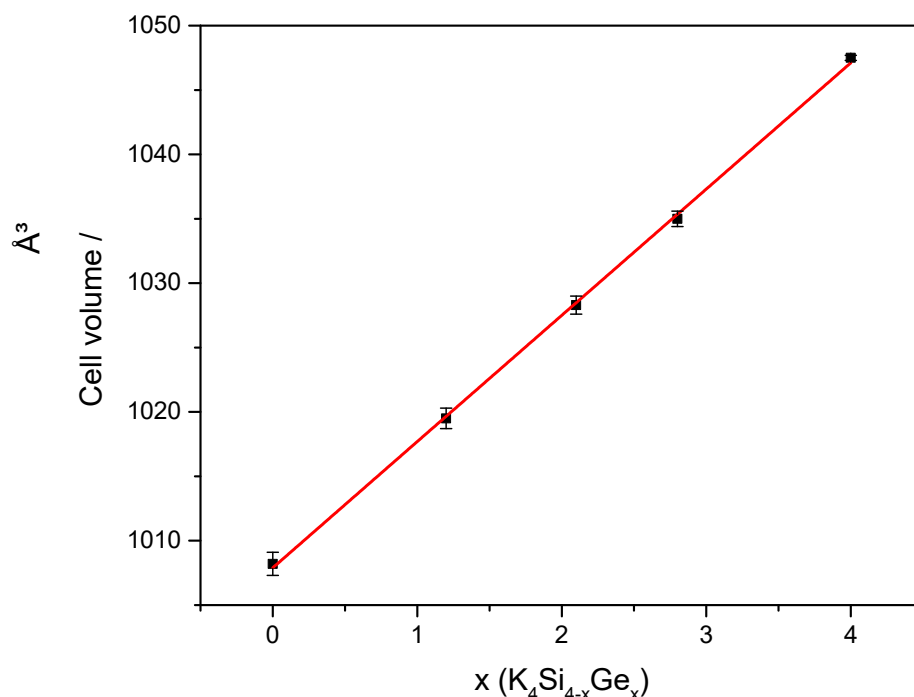


Figure 3.9. Determined cell volumes for $K_4Si_{4-x}Ge_x$ ($x = 0, 1.2, 2.1, 2.8, 4$) compounds. Experimental values are in good accordance with theoretical values derived from crystal data available in literature ($K_4Ge_{4,exp} = 1047.5 \pm 0.2 \text{ \AA}^3$, $K_4Ge_{4,theo} = 1044.6 \text{ \AA}^3$; $K_4Si_{4,exp} = 1008.2 \pm 0.9 \text{ \AA}^3$, $K_4Si_{4,theo} = 1005.0 \text{ \AA}^3$).^[126, 127]

Results and Discussion

Similar to $K_{12}Si_{17-x}Ge_x$ -phases, Raman spectra of $K_4Si_{4-x}Ge_x$ -phases ($x = 0, 1.2, 2.1, 2.8, 4$) feature characteristic bands that can be assigned to specific clusters (see Figure 3.10). The Raman spectrum obtained for the binary K_4Si_4 -phase is in good accordance with data available in the literature.^[142] The bands at 281, 333 and 356 and 477 cm^{-1} were described as $[Si_4]^{4-}$ cluster vibrations.^[142] Two additional weak bands at 546 and 563 cm^{-1} have not been described yet and therefore cannot be assigned to a specific vibration. For the band at 116 cm^{-1} , the libration of the $[Si_4]^{4-}$ clusters was suggested in the literature.^[235] For the binary K_4Ge_4 -phase, the strong band at 159 cm^{-1} as well as weak bands at 131 and 186 cm^{-1} are in good accordance with data available in the literature.^[133] However, two additional strong bands in the literature are found with only weak intensities at 108 and 276 cm^{-1} . An additional band at 314 cm^{-1} has not been described yet and therefore cannot be assigned to a specific vibration.

In the Raman spectra of ternary $K_4Si_{4-x}Ge_x$ -phases ($x = 0, 1.2, 2.1, 2.8, 4$), additional bands are detected due to vibrations originating from different Si-Ge ratios in the clusters. The intensity of the main band representing $[Ge_4]^{4-}$ (159 cm^{-1}) is detected for all mixed Si/Ge phases and is weakened for an increasing amount of silicon in the precursor as expected. Contrary to this, the main band representing $[Si_4]^{4-}$ (281 cm^{-1}) is weakened for an increasing amount of germanium in the precursor but is detected for all mixed Si/Ge phases as well. Additional bands cannot be matched to bare silicon or germanium clusters but are detected for all mixed Si/Ge phases (for example strong bands at 171 and 238 cm^{-1}) and therefore most likely represent vibrations originating from mixed Si-Ge clusters.

The combined information from powder diffraction patterns and Raman spectra of $K_{12}Si_{17-x}Ge_x$, $Rb_{12}Si_{17-x}Ge_x$ ($x = 0, 5, 9, 12, 17$) and $K_4Si_{4-x}Ge_x$ -phases ($x = 0, 1.2, 2.1, 2.8, 4$) proved the presence of well-defined mixed Si/Ge clusters. ZINTL phases of Group 14 elements containing such well-defined clusters are known to be at least partially soluble in highly polar solvents such as ethylene diamine (*en*).^[119, 120] Therefore, these phases were subsequently evaluated as soluble precursor materials for the synthesis of porous thin films as well as for the addition of ligands to the clusters.

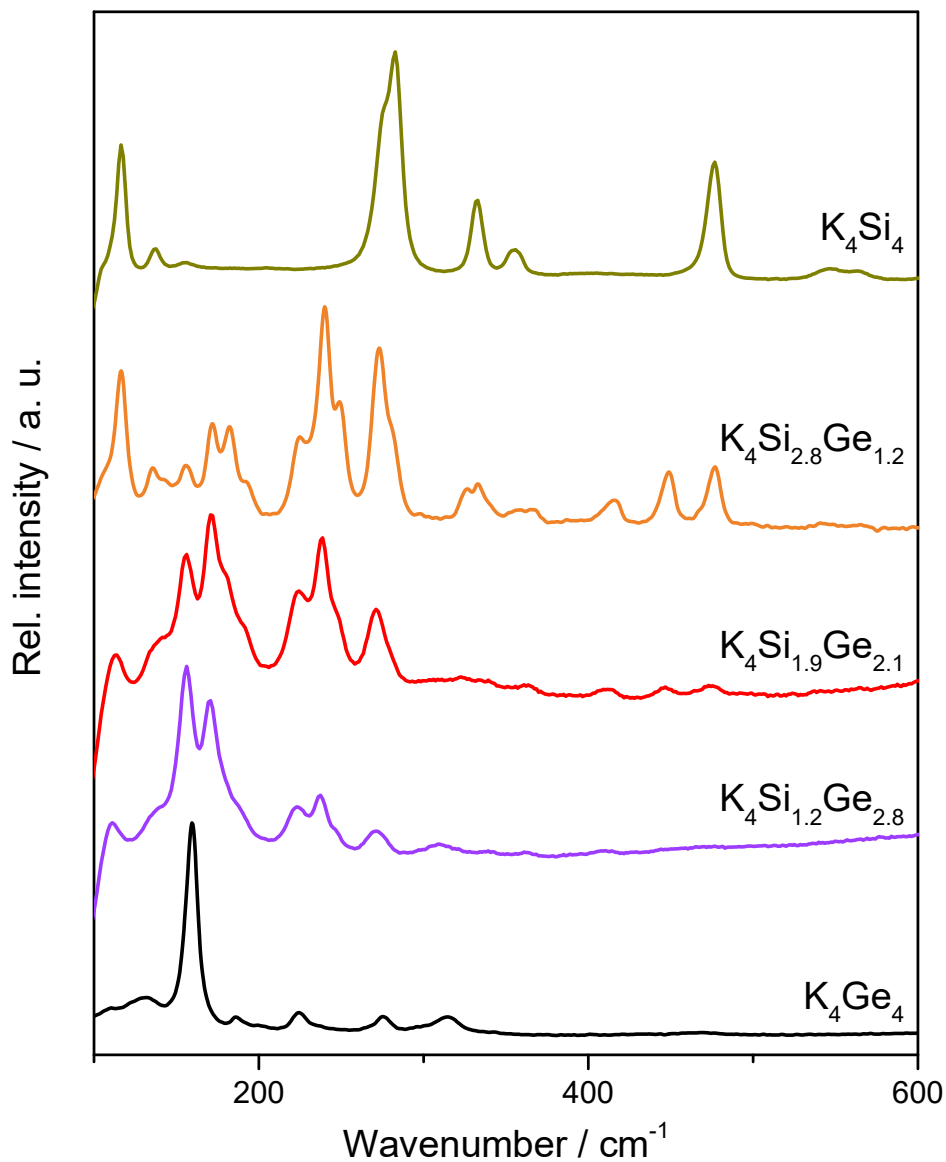







Figure 3.10. Recorded Raman spectra of $K_4Si_{4-x}Ge_x$ ($x = 0, 1.2, 2.1, 2.8, 4$) compounds. Spectra were measured at $\lambda = 532$ nm. The location of the bands found in K_4Ge_4 and K_4Si_4 resemble those found in the literature. K_4Ge_4 (lit.): 106, 135, 156, 185, 200 and 274 cm^{-1} ; (exp.): 109, 131, 159, 186, 225, 276 and 314 cm^{-1} ; K_4Si_4 (lit.): 287, 337, 364 and 481 cm^{-1} ; (exp.): 281, 333, 356 and 477 cm^{-1} .

3.2.2 Solubility of $K_{12}Si_{17-x}Ge_x$ -, $Rb_{12}Si_{17-x}Ge_x$ - and $K_4Si_{4-x}Ge_x$ -Phases in Ethylene Diamine

The solubility of the precursor phases in ethylene diamine (*en*) was evaluated as described in chapter 2.3.9. The results for solutions of $K_{12}Si_{17-x}Ge_x$ -phases after filtration are depicted in Table 3.2. In case of $K_{12}Ge_{17}$ as a precursor, $\approx 100\%$ of the phase are dissolved due to no residues remaining after filtration. However, only a fraction of all precursors containing silicon dissolves even after 3 d of reaction time. To determine the amount of these precursors dissolving, the dried filtrates are weighted as described in chapter 2.3.9. By addition of 2.2.2-crypt as a sequestering agent, the amount of precursor material dissolving can be drastically enhanced for all mixed silicon/germanium phases. The resulting solutions also show a deeper color when using 2.2.2-crypt. However, for $K_{12}Si_{17}$ as a precursor this is not the case.

Table 3.2. Solubility of $K_{12}Si_{17-x}Ge_x$ -phases ($x = 0, 5, 9, 12, 17$) in *en*. Only a fraction of the precursors dissolve in *en* except for $K_{12}Ge_{17}$. For $K_{12}Ge_{17} \approx 100\%$ are soluble due to no residues being detected by filtering the solution in either case. Addition of 2.2.2-crypt enhances the amount dissolved drastically for all precursors containing silicon with exception of $K_{12}Si_{17}$.






	$K_{12}Ge_{17}$	$K_{12}Si_5Ge_{12}$	$K_{12}Si_8Ge_9$	$K_{12}Si_{12}Ge_5$	$K_{12}Si_{17}$
Color	 dark green	 red	 red	 red	 yellow-green
% (dissolved)	≈ 100	38	34	34	30
% (dissolved) with addition of 2.2.2-crypt	≈ 100	68	65	58	35

The behavior of $Rb_{12}Si_{17-x}Ge_x$ -phases in *en* is almost identical to that of their corresponding potassium phases, but their synthesis is susceptible to yield undesired side products like $Rb_4Si_{4-x}Ge_x$ -phases or unreacted starting material in form of silicon or germanium. To avoid this, different peak temperatures are necessary during the synthesis depending on the desired Si/Ge ratio (see Figure 5.3 in the appendix).

3.2 Si/Ge-Clusters as Wet Chemical Precursors for Inverse Opal Structured Thin Films

For comparison, $K_4Si_{4-x}Ge_x$ -phases are also investigated regarding their solubility in *en*. The findings for these solubility experiments after filtration are listed in Table 3.3. A small amount of these precursor phases is also soluble in *en* after 3 d of stirring. However, the amount of precursor phase dissolved is significantly reduced compared to the corresponding $K_{12}Si_{17-x}Ge_x$ -phases mentioned in Table 3.2. Therefore, mainly $K_{12}Si_{17-x}Ge_x$ -phases were used for follow-up reactions (e. g. synthesizing inverse opal structured thin films).

Table 3.3. Solubility of $K_4Si_{4-x}Ge_x$ -phases ($x = 0, 1.2, 2.1, 2.8, 4$) in *en*. Only a small fraction of the precursor dissolves in *en* with exception of K_4Ge_4 . Addition of 2.2.2-crypt enhances the amount dissolved with exception of K_4Si_4 . The overall amount dissolved is lower than for corresponding $K_{12}Si_{17-x}Ge_x$ -phases ($x = 0, 5, 9, 12, 17$). Overall values dissolved were approximated through the amount of residue remaining after filtration of the solutions.

	K_4Ge_4	$K_4Si_{1.2}Ge_{2.8}$	$K_4Si_{1.9}Ge_{2.1}$	$K_4Si_{2.8}Ge_{1.2}$	K_4Si_4
Color	 yellow-green	 red	 red	 red	 dark yellow-brown
% (dissolved)	≈ 90	≈ 20	≈ 25	≈ 25	≈ 15
% (dissolved) with addition of 2.2.2-crypt	≈ 100	≈ 30	≈ 35	≈ 35	≈ 15

3.2.3 Characterization of Dried Residues ($K_{12}Si_{17-x}Ge_x/en$ Solutions)

To characterize the portion of $K_{12}Si_{17-x}Ge_x$ -precursors dissolved in *en*, the solvent was removed after filtration and the residue dried in dynamic vacuum. The product was then characterized using EDX (K, Si, Ge) and elemental analysis (C, H, N) to gain insight in the composition of the residues. The results of these measurements are listed in Table 3.4. In comparison to $K_{12}Ge_{17}$, a significantly higher weight percentage of organic components is detected in dried residues of mixed Si/Ge precursors, steadily increasing alongside the silicon content. In case of $K_{12}Si_{17}$, the dried residue has a viscous texture, preventing a characterization without annealing it.

Table 3.4. Elemental composition of dried residues from $K_{12}Si_{17-x}Ge_x/en$ solutions. Results are comprised by a combination of EDX (K, Si, Ge) and elemental analysis (C, H, N). n. a.: not applicable (not determined due to difficulties in preparation).

Precursor (Composition)	K	Si	Ge	C	N	H
$K_{12}Ge_{17}$ (41:59 %at.)	25(3) %wt. 21 %at.	–	68(3) %wt. 30 %at.	3.3 %wt. 9 %at.	2.9 %wt. 7 %at.	1.0 %wt. 33 %at.
$K_{12}Si_5Ge_{12}$ (41:18:41 %at.)	24(3) %wt. 9 %at.	13(3) %wt. 7 %at.	32(3) %wt. 6 %at.	13.6 %wt. 16 %at.	14.4 %wt. 15 %at.	3.3 %wt. 47 %at.
$K_{12}Si_{12}Ge_5$ (41:41:18 %at.)	24(4) %wt. 6 %at.	20(4) %wt. 7 %at.	6(3) %wt. 1 %at.	21.2 %wt. 16 %at.	23.5 %wt. 15 %at.	5.9 %wt. 55 %at.
$K_{12}Si_{17}$ (41:59 %at.)	59(5) %wt. 51 %at.	41(5) %wt. 49 %at.	–	n. a.	n. a.	n. a.

To gain further insight into the composition of the dried residues, Raman measurements were carried out (see Figure 3.11). In case of $K_{12}Ge_{17}$ as the precursor material, the Raman spectrum features three distinctive bands (146, 165 and 222 cm^{-1}). By comparison to the Raman spectrum of K_4Ge_9 it becomes evident that all these peaks can be attributed to $[Ge_9]^{4-}$, which is also in good accordance with data found in the literature.^[133] No clear indication of the tetrahedral clusters $[Ge_4]^{4-}$ of $K_{12}Ge_{17}$ is detected in the dried residue (also see chapter 3.2.1 for assignment of bands in the precursor materials $K_{12}Ge_{17}$ and $K_{12}Si_{17}$). Raman spectra of mixed Si/Ge precursors feature broad bands at around $270 - 285\text{ cm}^{-1}$ (most prominent for $K_{12}Si_{12}Ge_5$ at 282 cm^{-1}) that may be attributed to amorphous germanium (*a-Ge*).^[237]

3.2 Si/Ge-Clusters as Wet Chemical Precursors for Inverse Opal Structured Thin Films

Also, for $K_{12}Si_5Ge_{12}$ the broad band features a small shoulder at 300 cm^{-1} that can be attributed to crystalline germanium (α -Ge).^[237] For $K_{12}Si_{17}$ as a precursor, a band with high intensity is detected at 393 cm^{-1} and may be attributed to $[Si_9]^{4-}$.^[234] Two additional weak bands are detected at 250 and 299 cm^{-1} . Similar values were found in the literature for vibrations in Si_6 -clusters.^[238] However, other vibrations in Si_6 -clusters should result in bands located at 404 and 458 cm^{-1} with the latter being the most prominent of all vibrations. As these bands are not detected in the dried residue of $K_{12}Si_{17}$, Si_6 -cluster vibrations are unlikely to represent the additional weak bands. Characteristic bands for $[Si_4]^{4-}$ -clusters of $K_{12}Si_{17}$ are not detected in the dried residue either.

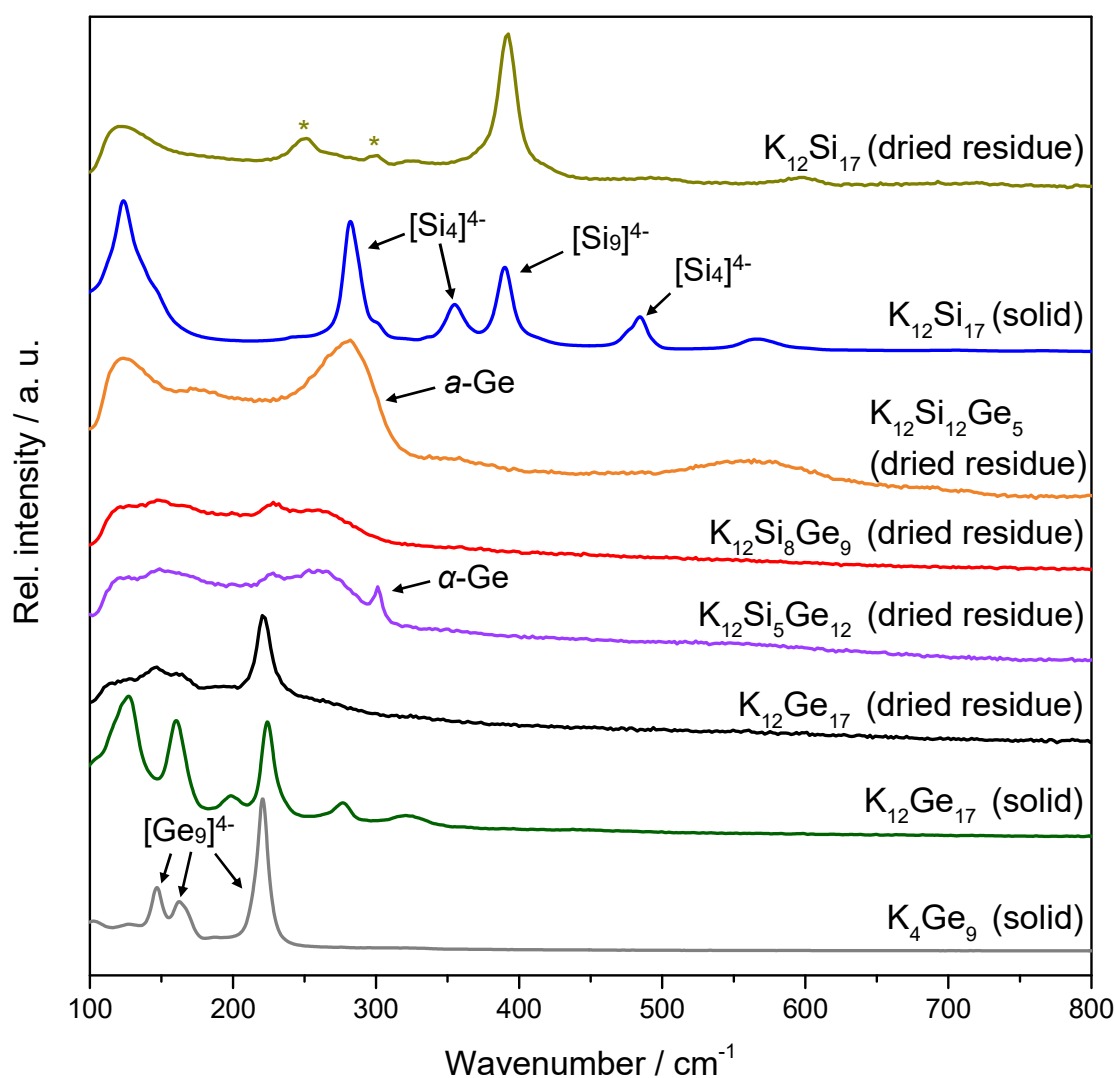


Figure 3.11. Raman spectra of dried residues from $K_{12}Si_{17-x}Ge_x/en$ solutions. Spectra were measured at $\lambda = 532\text{ nm}$. $[Si_4]^{4-}$, $[Si_9]^{4-}$, $[Ge_9]^{4-}$, a -Ge and α -Ge bands were assigned according to the literature ($K_6Rb_6Si_{17}$ as reference for experimental $K_{12}Si_{17}$).^[132, 133, 142, 234, 237]

Results and Discussion

Powder diffraction patterns of the dried residues feature almost exclusively broad and weak reflexes (see Figure 3.12). These broad reflexes indicate that mostly amorphous material is detected. A comparison of the diffraction patterns obtained for dried residues of solutions of $K_{12}Ge_{17}$ and $K_{12}Si_{17}$ precursors with the solid starting material also yields no clear indication of the species detected. To address this issue, the dried residues were subsequently annealed to induce crystallization.

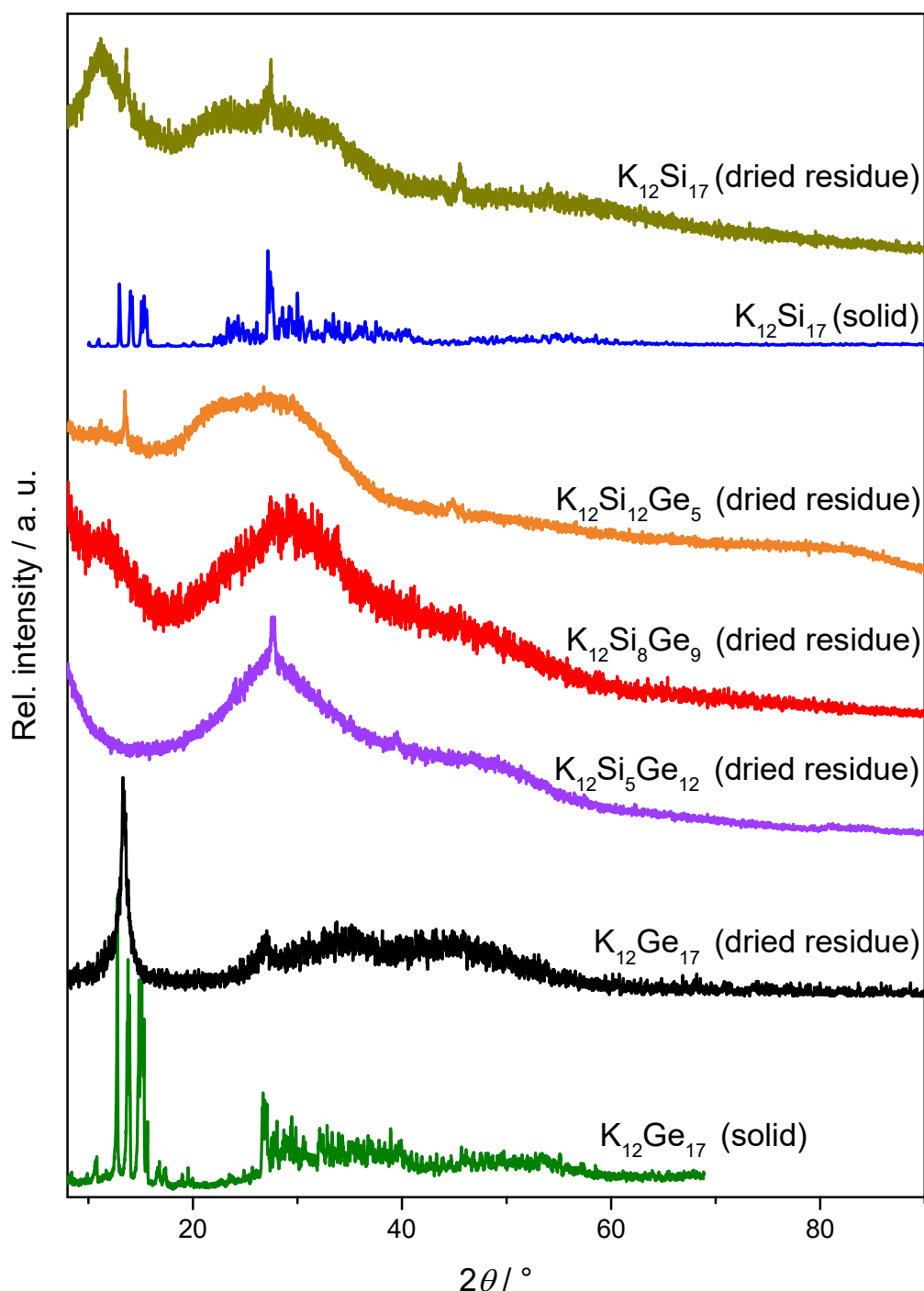


Figure 3.12. Powder diffraction patterns of dried residues from $K_{12}Si_{17-x}Ge_x/en$ solutions. Diffraction patterns were obtained using $Cu-K\alpha_1$ radiation, $\lambda = 1.54056 \text{ \AA}$. Broad reflexes indicate amorphous material being detected for all dried residues.

3.2 Si/Ge-Clusters as Wet Chemical Precursors for Inverse Opal Structured Thin Films

3.2.4 Characterization of Annealed Residues ($K_{12}Si_{17-x}Ge_x/en$ Solutions)

The dried residues were annealed at 373 K for 1 h, then 873 K for 1 h in dynamic vacuum to achieve crystallization (as described in chapter 2.1.8). The product was characterized using EDX (K, Si, Ge) and elemental analysis (C, H, N). The results of these measurements listed in Table 3.5. In comparison to the results of the dried residues (see Table 3.4), the detected amount of all organic components (C, H, N) is significantly reduced. For all starting materials, the nitrogen and hydrogen contents are influenced by a higher margin than the carbon content. In comparison to $K_{12}Ge_{17}$, mixed Si/Ge and silicon precursors retain a higher weight percentage of organic components, steadily increasing alongside the silicon content in the precursor. Furthermore, the potassium content is significantly reduced compared to the dried residues. This is especially the case for $K_{12}Ge_{17}$ as a precursor. This can be explained by elemental potassium being released from the dried residue upon annealing. For $K_{12}Ge_{17}$ as precursor material being annealed this can be detected with the naked eye as a thin potassium film is gradually forming on the cold end of the Schlenk. This behavior was already shown for K_4Ge_9 as a starting material.^[43]

Table 3.5. Elemental composition of annealed residues from $K_{12}Si_{17-x}Ge_x/en$ solutions. Results are comprised by a combination of EDX (K, Si, Ge) and elemental analysis (C, H, N).

Precursor (Composition)	K	Si	Ge	C	N	H
$K_{12}Ge_{17}$ (41:59 %at.)	11(1) %wt. 12 %at.	–	84(1) %wt. 49 %at.	3.3 %wt. 12 %at.	0.7 %wt. 2 %at.	0.6 %wt. 25 %at.
$K_{12}Si_5Ge_{12}$ (41:18:41 %at.)	29(3) %wt. 14 %at.	14(3) %wt. 9 %at.	36(3) %wt. 9 %at.	11.7 %wt. 18 %at.	7.2 %wt. 10 %at.	2.1 %wt. 40 %at.
$K_{12}Si_{12}Ge_5$ (41:41:18 %at.)	18(1) %wt. 6 %at.	31(1) %wt. 15 %at.	13(2) %wt. 3 %at.	18.9 %wt. 22 %at.	16.3 %wt. 16 %at.	2.7 %wt. 38 %at.
$K_{12}Si_{17}$ (41:59 %at.)	29(1) %wt. 9 %at.	26(1) %wt. 11 %at.	–	22.8 %wt. 22 %at.	18.4 %wt. 16 %at.	3.6 %wt. 42 %at.

Raman spectra of the of the annealed residues do not feature many bands (see Figure 3.13). A single band is detected at 298 – 300 cm^{-1} for precursor compounds containing germanium and can be attributed to crystalline germanium (α -Ge).^[237] No bands representing elemental silicon could be detected.

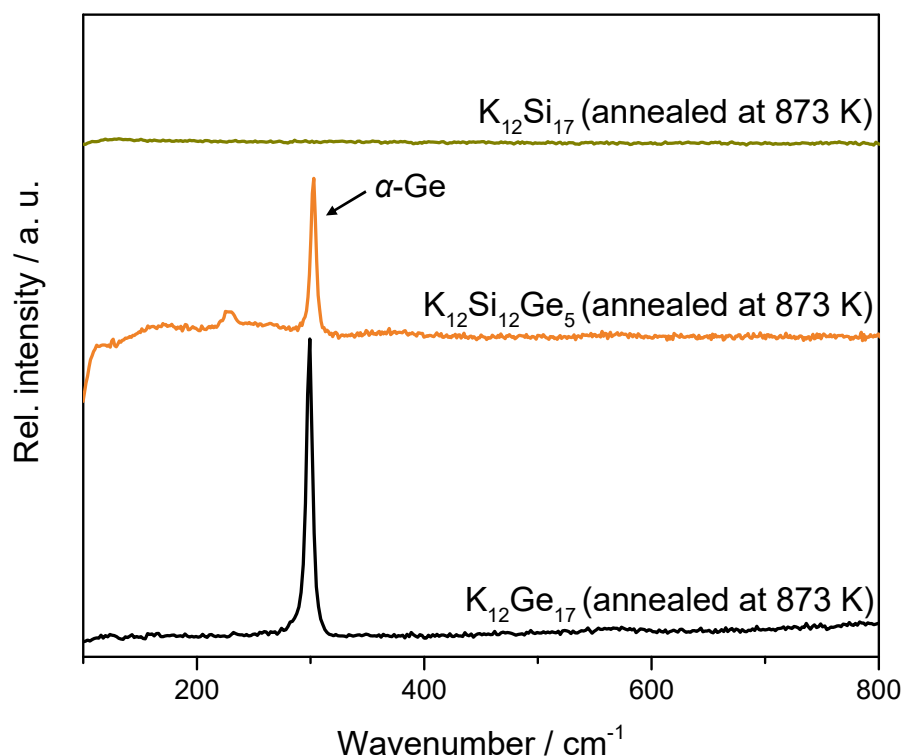


Figure 3.13. Raman spectra of residues from $K_{12}Si_{17-x}Ge_x/en$ solutions after annealing at 873 K. Spectra were measured at $\lambda = 532$ nm.

Powder diffraction patterns of annealed residues show sharper reflexes than the dried residues due to crystallization of the components at high temperatures (see Figure 3.14). For $K_{12}Ge_{17}$ as well as mixed Si/Ge precursors, reflexes representing crystalline germanium (α -Ge) are detected. However, no distinct reflexes representing crystalline silicon or silicon compounds could be detected. In combination with the results obtained from EDX and elemental analysis (see Table 3.5), this indicates the presence of amorphous silicon carbides and/or nitrides.

Next to crystalline germanium (α -Ge), reflexes in the powder diffraction pattern for $K_{12}Ge_{17}$ as a precursor can be attributed to the clathrate K_8Ge_{46} ,^[239] representing a transition step between the starting material and α -Ge (see Figure 3.14, black line). This serves as additional evidence for elemental potassium leaving the material. Small reflexes representing a clathrate structure can also be detected in the powder diffraction pattern using $K_{12}Si_{12}Ge_5$ as a precursor (see Figure 3.14, orange line). For the annealed residue of $K_{12}Si_{17}$, no reflexes representing silicon are detected. Instead, sharp reflexes can be attributed to potassium cyanide (KCN).^[240] The formation of KCN could be explained by degradation of solvent molecules (*en*) by reaction with the potassium of the precursor $K_{12}Si_{17}$.

3.2 Si/Ge-Clusters as Wet Chemical Precursors for Inverse Opal Structured Thin Films

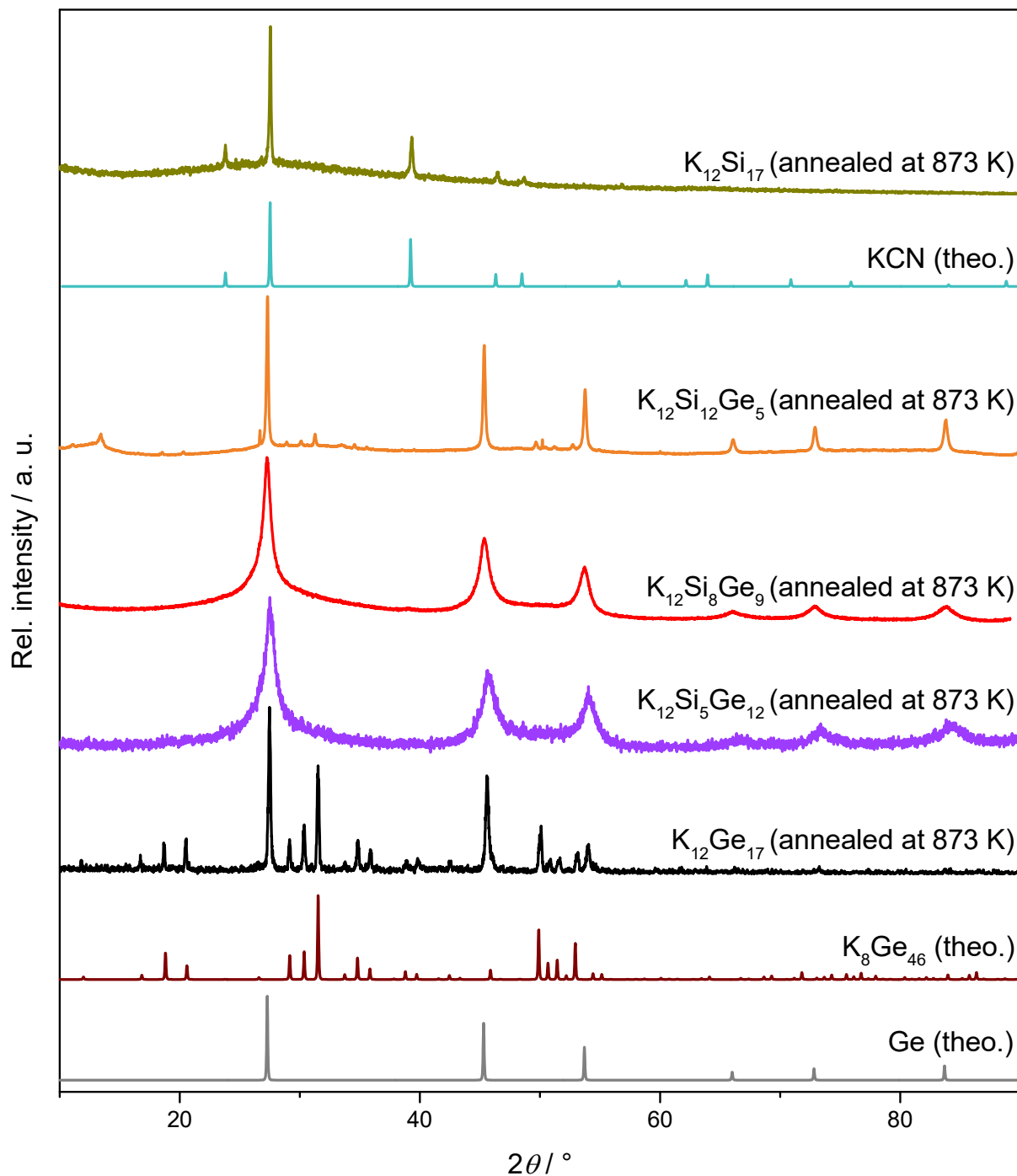


Figure 3.14. Powder diffraction patterns of residues from $K_{12}Si_{17-x}Ge_x/en$ solutions after annealing at 873 K. Diffraction patterns were obtained using Cu- $K\alpha_1$ radiation, $\lambda = 1.54056 \text{ \AA}$. Theoretical powder diffraction patterns were calculated from crystal data of the compounds available in literature.^[239-241]

3.2.5 Characterization of Silicon Species in $K_{12}Si_{17}/en$ Solution

Due to the absence of silicon in most of the characterization methods for dried and annealed residues of mixed Si/Ge as well as silicon precursor materials, a closer investigation of silicon species in solution was necessary. Raman spectra of dried residues from $K_{12}Si_{17}$ precursors featured a strong peak at 320 cm^{-1} that could be attributed to $[Si_9]^{4-}$ (see Figure 3.11 in chapter 3.2.3), indicating that silicon clusters are stable in solution. Therefore, a yellow solution with the highest possible silicon content ($K_{12}Si_{17}$ in *en*) was analyzed via NMR. For comparison, the $K_{12}Si_{17}$ precursor was “activated” by dissolution in liquid ammonia and addition of 2.2.2-crypt, then re-dissolved in pyridine- d_5 (pyr- d_5 , red solution) after evaporation of liquid ammonia (see Figure 3.15 and Figure 3.16b). The 1H spectrum in pyridine- d_5 features a small peak with a coupling of $^1J_{H_{Si}} = 9.8\text{ Hz}$, corresponding to the value for $[H_2Si_9]^{2-}$ in a non ^{29}Si enriched environment (see Figure 3.15) as described by Schiegerl *et al.*^[142]

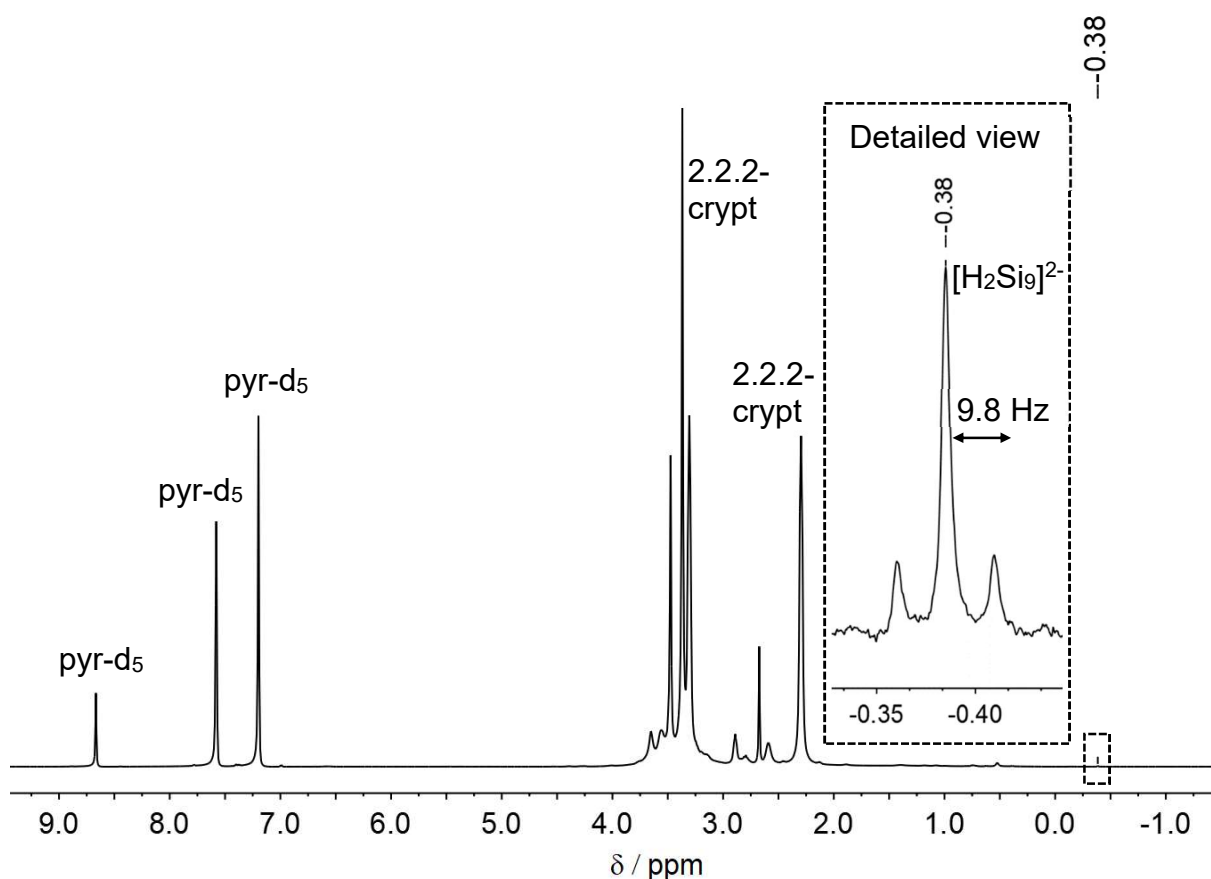


Figure 3.15. Recorded 1H -spectrum of $K_{12}Si_{17}$ in solution. The precursor was “activated” in liquid ammonia by addition of 2.2.2-crypt, then re-dissolved in pyridine- d_5 after evaporation of liquid ammonia.

The corresponding ^{29}Si -IG spectrum in pyridine- d_5 (see Figure 3.16b) features two peaks at $\delta = -321.25$ and -347.75 ppm. The latter of the two corresponds to the signal

3.2 Si/Ge-Clusters as Wet Chemical Precursors for Inverse Opal Structured Thin Films

of $[\text{H}_2\text{Si}_9]^{2-}$ detected by Schiegerl *et al.* in a 1:1 mixture of pyr- d_5 and THF- d_8 .^[142] However, the peak at -321.25 ppm was not detected in the same work. The shift of this peak is similar to a peak detected by Neumeier *et al.* in THF- d_8 , which was described as “[Si_4] $^{4-}$ ” and is referenced to in a recent publication by the same group as well.^[234, 242] However, the Raman spectrum of a dried residue (see Figure 3.11 in chapter 3.2.3) indicates that only Si_9 -clusters are present in solution as no characteristic bands of [Si_4] $^{4-}$ -clusters are detected. Additionally, theoretical data in the work by Schiegerl *et al.* indicates that [Si_4] $^{4-}$ in solution should rather result in a shift located at around $\delta = -484$ ppm.^[142]

In comparison to the ^{29}Si -IG spectrum in pyridine- d_5 , a spectrum of the *in situ* measurement in *en* features a single intense peak at a similar shift of $\delta = -324.18$ ppm (see Figure 3.16a). As there is no corresponding signal is detected in the ^1H -spectrum of the *in situ* measurement, protonated clusters like $[\text{H}_2\text{Si}_9]^{2-}$ or $[\text{HSi}_9]^{3-}$ can be ruled out as a source of this peak.^[142, 243] However, this peak is somewhat close to the calculated value of $\delta = -308$ ppm for $[\text{Si}_9]^{2-}$.^[142] This could lead to the assumption that [Si_9] $^{4-}$ clusters are at least partly oxidized to $[\text{Si}_9]^{2-}$ without addition of hydrogen. Depending on the solvent, the protonated species $[\text{H}_2\text{Si}_9]^{2-}$ is present as well.

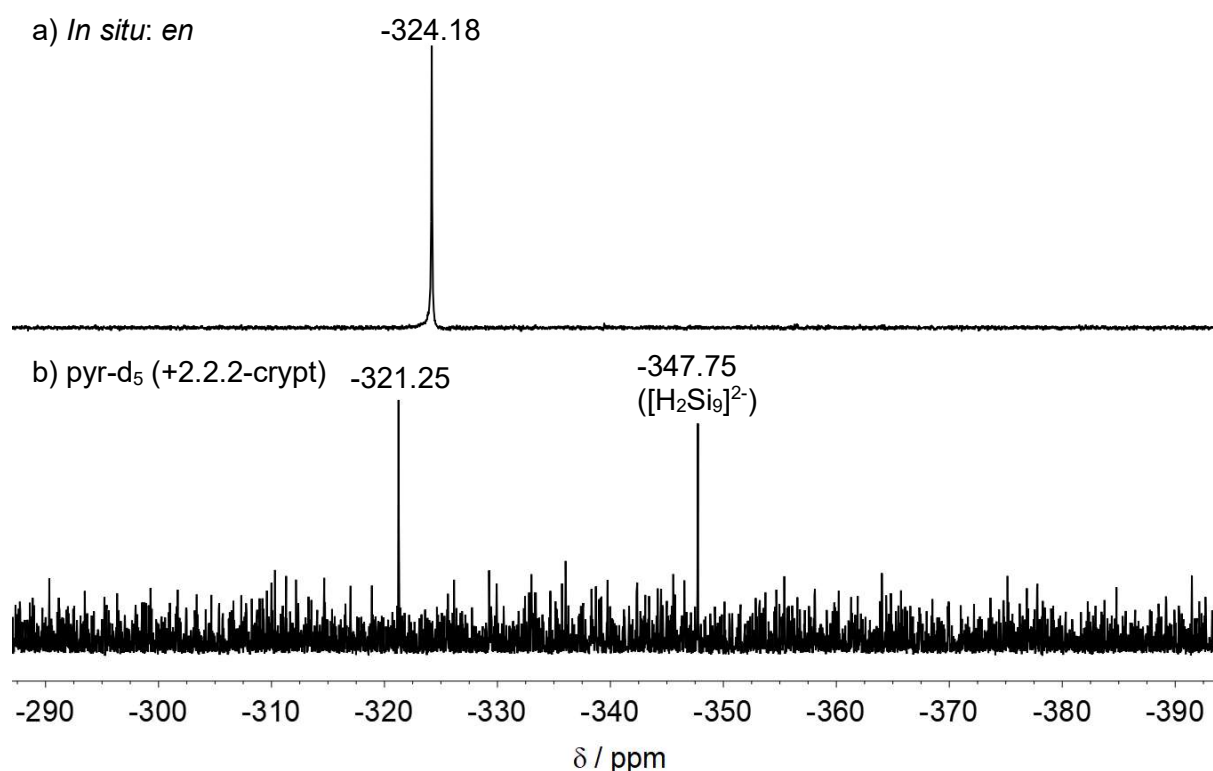


Figure 3.16. Recorded ^{29}Si -IG spectra of $\text{K}_{12}\text{Si}_{17}$ in solution. a) *In situ* measurement in *en* using CDCl_3 as an external standard. b) “Activation” by liquid ammonia with addition of 2.2.2-crypt; measurement in pyridine- d_5 after evaporation of liquid ammonia.

3.2.6 Synthesis and Characterization of Inverse Opal Structured Mixed Si/Ge as well as Si Thin Films

Synthesis of inverse opal structured thin films starting with ZINTL-clusters in solution was established by Bentlohner *et al.* for germanium.^[43] Within this work, next to the determination of charge carrier mobility within Ge thin films (see chapter 3.1.2), this synthesis method is applied to mixed silicon/germanium as well as bare silicon clusters in the precursors. PMMA beads are dip coated onto various substrates, forming an opal like structure (see Figure 3.17, for details also see chapter 2.1.6). Afterwards, the cavities within this structure are infiltrated with a $K_{12}Si_{17-x}Ge_x$ solution (0.06 mmol/mL, for details on the synthesis see chapter 2.2.9 and chapter 2.2.10) in *en* by drop casting (see Figure 3.17i). The solvent (*en*) is removed by evaporation and a cross-linker (ECl_4 , $E = Ge, Si$) is added *via* vapor deposition (see Figure 3.17ii and iii). Mixed Si/Ge samples are treated with $GeCl_4$ while pure silicon samples are treated with $SiCl_4$. The samples are annealed at 373 K for 1 h followed by 773 K for 5 min to remove the PMMA beads (see Figure 3.17iv). Finally, the thin films are washed with DMSO followed by THF for 30 min each (see Figure 3.17v and vi). This way, any KCl originating from a reaction of the cross-linker ECl_4 with the precursor material $K_{12}Si_{17-x}Ge_x$ as well as left-over decomposition products from the PMMA beads are removed. The material is then dried in dynamic vacuum to yield inverse opal structured thin films.

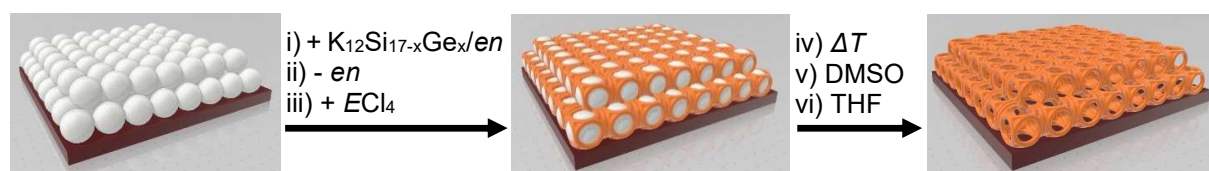


Figure 3.17. Synthesis of inverse opal structured mixed Si/Ge and silicon thin films.^[43] i) Infiltration of PMMA beads with a $K_{12}Si_{17-x}Ge_x/en$ solution, ii) removal of *en* *via* evaporation, iii) addition of ECl_4 ($E = Ge$ for mixed Si/Ge samples and $E = Si$ for pure silicon samples) as a linker, iv) removal of PMMA beads by annealing (ΔT), v) + vi) removal of residual KCl and left-over degradation products from PMMA beads by washing with DMSO and THF.

The size of the empty spheres in the inverse opal structured thin films is a direct result of the size of the PMMA template beads. The size distribution of the PMMA beads can be controlled by varying the amount of SDS in their synthesis, with an increased amount resulting in smaller PMMA beads (for details on the synthesis see chapter 2.3.8). However, PMMA beads with a diameter of 100 nm or smaller cannot be isolated by centrifugation. For preparation of thin films, PMMA spheres with a size of

3.2 Si/Ge-Clusters as Wet Chemical Precursors for Inverse Opal Structured Thin Films

250 – 300 nm result in the best homogeneity of the inverse opal structured thin films. The size distribution can be determined by dynamic light scattering (DLS) or by using the software ImageJ on a suitable SEM picture (see Figure 3.18). For example, Figure 3.18a reveals an average size of 301 nm throughout 475 PMMA beads measured with ImageJ.

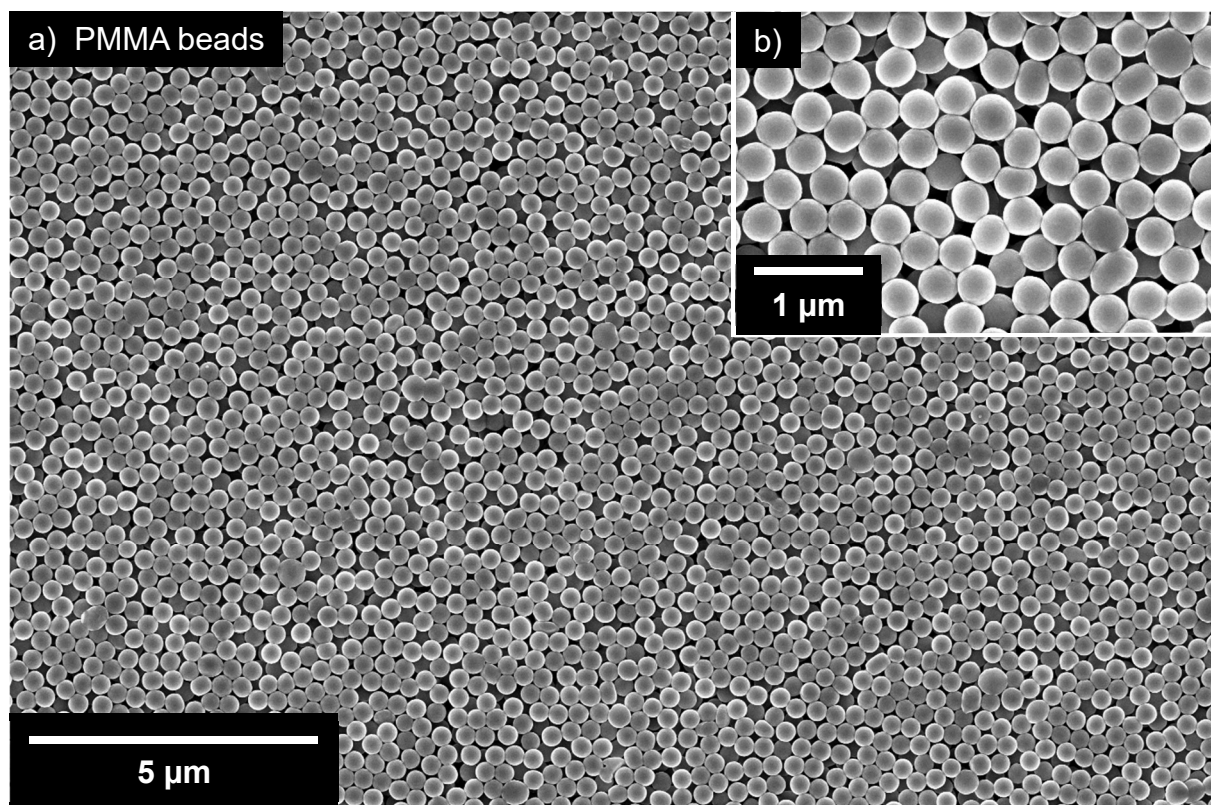


Figure 3.18. SEM pictures of 300 nm sized PMMA beads. a) 10.000x magnification and b) 50.000x magnification.

The size distribution of the empty spheres in inverse opal structured mixed Si/Ge and silicon thin films obtained from treating these PMMA films with $K_{12}Si_{17-x}Ge_x$ solutions is determined with ImageJ as well. Furthermore, elemental composition within the films is determined *via* EDX. The results of this analysis are listed in Table 3.6. Only small amounts of potassium and chlorine remained on the thin films even after treatment with DMSO and THF. Mainly, germanium and silicon are detected. Also, the amount of silicon detected in the thin films is increased when using precursors with a higher silicon content. The determined size of the empty spheres in the inverse opal structured materials matches the size of the initially used PMMA beads quite well (see Table 3.6; 294 nm and 323 nm average diameter for 300 nm PMMA, 245 nm and 262 nm average diameter for 250 nm PMMA used).

Results and Discussion

Table 3.6. Elemental composition (EDX) and size distribution of the empty spheres in inverse opal structured thin films from $K_{12}Si_{17-x}Ge_x$.

Precursor (Composition)	Si	Ge	K	Cl	Size _{sphere} / nm	No. _{sphere}
$K_{12}Si_5Ge_{12}$ (41:18:41 %at.)	20(2) %wt. 37 %at.	73(2) %wt. 53 %at.	5.6(5) %wt. 7.6 %at.	1.1(2) %wt. 1.6 %at.	323 ⁱ⁾	319
$K_{12}Si_8Ge_9$ (41:28:31 %at.)	28(3) %wt. 47 %at.	61(2) %wt. 39 %at.	7.0(6) %wt. 8.4 %at.	4.0(3) %wt. 5.2 %at.	294 ⁱ⁾	322
$K_{12}Si_{12}Ge_5$ (41:41:18 %at.)	63(1) %wt. 79 %at.	33(1) %wt. 16 %at.	2.0(3) %wt. 1.8 %at.	2.6(8) %wt. 2.6 %at.	245 ⁱⁱ⁾	194
$K_{12}Si_{17}$ (41:59 %at.)	93(2) %wt. 95 %at.		5(1) %wt. 3 %at.	2.1(4) %wt. 1.7 %at.	262 ⁱⁱ⁾	243

i) 300 nm PMMA used as depicted in Figure 3.18, ii) 250 nm PMMA from another batch used as the template. No._{sphere}: number of empty spheres measured for size determination.

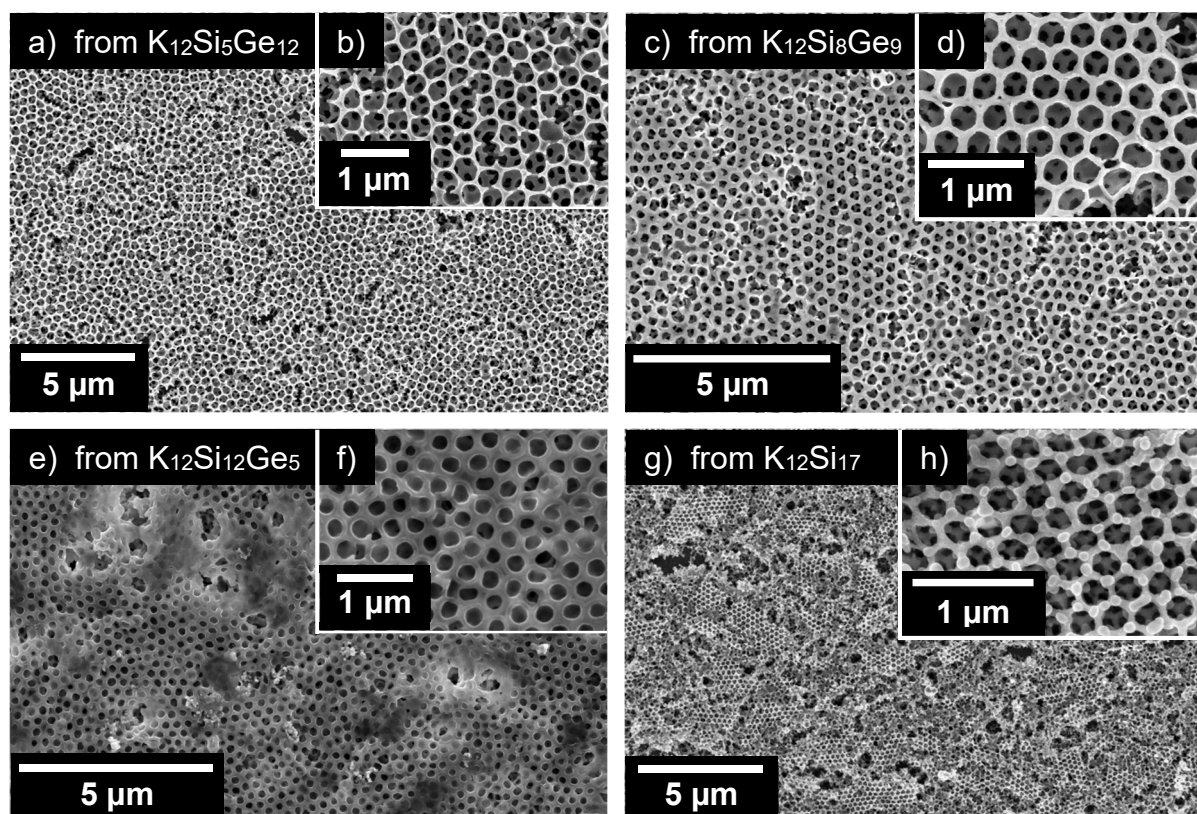


Figure 3.19. SEM pictures of inverse opal structured mixed Si/Ge as well as pure silicon thin films. a) 10.000x magnification and b) 50.000x magnification starting from $K_{12}Si_5Ge_{12}$, c) 15.000x magnification and d) 50.000x magnification starting from $K_{12}Si_8Ge_9$, e) 15.000x magnification and f) 50.000x magnification starting from $K_{12}Si_{12}Ge_5$, g) 10.000x magnification and h) 100.000x magnification starting from $K_{12}Si_{17}$.

3.2 Si/Ge-Clusters as Wet Chemical Precursors for Inverse Opal Structured Thin Films

For Ge thin films, measurements are carried out on silicon wafers as substrates due to their low cost. However, for thin films containing silicon this would be counterproductive as the substrate would influence the results of several characterization techniques. Therefore, sapphire (Al_2O_3 , for SEM, EDX) or copper (for Raman and XPS) substrates are used instead. Sapphire substrates provide an equally homogenous distribution of the inverse opal structure as silicon wafers.

The inverse opal structure can be detected throughout a large area for all Si/Ge precursors analyzed (Figure 3.19). At least the top two layers of the structure can be detected in most cases (see Figure 3.19b, d and h). Consistently, small cracks are detected in the structure as a result of the drying and annealing process. Nevertheless, the mostly homogenous structure indicates only a few of these spots for possible charge carrier trapping. Therefore, a comparatively high carrier mobility to bulk thin films should be possible, making this material interesting for several possible applications. To investigate and substantiate this suspicion, carrier mobility within these thin films was determined via terahertz spectroscopy (see chapter 3.2.7).

As for dried and annealed residues of Si/Ge precursors in solution (see chapter 3.2.3 and 3.2.4), the detection of silicon within the thin films outside of EDX proved to be difficult for the thin films. For example, a Raman spectrum under usual conditions (532 nm laser, 5 – 10% intensity) only features a band representing germanium in case of mixed Si/Ge precursors (see Figure 3.20). For $\text{K}_{12}\text{Si}_{17}$ as the precursor, no bands are detected at all. However, by deliberately decomposing a small spot of the structure at high laser intensities (> 20%) it is possible to crystallize the silicon on the sheet (Figure 3.20, grey line). For thin films from precursors with high silicon content, weak broad bands are frequently present around 600 and 800 cm^{-1} (*, Figure 3.20, orange line). Similar bands can be found in the literature for Si-H^[244], Si-C^[245] as well as Si-N^[246] vibrations. However, the intensities of these bands are too weak to draw certain conclusions. Therefore, X-ray photoelectron spectroscopy (XPS) studies were conducted on the thin films.

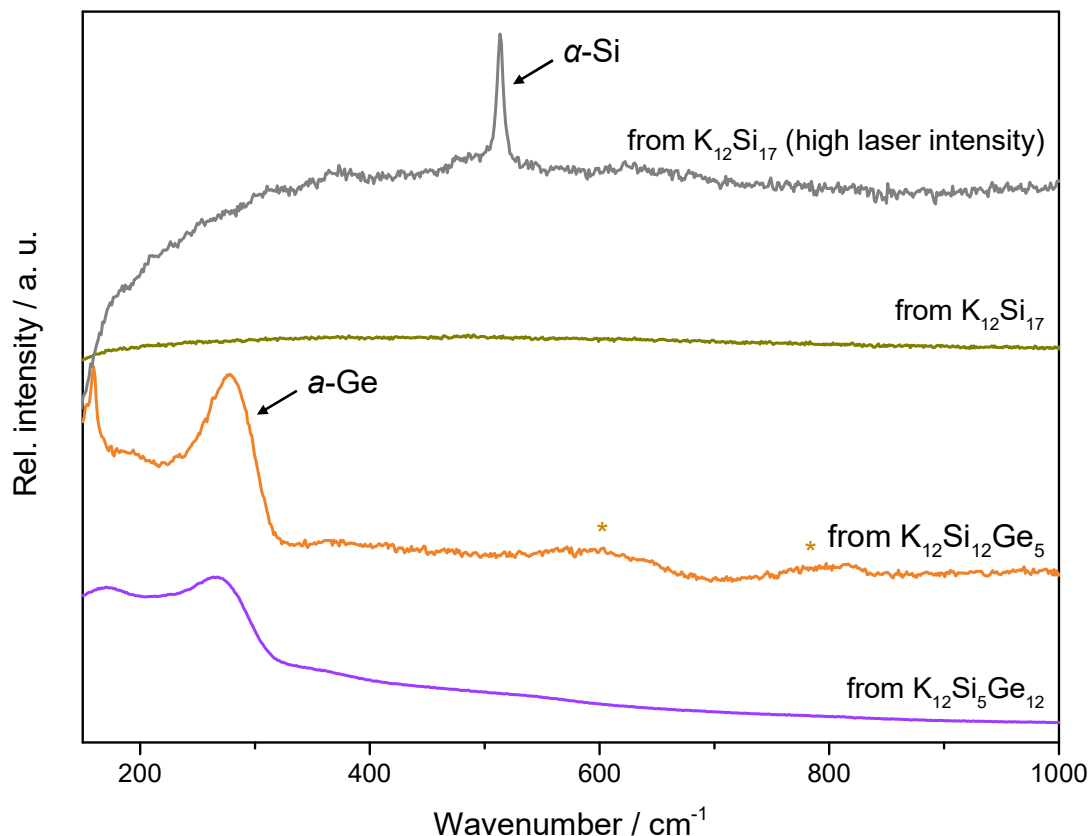


Figure 3.20. Raman spectra of mixed Si/Ge as well as silicon thin films at varying laser intensities. Spectra were measured at $\lambda = 532$ nm. Thin films were annealed at 373 K for 1h and 773 K for 5 min prior to the measurements.

On the surface of mixed Si/Ge thin films, the germanium content is mostly oxidized to Ge (+IV) (see Figure 3.21a). However, after etching off the surface through 40 min of Ar^+ sputtering, the inner structure of these thin films reveals Ge(0) as the main oxidation state (see Figure 3.21b). This is in good accordance with behavior found for inverse opal structured germanium thin films.^[43, 95] Relative values of oxidation states of germanium in mixed Si/Ge thin films are listed in Table 5.15 (without sputtering) and Table 5.16 (after 40 min of Ar^+ sputtering) in the appendix for Ge 2p. A similar behavior is detected for Ge 3d as depicted in Figure 5.44 as well as listed in Table 5.17 and Table 5.18 in the appendix. For the silicon content in these thin films, the situation is different. Without sputtering as well as after 40 min of Ar^+ sputtering, only a single component is detected and can be identified as Si(+IV) (see Figure 3.22). This supports the assumption that even after annealing within the synthesis, silicon is present as Si(+IV) in these inverse opal structured films.

3.2 Si/Ge-Clusters as Wet Chemical Precursors for Inverse Opal Structured Thin Films

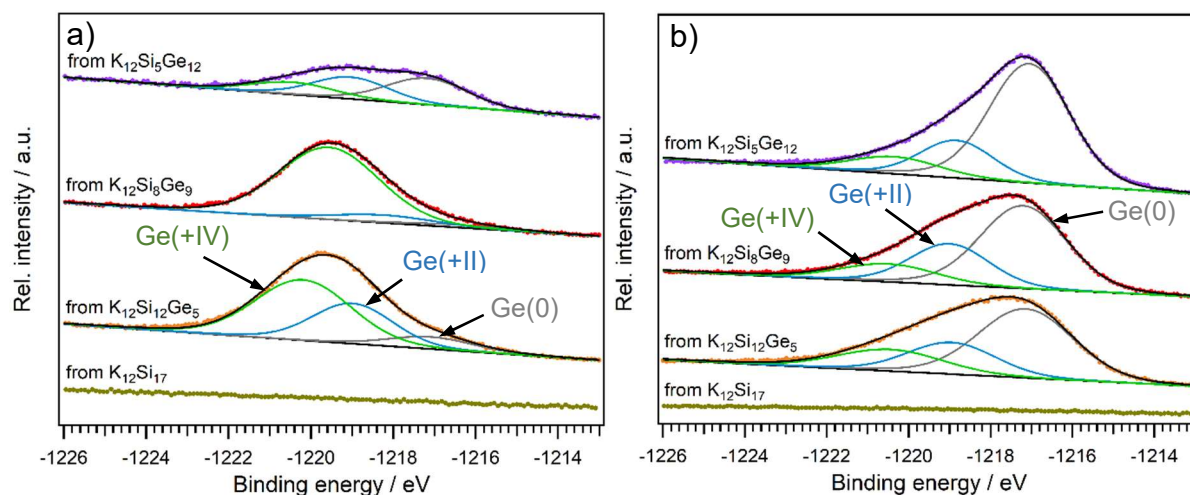


Figure 3.21. Ge 2p XPS spectra of inverse opal structured thin films from $K_{12}Si_5Ge_{12}$, $K_{12}Si_8Ge_9$, $K_{12}Si_{12}Ge_5$ and $K_{12}Si_{17}$ a) without and b) after 40 min of Ar^+ sputtering. Surface Ge is mostly oxidized to Ge(+IV), but sputtering reveals Ge(0) as the main component of the inner structure for all thin films containing Ge.

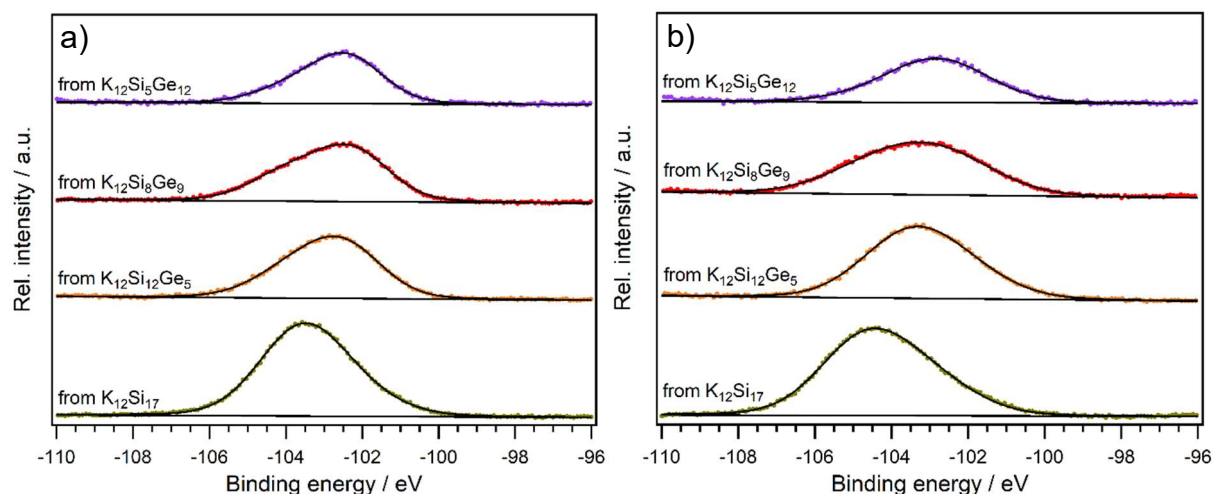


Figure 3.22. Si 2p XPS spectra of inverse opal structured thin films from $K_{12}Si_5Ge_{12}$, $K_{12}Si_8Ge_9$, $K_{12}Si_{12}Ge_5$ and $K_{12}Si_{17}$ a) without and b) after 40 min of Ar^+ sputtering. For both cases only Si(+IV) is detected, revealing that the inner structure only contains oxidized Si for all thin films.

Results and Discussion

XPS measurements also reveal that the nitrogen content in inverse opal structured thin films increases alongside the silicon content (see Figure 3.23). Nitrogen contamination on the surface (black empty squares) is thereby significantly higher than in the inner structure (blue empty squares). The N/Si ratio increases alongside the silicon content of the precursor with exception of $K_{12}Si_{17}$. However, when referring the detected nitrogen content to the combined amount of silicon and germanium, the trend becomes evident for all thin films (Figure 3.23, red squares). Therefore, these measurements support the assumption that silicon is present as Si(+IV) due to a reaction with the solvent (*en*).

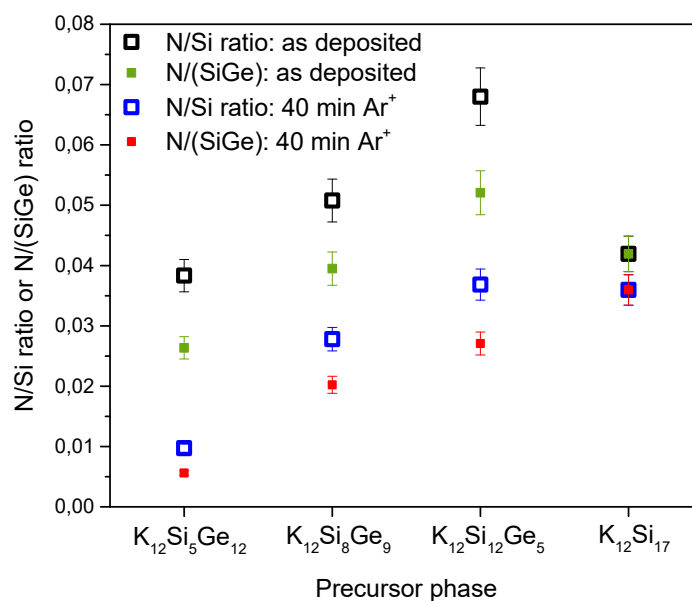


Figure 3.23. N/Si as well as N/(SiGe) ratio in inverse opal structured thin films. N content on the surface is increasing alongside Si with exception of $K_{12}Si_{17}$. After 40 min of Ar⁺ sputtering, the trend becomes evident for all thin films. Error bars for low N content are too small to be showing in some cases. Contents were determined through absolute values detected in the XPS.

3.2 Si/Ge-Clusters as Wet Chemical Precursors for Inverse Opal Structured Thin Films

3.2.7 Charge Carrier Mobility in Inverse Opal Structured Mixed Si/Ge Thin Films (Terahertz Spectroscopy)

Carrier mobility within inverse opal structured thin films was determined using time resolved terahertz spectroscopy (TRTS).^[217] As described in chapter 2.2.8, the power of the laser in the setup could be adjusted prior to entering the sample chamber, allowing for fluence (F , laser power per area of the sample) dependent measurements on the samples. Additionally, a cold finger cryostat could be used for a temperature dependent setup. Measurements were carried out for inverse opal structured thin films starting with varying Si/Ge ratios in the precursor. For a high germanium content (starting from $K_{12}Si_5Ge_{12}$), a distinct trend is observed (Figure 3.24). The transient photoconductivity $|\Delta T/T_0|$ is increasing alongside an increase in initial laser power (Figure 3.24a) as well as in temperature (Figure 3.24b). However, changing the fluence has a stronger influence on the resulting signal than a change in temperature. The value of $|\Delta T/T_0|$ (peak) represents the maximum in reduction of THz transmission.

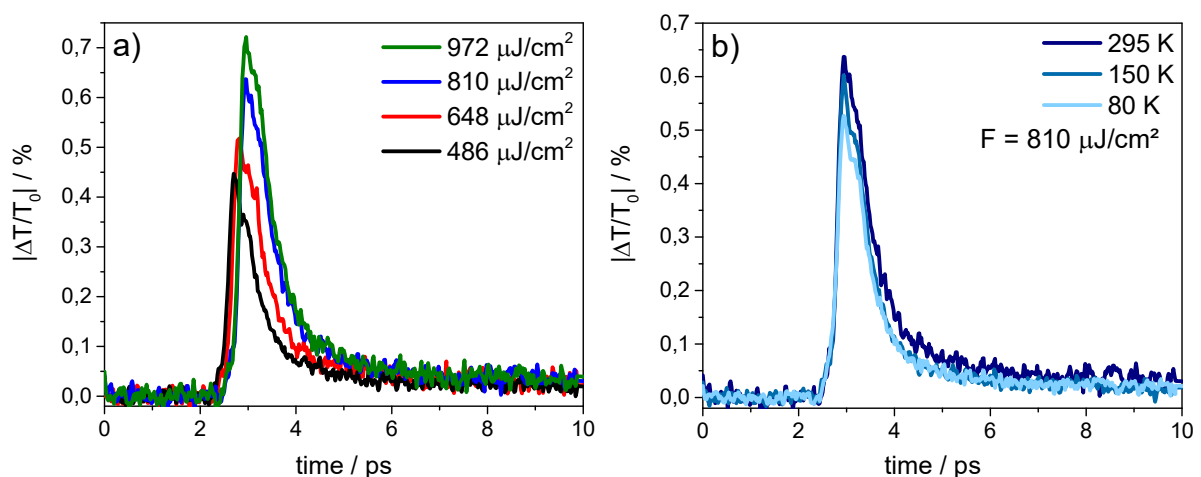


Figure 3.24. Transient photoconductivity $|\Delta T/T_0|$ for an inverse opal structured mixed Si/Ge thin film starting from $K_{12}Si_5Ge_{12}$. a) Fluence dependency at room temperature (295 K), b) temperature dependency at $F = 810 \mu J/cm^2$.

These two types of measurements can be combined into one, depicting the peak value of the transient photoconductivity $|\Delta T/T_0|$ (peak) as a fluence and temperature dependent parameter (Figure 3.25). For an inverse opal structured thin film starting from a $K_{12}Si_5Ge_{12}$ precursor this measurement results in a clear trend (Figure 3.25a). However, with increasing silicon content in the precursor values for $|\Delta T/T_0|$ (peak) become more irregular (Figure 3.25b for $K_{12}Si_{12}Ge_5$ precursor and Figure 3.25c for $K_{12}Si_{17}$ precursor). Especially the temperature parameter becomes increasingly

Results and Discussion

irrelevant. Furthermore, the overall value of $|\Delta T/T_0|$ (peak) is drastically decreasing alongside an increase in silicon content (Figure 3.25d). This is caused by the nature of the samples. To achieve a good signal for $|\Delta T/T_0|$ (peak), a certain degree of absorption by the sample is necessary. For example, a transmission of $T = 0.33$ (67% absorption) is reached at a penetration depth of 270 nm for germanium.^[247] However, for silicon the same is just achieved at 12 μm thickness.^[248] Furthermore, the inverse opal structured material is just covering about 35 – 45% of the space on the substrate. The rest is occupied by the empty spheres left behind by the PMMA template beads. Therefore, the penetration depth is even higher for such a material. The thickness of thin films measured varied between 0.8 and 1.2 μm , heavily limiting the absorption in thin films mainly containing silicon. To counteract this problem, measurements on thin films with high silicon content (e. g. starting with $\text{K}_{12}\text{Si}_{17}$ as a precursor) were performed at a higher fluence to maximize the resulting signal.

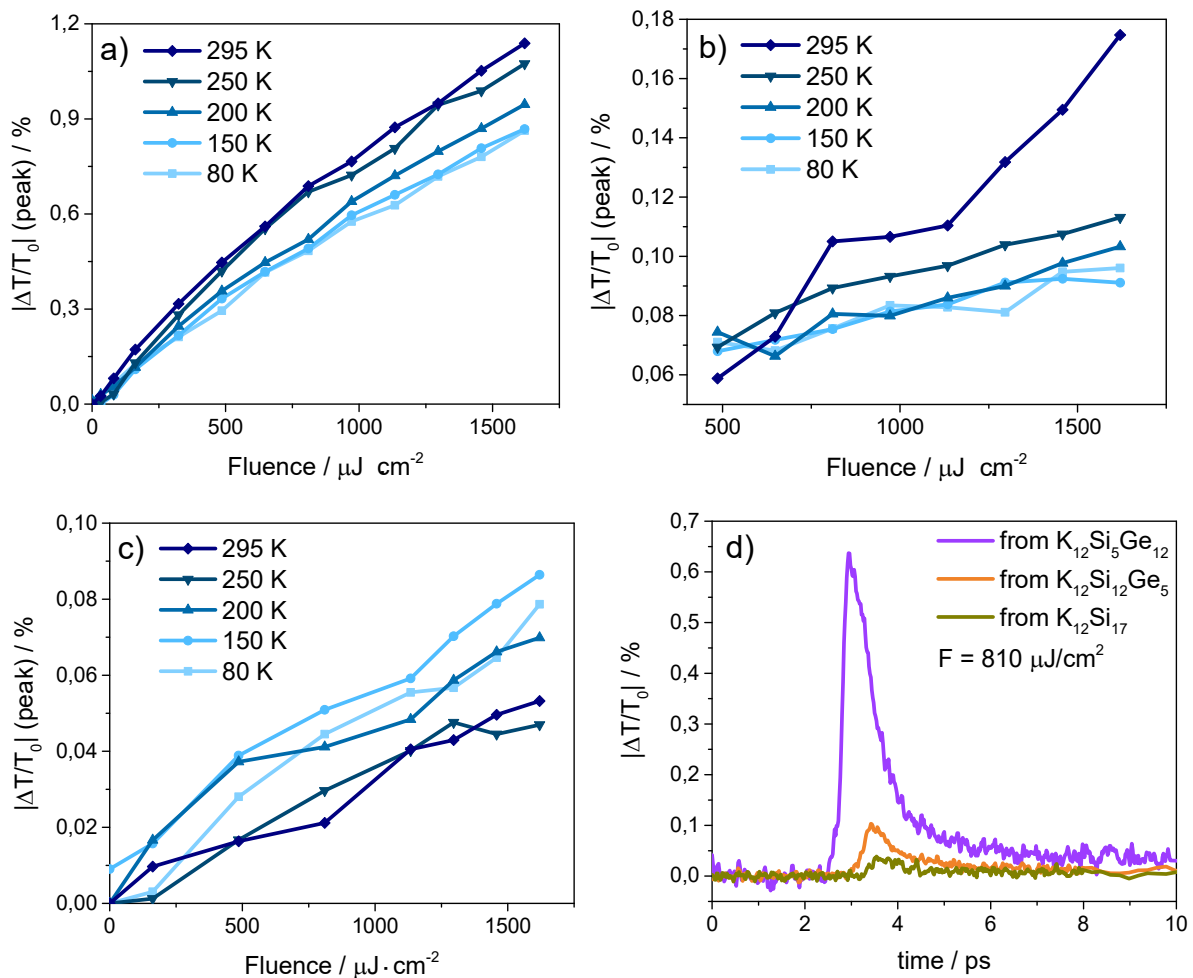


Figure 3.25. Fluence and temperature dependency of peak signal for transient photoconductivity $|\Delta T/T_0|$ (peak) of inverse opal structured thin films and comparison of $|\Delta T/T_0|$ for different ZINTL precursors. a) starting from $\text{K}_{12}\text{Si}_5\text{Ge}_{12}$, b) starting from $\text{K}_{12}\text{Si}_{12}\text{Ge}_5$, c) starting from $\text{K}_{12}\text{Si}_{17}$. d) Comparison of transient photoconductivity $|\Delta T/T_0|$ for different precursor materials.

3.2 Si/Ge-Clusters as Wet Chemical Precursors for Inverse Opal Structured Thin Films

The transient photoconductivity $|\Delta T/T_0|$ has a fast rise time for all samples and conditions measured (0.2 – 0.4 ps, see Figure 3.26a as well as Figure 5.9a and Figure 5.10a in the appendix), decreasing alongside the silicon content in the thin film. These values (< 0.5 ps) are in the range of the minimum response time of the THz pulse detection setup used, indicating a fast photoexcitation of mobile carriers.^[200] These free carriers could lead to the formation of polarons (caused by local lattice deformations), decreasing carrier mobility due to an increase in effective mass.^[218] This has already been described for a variety of disordered amorphous semiconductors.^[219]

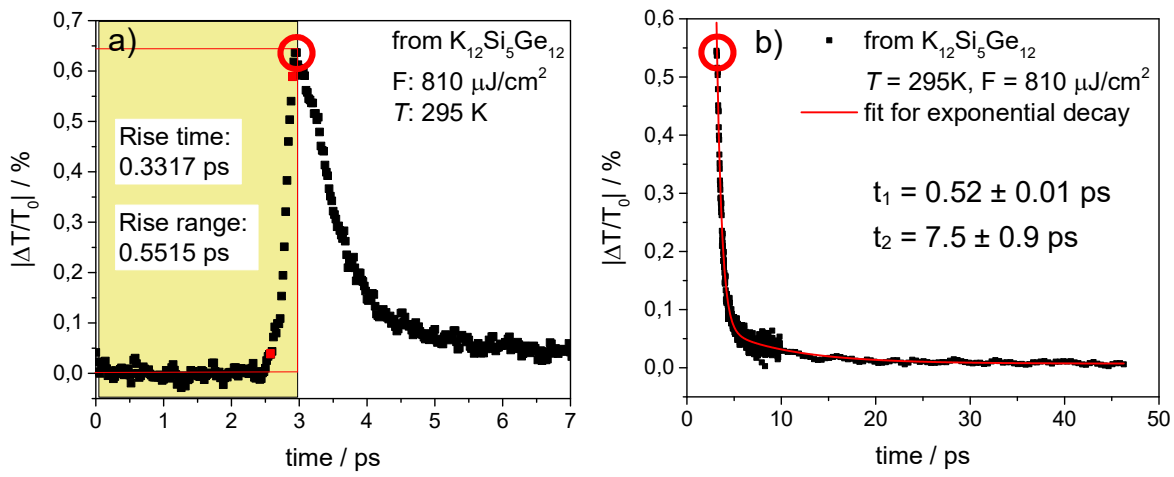


Figure 3.26. Rise time (a) and signal decay (b) for an inverse opal structured mixed Si/Ge thin film starting from $K_{12}Si_5Ge_{12}$. Starting point for signal decay plot is the peak signal for transient photoconductivity (red circle in both graphs). Decay times are indicated as t_1 and t_2 .

After the transient photoconductivity $|\Delta T/T_0|$ reached its peak, the decay mechanism can be deduced while the transmission recovers (see Figure 3.26b as well as Figure 5.9b and Figure 5.10b in the appendix). Compared to Ge thin films (see chapter 3.1.2), all Si/Ge and Si thin films measured show an even faster decay time of < 20 ps, decreasing further alongside an increase in silicon content (< 10 ps for $K_{12}Si_{12}Ge_5$ and < 5 ps for $K_{12}Si_{17}$ precursor). The Si/Ge and Si thin films consisted of amorphous material. Therefore, a lack of long-range order interfering with carrier migration, resulting in localization of charge carriers and fast decay of photoconductivity is to be expected. The time constants determined for these inverse opal structured thin films are well within the range of the sub-picosecond values previously reported for amorphous silicon samples.^[225, 249, 250] For $K_{12}Si_{12}Ge_5$ as a precursor, the transient photoconductivity exhibits a bi-exponential decay as indicated by t_1 and t_2 in Figure 3.26b. In contrast, thin films from $K_{12}Si_{12}Ge_5$ and $K_{12}Si_{17}$ precursors exhibit a single exponential decay. These carrier dynamics remain similar throughout varying fluences

Results and Discussion

and temperatures measured (see Table 5.1 – Table 5.5 in the appendix). However, at lower thermal energy (lower temperature) carriers drift at a faster rate, decreasing their lifetime t_1 (and t_2). In all cases, photo-excited carriers seem to be trapped into defects on the surface or at the grain boundaries within the structure, hence resulting in the fast decay time.

In contrast to the time-dependent conductivity (transient photoconductivity), the frequency-resolved complex conductivity σ can be deduced from the THz transmission at a fixed delay time (Δt). For these inverse opal structured samples, $\sigma(\omega)$ is approximated by a Drude-Smith model of carrier localization (see equation 1 in chapter 3.1.2). The effective mass of an electron in the thin films was set as $m^* = 0.12 m_e^*/m_0$ for germanium and $m^* = 0.26 m_e^*/m_0$ for silicon, providing a close estimate for the mobility in the bulk materials. For mixed Si/Ge precursors, an averaged effective mass corresponding to the ratio of silicon and germanium in the precursor was used. Beyond the Drude model of free-electron gas^[224], equation (1) describes suppressed long-range transport of carriers in materials due to disorder.^[218, 223] The velocity parameter c thereby provides a good estimate of the carrier backscattering within the material due to structural confinement, with c in between 0 (free carriers, restoring the Drude model) and -1 (complete backscattering of carriers).

The complex conductivity of the time-resolved terahertz spectroscopy measurements was extracted at 0.5 ps after the peak of $|\Delta T/T_0|$ ($\Delta t \approx 0.7 - 0.9$ ps after inducing the photoexcitation). Both imaginary ($\sigma_i < 0$) and real part ($\sigma_r > 0$) were fitted applying the Drude-Smith model (see Figure 3.27, blue lined fit for σ_i and red lined fit for σ_r). For a thin film starting with $K_{12}Si_5Ge_{12}$ precursor, the fit matches quite well (Figure 3.27a). However, for higher silicon contents in the thin films (Figure 3.27b starting with $K_{12}Si_5Ge_{12}$ precursor and Figure 3.27c starting with $K_{12}Si_{17}$ precursor) the overall value of σ is significantly reduced. It is getting closer to the uncertainty of each measured point, resulting in a broader distribution. The parameters extracted from these fits are listed in Table 3.7. For parameters extracted from additional fluences and temperatures measured, see Table 5.6 – Table 5.10 in the appendix.

3.2 Si/Ge-Clusters as Wet Chemical Precursors for Inverse Opal Structured Thin Films

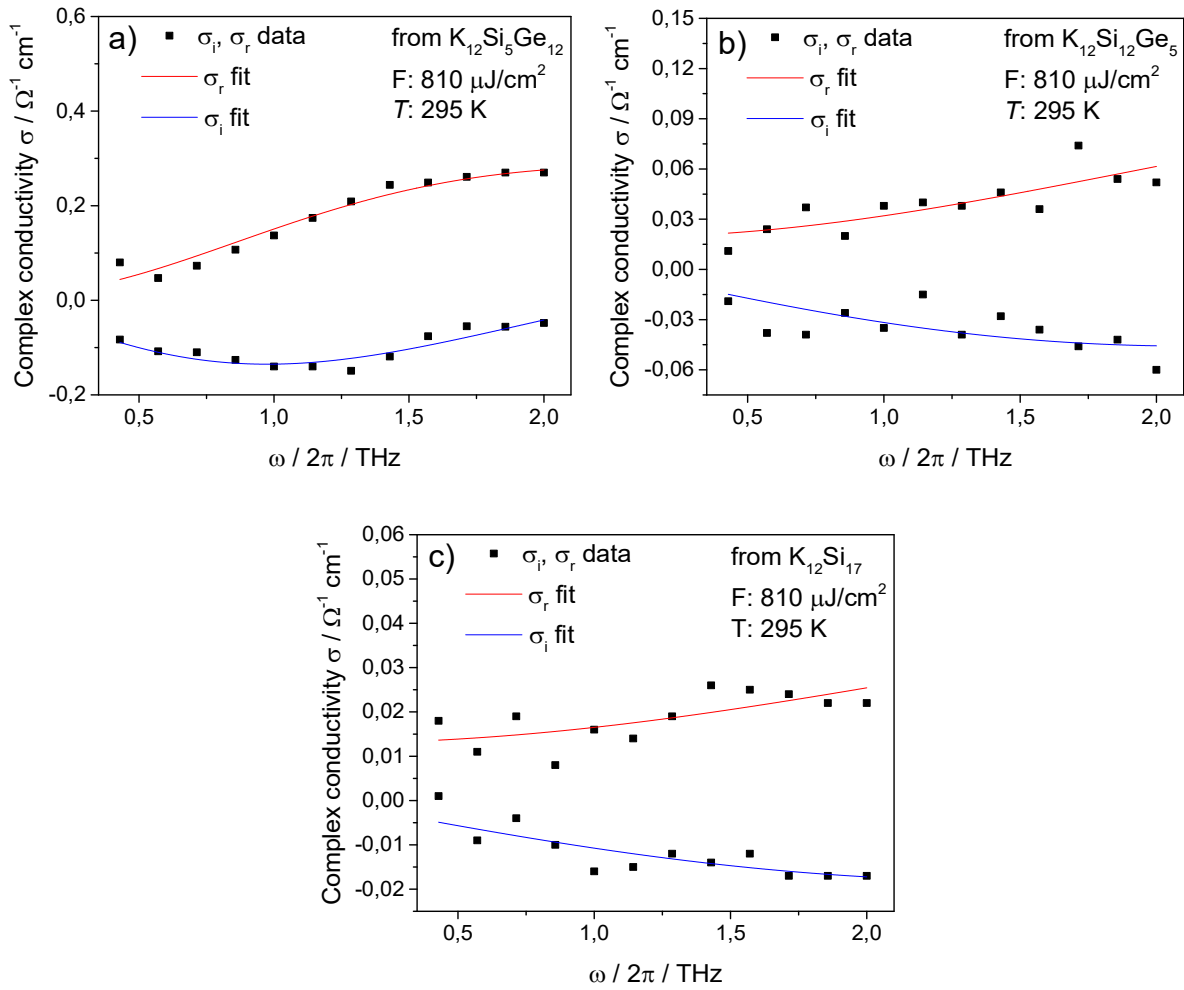


Figure 3.27. Complex conductivity $\sigma(\omega)$ plots for inverse opal structured thin films. a) starting from $\text{K}_{12}\text{Si}_5\text{Ge}_{12}$, b) starting from $\text{K}_{12}\text{Si}_{12}\text{Ge}_5$, c) starting from $\text{K}_{12}\text{Si}_{17}$. Both imaginary (σ_i , blue line) and real part (σ_r , red line) were fitted applying the Drude-Smith model.

Table 3.7. Parameters obtained from complex conductivity $\sigma(\omega)$ plots of inverse opal structured thin films using the Drude-Smith model (equation 1) at room temperature (295 K).

Fluence / $\mu\text{J} \cdot \text{cm}^{-2}$	Precursor material	$\tau_{\text{DS}} / \text{fs}$	c	$\mu_{\text{m}} / \text{cm}^2 \text{V}^{-1} \text{s}^{-1}$
810	$\text{K}_{12}\text{Si}_5\text{Ge}_{12}$	67.0 ± 2.7	-0.98 ± 0.01	14 ± 12
810	$\text{K}_{12}\text{Si}_{12}\text{Ge}_5$	29.5 ± 6.3	-0.92 ± 0.02	19 ± 4
810	$\text{K}_{12}\text{Si}_{17}$	23.7 ± 5.8	-0.88 ± 0.01	20 ± 6
972	$\text{K}_{12}\text{Si}_5\text{Ge}_{12}$	64.6 ± 2.7	-0.95 ± 0.01	34 ± 9
972	$\text{K}_{12}\text{Si}_{12}\text{Ge}_5$	30.3 ± 5.4	-0.89 ± 0.01	27 ± 5
1296	$\text{K}_{12}\text{Si}_{17}$	33.2 ± 5.5	-0.88 ± 0.01	26 ± 4

Results and Discussion

The c parameters for inverse opal structured Si/Ge and Si thin films were found to be -0.88 or lower, indicating that most of the carriers backscatter and only up to 12% are able to drift across the intergranular boundaries. This limitation becomes even more evident for mixed Si/Ge thin films in comparison to a Si thin film, indicating that grain boundaries between silicon and germanium are responsible for an increased carrier backscattering. Also, the c value is generally increased for higher fluences. Furthermore, the faster scattering time τ_{DS} for an increasing silicon content in the thin films (≈ 30 fs) implies a reduced carrier mean free path.^[225]

In addition, the macroscopic mobility $\mu_m = (1 + c)\mu$, can be calculated from the values for c and τ_{DS} . The macroscopic mobility values are increased alongside the carrier density (higher fluence), indicating an electron-hole recombination process as observed in polycrystalline silicon.^[225] Lowering the temperature did not enhance the mobility (see Table 5.7 and Table 5.9 in the appendix), indicating persistent structural disorder in the thin films. The values derived for μ_m are similar for all thin films tested. This indicates that the increased overall value of the conductivity for samples with high germanium content is counteracted by a higher recombination rate (lower c value). Due to the c value nearing -1 for the thin film starting from $K_{12}Si_5Ge_{12}$, standard deviation values of μ_m are quite high for this sample.

However, the average macroscopic mobilities derived for these thin films are exceed the value reported for amorphous silicon ($< 13 \frac{cm^2}{V \cdot s}$)^[222] (electron-drift mobility using a SCHOTTKY-diode circuit) and are comparable to values found for polycrystalline silicon ($30 - 40 \frac{cm^2}{V \cdot s}$) which were grown by molecular beam epitaxy.^[225] However, inverse opal structured Ge thin films are available through wet-chemical synthesis and do not undergo long annealing processes at high temperatures. Therefore, macroscopic mobility values of $\mu_m = 20 - 30 \frac{cm^2}{V \cdot s}$ for inverse opal structured thin films containing high silicon contents are remarkable. This makes these inverse opal structured materials potential candidates for application as amorphous materials in optoelectronics. However, the macroscopic mobility values obtained for Ge thin films are still out of reach.

3.3 Ge/Se and Ge/Te Thin Films

Synthesis of inverse opal structured thin films through wet chemical precursors in solution was established for group IV elements such as Ge^[43] and Sn as well as mixtures of the former^[95] and was expanded to mixed Si/Ge as well as silicon precursors within this work (see chapter 3.2). The next step was to check if this behavior can be adapted onto other starting materials. Due to their solubility in *en*, interesting candidates were mixtures of germanium with the group VI elements selenium and tellurium.^[251] Herein, K₄Ge₉/*en* solutions (0.06 mmol/mL) were mixed with selenium/*en* and tellurium/*en* solutions of various concentrations. However, while selenium is readily dissolving in *en*, tellurium is insoluble. Therefore, a deep red K₂Te precursor solution was used (see Figure 3.28a, for details on the synthesis see chapter 2.3.9). This solution was added to a K₄Ge₉/*en*, yielding red solution after filtration. However, drop casting of this solution followed by evaporation of the solvent did not provide sufficient coverage of the PMMA template film (Figure 3.28b). Exposition to DMSO and THF during the washing process only yielded the blank substrate.

Selenium is soluble in *en* at high concentrations (0.18 mmol/mL, see Figure 3.28c). Even after dilution, a clear yellow-brown liquid is obtained (0.06 mmol/mL, see Figure 3.28d). Combining a concentrated solution of Se/*en* with K₄Ge₉/*en* yielded a brown liquid after filtration. Drop casting this liquid onto a PMMA template film and letting it dry resulted in a brown thin film (see Figure 3.28e). However, treatment with DMSO and THF only left a brittle film, easily peeling off the substrate. Due to this, a morphology check *via* SEM wasn't possible. Instead, the thin film was tested in EDX, XRD and Raman to reveal its elemental composition.

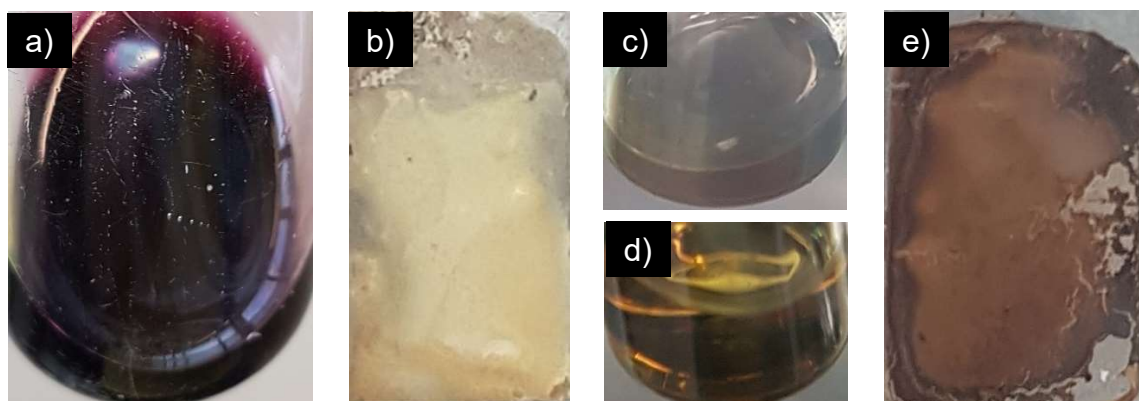


Figure 3.28. Pictures of K₂Te and selenium solutions as well as thin films. a) K₂Te solution in *en*, b) PMMA film after treatment with K₂Te/K₄Ge₉/*en* solution, c) solution of selenium in *en* (0.18 mmol/mL), d) diluted solution of selenium in *en* (0.06 mmol/mL), e) Se/K₄Ge₉/*en* thin film.

Results and Discussion

Unfortunately, the characteristic Raman band for selenium ($\approx 235 \text{ cm}^{-1}$) is close to the main band for Ge_9 -clusters ($\approx 220 \text{ cm}^{-1}$). Therefore, a distinction for broad bands would be difficult. However, the relatively sharp bands detected in spectra of Se:Ge mixtures mainly indicate the presence of Ge-clusters from the precursor (see Figure 3.29a). The powder diffraction patterns of dried residues of the Se:Ge mixtures only feature broad amorphous reflexes next to the main reflexes of K_4Ge_9 (see Figure 3.29b). Additional sharp reflexes found for compositions containing higher contents of selenium do not match any main reflexes in known crystal structures of phases containing selenium or germanium (see Figure 3.29b, brown line).

For low contents (initial composition Se:Ge of 1:36), selenium could not be detected by EDX measurements (see Table 3.8). For higher contents (initial composition 1:18 and 1:9), a small amount of selenium could be detected. However, increasing the content of selenium in the initial composition did not improve the resulting amount beyond 2 %wt. Therefore, mixing selenium solutions with a K_4Ge_9 solution seems to heavily influence the amount of selenium allowed to remain in solution. Due to this strong limitation, other starting materials were investigated regarding their solubility and therefore likelihood to the form inverse opal structured thin films.

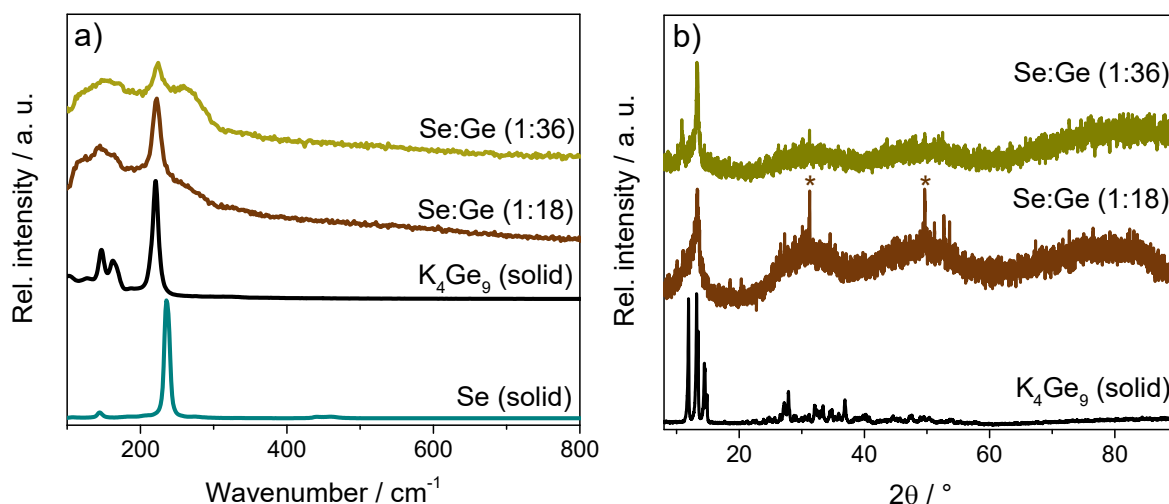


Figure 3.29. Raman spectra (a) and powder diffractograms (b) of different Se:Ge ratios compared to solid K_4Ge_9 . Raman spectra were measured at $\lambda = 532 \text{ nm}$. Diffractograms were obtained using Cu- $\text{K}\alpha_1$ radiation, $\lambda = 1.54056 \text{ \AA}$.

Table 3.8. Elemental composition (EDX) of dried Se/K₄Ge₉/en mixtures.

Initial atomic ratio (Composition)	K	Ge	Se
Se:Ge 1:18 (5:95 %at.)	25(4) %wt. 38 %at.	73(3) %wt. 60 %at.	2.2(6) %wt. 1.7 %at.
Se:Ge 1:36 (3:97 %at.)	54(6) %wt. 69 %at.	46(6) %wt. 31 %at.	—
Se:Ge 1:9 (10:90 %at.)	42(5) %wt. 57 %at.	56(4) %wt. 42 %at.	1.4(3) %wt. 1.0 %at.

3.4 Sn/Bi Thin Films with High Surface Area

As already demonstrated by S. C. Critchlow and J. D. Corbett^[252] as well as F. Lips *et al.*^[253], alloys with a nominal composition of “K₂Sn₂Bi₂” can be dissolved in *en* and yield tetrahedral [Sn₂Bi₂]²⁻ clusters when sequestered with 2.2.2-crypt^[252] or 18-crown-6^[253]. Potentially, this could be a starting point for the synthesis of Sn/Bi mixed thin films. However, most likely these tetrahedral clusters only form by sequestering potassium in solution. Solid state synthesis only yielded the literature known phase K₂SnBi^[216] (see Figure 5.7 in the appendix). This phase consists of folded zigzag chains of alternating Sn and Bi atoms rather than discrete clusters and is soluble in *en*, yielding a deep red solution (see Figure 3.30a). This solution was drop casted onto a PMMA template coated substrate. After evaporation of the solvent, either SnCl₄ (at reduced pressure) or SiCl₄ were added as a linker *via* vapor deposition before annealing the thin films at 373 or 423 K for 20 min. Treatment with DMSO followed by THF left metallic-brown films (see Figure 3.30b, for details on the synthesis see chapter 2.3.10).

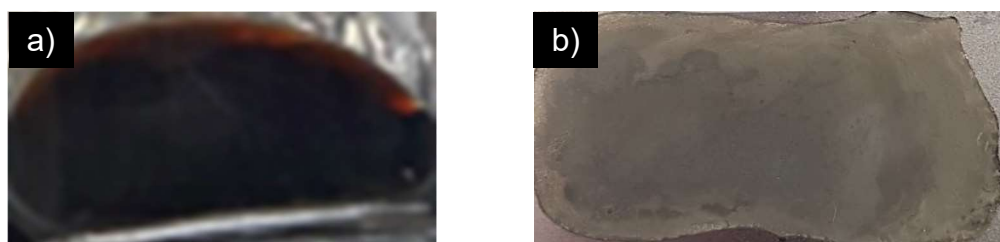


Figure 3.30. Pictures of K₂SnBi/*en* solution (a) and Sn/Bi thin film (b).

Results and Discussion

To assess the formation of these thin films, Raman spectra and powder diffraction patterns were obtained for each step in the synthesis using SiCl_4 as the linker. In Raman spectra of all steps, two intense bands are observed (see Figure 3.31). For a thin film where the solvent just evaporated under ambient conditions (as deposited) these bands are located at 70 cm^{-1} and 95 cm^{-1} . These values are also observed for the starting material K_2SnBi (see Figure 3.31, brown line). Both bands could be resulting from different Bi-Bi vibration modes^[254]. However, if that was the case the second band (95 cm^{-1}) would be expected to be much less intense. Since this band is also present in the starting material K_2SnBi , it is reasonable to assume that it indicates a Sn-Bi vibration instead. After application of the linker, both bands are detected at slightly lower wavenumbers (62 cm^{-1} and 87 cm^{-1}). The band representing Sn-Sn vibrations in the precursor ($\approx 125\text{ cm}^{-1}$, equal to the value found in β -tin^[255]) is missing in the deposited films. An influence of the linker (SiCl_4) cannot be confirmed *via* Raman spectroscopy either.

The powder diffraction pattern of a thin film where the solvent just evaporated under ambient conditions (as deposited), shows that the precursor partly decomposed to elemental tin and bismuth (see Figure 3.32, black line). However, the main product detected is KBi_2 . The formation of the Laves phase KBi_2 is in accordance with observations in the literature where the filtration of solutions of ternary alkali-metal bismuth phases yielded KBi_2 .^[256] Through addition of the linker (SiCl_4) in a stoichiometric amount, KBi_2 is almost removed (see Figure 3.32, red line). Annealing the thin film at 373 K for 20 min does not result in significant changes. In the end, mainly elemental tin and bismuth can be detected. The influence of the linker (SiCl_4) is questionable in this case, due to the material being scraped off a silicon substrate for a capillary measurement. However, a strong increase in intensity of the silicon reflexes is observed for both films measured after application of the linker (Figure 3.32, intensity in red and blue line compared to black line).

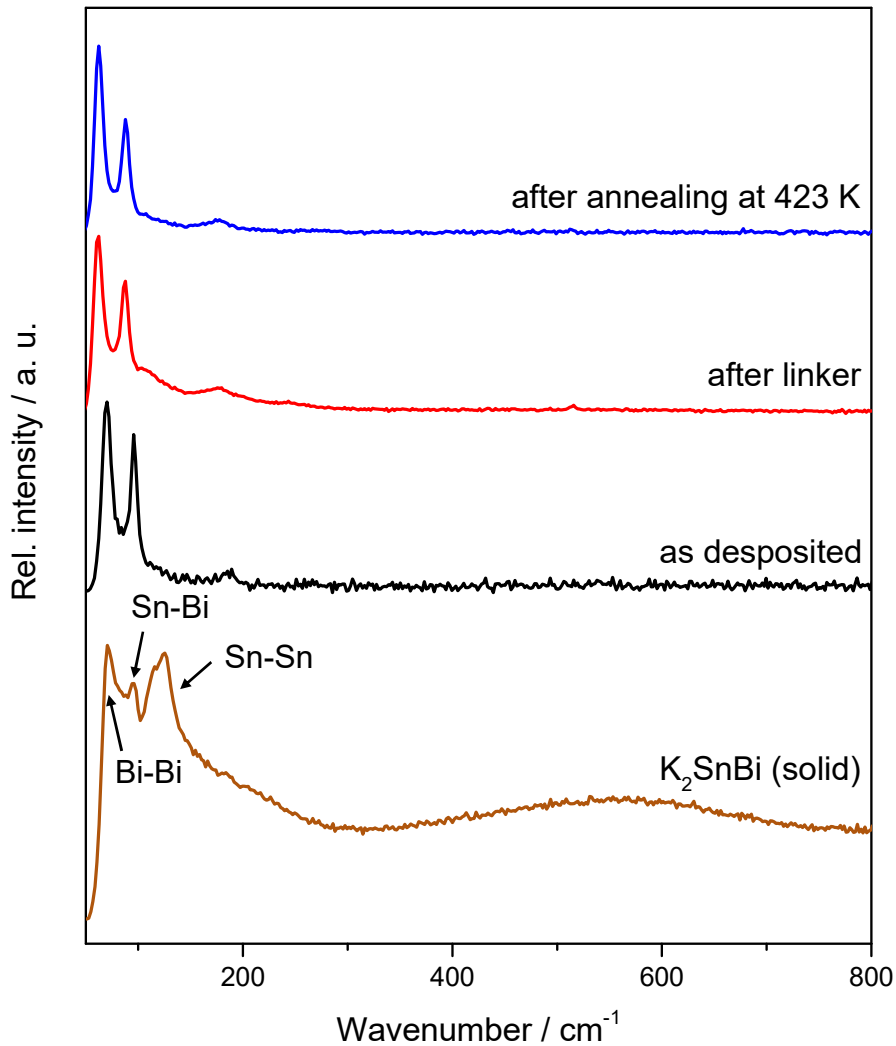


Figure 3.31. Raman spectra of Sn/Bi thin film at different steps in the synthesis compared to solid K_2SnBi . Spectra were measured at $\lambda = 532$ nm.

Elemental analysis through EDX proves that the influence of the linker cannot be neglected (see Table 3.9). $SnCl_4$ has a distinctly higher boiling point than $SiCl_4$. To compensate for this, vapor deposition of $SnCl_4$ was performed under reduced pressure ($\approx 1 \cdot 10^{-1}$ mbar). However, even under reduced pressure an excess amount of $SnCl_4$ is needed to react with the entire amount of potassium so that it can be removed as KCl through washing with DMSO and THF. In contrast, a stoichiometric amount of $SiCl_4$ is enough to accomplish the same result (see Table 3.9).

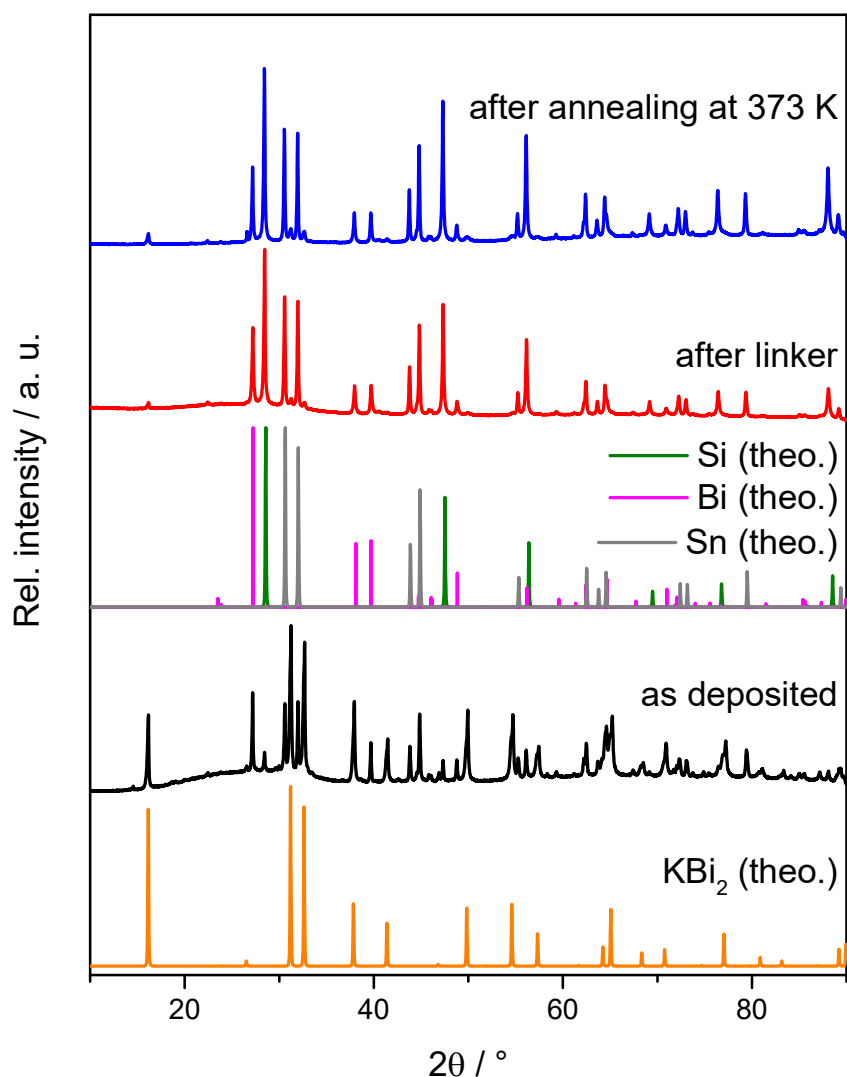


Figure 3.32. Powder diffraction patterns of Sn/Bi thin film at different steps in the synthesis. Diffraction patterns were obtained using Cu-K α_1 radiation, $\lambda = 1.54056$ Å. Theoretical diffraction patterns were calculated from crystal data of the compounds available in literature.^[257-260]

Table 3.9. Elemental composition (EDX) of Sn/Bi thin films after treatment with various linkers at different concentrations. Thin films were annealed at 373 K for 20 min and washed with DMSO followed by THF for 30 min.

Linker (ratio)	K / %at.	Sn / %at.	Bi / %at.
SnCl ₄ (stoichiometric)	36(1)	35(1)	29(1)
SnCl ₄ (excess)	–	53(5)	47(5)
SiCl ₄ (stoichiometric)	–	43(1)	57(1)

3.4 Sn/Bi Thin Films with High Surface Area

The linker also seems to have an influence on the morphology of the resulting thin film. SEM pictures show that using SnCl_4 as a linker yields no porous material at all (see Figure 3.33a). Using excess of SnCl_4 simply thickens the material (see Figure 3.33b and c). Using SiCl_4 as a linker instead does not provide an inverse opal structured material either (see chapter 3.1.1 for Ge precursor in comparison). However, the resulting material is still porous with a high surface area (see Figure 3.33d and e). This is still the case after annealing the thin film at a higher temperature of 423 K for 20 min (see Figure 3.33f and g). Therefore, Sn/Bi thin films linked with SiCl_4 could be of interest for potential applications such as batteries or solar cells in need of smaller band gaps (increased metallic behavior).

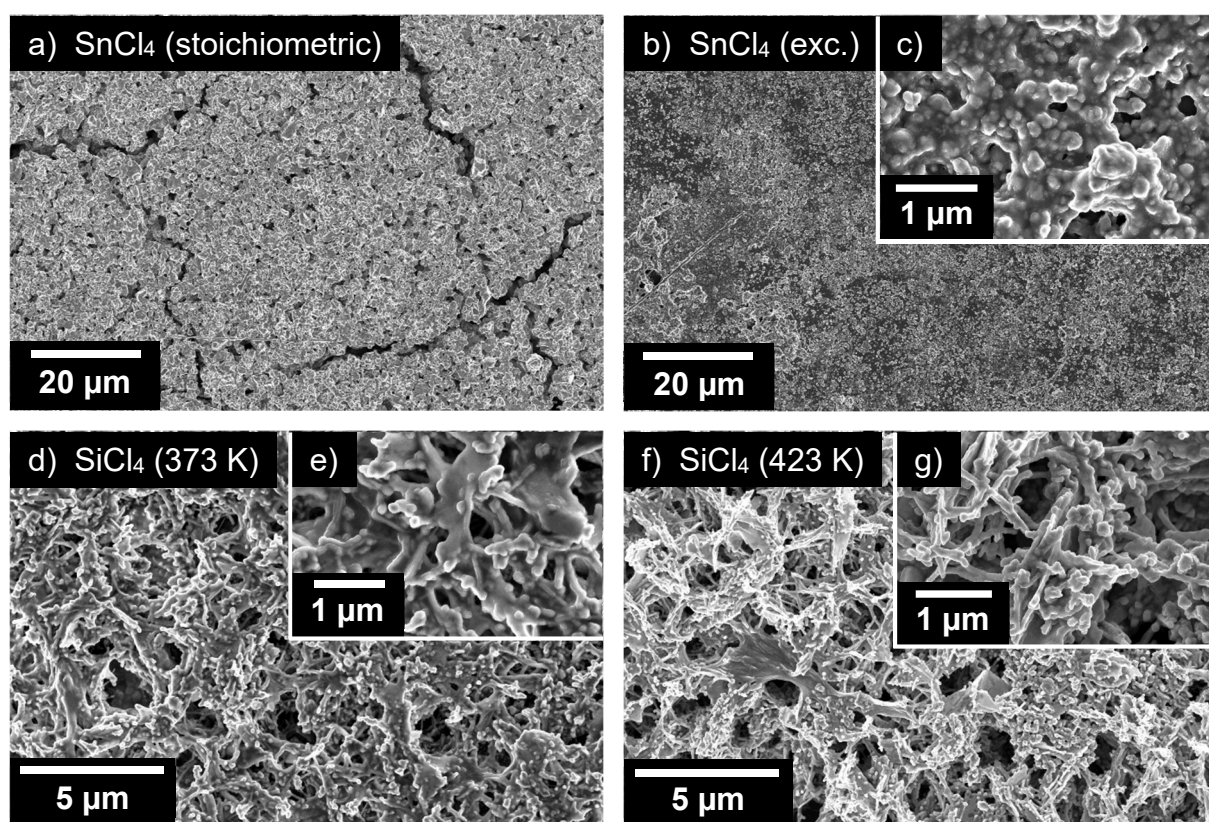


Figure 3.33. SEM pictures of Sn/Bi thin films after treatment with various linkers at different concentrations. a) 2.000x magnification after treatment with stoichiometric amount of SnCl_4 , b) 2.000x and c) 50.000x magnification after treatment with excess amount of SnCl_4 , d) 10.000x and e) 50.000x magnification after treatment with stoichiometric amount of SiCl_4 . f) 10.000x and g) 50.000x magnification after treatment with stoichiometric amount of SiCl_4 after annealing at 423 K for 20 min (instead of 373 K for a – e).

3.5 Silylation of Mixed Nine Atomic Si/Ge Clusters

Solubility of bare Si/Ge clusters is heavily limited due to their high charge. So far, almost any accessibility to soluble products is limited to *en* or liquid ammonia as a solvent. Solubility in liquid ammonia also requires addition of crown ethers or cryptands (e. g. 18-crown-6 or 2.2.2-crypt) as sequestering agents. Other solvents such as pyridine require prior activation of the starting material by liquid ammonia. Therefore, it is favorable to shift the polarity of clusters by attaching substituents. A substituent of particular interest in that regard is tris(trimethylsilyl)silane $-\text{Si}(\text{Si}(\text{CH}_3)_3)_3$ (“hypersilyl group”, *hyp*). As already demonstrated for Ge_9 -clusters, attaching hypersilyl groups to clusters enables the solubility in common laboratory solvents such as acetonitrile (MeCN) or THF.^[161, 162] This fact recently facilitated a growing interest in follow-up reactions such as functionalization with an additional ligand (stabilized transition metals^[164, 173, 180, 189] or alkyl groups^[174, 178]) or oxidative coupling of silylated clusters through transition metal cations^[180, 261]. For K_4Ge_9 as a precursor, silylation with hypersilylchloride (*hyp*-Cl) was developed as a stoichiometric (3 equivalents *hyp*-Cl), heterogenous reaction in acetonitrile.^[162]

Within this work, the silylation reaction was applied to mixed nine atomic Si/Ge clusters as well as bare silicon clusters starting from $\text{K}_{12}\text{Si}_{17-x}\text{Ge}_x$ -phases ($x = 0, 5, 9, 12, 17$). However, for mixed Si/Ge clusters a heterogeneous reaction using only 3 equivalents *hyp*-Cl was found to result in the formation of several reaction products which could not be separated from each other. Therefore, an excess amount of *hyp*-Cl (12 equivalents) was used instead, yielding pale yellow to orange solutions after filtration (see Figure 3.34a; for details on the synthesis also see chapter 2.3.11). Due to the limited solubility of the reaction product in acetonitrile, the solvent was removed and the residue re-dissolved in less polar solvents such as toluene (Tol) for crystallization, yielding orange to deep red solutions (see Figure 3.34b) of $\text{K}[\text{E}_9(\text{hyp})_3]$ (*E*: Si, Ge).

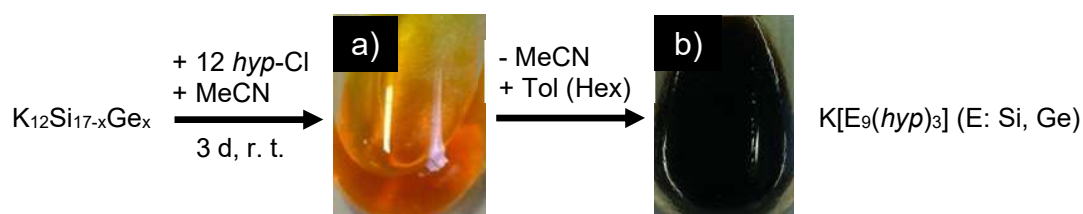


Figure 3.34. Synthesis of $\text{K}[\text{E}_9(\text{hyp})_3]$ (*E*: Si, Ge). a) Reaction of $\text{K}_{12}\text{Si}_{17-x}\text{Ge}_x$ with excess *hyp*-Cl (12 eq) in acetonitrile (MeCN) yields orange solutions after filtration. b) Enhanced solubility in less polar solvents such as toluene (tol) or hexane (hex) after removal of MeCN (yielding deep red solutions). R. t.: room temperature.

3.5 Silylation of Mixed Nine Atomic Si/Ge Clusters

Mass spectra of $K[E_9(hyp)_3]$ (E : Si, Ge) were carried out with diluted reaction solutions in acetonitrile. A statistical distribution of different Si/Ge ratios in $K[E_9(hyp)_3]$ (E : Si, Ge) is detected (see Figure 3.35a). Furthermore, 2.2.2-crypt was added to reaction solutions of $K[E_9(hyp)_3]$ (E : Si, Ge) in toluene to achieve crystal growth. The resulting crystals (orange needles) could be isolated and dissolved in THF, yielding a similar distribution of different Si/Ge ratios in $K[E_9(hyp)_3]$ (E : Si, Ge; see Figure 3.35b). However, a reduction in intensity for $Si_3Ge_6(hyp)_3^-$ while additionally detecting $Si_5Ge_4(hyp)_3^-$ for a THF solution of dissolved crystals is indicating an extension of the statistical distribution through crystallization.

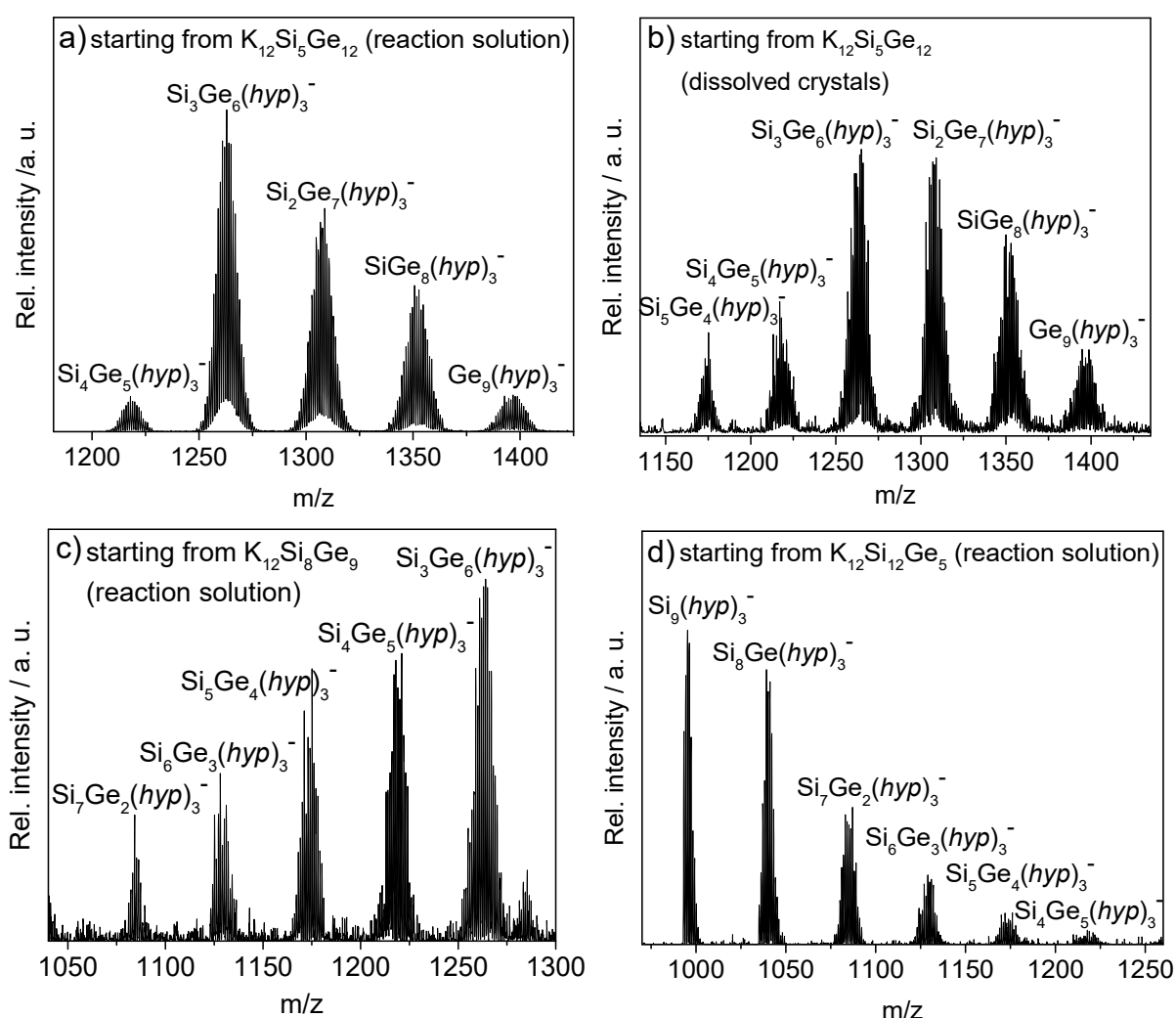


Figure 3.35. ESI-MS spectra of $[E_9(hyp)_3]^-$ (E : Si, Ge) in negative ($-$) ion mode. a) diluted acetonitrile reaction solution (reaction product of $K_{12}Si_5Ge_{12}$ with excess of *hyp*-Cl) monitoring the compounds with a K^+ moiety cleaved, b) THF solution of dissolved crystals (crystal growth through cooling of a reaction solution of $K_{12}Si_5Ge_{12}$ with excess of *hyp*-Cl after addition of 2.2.2-crypt) monitoring the compounds with a $[K(2.2.2\text{-crypt})]^+$ moiety cleaved; diluted acetonitrile reaction solutions (reaction product of $K_{12}Si_8Ge_9$ (c) and $K_{12}Si_{12}Ge_5$ (d) with excess of *hyp*-Cl) monitoring the compounds with a K^+ moiety cleaved. Composition of the compounds is highlighted on top of the distinct peaks.

Results and Discussion

Changing the Si/Ge ratio in the ZINTL-precursor $K_{12}Si_{17-x}Ge_x$ ($x = 0, 5, 9, 12$) has a direct influence on the species detected (e. g. $Si_9(hyp)_3^-$ as main component starting from $K_{12}Si_{12}Ge_5$, see Figure 3.35d). However, $Si_3Ge_6(hyp)_3^-$ seems to be a quite stable and preferred composition as it is detected as the peak with highest intensity starting from $K_{12}Si_5Ge_{12}$ and $K_{12}Si_8Ge_9$ (see Figure 3.35a and c).

High resolution data were obtained for all possible Si/Ge ratios in the E_9 -cluster. Experimental data is in good accordance with theoretical isotopic patterns in all cases (for an overview on all Si/Ge ratios in the E_9 -cluster see Figure 5.15 – Figure 5.19 in the appendix). In general, introducing germanium significantly broadens the pattern due to its complex isotopic distribution (see Figure 3.36; the pattern of $Si_7Ge_2(hyp)_3^-$ is spread over 20 m/z while the pattern of $Si_2Ge_7(hyp)_3^-$ is spread over 30 m/z).

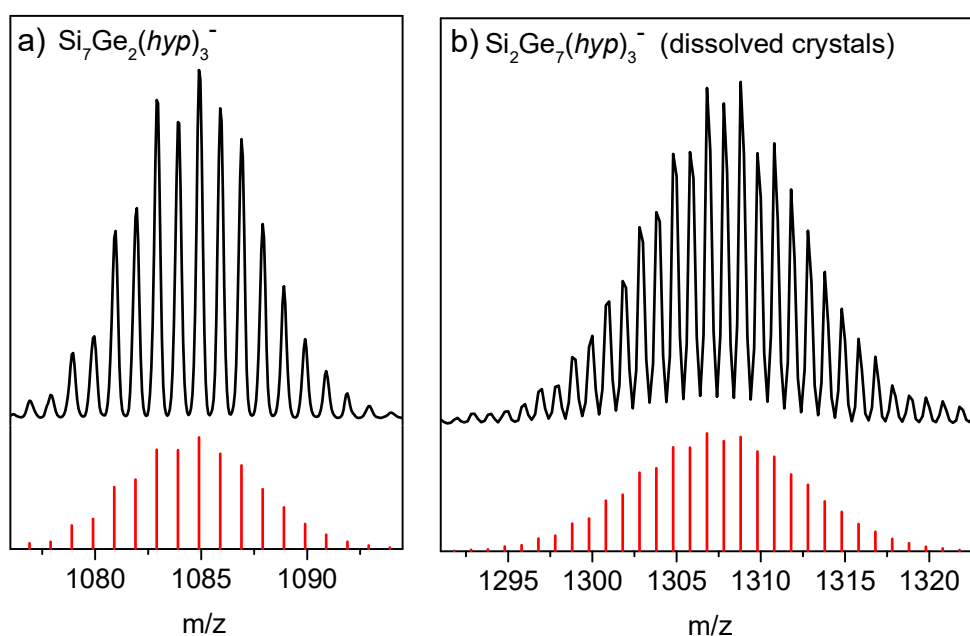


Figure 3.36. Selected high resolution areas of the ESI-MS spectrum of $[E_9(hyp)_3]^-$ (E : Si, Ge) in negative ($-$) ion mode. a) monitoring $[Si_7Ge_2(hyp)_3]^-$ at 1084.9 m/z in a diluted acetonitrile reaction solution with a K^+ moiety cleaved, b) monitoring $[Si_2Ge_7(hyp)_3]^-$ at 1307.8 m/z in a THF solution of dissolved crystals (crystal growth through cooling of a reaction solution of $K_{12}Si_5Ge_{12}$ with excess of *hyp*-Cl after addition of 2.2.2-crypt) with a $[K(2.2.2-crypt)]^+$ moiety cleaved. Simulated mass spectra with their isotopic distribution are shown below as red bars.

3.5 Silylation of Mixed Nine Atomic Si/Ge Clusters

NMR studies of the reaction solutions feature three distinct peaks for the TMS groups in the ^1H and ^{13}C spectrum (see Figure 3.37 and Figure 3.39 for $\text{K}_{12}\text{Si}_8\text{Ge}_9$ as a precursor). These three peaks are present for all other tested Si/Ge ratios in the precursor $\text{K}_{12}\text{Si}_{17-x}\text{Ge}_x$ ($x = 0, 5, 12, 17$) as well (see highlighted areas of the respective ^1H spectra in Figure 3.38; additionally see Figure 5.23 – Figure 5.26 in the appendix for full ^1H spectra). However, for $\text{K}_{12}\text{Ge}_{17}$ ($x = 17$) the main product detected, $\text{K}[\text{Ge}_9(\text{hyp})_3]$ is resulting in an additional peak at 0.45 ppm (see Figure 3.38d). 2D NMR experiments (via HMBC) revealed that the CH_3 groups within a TMS group do not split up in different peaks. Therefore, the three different peaks either represent the three different *hyp* groups or the different TMS groups within a *hyp* group.

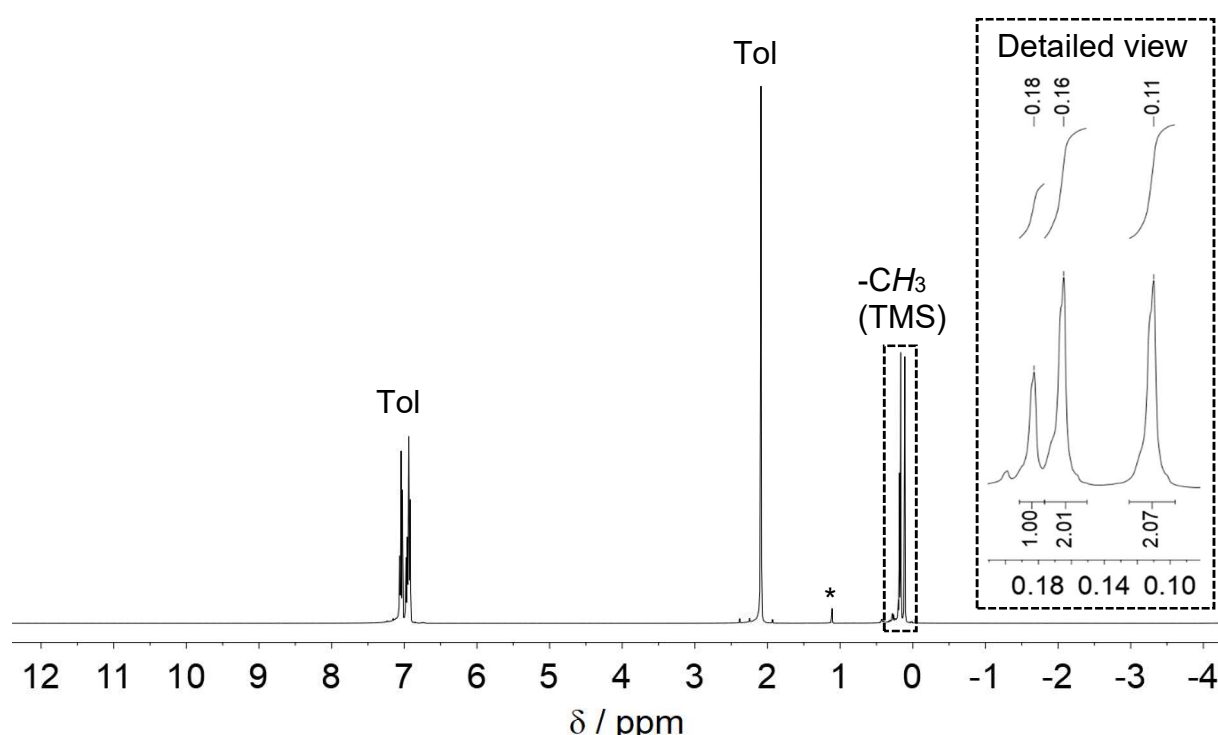


Figure 3.37. ^1H -NMR of reaction solution of $\text{K}[\text{E}_9(\text{hyp})_3]$ (E : Si, Ge) starting from $\text{K}_{12}\text{Si}_8\text{Ge}_9$ as a precursor. *In situ* study in toluene. Next to the solvent peaks, only a small byproduct (*) is present.

Results and Discussion

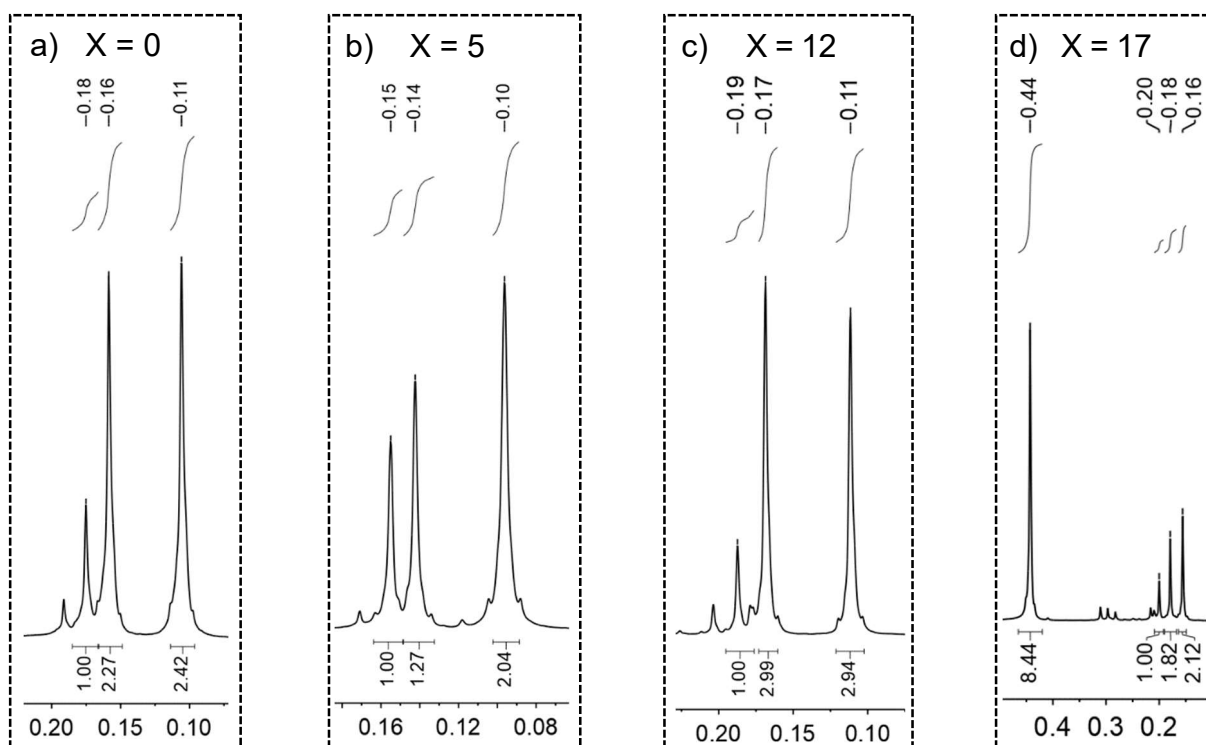


Figure 3.38. Detailed view of the $-CH_3$ (TMS) peaks in 1H -NMRs of reaction solutions of $K[E_9(hyp)_3]$ (E : Si, Ge) compounds starting from $K_{12}Si_{17-x}Ge_x$ ($x = 0, 5, 12, 17$) as a precursor. *In situ* study in toluene.

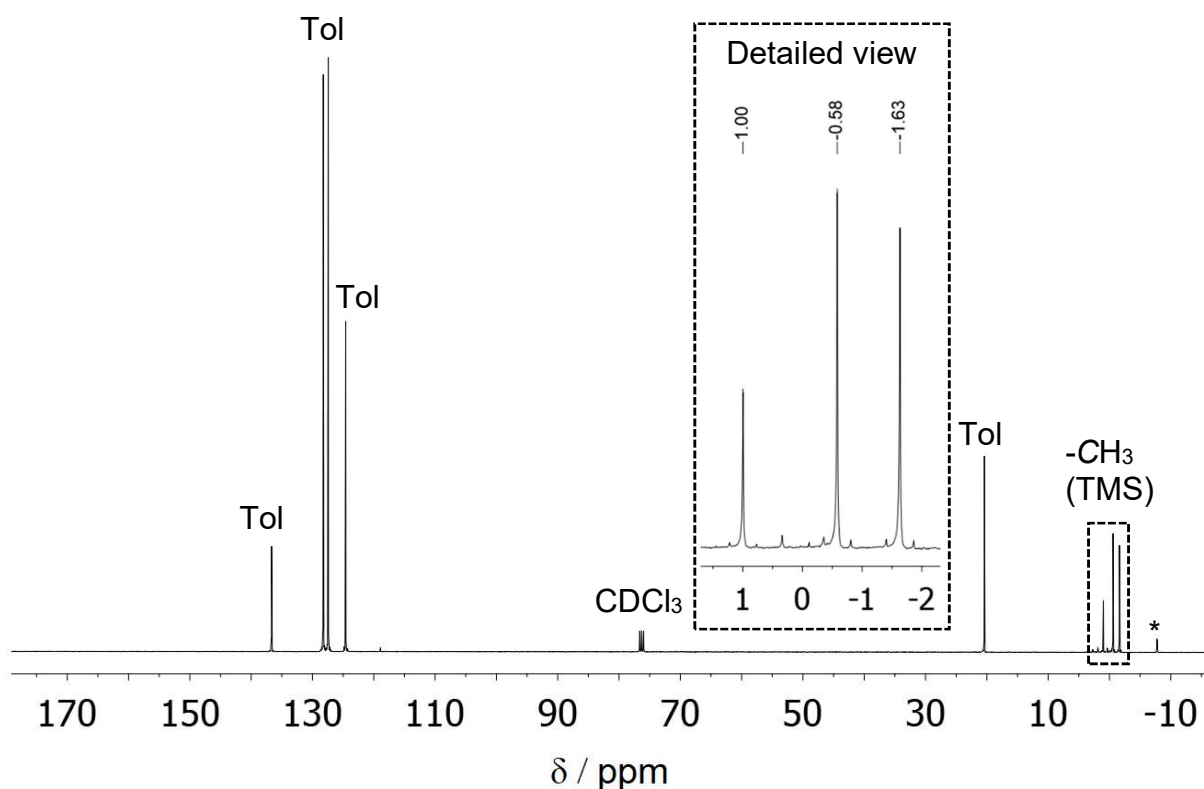


Figure 3.39. ^{13}C -NMR of reaction solution of $K[E_9(hyp)_3]$ (E : Si, Ge) starting from $K_{12}Si_8Ge_9$ as a precursor. *In situ* study in toluene using $CDCl_3$ as external standard. Next to the solvent peaks, only a small byproduct (*) is present.

3.5 Silylation of Mixed Nine Atomic Si/Ge Clusters

The ^{29}Si -IG spectrum of the reaction solutions features no such split in three distinct peaks (see Figure 3.40a for $\text{K}_{12}\text{Si}_8\text{Ge}_9$ as a precursor). However, the silicon peaks originating from the TMS groups are split when running the sample in a ^{29}Si -INEPT setup boosting the intensity of any silicon with hydrogen in the vicinity (see Figure 3.40b). Furthermore, a peak representing a byproduct (*) is detected with boosted intensity due to hydrogen in the vicinity and most likely represents a reaction product of the excess of *hyp*-Cl used in the synthesis. This behavior is consistent for all other tested Si/Ge ratios in the precursor $\text{K}_{12}\text{Si}_{17-x}\text{Ge}_x$ ($x = 0, 5, 12, 17$) as well (see Figure 5.27 – Figure 5.32 in the appendix). In $\text{K}[\text{E}_9(\text{hyp})_3]$ (E : Si, Ge), only the intensity of the silicon in the TMS groups is boosted by running ^{29}Si -INEPT experiments. The intensity of the silicon attached to the cluster remains low due to lack of hydrogen in the vicinity.

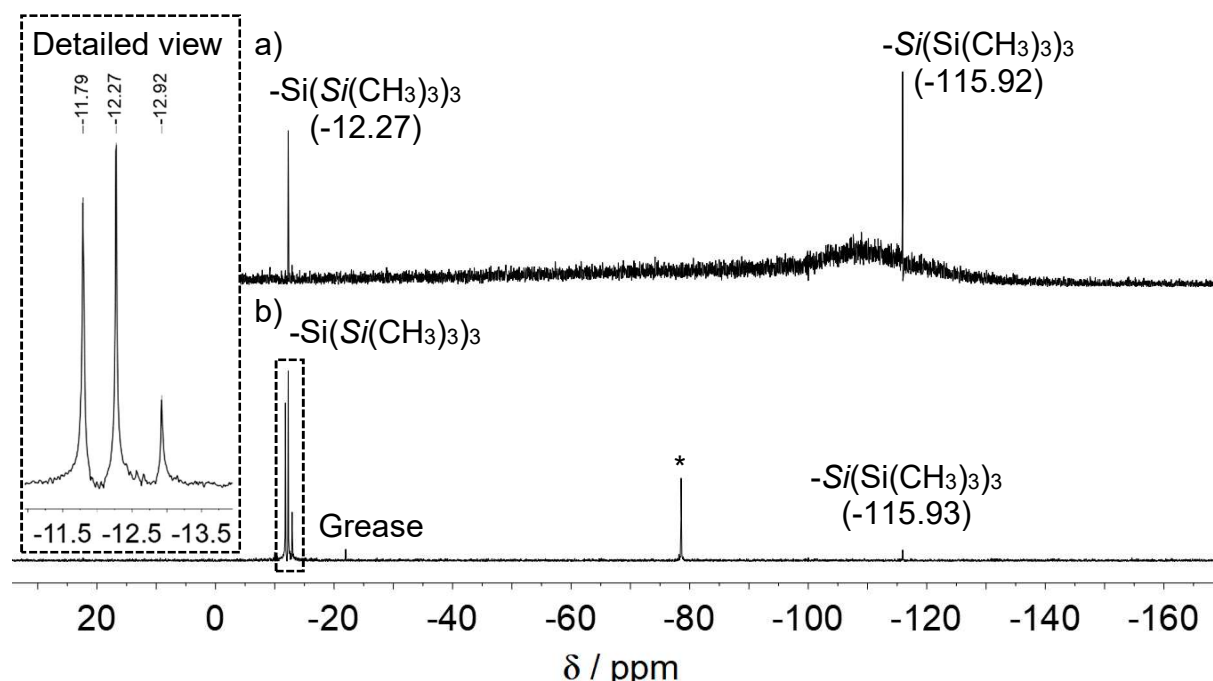


Figure 3.40. ^{29}Si -NMR spectra of reaction solution of $\text{K}[\text{E}_9(\text{hyp})_3]$ (E : Si, Ge) starting from $\text{K}_{12}\text{Si}_8\text{Ge}_9$ as a precursor. *In situ* study in toluene. a) Long-term ^{29}Si -IG spectrum without byproduct and b) ^{29}Si -INEPT spectrum featuring byproduct (*) with boosted intensity.

Crystal growth was achieved by adding 2.2.2-crypt to reaction solutions of $\text{K}[\text{E}_9(\text{hyp})_3]$ (E : Si, Ge) in toluene and storing them in a fridge at 241 K. After a few days, many small orange needles formed. Single crystal measurements of these needles indicated an orthorhombic unit cell in the space group $\text{P}2_12_12_1$ with a high cell volume ($a = 30.688(6)$ Å, $b = 32.856(7)$ Å, $c = 34.232(7)$ Å, $V = 34515(12)$ Å³ for needles obtained starting from $\text{K}_{12}\text{Si}_5\text{Ge}_{12}$ precursor). Similar cell parameters were obtained for needles crystallized starting from other precursors $\text{K}_{12}\text{Si}_{17-x}\text{Ge}_x$ ($x = 0, 9$). The

scattering intensities of these needles were weak, making them unsuitable for crystal structure determination. However, using a precursor with relatively low Si content ($K_{12}Si_5Ge_{12}$) resulted in the additional formation of orange-red blocks after three months. These block shaped crystals showed a monoclinic unit cell in the space group $P2_1/c$ and exactly half the volume determined for the needles ($a = 26.7403(8) \text{ \AA}$, $b = 24.0116(4) \text{ \AA}$, $c = 29.2996(9) \text{ \AA}$, $\beta = 113.356(2)^\circ$, $V = 17271.1(8) \text{ \AA}^3$). Their unit cell contains two independent E_9 -clusters and two sequestered K^+ cations with 2.2.2-crypt. These values are close to the cell parameters found by Li and Sevov for $K(2.2.2\text{-crypt})[Ge_9(hyp)_3]$ ($P2_1/c$, $a = 26.497(3) \text{ \AA}$, $b = 24.090(2) \text{ \AA}$, $c = 29.268(3) \text{ \AA}$, $\beta = 113.888(2)^\circ$, $V = 17081(3) \text{ \AA}^3$).^[162] However, in case of the red blocks formed from $K_{12}Si_5Ge_{12}$ as a precursor, the three positions in the E_9 -cluster cluster with an exo bond to a silyl group are occupied by a mixture of silicon and germanium (56% average occupation by Si). In contrast, the other six positions in the cluster are only occupied by germanium, adding up to $K(2.2.2\text{-crypt})[Si_{1.68(1)}Ge_{7.32(1)}(hyp)_3]$ as the molecular structure (see Figure 3.41a).

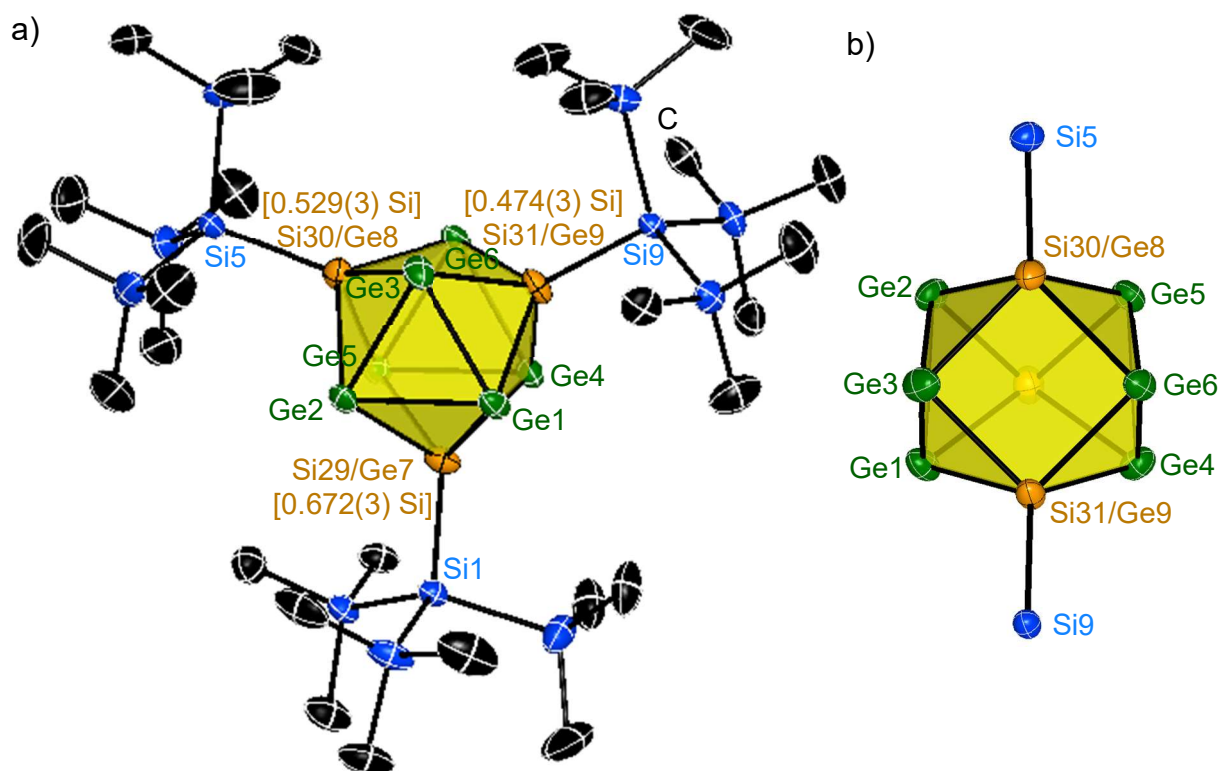


Figure 3.41. Molecular structure of a silylated cluster in $K(2.2.2\text{-crypt})[Si_{1.68(1)}Ge_{7.32(1)}(hyp)_3]$. a) front view of the $[Si_{1.68(1)}Ge_{7.32(1)}(hyp)_3]^-$ unit revealing D_{3h} symmetry of the cluster. For clarity, hydrogen atoms and co-crystallized $K(2.2.2\text{-crypt})^+$ moiety are omitted. b) top view of the central $[Si_{1.68(1)}Ge_{7.32(1)}]$ unit. Displacement ellipsoids are depicted at a 50% probability level in both cases.

3.5 Silylation of Mixed Nine Atomic Si/Ge Clusters

Crystallographic data of the measurement of $K(2.2.2\text{-crypt})[Si_{1.68(1)}Ge_{7.32(1)}(hyp)_3]$ is listed in Table 3.10. The fractional site occupation in the two independent E_9 -clusters is listed in Table 5.11 in the appendix. Si-Si exo bonds being favored over Ge-Si exo bonds is supported by $[Si_3Ge_6(hyp)_3]^-$ being the main species detected in ESI-MS if possible. A similar behavior was also observed in protonated mixed Si/Ge clusters by Henneberger, Klein and Fässler where the protonated positions in the E_9 -cluster were only occupied by silicon while all other positions were occupied by a mixture of silicon and germanium.^[262]

Table 3.10. Crystallographic data of $K(2.2.2\text{-crypt})[Si_{1.68(1)}Ge_{7.32(1)}(hyp)_3]$.

	$K(2.2.2\text{-crypt})[Si_{1.68(1)}Ge_{7.32(1)}(hyp)_3]$
composition	$K_2Ge_{14.64}Si_{27.36}C_{90}O_{12}N_4H_{234}$
crystal system	monoclinic
space group (no.)	$P2_1/c$ (14)
$a / \text{\AA}$	26.7403(8)
$b / \text{\AA}$	24.0116(4)
$c / \text{\AA}$	29.2996(9)
$\alpha / ^\circ$	90
$\beta / ^\circ$	113.356(2)
$\gamma / ^\circ$	90
$V / \text{\AA}^3$	17271.1(8)
Z	8
T / K	150(2)
$\lambda / \text{\AA}$	0.71073 (Mo- K_α)
$\bar{\rho}_{\text{calc.}} / \text{g cm}^{-3}$	1.336
μ / mm^{-1}	2.786
collected reflections	498536
independent reflections	33918
R_{int}	0.192
$R_1 [I > 2\sigma(I)]$ (all data)	0.0492 (0.1052)
$wR_2 [I > 2\sigma(I)]$ (all data)	0.0930 (0.1122)
parameters/restraints	1569/18
goodness of fit (F^2)	1.013
max. and min. difference el. density / $e \text{\AA}^{-3}$	0.86 and -0.61

Results and Discussion

The central $[\text{Si}_{1.68(1)}\text{Ge}_{7.32(1)}]$ unit in the structure adopts the shape of a slightly distorted D_{3h} -symmetric tri-capped trigonal prism (Figure 3.42a) in which the mixed Si/Ge atoms (all caps of the trigonal prism; Si30/Ge8, Si31/Ge9 and Si29/Ge7) carry silyl groups. C_{4v} -symmetry would be expressed by the ratio of the diagonal lengths of the open square of the best mono-capped square antiprism $d_2(\text{Ge3-Ge6})/d_1(\text{Si30/Ge8-Si31/Ge9}) = 1.01$ (with $d_2/d_1 = 1$ for a perfect C_{4v} -symmetry) and is nearly ideal (see Figure 3.41b). However, the dihedral angle of the two halves of the most planar square face of the cluster $\gamma(\text{Ge3-Ge6-Si30/Ge8-Si31/Ge9}) = 19.12(3)$ (with $\gamma = 0$ for a perfect C_{4v} -symmetry) prohibits C_{4v} -symmetry (see Figure 3.42b). With the heights of the trigonal prism h being off for one of the two independent E_g -clusters, a slightly distorted D_{3h} shape is the result (see Table 3.11). This symmetry works well with the values found for the literature known structure $\text{K}(2.2.2\text{-crypt})[\text{Ge}_9(\text{hyp})_3]$.^[162]

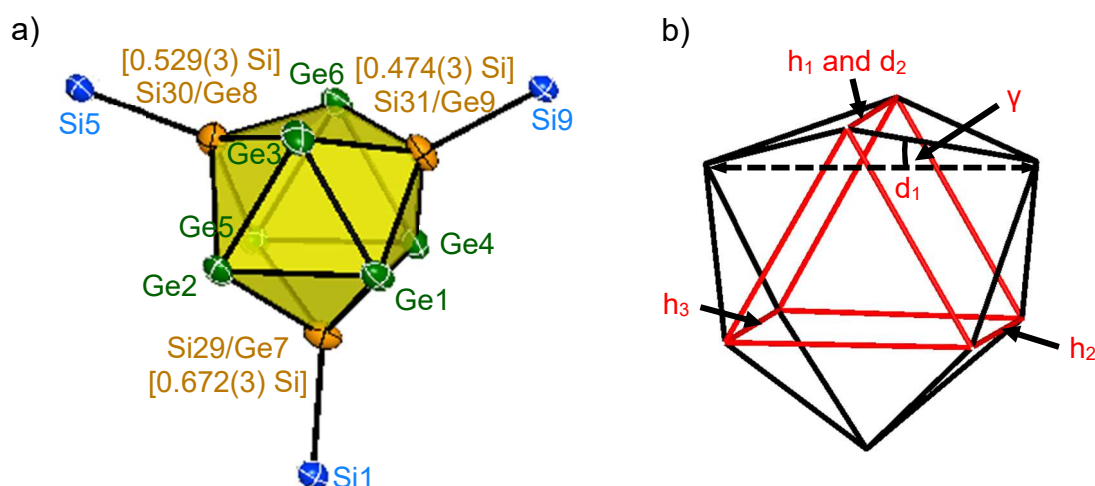


Figure 3.42. a) Front view of the central $[\text{Si}_{1.68(1)}\text{Ge}_{7.32(1)}]$ unit in $\text{K}(2.2.2\text{-crypt})[\text{Si}_{1.68(1)}\text{Ge}_{7.32(1)}(\text{hyp})_3]$ and b) schematic view of the central $[\text{Si}_{1.68(1)}\text{Ge}_{7.32(1)}]$ unit highlighting important parameters for symmetry of the cluster. Displacement ellipsoids in a) are depicted at a 50% probability level.

Table 3.11. Comparison of the ZINTL cluster shape in $\text{K}(2.2.2\text{-crypt})[\text{Si}_{1.68(1)}\text{Ge}_{7.32(1)}(\text{hyp})_3]$ with literature known compound $\text{K}(2.2.2\text{-crypt})[\text{Ge}_9(\text{hyp})_3]$ ^[162]. h : Heights of the trigonal prism, d : diagonal lengths of the open square of the best mono-capped square antiprism, γ : dihedral angle of the two halves of the most planar square face.

Distance or Angle	$\text{K}(2.2.2\text{-crypt})\text{-}[\text{Si}_{1.68(1)}\text{Ge}_{7.32(1)}\{\text{Si}(\text{TMS})_3\}_3]$	$\text{K}(2.2.2\text{-crypt})[\text{Ge}_9\{\text{Si}(\text{TMS})_3\}_3]$ ^[162]
$h_1 / \text{\AA}$	3.1470(8) and 3.2688(8)	3.1413(2) and 3.2206(2)
$h_2 / \text{\AA}$	3.4223(8) and 3.3046(9)	3.5186(2) and 3.4964(2)
$h_3 / \text{\AA}$	3.4906(8) and 3.4802(9)	3.5319(3) and 3.4894(2)

3.5 Silylation of Mixed Nine Atomic Si/Ge Clusters

h_2/h_1	1.09 and 1.01	1.12 and 1.09
h_3/h_1	1.11 and 1.06	1.12 and 1.08
$d_1 / \text{Å}$	3.4906(8) and 3.4802(9)	3.5319(3) and 3.4964(2)
$d_2 / \text{Å}$	3.5102(12) and 3.5040(12)	3.5477(2) and 3.5487(3)
d_2/d_1	1.01 and 1.01	1.00 and 1.02
$\gamma / ^\circ$	19.12(3) and 19.62(3)	18.76(1) and 19.93(1)

The elemental composition derived for $\text{K}(2.2.2\text{-crypt})[\text{Si}_{1.68(1)}\text{Ge}_{7.32(1)}(\text{hyp})_3]$ is supported by EDX results (see Table 3.12). Notably, the values obtained for needles with weak scattering of the same experiment are similar to values found for red blocks of $\text{K}(2.2.2\text{-crypt})[\text{Si}_{1.68(1)}\text{Ge}_{7.32(1)}(\text{hyp})_3]$.

Table 3.12. Elemental composition (EDX) of $\text{K}(2.2.2\text{-crypt})[\text{Si}_{1.68(1)}\text{Ge}_{7.32(1)}(\text{hyp})_3]$ (red blocks) compared to the values obtained for orange needles found in the same crystallization experiment.

Compound	K / %at.	Ge / %at.	Si / %at.
$\text{K}(2.2.2\text{-crypt})[\text{Si}_{1.68(1)}\text{Ge}_{7.32(1)}(\text{hyp})_3]$ (red blocks)	4.7(2)	23.7(5)	71.6(5)
orange needles	5(1)	22(1)	73(1)

A combination of these EDX results and ESI-MS measurements (see Figure 3.35b) for $\text{K}[E_9(\text{hyp})_3]$ (E : Si, Ge) of re-dissolved orange needles indicates that though the molecular structure of the needles could not be determined, they represent the same composition as found for the red blocked crystals when formed from the same precursor. Therefore, an isolation of $\text{K}[E_9(\text{hyp})_3]$ *via* crystallization was successful for higher silicon contents as well (other precursors $\text{K}_{12}\text{Si}_{17-x}\text{Ge}_x$ with $x = 0, 9$). A comparison of Raman spectra of these two crystal types supports this assumption. The Raman spectrum of red blocked $\text{K}(2.2.2\text{-crypt})[\text{Si}_{1.68(1)}\text{Ge}_{7.32(1)}(\text{hyp})_3]$ features the same bands as orange needles with weak scattering of the same crystallization experiment (see Figure 5.22 in the appendix). Raman spectra were obtained for crystals (needles) of silylated clusters starting from various Si/Ge ratios in the precursor (from $\text{K}_{12}\text{Si}_{17-x}\text{Ge}_x$ with $x = 0, 9, 12$; see Figure 3.43) and feature characteristic Si-C and C-H vibrations in the TMS groups of the *hyp* ligands. These bands are in good accordance with values obtained for the *hyp*-Cl precursor (see Figure 3.43, grey line).

The bands obtained for *hyp*-Cl were assigned according to the literature (an earlier work by R. Wochele^[263]). Next to Si-C and C-H vibrations, several bands originating from the E_9 -cluster (*, bending or breathing vibrations) were detected. Theoretical values of $[\text{Si}_2\text{Ge}_7\{\text{Si}(\text{SiH}_3)_3\}_3]^-$ (for computational details see chapter 2.2.12) showed a wide variety of these vibrations originating from the cluster in the range of 100–300 cm^{-1} , thus preventing an assignment of distinct vibrations to the experimental values. However, similar strong bands were detected for the known compound $\text{K}(2.2.2\text{-crypt})[\text{Ge}_9(\text{hyp})_3]$ in the literature and were assigned to Ge-Ge cluster vibrations.^[133, 264] For example, the band at 119 cm^{-1} was assigned to a vibration of the vertices bearing silyl groups, resulting in a change of the prism heights in the cluster while the band at 161 cm^{-1} was assigned to a breathing mode of the cluster.^[264]

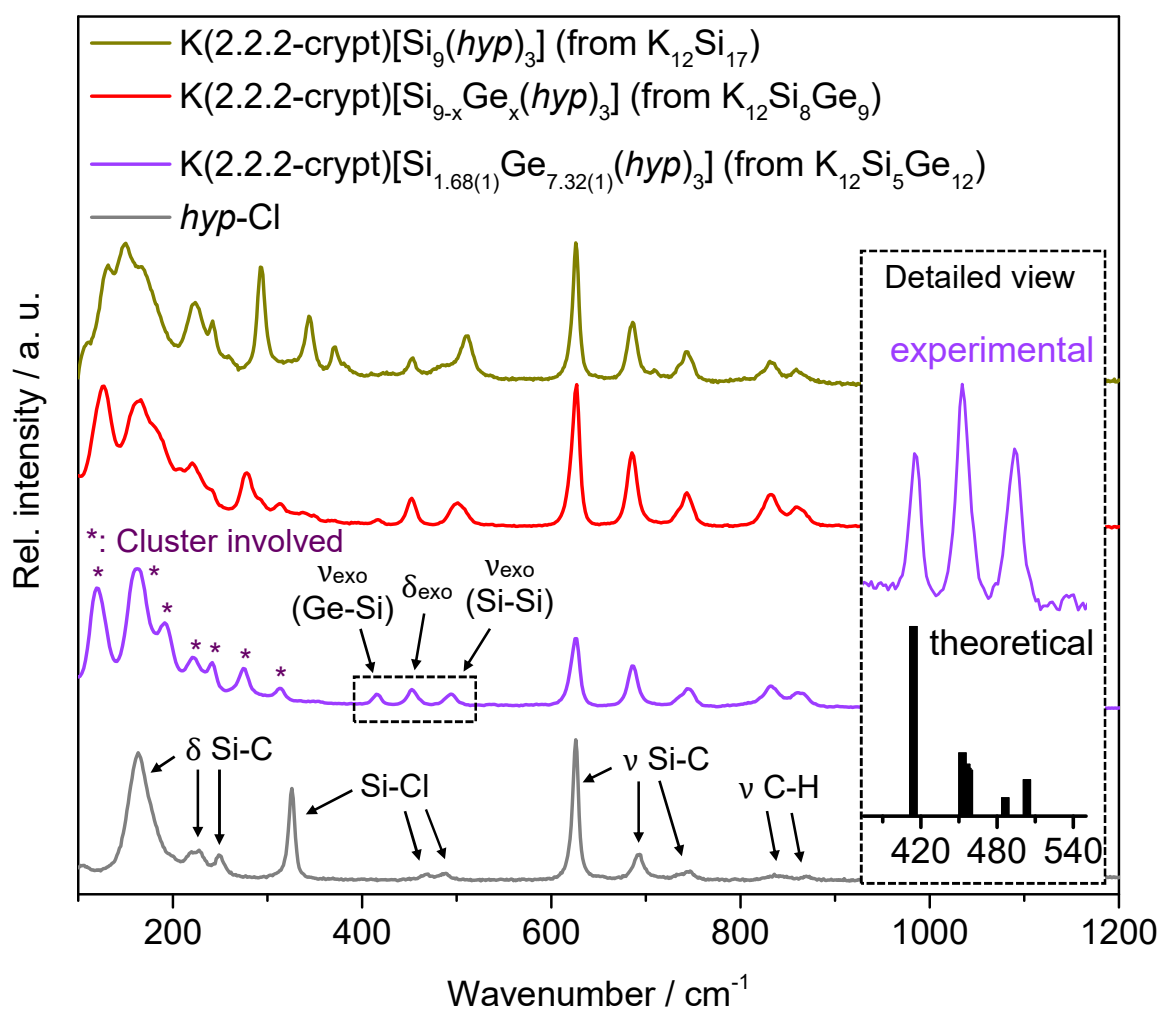


Figure 3.43. Raman spectra of various $\text{K}(2.2.2\text{-crypt})[E_9\{\text{Si}(\text{TMS})_3\}_3]$ (E : Si, Ge) compounds. ν : stretching vibration, δ : bending vibration, *: vibration in the E_9 -cluster (breathing, deformation; according to theoretical values of $[\text{Si}_2\text{Ge}_7\{\text{Si}(\text{SiH}_3)_3\}_3]^-$). Vibrations of cluster exo bonds to the silyl groups are compared to theoretical values of $[\text{Si}_2\text{Ge}_7\{\text{Si}(\text{SiH}_3)_3\}_3]^-$ (black bars; for computational details see chapter 2.2.12). Spectra were measured at $\lambda = 532$ nm.

3.5 Silylation of Mixed Nine Atomic Si/Ge Clusters

Additionally, three characteristic bands located at 415 cm^{-1} , 453 cm^{-1} and 494 cm^{-1} were detected for crystals of $\text{K}(2.2.2\text{-crypt})[\text{Si}_{1.68(1)}\text{Ge}_{7.32(1)}(\text{hyp})_3]$ (see Figure 3.43, purple line). By comparison to theoretical values of $[\text{Si}_2\text{Ge}_7\{\text{Si}(\text{SiH}_3)_3\}_3]^-$ (see Figure 3.43, black bars), these bands were found to represent bending (δ_{exo}) and stretching (ν_{exo}) vibrations of the cluster exo bonds towards the silyl groups. Theoretical values obtained for $[\text{Si}_2\text{Ge}_7\{\text{Si}(\text{SiH}_3)_3\}_3]^-$ show that the exo bond bending vibrations ($\delta_{\text{exo,theo}} = 453\text{--}457\text{ cm}^{-1}$) are mostly unaffected by the mixed occupation of silicon and germanium in the cluster (see Figure 3.44b). However, for the stretching vibration (ν_{exo}) this is not the case. The band located at 415 cm^{-1} represents a Ge-Si exo bond stretching vibration whereas the band at 494 cm^{-1} represents a Si-Si exo bond stretching vibration (Figure 3.44a and c). The experimental value of the Si-Si exo bond stretching vibration is found as a mean value of the two theoretical bands of $[\text{Si}_2\text{Ge}_7\{\text{Si}(\text{SiH}_3)_3\}_3]^-$ ($\nu_{\text{exo,theo}} = 486$ and 503 cm^{-1}). These assumptions derived from theoretical values are supported by the experimental data, as the Ge-Si exo bond stretching vibration (415 cm^{-1}) is reduced in intensity for higher Si content in the cluster and is missing for a cluster only containing silicon (see Figure 3.43). Meanwhile, the intensity of the Si-Si exo bond stretching vibration (494 cm^{-1}) increases alongside the silicon content in the cluster.

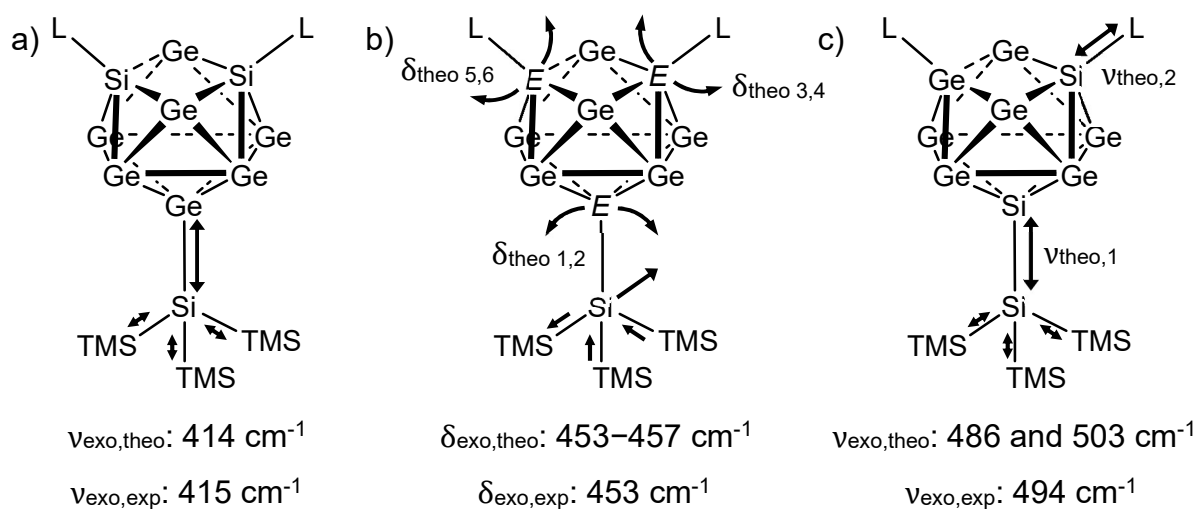


Figure 3.44. Experimental values for Ge-Si stretching (a), E-Si (E : Si, Ge) bending (b) and Si-Si stretching (c) vibration of the cluster exo bonds in $[\text{E}_9\{\text{Si}(\text{TMS})_3\}_3]^-$ (E : Si, Ge) compared to theoretical values for $[\text{Si}_2\text{Ge}_7\{\text{Si}(\text{SiH}_3)_3\}_3]^-$. L: $\text{Si}(\text{TMS})_3$. Theoretical values for E-Si (E : Si, Ge) exo bond bending vibrations consist of two distinct vibrations per bond, resulting in a total of six vibrations in the range of $453\text{--}457\text{ cm}^{-1}$. The experimental value for the Si-Si exo bond stretching vibrations is found as a mean value of the two distinct theoretical bands.

3.6 Conversion of Silylated Ge-Clusters with Coinage Metal NHC Compounds

Bare ZINTL-clusters are often stabilized by reaction with transition metal complexes. These reactions lead to substituted compounds (e. g. $[E_9ZnPh]^{3-}$ with $E = Si - Pb$ [265]), coinage metal bridged dimeric species like $[(\eta^4-Ge_9)Cu(\eta^1-Ge_9)]^{7-}$ [266], endohedrally filled clusters like $[Cu@E_9]^{3-}$ with $E = Sn, Pb$ [267] and even polymers like $Zn[(\eta^4:\eta^1-Ge_9)]^{2-}$ [268]. Recently, N-heterocyclic carbene ligands (NHCs) were introduced to ZINTL-cluster chemistry by reaction of coinage metal carbene compounds $NHC^{Dipp}MCl$ ($M = Cu, Ag, Au$) with bare or silylated ZINTL-clusters. As described in chapter 3.5, silylated ZINTL-clusters represent an interesting starting material for follow-up reactions due to their enhanced solubility in common laboratory solvents such as acetonitrile, THF or toluene. The reaction of coinage metal NHC compounds with tris-silylated clusters $[Ge_9R_3]^-$ ($R = Si(TMS)_3$ [269], $Si(tBu)_3$ [163]) obtained from silylation of K_4Ge_9 leads to formation of $NHC^{Dipp}M[\eta^3-Ge_9R_3]$ ($M = Cu, Ag, Au$). These uncharged complexes can be dissolved in common solvents such as THF or toluene and are stable at room temperature except for $NHC^{Dipp}Ag[\eta^3-Ge_9(Si(TMS)_3)_3]$. [269]

Within this work, reactivity of coinage metal NHC compounds towards silylated clusters obtained from silylation of the ZINTL-phase $K_{12}Ge_{17}$ (see Figure 3.45, Route A) and reactivity towards the bis-silylated cluster $[Ge_9\{Si(TMS)_3\}_2]^{2-}$ (see Figure 3.45, Route B) were investigated. [188] Just as for K_4Ge_9 [162], a heterogenous reaction of $K_{12}Ge_{17}$ with hypersilylchloride (*hyp*-Cl, 6 eq.) in acetonitrile leads to a deep red solution upon stirring over night at room temperature (for details on the synthesis also see chapter 2.3.12). Filtration and addition of a solution of $NHC^{Dipp}MCl$ ($M = Cu, Ag, Au$) in acetonitrile immediately leads to the formation of a brown precipitate which was isolated by filtering off the supernatant solution. The solid can be re-dissolved in toluene and filtered to remove KCl formed during the reaction. The solvent is removed *in vacuo* to yield a brown solid as the crude product. For crystallization, the solution was reduced to half its original volume and stored in a freezer at 233 K, yielding red plate-shaped crystals after 7 d. The possibility to also introduce other NHC ligands by this method was investigated by reaction of the bis-silylated cluster $[Ge_9\{Si(TMS)_3\}_2]^{2-}$ with $NHC^{Mes}CuCl$, bearing smaller mesityl substituents.

3.6 Conversion of Silylated Ge-Clusters with Coinage Metal NHC Compounds

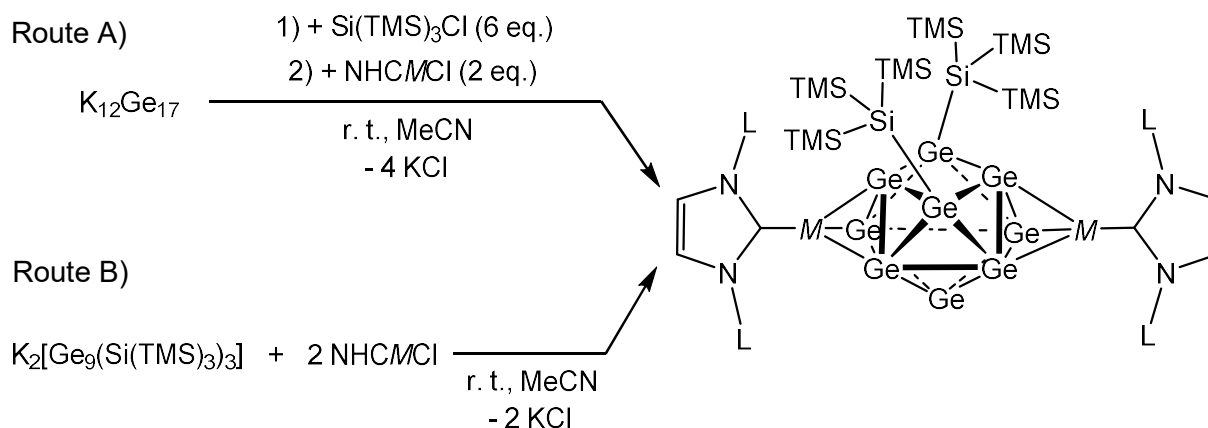


Figure 3.45. Synthesis of binuclear ZINTL-cluster coinage metal NHC compounds $[(NHCM)_2\{\eta^3, \eta^3-Ge_9(Si(TMS)_3)_2\}]$. Starting from ZINTL-phase $K_{12}Ge_{17}$ (Route A) or bis-silylated cluster $K_2[Ge_9(Si(TMS)_3)_2]$ (Route B). $M = Cu, Ag, Au$. $L = Dipp$ (diisopropylphenyl), Mes (mesityl). r. t.: room temperature.

The 1H -NMR spectra of the resulting compounds indicates the attachment of $[NHC^{Dipp}M]^+$ moieties to the Ge_9 -cluster by a significant shift for the doublets assigned to the methyl groups of the diisopropylphenyl groups of the NHC ligand (see Figure 3.46 for $M = Cu$; additionally Figure 5.33, Figure 5.36 and Figure 5.39 in the appendix show 1H NMR spectra for $M = Ag, Au$ and the mesityl ligand). This significant shift for the doublets of the methyl groups had already been observed for similar reaction products bearing only one NHC moiety $[Ge_9R_3]^-$ ($R = Si(TMS)_3, Si(tBu)_3$) and is therefore a suitable indicator for a successful attachment of $[NHC^{Dipp}M]^+$.^[163, 269] Next to a good solubility in non-polar solvents such as toluene, the 1:1 ratio of the signals assigned to the protons of the hypersilyl groups and those of the NHC^{Dipp} ligand indicates the presence of an uncharged species with the composition $[(NHC^{Dipp}M)_2\{\eta^3, \eta^3-Ge_9(Si(TMS)_3)_2\}]$. ^{13}C - and ^{29}Si -INEPT measurements support this assumption (see Figure 3.47 and Figure 3.48 for $M = Cu$; additionally Figure 5.34 – Figure 5.41 in the appendix show ^{13}C - and ^{29}Si -INEPT measurements for $M = Ag, Au$ and the mesityl ligand). A peak with a characteristic high field shift representing the silicon of the silyl group directly attached to the cluster (≈ -106 ppm) could be detected in ^{29}Si -INEPT NMR spectra for all three coinage metals as well as for a Cu-NHC compound with the mesityl ligand.

Results and Discussion

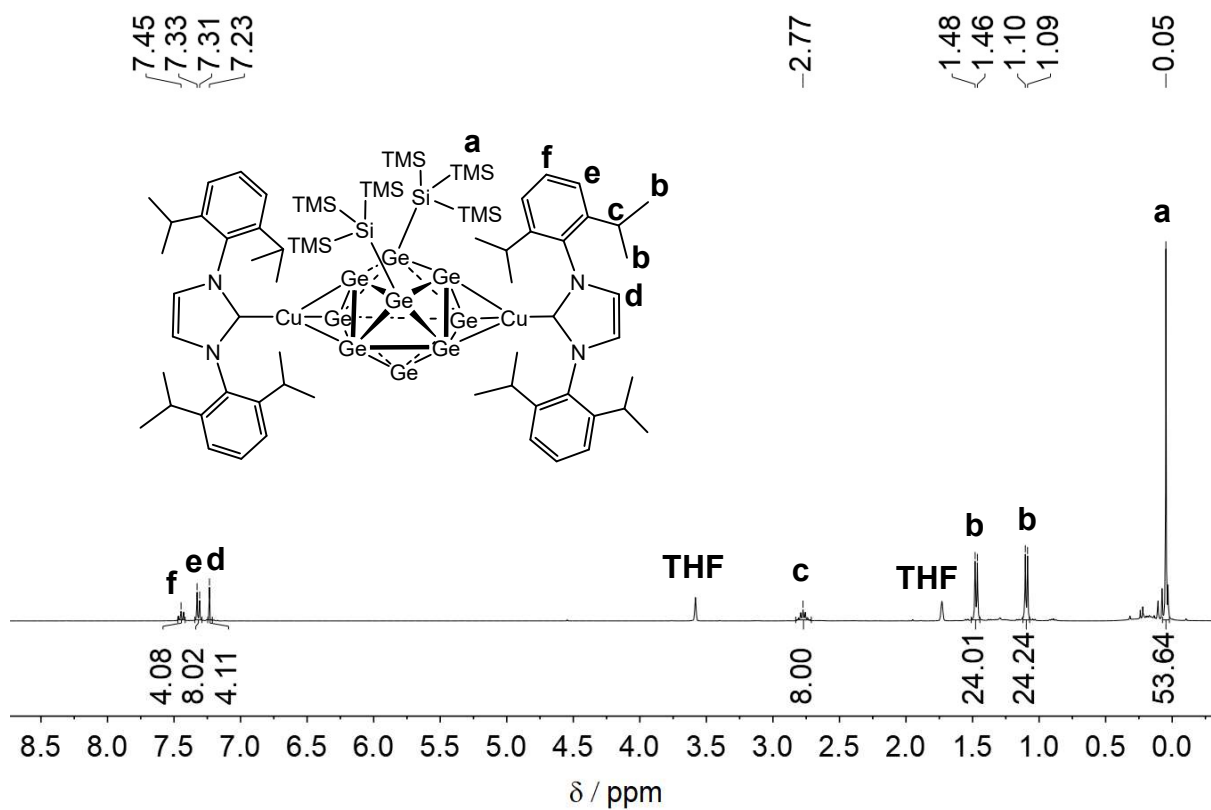


Figure 3.46. $^1\text{H-NMR}$ of $[(\text{NHC}^{\text{Dipp}}\text{Cu})_2\{\eta^3, \eta^3\text{-Ge}_9(\text{Si}(\text{TMS})_3)_2\}]$ in $\text{THF-}d_8$.

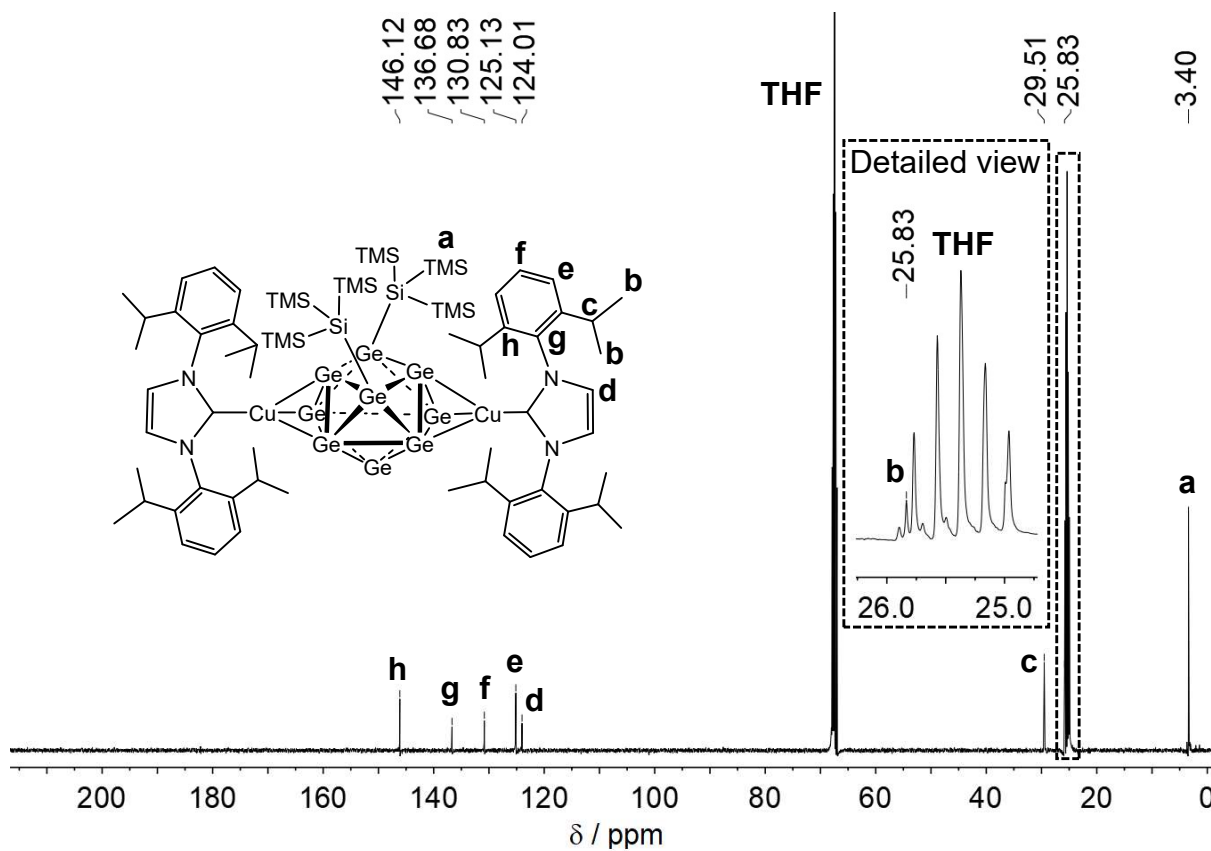


Figure 3.47. $^{13}\text{C-NMR}$ of $[(\text{NHC}^{\text{Dipp}}\text{Cu})_2\{\eta^3, \eta^3\text{-Ge}_9(\text{Si}(\text{TMS})_3)_2\}]$ in $\text{THF-}d_8$.

3.6 Conversion of Silylated Ge-Clusters with Coinage Metal NHC Compounds

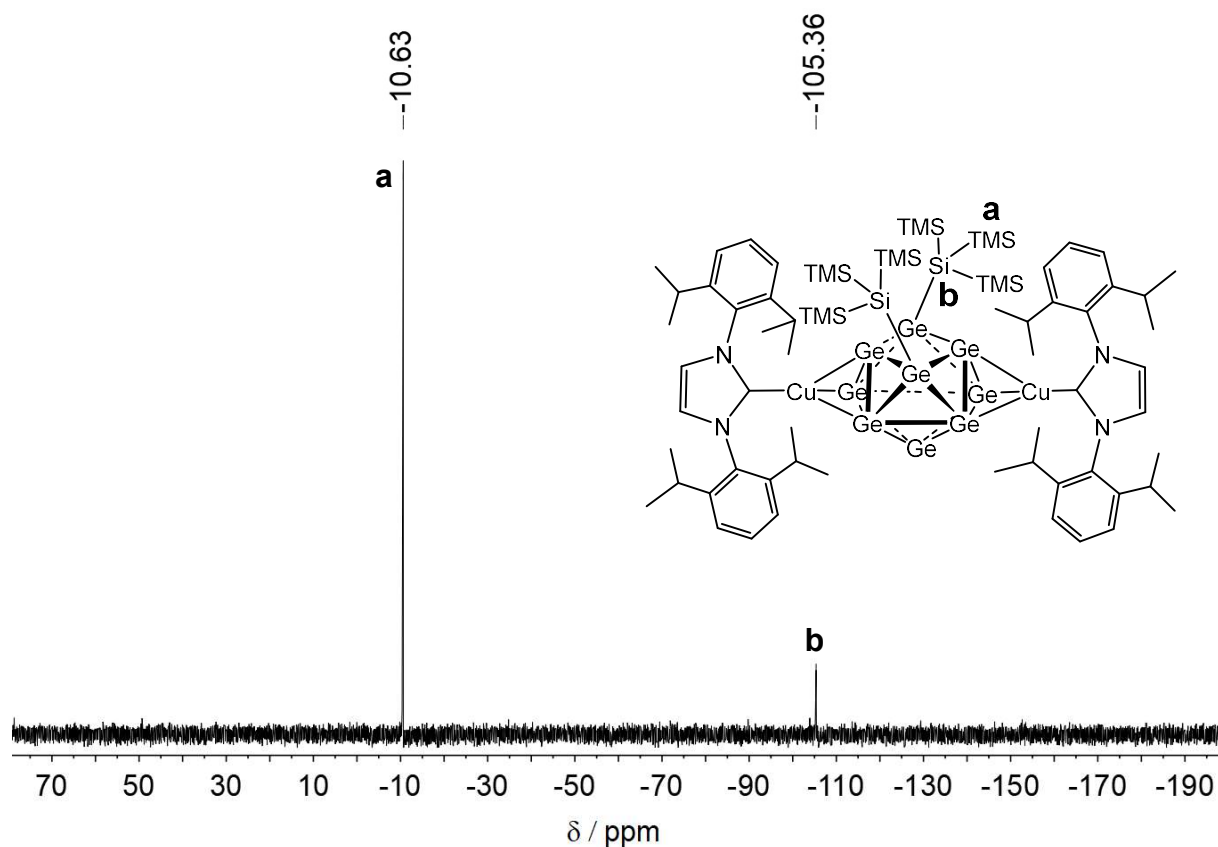


Figure 3.48. ^{29}Si -INEPT NMR of $[(\text{NHC}^{\text{Dipp}}\text{Cu})_2\{\eta^3, \eta^3\text{-Ge}_9(\text{Si}(\text{TMS})_3)_2\}]^-$ in $\text{THF-}d_8$.

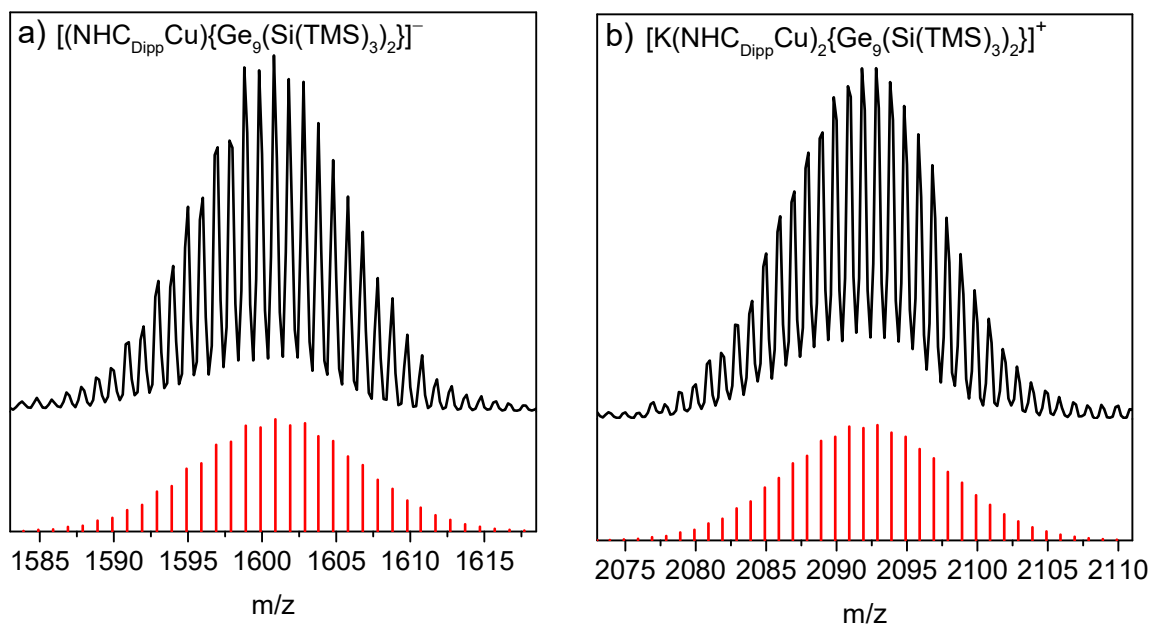


Figure 3.49. Selected high resolution areas of the ESI-MS spectrum of an acetonitrile solution of $[(\text{NHC}^{\text{Dipp}}\text{Cu})_2\{\eta^3, \eta^3\text{-Ge}_9(\text{Si}(\text{TMS})_3)_2\}]^-$. a) Monitoring $[(\text{NHC}^{\text{Dipp}}\text{Cu})_2\{\eta^3, \eta^3\text{-Ge}_9(\text{Si}(\text{TMS})_3)_2\}]^-$ at 1600.8 m/z in negative (-) ion mode with a $(\text{NHC}^{\text{Dipp}}\text{Cu})^+$ moiety cleaved, b) monitoring $[\text{K}(\text{NHC}^{\text{Dipp}}\text{Cu})_2\{\eta^3, \eta^3\text{-Ge}_9(\text{Si}(\text{TMS})_3)_2\}]^+$ at 2092.8 m/z in positive (+) ion mode with a K^+ moiety attached. Simulated mass spectra with their isotopic distribution are shown below as red bars.

Results and Discussion

ESI-MS measurements of the compounds in acetonitrile support the assumption of $[(\text{NHCM})_2\{\eta^3, \eta^3\text{-Ge}_9(\text{Si}(\text{TMS})_3)_2\}]$ being the prominent species in solution. Signals with characteristic isotope distribution were detected corresponding to $[(\text{NHCM})\{\eta^3, \eta^3\text{-Ge}_9(\text{Si}(\text{TMS})_3)_2\}]^-$ in the negative and $[\text{K}(\text{NHCM})_2\{\eta^3, \eta^3\text{-Ge}_9(\text{Si}(\text{TMS})_3)_2\}]^+$ in the positive ion mode (see Figure 3.49 for NHC^{Dipp} ligand with $M = \text{Cu}$; additionally Figure 5.20 and Figure 5.21 in the appendix show ESI-MS spectra for $M = \text{Ag}, \text{Au}$ and NHC^{Mes} ligand).

Single crystals suitable for X-ray diffraction structure determination were obtained from toluene at 233 K after 7 d. The structure was found to support the assumptions derived from the NMR and ESI-MS measurements and revealed $[(\text{NHC}^{\text{Dipp}}\text{Cu})_2\{\eta^3, \eta^3\text{-Ge}_9(\text{Si}(\text{TMS})_3)_2\}]$ as the first dinuclear ZINTL-cluster coinage metal NHC complex (see Figure 3.50). Crystallographic data of $[(\text{NHC}^{\text{Dipp}}\text{Cu})_2\{\eta^3, \eta^3\text{-Ge}_9(\text{Si}(\text{TMS})_3)_2\}]$ is listed in Table 3.13. The central $[\text{Ge}_9]$ unit in $[(\text{NHC}^{\text{Dipp}}\text{Cu})_2\{\eta^3, \eta^3\text{-Ge}_9(\text{Si}(\text{TMS})_3)_2\}]$ adopts a distorted C_{2v} -shaped mono-capped square antiprism, in which the two opposite Ge atoms (Ge6 and Ge8) of the open square (Ge6-Ge7-Ge8-Ge9) carry silyl groups (see Figure 3.50a).

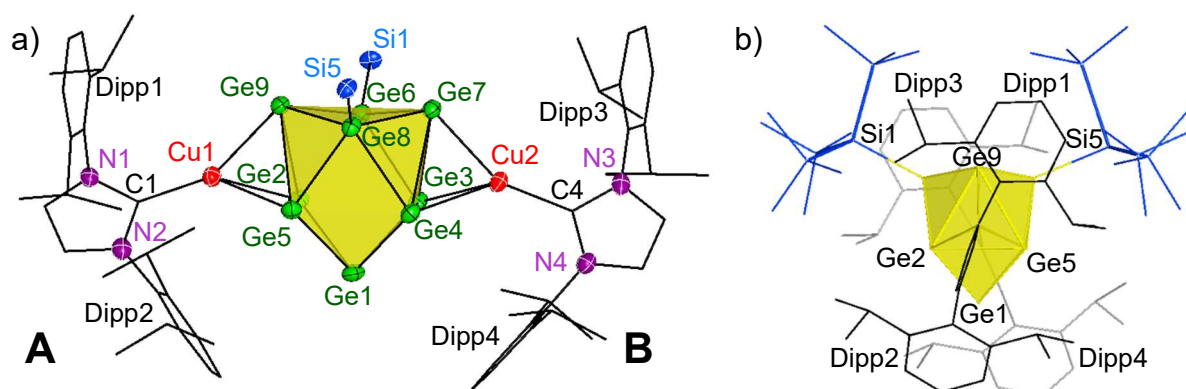


Figure 3.50. Molecular structure of $[(\text{NHC}^{\text{Dipp}}\text{Cu})_2\{\eta^3, \eta^3\text{-Ge}_9(\text{Si}(\text{TMS})_3)_2\}]$. a) Front view of $[(\text{NHC}^{\text{Dipp}}\text{Cu})_2\{\eta^3, \eta^3\text{-Ge}_9(\text{Si}(\text{TMS})_3)_2\}]$ revealing C_{2v} symmetry of the central $[\text{Ge}_9]$ unit. For clarity reasons, hydrogen atoms, co-crystallized toluene molecules and the TMS groups are omitted. Displacement ellipsoids are depicted at 50% probability level. The two $[\text{NHC}^{\text{Dipp}}\text{Cu}]^+$ moieties are labelled as **A** and **B**. b) Side view along the Cu1-Cu2 axis showing the staggered orientation of the two NHC^{Dipp} moieties and the silyl groups towards each other. For clarity reasons, all ligands are depicted as wire frames, the NHC^{Dipp} ligand in the background is depicted in grey and the silyl groups are depicted in blue. Selected bond lengths are listed in Table 3.15 as well as Table 5.13 in the appendix.

3.6 Conversion of Silylated Ge-Clusters with Coinage Metal NHC Compounds

Table 3.13. Crystallographic data of $[(\text{NHC}^{\text{Dipp}}\text{Cu})_2\{\eta^3, \eta^3\text{-Ge}_9(\text{Si}(\text{TMS})_3)_2\}]$.

	$[(\text{NHC}^{\text{Dipp}}\text{Cu})_2\{\eta^3, \eta^3\text{-Ge}_9(\text{Si}(\text{TMS})_3)_2\}]$
composition	$\text{C}_{72}\text{H}_{128}\text{Ge}_9\text{Cu}_2\text{N}_4\text{Si}_8 \cdot 4 \text{ Tol}$
crystal system	triclinic
space group (no.)	$P\bar{1}$ (2)
$a / \text{\AA}$	15.102(2)
$b / \text{\AA}$	16.831(3)
$c / \text{\AA}$	25.659(5)
$\alpha / ^\circ$	108.951(9)
$\beta / ^\circ$	101.847(8)
$\gamma / ^\circ$	90.837(8)
$V / \text{\AA}^3$	6013.8(2)
Z	2
T / K	100(2)
$\lambda / \text{\AA}$	0.71073 (Mo- K_α)
$\delta_{\text{calc.}} / \text{g cm}^{-3}$	1.338
μ / mm^{-1}	2.680
collected reflections	90837
independent reflections	21064
R_{int}	0.0914
$R_1 [I > 2\sigma(I)]$ (all data)	0.0468 (0.0985)
$wR_2 [I > 2\sigma(I)]$ (all data)	0.0953 (0.1126)
parameters/restraints	1273/366
goodness of fit (F^2)	0.998
max. and min. difference el. density / e \AA^{-3}	0.83 and -0.65

The deviation from C_{4v} -symmetry is expressed by the ratio of the diagonal lengths of the open square of best mono-capped square antiprism $d_2(\text{Ge7-Ge9})/d_1(\text{Ge6-Ge8}) = 3.6969/3.3325 = 1.11$ (with $d_2/d_1 = 1$ for a perfect C_{4v} -symmetry). The deviation from a D_{3h} -symmetric tri-capped trigonal prism is expressed by one height of the trigonal prism being significantly elongated while the other heights are shortened in comparison to literature known compounds bearing three silyl groups and only one coinage metal NHC ligand (see Table 3.14; $h_3/h_1 = 1.27$ in $[(\text{NHC}^{\text{Dipp}}\text{Cu})_2\{\eta^3, \eta^3\text{-Ge}_9(\text{Si}(\text{TMS})_3)_2\}]$ with h_2/h_1 and $h_3/h_1 = 1$ for perfect D_{3h} symmetry).

Results and Discussion

Table 3.14. Comparison of the ZINTL cluster shape in $[(\text{NHC}^{\text{Dipp}}\text{Cu})_2\{\eta^3, \eta^3\text{-Ge}_9(\text{Si}(\text{TMS})_3)_2\}]$ with literature known compounds $[(\text{NHC}^{\text{Dipp}}\text{Cu})\{\eta^3\text{-Ge}_9(\text{Si}(\text{R})_3)_3\}]$ (R = TMS ^[269], ^{*i*}Bu ^[163]). *h*: Heights of the trigonal prism.

Distances	$[(\text{NHC}^{\text{Dipp}}\text{Cu})_2\{\eta^3, \eta^3\text{-Ge}_9(\text{Si}(\text{TMS})_3)_2\}]$	$[(\text{NHC}^{\text{Dipp}}\text{Cu})\{\eta^3\text{-Ge}_9(\text{Si}(\text{TMS})_3)_3\}]$ ^[269]	$[(\text{NHC}^{\text{Dipp}}\text{Cu})\{\eta^3\text{-Ge}_9(\text{Si}(\text{iBu})_3)_3\}]$ ^[163]
$h_1 / \text{Å}$	2.900(1)	3.3029(8)	3.1947(1)
$h_2 / \text{Å}$	2.9054(9)	3.3253(8)	3.3918(1)
$h_3 / \text{Å}$	3.6969(9)	3.4028(8)	3.4235(1)
h_2/h_1	1.00	1.01	1.06
h_3/h_1	1.27	1.03	1.08

The two $[\text{NHC}^{\text{Dipp}}\text{Cu}]^+$ moieties coordinate in a η^3 -fashion to two opposed trigonal faces of the central $[\text{Ge}_9]$ unit and only include germanium atoms which do not bind to a silyl group (see Figure 3.50). Therefore, the coordination mode of the $[\text{NHC}^{\text{Dipp}}\text{Cu}]^+$ moieties with the bis-silylated $[\text{Ge}_9]$ cluster in $[(\text{NHC}^{\text{Dipp}}\text{Cu})_2\{\eta^3, \eta^3\text{-Ge}_9(\text{Si}(\text{TMS})_3)_2\}]$ is similar to that of previously reported ZINTL-cluster coinage metal NHC compounds of tris-silylated $[\text{Ge}_9]$ clusters.^[163, 269] The mean Cu-Ge distances $d_{\text{mean}}(\text{Cu-Ge})$ in $[(\text{NHC}^{\text{Dipp}}\text{Cu})_2\{\eta^3, \eta^3\text{-Ge}_9(\text{Si}(\text{TMS})_3)_2\}]$ and Cu- $\text{C}_{\text{Carbene}}$ distances are in good agreement with values found for $[(\text{NHC}^{\text{Dipp}}\text{Cu})\{\eta^3\text{-Ge}_9(\text{Si}(\text{R})_3)_3\}]$ (R = TMS ^[269], ^{*i*}Bu ^[163]). However, the coordination of Cu by the NHC ligand and the $[\text{Ge}_9]$ cluster deviates more from linearity (see Table 3.15). Furthermore, the two $[\text{NHC}^{\text{Dipp}}\text{Cu}]^+$ moieties are oriented in a staggered fashion towards each other and the silyl groups (see Figure 3.50b). This can be explained by interactions between the silyl groups and the Dipp groups of the NHC ligands.

3.6 Conversion of Silylated Ge-Clusters with Coinage Metal NHC Compounds

Table 3.15. Selected distances and angles in $[(\text{NHC}^{\text{Dipp}}\text{Cu})_2\{\eta^3, \eta^3\text{-Ge}_9(\text{Si}(\text{TMS})_3)_2\}]$. The two $[\text{NHC}^{\text{Dipp}}\text{Cu}]^+$ moieties labelled **A** and **B** are depicted in Figure 3.50a. The copper-germanium distances $d(\text{Cu-Ge})$ are defined as **A**: $d_1(\text{Cu1-Ge2})$, $d_2(\text{Cu1-Ge5})$, $d_3(\text{Cu1-Ge9})$ and **B**: $d_1(\text{Cu2-Ge3})$, $d_2(\text{Cu2-Ge4})$, $d_3(\text{Cu2-Ge7})$. $d_{\text{mean}}(\text{Cu-Ge})$: average Cu-Ge distance, ctf: center of the coordinating atoms of the triangular faces of the $[\text{Ge}_9]$ cluster.

Distances / Å	A	B
$d_1(\text{Cu-Ge})$	2.601(1)	2.532(1)
$d_2(\text{Cu-Ge})$	2.532(1)	2.582(1)
$d_3(\text{Cu-Ge})$	2.405(1)	2.413(1)
$d_{\text{mean}}(\text{Cu-Ge})$	2.513(1)	2.509(1)
$d(\text{Cu-C}_{\text{Carbene}})$	1.941(5)	1.913(5)
Angle / °		
ctf-Cu-C _{Carbene}	162.88(2)	163.92(2)

An investigation of the deep red solution obtained by silylation of $\text{K}_{12}\text{Ge}_{17}$ with *hyp*-Cl (6 eq.) *via* NMR revealed that the bis-silylated cluster $[\text{Ge}_9\{\text{Si}(\text{TMS})_3\}_2]^{2-}$ is formed as the main product, despite the excess of *hyp*-Cl used. For K_4Ge_9 as a precursor, this reaction would exclusively yield the tris-silylated cluster $[\text{Ge}_9\{\text{Si}(\text{TMS})_3\}_3]^-$. This leads to the assumption that the $[\text{Ge}_4]^{4-}$ clusters of $\text{K}_{12}\text{Ge}_{17}$ also partially react with *hyp*-Cl, forming by-products which can be detected in ^1H and ^{29}Si -INEPT NMR measurements (see Figure 5.42 and Figure 5.43 in the appendix). However, using the bis-silylated cluster $[\text{Ge}_9\{\text{Si}(\text{TMS})_3\}_2]^{2-}$ as a precursor yields analytically pure $[(\text{NHC}^{\text{L}}\text{M})_2\{\eta^3\text{-Ge}_9(\text{Si}(\text{TMS})_3)_2\}]$ (L: Dipp, Mes; M: Cu, Ag, Au).

4 Summary and Conclusion

In times of climate change, the need for renewable energy applications for generation (solar cells) and storage (batteries) of energy is increasing. However, the application of common silicon solar cells is mostly limited to larger stationary devices due to their inflexibility. A new generation of solar flexible solar cells trying to overcome this limitation is currently emerging. Porous nanostructured semiconducting materials of Group 14 elements can play an important role in these devices due to their high surface area and tunable electronic properties. However, in contrast to approaches which yield nanoparticles or nanowires of inorganic semiconductors, routes to periodic porous materials are scarce. Intermetallic compounds with the composition A_4E_9 ($A = \text{K-Cs}$; $E = \text{Ge-Pb}$) and $A_{12}E_{17}$ ($A = \text{Na-Cs}$; $E = \text{Si-Pb}$) contain well-defined ZINTL clusters and are easily accessible at macroscopic yield *via* a one-step solid state synthesis from the elements. Therefore, they represent interesting precursors for the solution-based fabrication of such porous nanostructured materials.

Within this work, such a solution-based process was used for the fabrication Ge thin films obtained from K_4Ge_9 in solution (see Figure 4.2a). Carrier mobilities obtained for inverse opal structured thin films with different sizes in the inverse opal structure were similar to values obtained for unstructured films using K_4Ge_9 as the precursor. An inverse opal morphology thereby does not inhibit carrier mobilities in these materials. Carrier mobilities of $\mu_m \approx 200 \frac{\text{cm}^2}{\text{V}\cdot\text{s}}$ obtained for these Ge thin films are in the range of values obtained for polycrystalline Ge films synthesized at high temperatures. Therefore, Ge thin films synthesized through a solution-based approach are promising candidates for porous materials in applications like solar cells.

Furthermore, macroporous Si (see Figure 4.1a) as well as mixed Si/Ge (see Figure 4.1b and c) thin films could be obtained through a solution-based process starting from $\text{K}_{12}\text{Si}_{17-x}\text{Ge}_x$ -phases ($x = 0, 5, 9, 12$) as precursors. XPS investigations on these films revealed that in case of the mixed Si/Ge thin films, the Ge content in the films is mostly present as Ge(0). Whereas, silicon is only detected as Si(+IV) in Si as well as mixed Si/Ge thin films due to reaction with the solvent (*en*). However, carrier mobilities obtained inverse opal structured mixed Si/Ge and pure Si thin films $\mu_m \approx 20\text{-}30 \frac{\text{cm}^2}{\text{V}\cdot\text{s}}$ were well within the range of values obtained for polycrystalline silicon structures.

Therefore, inverse opal structured thin films with a high silicon content are promising candidates for porous materials in applications like solar cells as well.

Investigations were carried out to transfer the synthetic procedure to other elements such as Sn and Bi. Despite the absence of discrete mixed Sn/Bi clusters in well-defined precursors, the solubility of K_2SnBi containing Sn-Bi zig-zag chains was investigated. Using $SiCl_4$ as a linker led to the formation of porous Sn/Bi thin films with a high surface area (see Figure 4.2b), while thin films obtained using $SnCl_4$ as the linker showed no porous structure. Ordered, inverse opal structured thin films could not be obtained for K_2SnBi as a solid precursor, indicating that well-defined clusters are necessary to achieve an inverse opal structured morphology. Porous Sn/Bi thin films with a high surface area expand the range of materials accessible through a simple wet-chemical process and could therefore be of interest for applications like Li-ion batteries.

In order to expand the limited solubility of bare $[Si_{9-x}Ge_x]^{4-}$ clusters in $K_{12}Si_{17-x}Ge_x$ precursors, ligands were attached to the bare clusters, effectively reducing their charge and polarity. Reactions with chloro-tris(trimethylsilyl)silane (*hyp*-Cl) led to the formation of crystals of silylated $[E_9(hyp)_3]^-$ clusters ($E = Si, Ge$; see Figure 4.1d for $K(2.2.2\text{-crypt})[Si_{1.68(1)}Ge_{7.32(1)}(hyp)_3]$) with tunable Si/Ge ratio and therefore potential tunable electronic properties of thin films. ESI-MS measurements of $[E_9(hyp)_3]^-$ clusters in reaction solutions as well as isolated and dissolved crystals reveal a statistical distribution of different Si/Ge ratios in the clusters (see Figure 4.1e). A combination of Raman spectroscopic measurements with theoretical calculations revealed that Si-Si exo bonds are favored in these compounds, resulting in a Si favored occupation of cluster vertices containing exo bonds. Introduction of coinage metal NHC compounds to bis-silylated Ge_9 clusters led to the formation of a series of uncharged $[(NHCM)_2\{\eta^3\text{-}Ge_9(Si(TMS)_3)_2\}]$ clusters ($M = Cu, Ag, Au$), further expanding the solubility range. The two $[NHC^{Dipp}Cu]^+$ moieties thereby coordinate in a η^3 -fashion to two opposed trigonal faces of the central $[Ge_9]$ unit and only include germanium atoms which do not bind to a silyl group (see Figure 4.1f). By replacing PMMA as a template (e. g. through block copolymers or polystyrene), silylated clusters could be implemented into the solution-based fabrication of thin films of semiconducting materials and could therefore enable new applications (e. g. in solar cells).

Summary and Conclusion

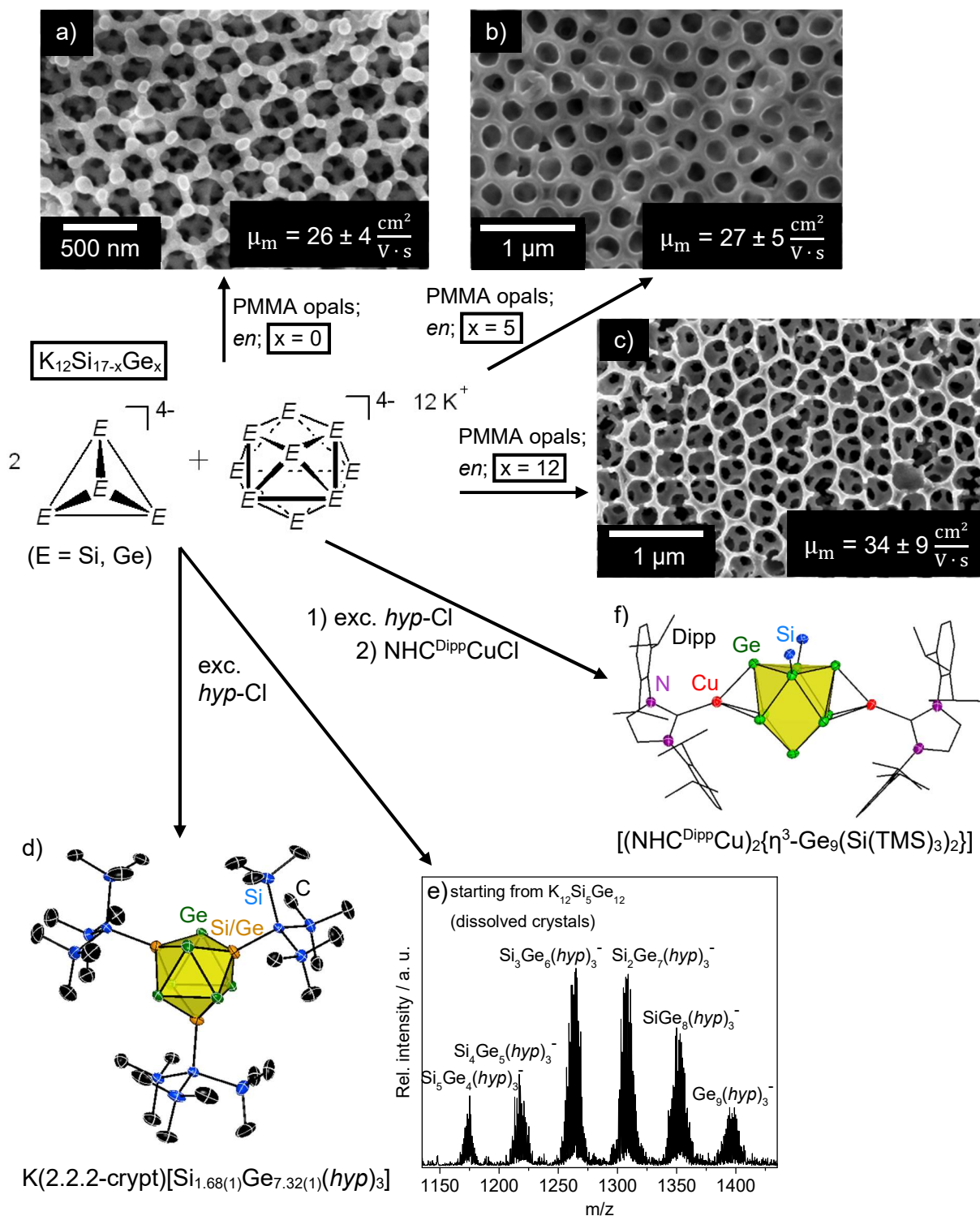


Figure 4.1. Schematic display of the formation of inverse opal structured thin films and functionalized clusters obtained from reaction of bare $\text{K}_{12}\text{Si}_{17-x}\text{Ge}_x$ -phases ($x = 0, 5, 9, 12, 17$) within this work. *hyp*: tris(trimethylsilyl)silane.

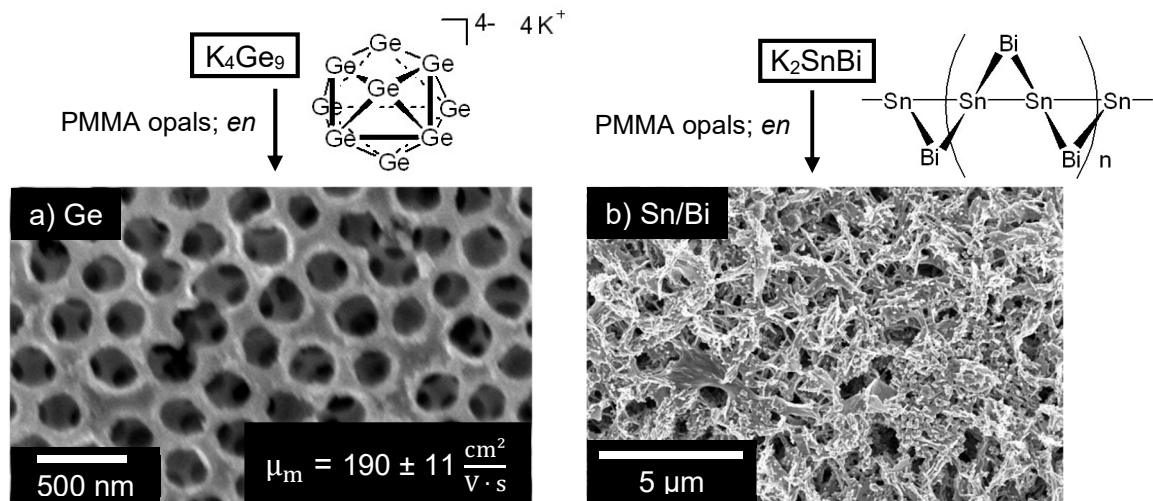


Figure 4.2. Schematic display of porous thin films obtained by a wet-chemical process involving K_4Ge_9/en (a) and K_2SnBi/en (b) solutions.

Conclusively, the developed wet-chemical process involving ZINTL clusters in solution allows for an easily accessible production of inverse opal structured thin films. Thin films of Si, Ge as well as Si/Ge mixtures show high carrier mobilities and therefore possible application in solar cells. Additionally obtained, highly porous Sn/Bi films should be investigated further for their potential applications. Silylated clusters with a reduced charge show a broad solubility and good stability in solution and could therefore be implemented in a solution-based fabrication of thin films as well.

5 Appendix

5.1 Powder Diffraction Patterns and Raman Spectra of Precursor Compounds

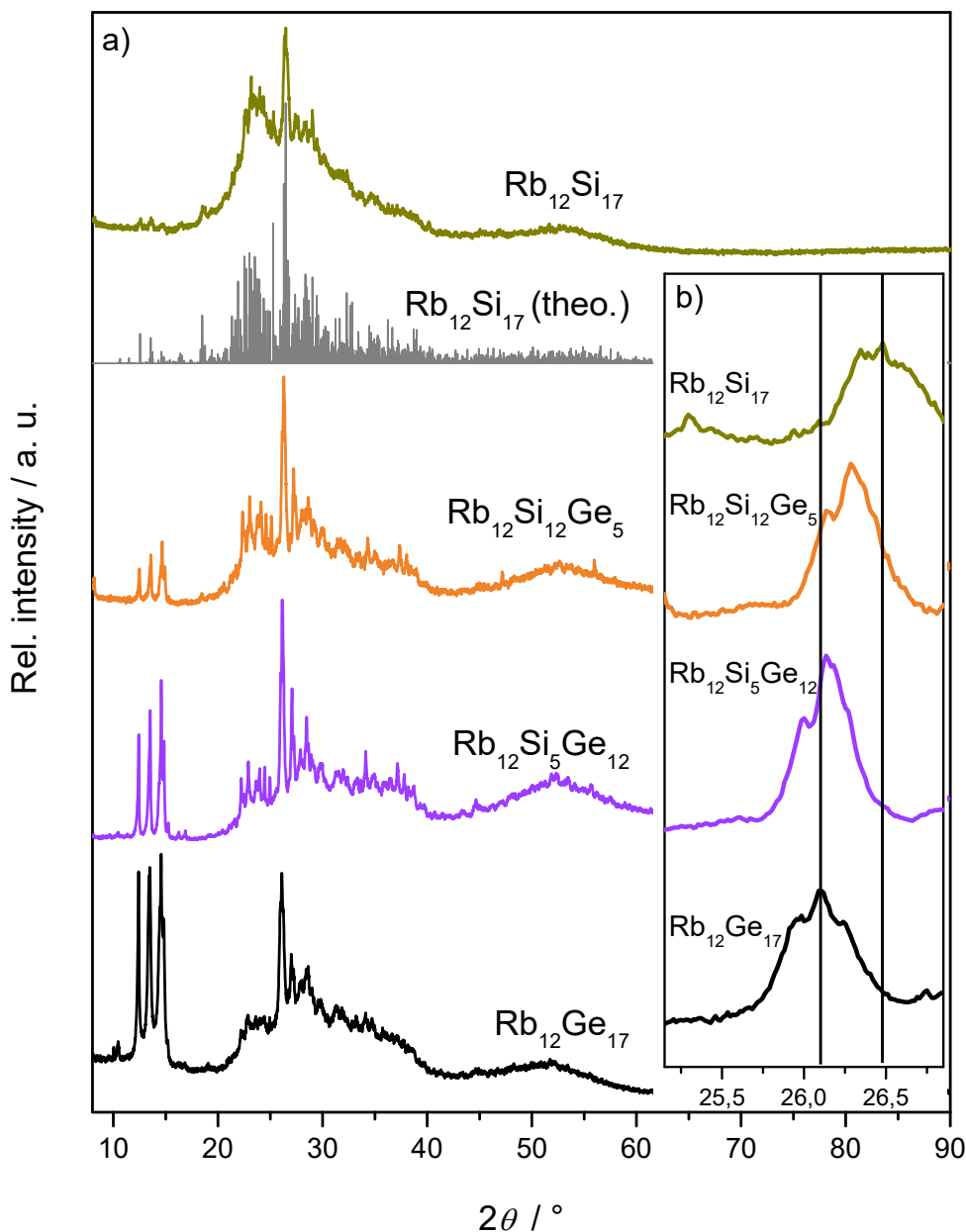


Figure 5.1. a) Powder diffraction patterns of $\text{Rb}_{12}\text{Si}_{17-x}\text{Ge}_x$ ($x = 0, 5, 9, 12, 17$) compounds. b) highlighted area of the compounds featuring a shift for the main reflex. Powder diffraction patterns were obtained using $\text{Cu-K}\alpha_1$ radiation, $\lambda = 1.54056 \text{ \AA}$. No common side products like unreacted silicon and germanium or phases containing only tetrahedral clusters ($\text{Rb}_4\text{Si}_{4-x}\text{Ge}_x$) are detected. For all diffraction patterns obtained from rubidium phases the intensity of single reflexes is quite low. However, the strongest reflexes of $\text{Rb}_{12}\text{Si}_{17}$ are in good accordance with a theoretical powder diffraction pattern obtained from crystal data available in literature^[233], indicating that the precursor materials are phase pure.

5.1 Powder Diffraction Patterns and Raman Spectra of Precursor Compounds

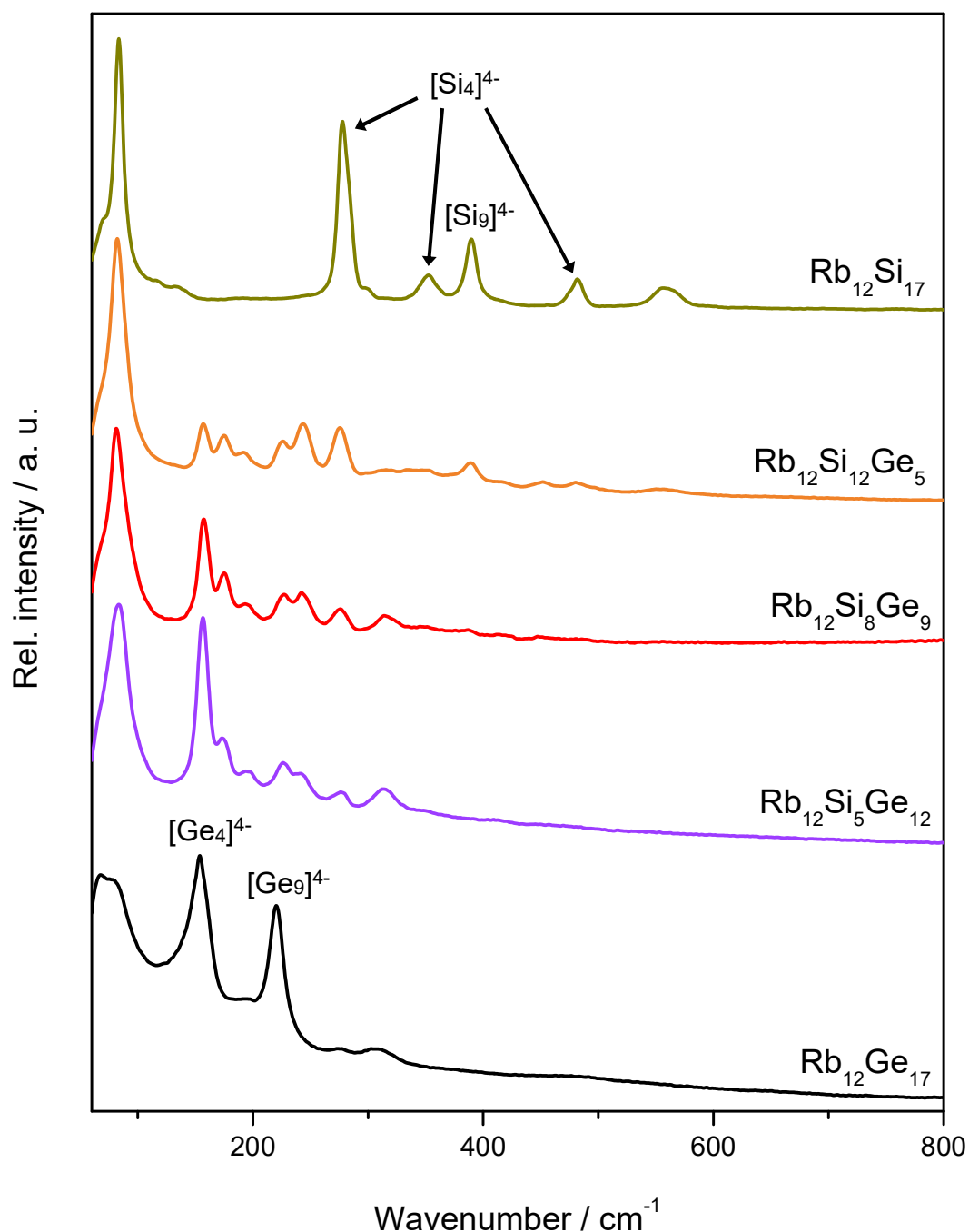


Figure 5.2. Recorded Raman spectra of $\text{Rb}_{12}\text{Si}_{17-x}\text{Ge}_x$ ($x = 0, 5, 9, 12, 17$) compounds. The location of the bands found in $\text{Rb}_{12}\text{Si}_{17}$ resemble those found for $[\text{Si}_4]^{4-}$ and $[\text{Si}_9]^{4-}$ in the literature.^[132, 142, 234] $[\text{Si}_4]^{4-}$ (lit., $\text{Rb}_6\text{K}_6\text{Si}_{17}$): 282.6, 355.9 and 479.3 cm^{-1} ; (exp.): 278, 352 and 481 cm^{-1} ; $[\text{Si}_9]^{4-}$ (lit., $\text{Rb}_6\text{K}_6\text{Si}_{17}$): 391.6 cm^{-1} ; (exp.): 390 cm^{-1} . The location of the bands found in $\text{Rb}_{12}\text{Ge}_{17}$ also resemble the main bands found in the literature.^[133] $[\text{Ge}_4]^{4-}$ (lit.): 156 cm^{-1} ; (exp.): 154 cm^{-1} ; $[\text{Ge}_9]^{4-}$ (lit.): 224 cm^{-1} ; (exp.): 221 cm^{-1} . Spectra were measured at $\lambda = 532 \text{ nm}$.

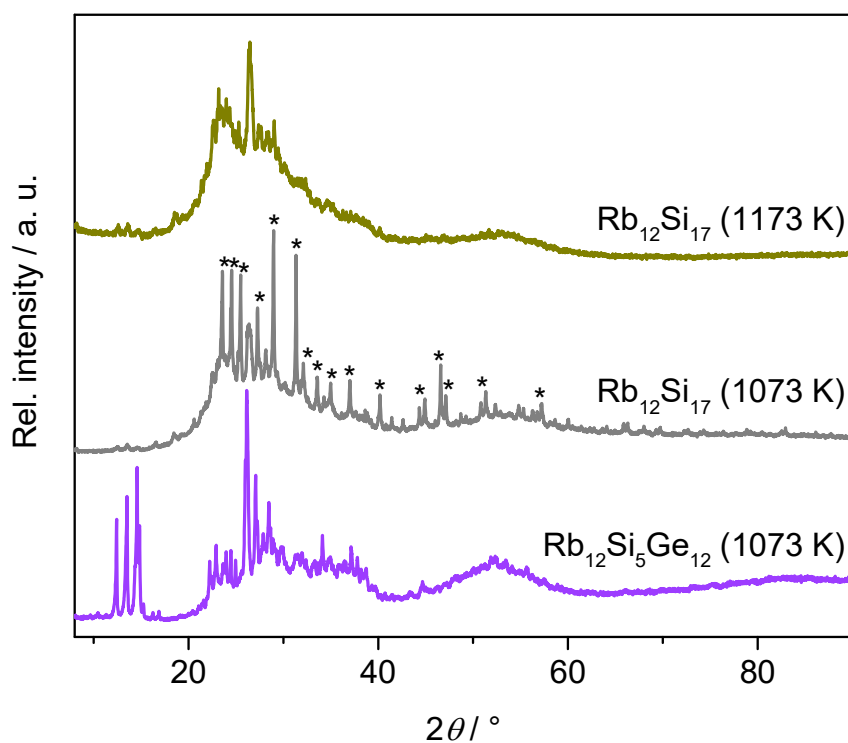


Figure 5.3. Powder diffraction patterns of $\text{Rb}_{12}\text{Si}_{17-x}\text{Ge}_x$ ($x = 0, 12$) compounds at different temperatures. Diffraction patterns were obtained using $\text{Cu-K}\alpha_1$ radiation, $\lambda = 1.54056 \text{ \AA}$. The peak temperature during the synthesis is important. While the reaction yields no side product at 1073 K for $\text{Rb}_{12}\text{Si}_5\text{Ge}_{12}$, the same conditions lead to the formation of a side phase (*) in case of $\text{Rb}_{12}\text{Si}_{17}$. To avoid the formation of the side phase, a higher temperature of 1173 K is necessary.

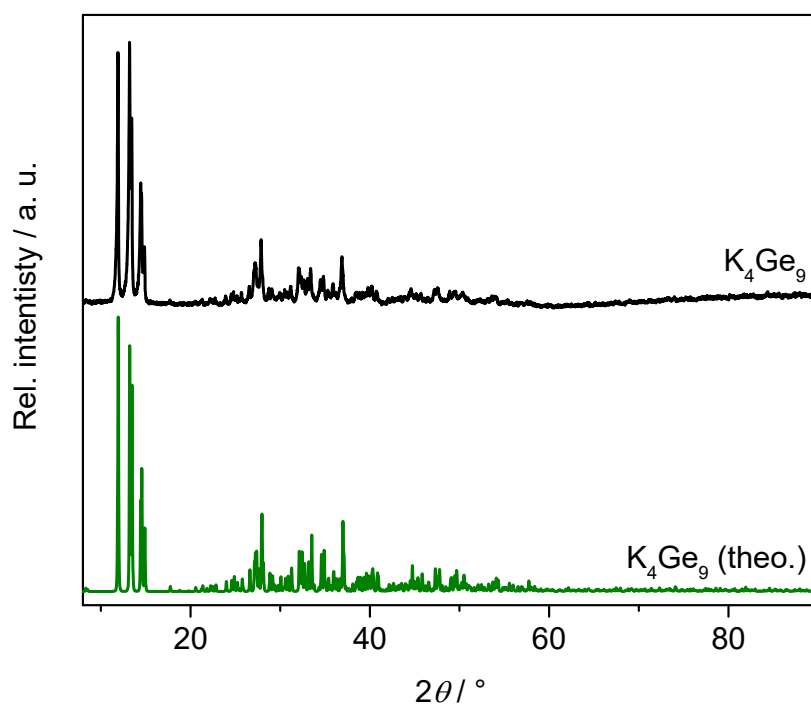


Figure 5.4. Powder diffraction pattern of K_4Ge_9 . The experimental diffraction pattern obtained is in good accordance with a theoretical diffraction pattern obtained from crystal data available in literature,^[270] indicating a phase pure material.

5.1 Powder Diffraction Patterns and Raman Spectra of Precursor Compounds

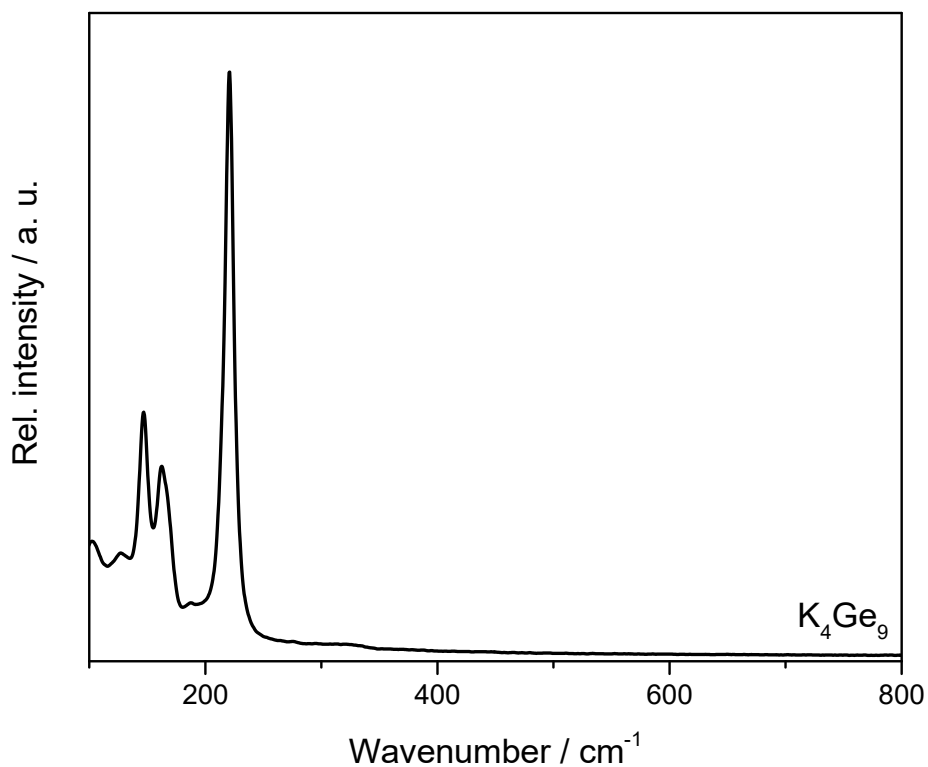


Figure 5.5. Recorded Raman spectrum of K_4Ge_9 . Spectrum was measured at $\lambda = 532$ nm.

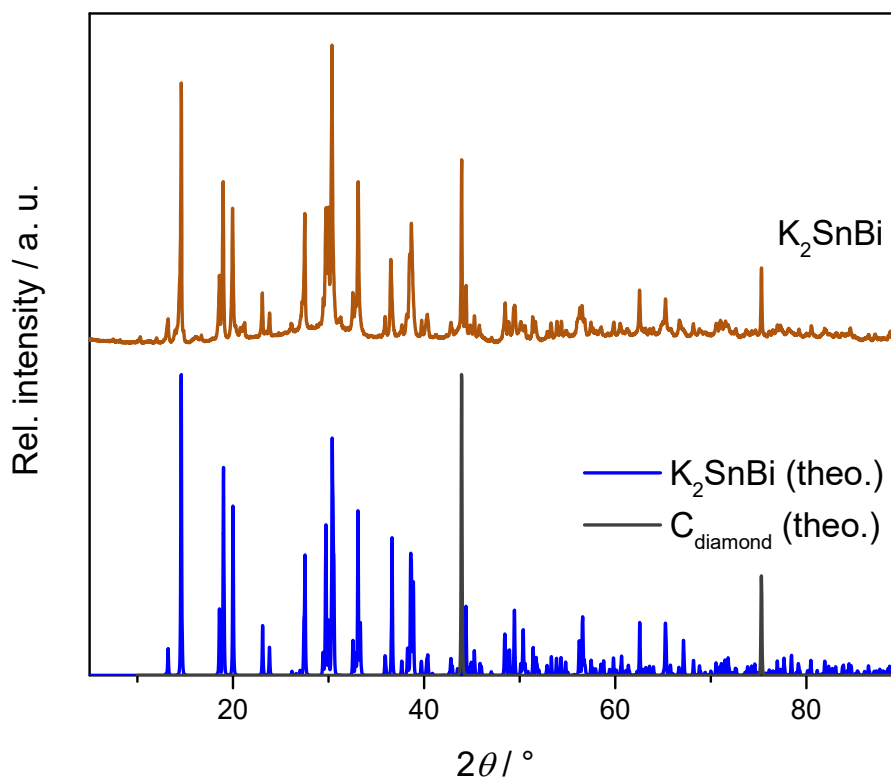


Figure 5.6. Powder diffraction pattern of K_2SnBi . The experimental diffraction pattern is in good accordance with a theoretical diffraction pattern obtained from crystal data available in literature,^[216] indicating a phase pure material. Diamond powder was used to compensate for the strong absorption of the material (Sn, Bi).

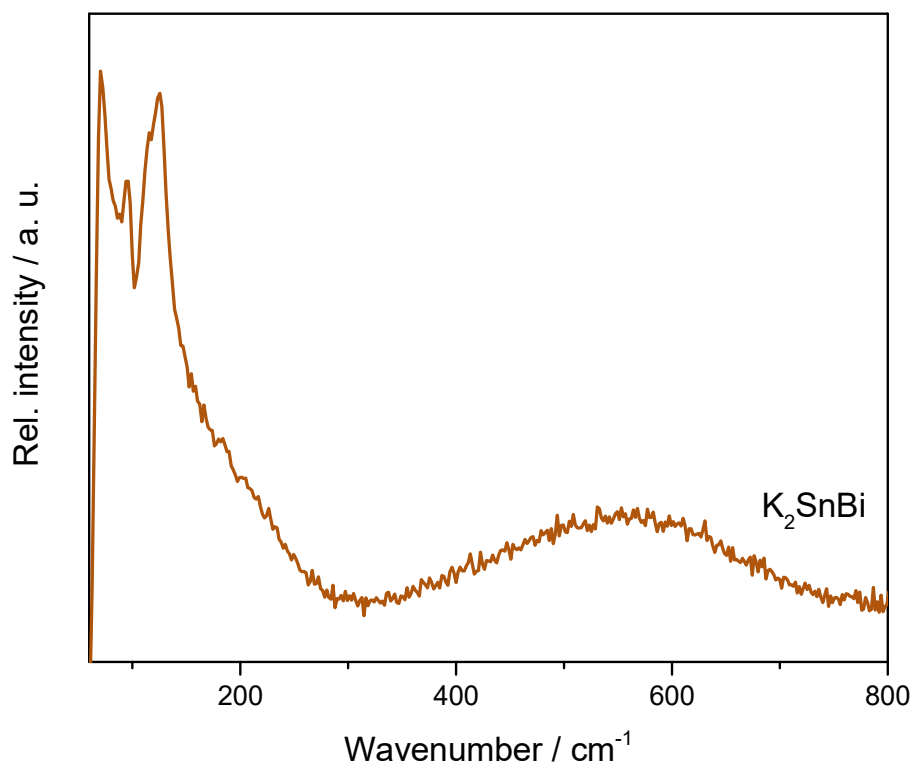


Figure 5.7. Recorded Raman spectrum of K_2SnBi . Spectrum was measured at $\lambda = 532$ nm.

5.1 Powder Diffraction Patterns and Raman Spectra of Precursor Compounds

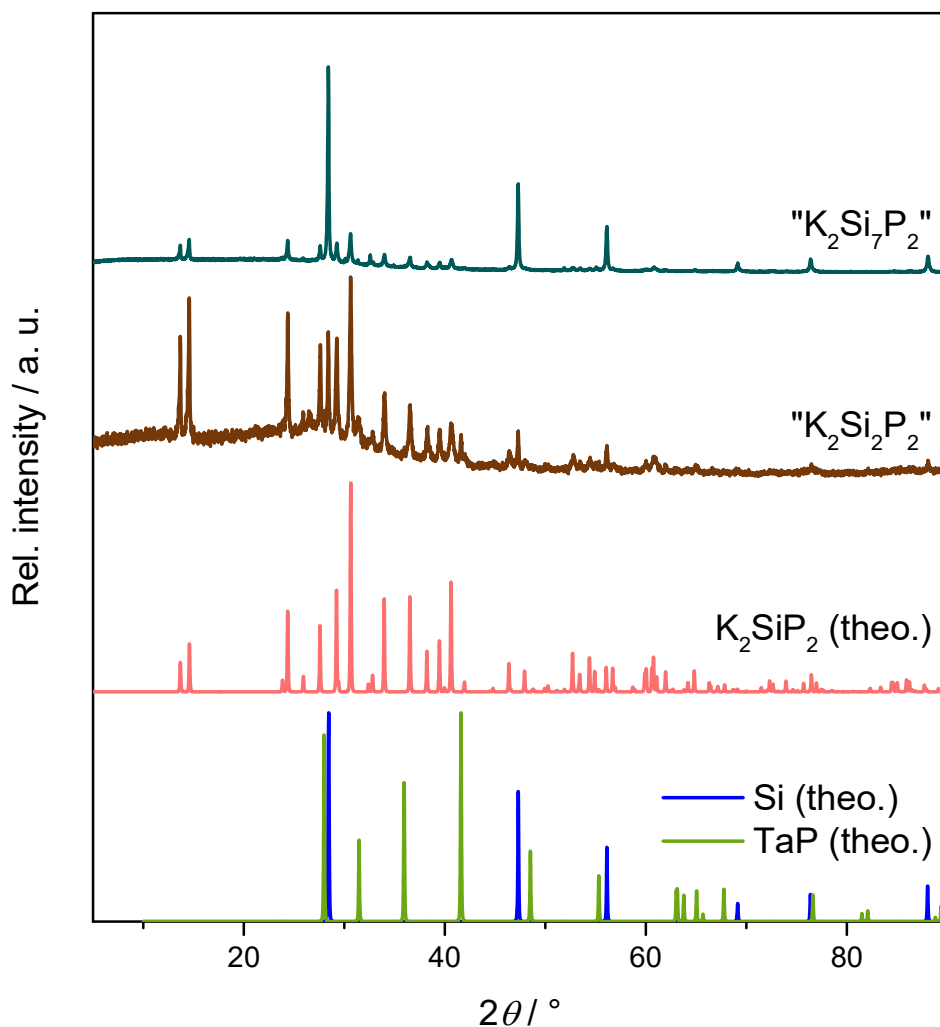


Figure 5.8. Powder diffraction patterns of “K₂Si₂P₂” and “K₂Si₇P₂”. Both diffraction patterns mainly feature the literature known phase K₂SiP₂.^[271] Furthermore, some reflexes of unreacted silicon can be identified. The amount of remaining silicon is drastically increased when aiming for the composition “K₂Si₇P₂” instead of “K₂Si₂P₂”. Additionally, a small amount of tantalum phosphide (TaP) can be detected, leading to the conclusion that phosphorus starts to react with the ampoule material used. When using higher temperatures for the synthesis (1173 K), silicon reacts with the ampoule material as well. This can be detected in form of TaSi₂ rather than unreacted silicon in the powder diffraction pattern.

5.2 Terahertz Measurements

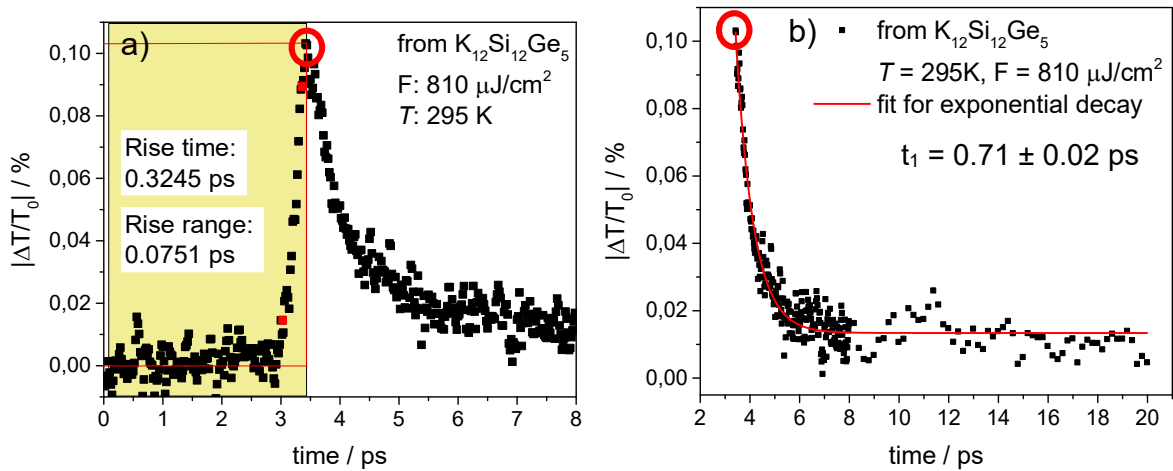


Figure 5.9. Rise time (a) and signal decay (b) for an inverse opal structured mixed Si/Ge thin film starting from $K_{12}Si_{12}Ge_5$. Starting point for signal decay plot is the peak signal for transient photoconductivity (red circle in both graphs). Decay time is indicated as t_1 .

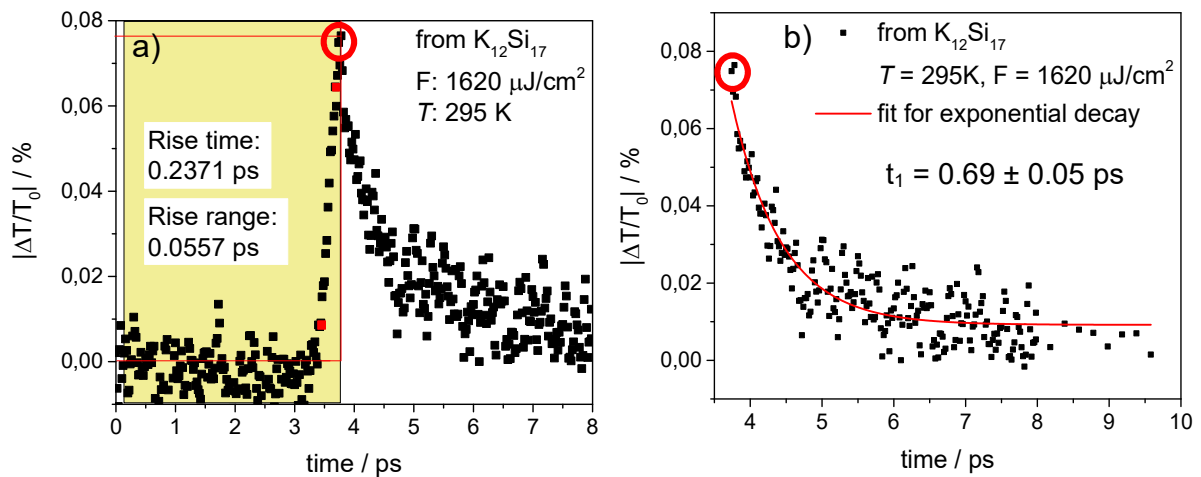


Figure 5.10. Rise time (a) and signal decay (b) for an inverse opal structured mixed Si/Ge thin film starting from $K_{12}Si_{17}$. Starting point for signal decay plot is the peak signal for transient photoconductivity (red circle in both graphs). Decay time is indicated as t_1 .

Bi-exponential decay: $y = A_1 \cdot e^{-\frac{x}{t_1}} + A_2 \cdot e^{-\frac{x}{t_2}} + y_0$

with A_1 and A_2 being pre-factors, y_0 being the y-intercept and t_1 and t_2 being the decay time constants.

Table 5.1. Values for bi-exponential signal decay in fluence dependent measurements of an inverse opal structured thin film from $K_{12}Si_5Ge_{12}$ at room temperature (295 K).

Fluence / $\mu J \cdot cm^{-2}$	$A_1 / \%$	t_1 / ps	$A_2 / \%$	t_2 / ps	$y_0 / \%$
486	435 ± 87	0.41 ± 0.01	0.11 ± 0.01	3.9 ± 0.4	0.009 ± 0.001
648	220 ± 35	0.48 ± 0.01	0.08 ± 0.01	6.8 ± 1.2	0.007 ± 0.003
810	199 ± 21	0.53 ± 0.01	0.09 ± 0.01	7.5 ± 0.9	0.007 ± 0.002
972	482 ± 66	0.47 ± 0.01	0.13 ± 0.02	5.0 ± 0.5	0.012 ± 0.001

Table 5.2. Values for bi-exponential signal decay in temperature dependent measurements of an inverse opal structured thin film from $K_{12}Si_5Ge_{12}$ at $F = 810 \mu J/cm^2$.

T / K	$A_1 / \%$	t_1 / ps	$A_2 / \%$	t_2 / ps	$y_0 / \%$
80	1251 ± 181	0.399 ± 0.007	0.107 ± 0.010	4.2 ± 0.3	0.0081 ± 0.0006
150	1420 ± 197	0.398 ± 0.007	0.131 ± 0.014	3.7 ± 0.3	0.0067 ± 0.0006
200	412 ± 38	0.446 ± 0.006	0.108 ± 0.008	6.0 ± 0.5	0.008 ± 0.001
250	494 ± 44	0.433 ± 0.006	0.117 ± 0.007	5.6 ± 0.4	0.0116 ± 0.0009
295	199 ± 21	0.529 ± 0.010	0.093 ± 0.009	7.5 ± 0.9	0.007 ± 0.002

Single exponential decay: $y = A \cdot e^{-\frac{x}{t_1}} + y_0$

with A_1 being a pre-factor, y_0 being the y-intercept and t_1 being the decay time constant.

Table 5.3. Values for single exponential signal decay in fluence dependent measurements of an inverse opal structured thin film from $K_{12}Si_{12}Ge_5$ at room temperature (295 K).

Fluence / $\mu J \cdot cm^{-2}$	$A / \%$	t_1 / ps	$y_0 / \%$
810	11.1 ± 1.8	0.71 ± 0.02	0.0134 ± 0.0004
972	15.3 ± 2.6	0.67 ± 0.02	0.0130 ± 0.0004
1134	8.4 ± 1.1	0.78 ± 0.02	0.0131 ± 0.0004

Appendix

Table 5.4. Values for single exponential signal decay in temperature dependent measurements of an inverse opal structured thin film from $K_{12}Si_{12}Ge_5$ at $F = 810 \mu J/cm^2$.

T / K	$A / \%$	t_1 / ps	$y_0 / \%$
80	21 ± 7	0.54 ± 0.03	0.0032 ± 0.0004
150	27 ± 9	0.54 ± 0.03	0.0040 ± 0.0005
200	23 ± 8	0.53 ± 0.03	0.0036 ± 0.0004
250	5 ± 1	0.71 ± 0.02	0.0070 ± 0.0002
295	11 ± 2	0.71 ± 0.02	0.0134 ± 0.0004

Table 5.5. Values for single exponential signal decay in fluence dependent measurements of an inverse opal structured thin film from $K_{12}Si_{17}$ at room temperature (295 K).

Fluence / $\mu J \cdot cm^{-2}$	$A / \%$	t_1 / ps	$y_0 / \%$
810	11.5 ± 12.4	0.60 ± 0.11	0.0069 ± 0.0016
1296	18.9 ± 7.4	0.62 ± 0.04	0.0106 ± 0.0005
1620	12.9 ± 4.8	0.69 ± 0.05	0.0092 ± 0.0007

Table 5.6. Parameters obtained from complex conductivity of an inverse opal structured thin from $K_{12}Si_5Ge_{12}$ using the Drude-Smith model at room temperature (295 K).

Fluence / $\mu J \cdot cm^{-2}$	τ_{DS} / fs	c	$\mu_m / cm^2 V^{-1} s^{-1}$
486	71.7 ± 3.8	-0.98 ± 0.02	13 ± 19
648	81.7 ± 4.8	-1	0
810	67.0 ± 2.7	-0.98 ± 0.01	14 ± 12
972	64.6 ± 2.3	-0.95 ± 0.01	34 ± 9

Table 5.7. Parameters obtained from complex conductivity of an inverse opal structured thin from $K_{12}Si_5Ge_{12}$ using the Drude-Smith model at $F = 810 \mu J/cm^2$.

T / K	τ_{DS} / fs	c	$\mu_m / cm^2 V^{-1} s^{-1}$
80	71.6 ± 2.7	-0.98 ± 0.01	16 ± 13
150	74.3 ± 3.1	-0.97 ± 0.02	27 ± 13
200	73.8 ± 2.4	-0.98 ± 0.01	15 ± 12
250	73.7 ± 2.5	-0.97 ± 0.01	23 ± 15
295	67.0 ± 2.7	-0.98 ± 0.01	14 ± 12

Table 5.8. Parameters obtained from complex conductivity of an inverse opal structured thin from $K_{12}Si_{12}Ge_5$ using the Drude-Smith model at room temperature (295 K).

Fluence / $\mu\text{J} \cdot \text{cm}^{-2}$	τ_{DS} / fs	c	$\mu_m / \text{cm}^2 \text{V}^{-1} \text{s}^{-1}$
810	29.5 ± 6.3	-0.92 ± 0.02	19 ± 4
972	30.3 ± 5.4	-0.89 ± 0.01	27 ± 5
1134	37.5 ± 4.0	-0.91 ± 0.01	27 ± 3

Table 5.9. Parameters obtained from complex conductivity of an inverse opal structured thin from $K_{12}Si_{12}Ge_5$ using the Drude-Smith model at $F = 810 \mu\text{J}/\text{cm}^2$.

T / K	τ_{DS} / fs	c	$\mu_m / \text{cm}^2 \text{V}^{-1} \text{s}^{-1}$
80	33.5 ± 3.6	-0.91 ± 0.01	24 ± 3
150	14.2 ± 6.8	-0.94 ± 0.01	7 ± 5
200	15.9 ± 5.0	-0.92 ± 0.01	10 ± 5
250	34.1 ± 5.3	-0.93 ± 0.02	19 ± 4
295	29.5 ± 6.3	-0.92 ± 0.02	19 ± 4

Table 5.10. Parameters obtained from complex conductivity of an inverse opal structured thin from $K_{12}Si_{17}$ using the Drude-Smith model at room temperature (295 K).

Fluence / $\mu\text{J} \cdot \text{cm}^{-2}$	τ_{DS} / fs	c	$\mu_m / \text{cm}^2 \text{V}^{-1} \text{s}^{-1}$
810	23.7 ± 5.8	-0.88 ± 0.01	20 ± 6
1296	33.2 ± 5.5	-0.88 ± 0.01	26 ± 4
1620	41.4 ± 7.0	-0.94 ± 0.03	15 ± 7

Appendix

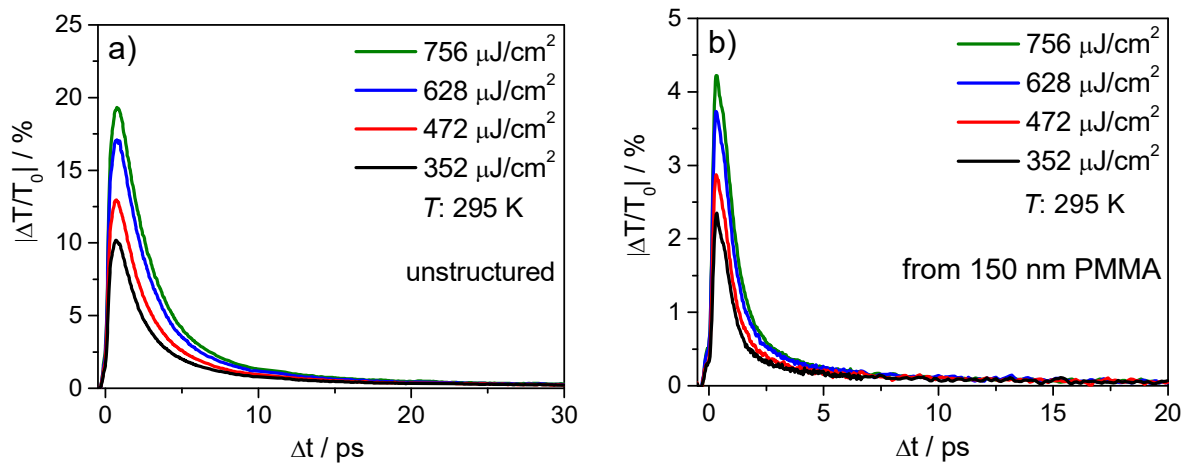


Figure 5.11. Transient photoconductivity $|\Delta T/T_0|$ for germanium thin films. Fluence dependency at room temperature (295 K) for a) unstructured thin film, b) inverse opal structured thin film starting with 150 nm PMMA template beads.

Single exponential decay: $y = A \cdot e^{-\frac{x}{t_1}} + y_0$

Power law 1: $y = B \cdot x^{-\beta_1} + y_0$

Power law 2: $y = C \cdot x^{-\beta_2} + y_0$

With A , B and C being pre factors, y_0 being the y-intercept, t_1 being the decay time constant and β_1 and β_2 being power law exponents.

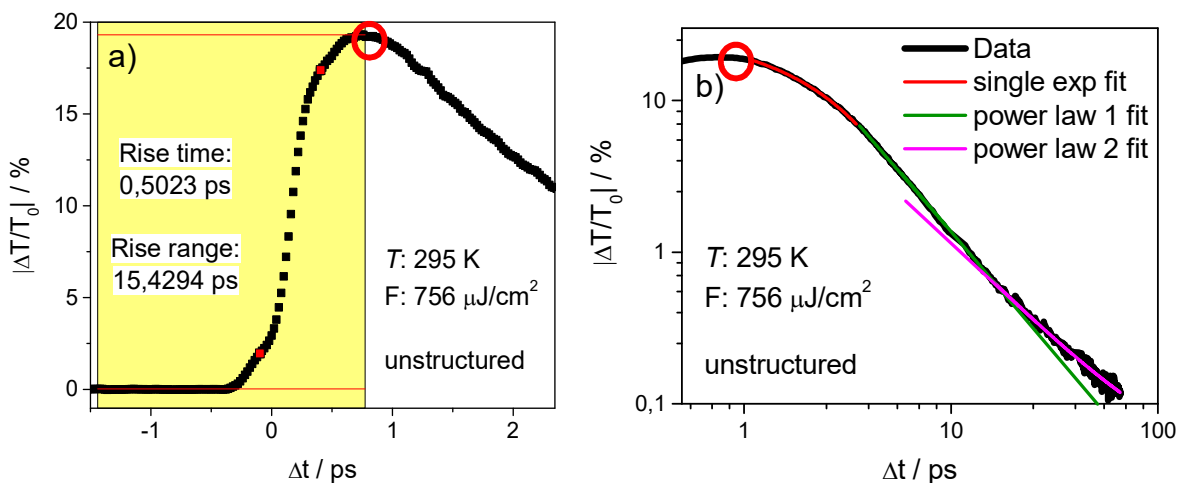


Figure 5.12. Rise time (a) and signal decay (b) for an unstructured germanium thin film. Starting point for signal decay plot is the peak signal for transient photoconductivity (red circle in both graphs). Signal decay plot is depicted in logarithmic scale to show power law dependency.

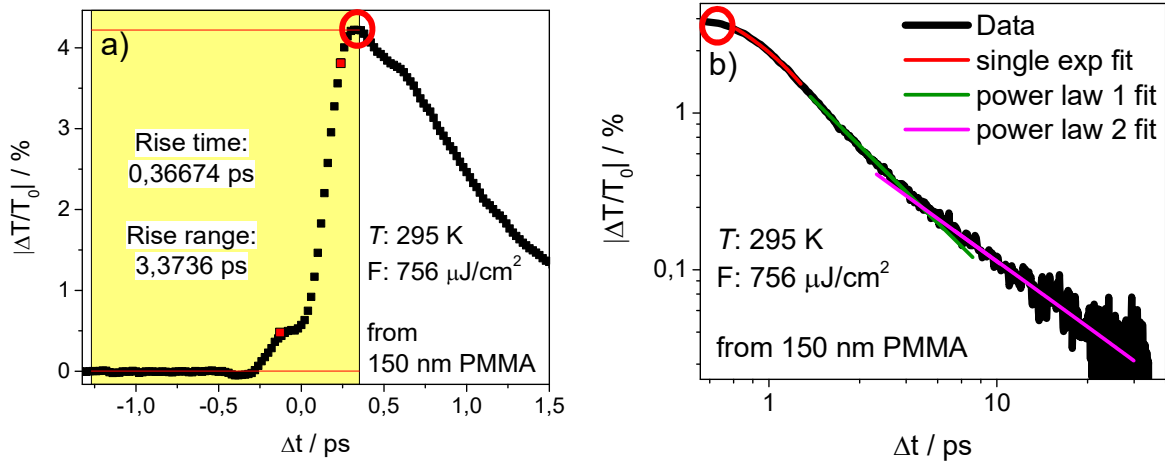


Figure 5.13. Rise time (a) and signal decay (b) for an inverse opal structured germanium thin film starting from 150 nm PMMA template beads. Starting point for signal decay plot is the peak signal for transient photoconductivity (red circle in both graphs). Signal decay plot is depicted in logarithmic scale to show power law dependency.

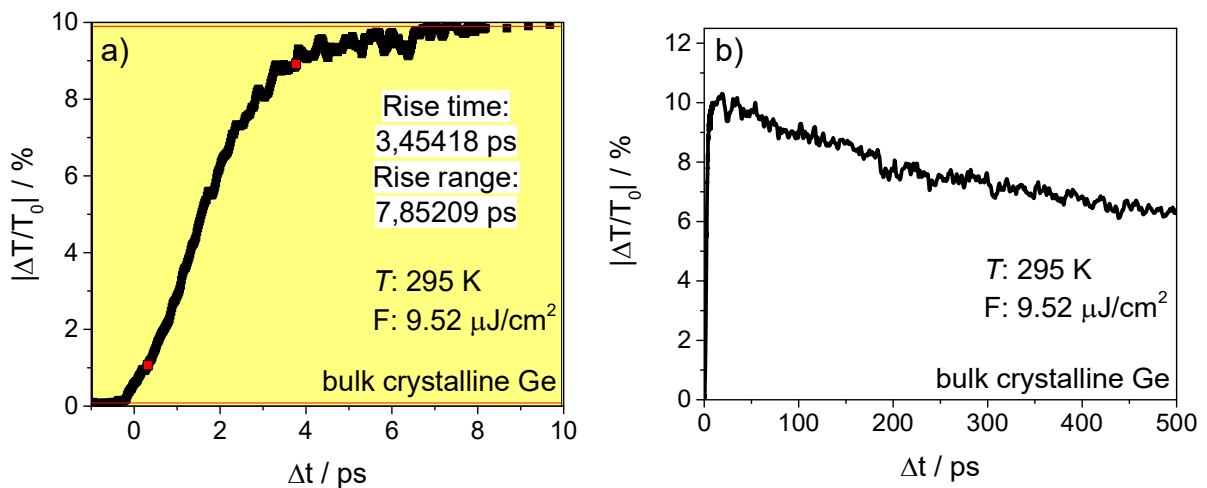


Figure 5.14. Rise time (a) and signal decay (b) for bulk crystalline germanium.

5.3 ESI-MS Measurements

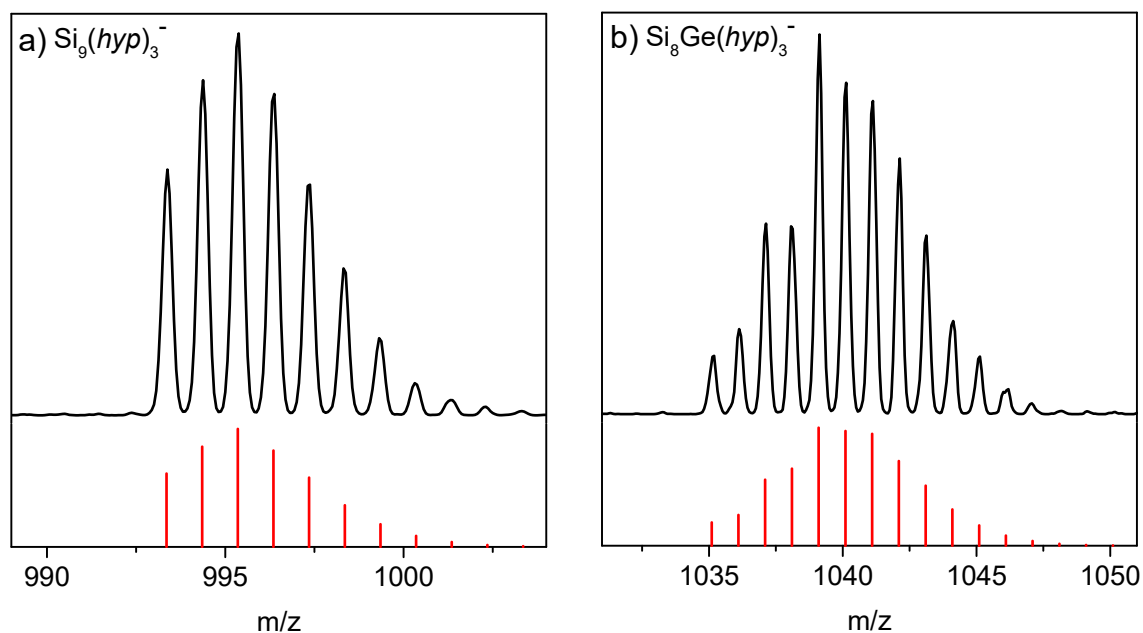


Figure 5.15. Selected high resolution areas of the ESI-MS spectrum of $[E_9(hyp)_3]^-$ (E : Si, Ge) in negative ($-$) ion mode. a) Monitoring at 995.3 m/z $[Si_9(hyp)_3]^-$ and b) monitoring $[Si_8Ge(hyp)_3]^-$ at 1040.1 m/z in an acetonitrile solution with a K^+ moiety cleaved. Simulated mass spectra with their isotopic distribution are shown below as red bars.

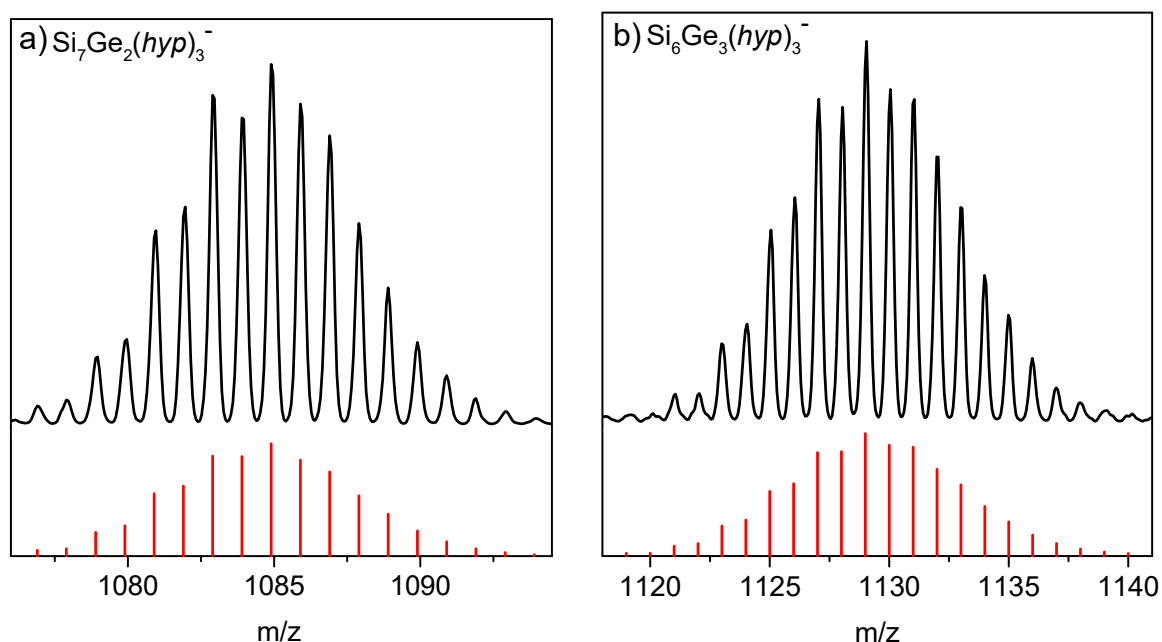


Figure 5.16. Selected high resolution areas of the ESI-MS spectrum of $[E_9(hyp)_3]^-$ (E : Si, Ge) in negative ($-$) ion mode. a) Monitoring $[Si_7Ge_2(hyp)_3]^-$ at 1084.9 m/z and b) monitoring $[Si_6Ge_3(hyp)_3]^-$ at 1129.0 m/z in an acetonitrile solution with a K^+ moiety cleaved. Simulated mass spectra with their isotopic distribution are shown below as red bars.

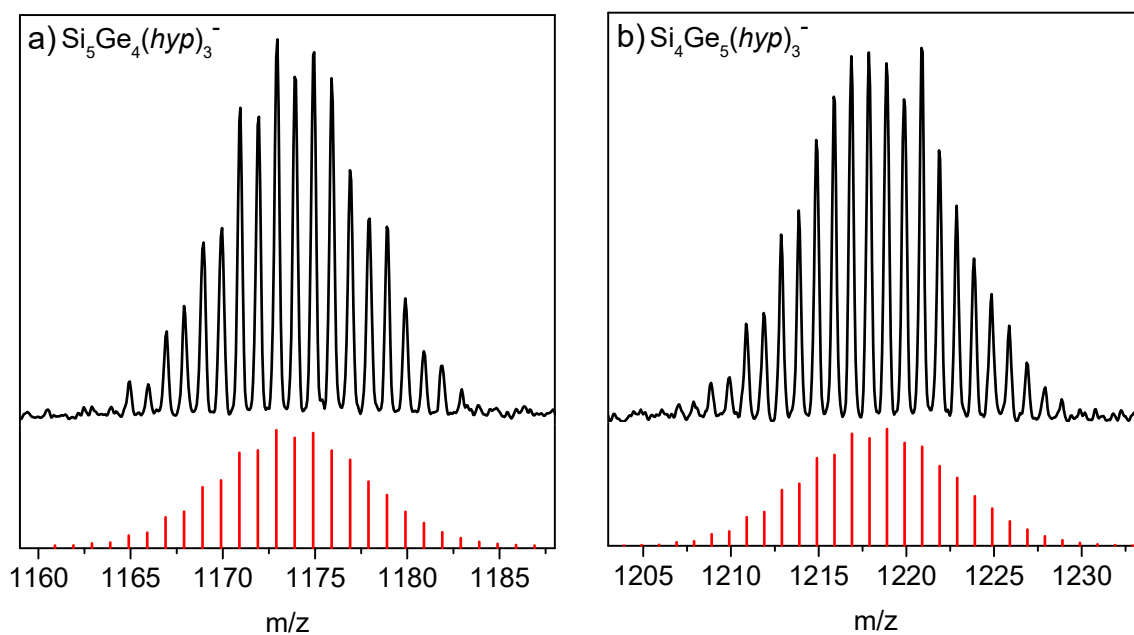


Figure 5.17. Selected high resolution areas of the ESI-MS spectrum of $[\text{E}_9(\text{hyp})_3]^-$ (E : Si, Ge) in negative ($-$) ion mode. a) Monitoring $[\text{Si}_5\text{Ge}_4(\text{hyp})_3]^-$ at 1173.9 m/z and b) monitoring $[\text{Si}_4\text{Ge}_5(\text{hyp})_3]^-$ at 1218.9 m/z in an acetonitrile solution with a K^+ moiety cleaved. Simulated mass spectra with their isotopic distribution are shown below as red bars.

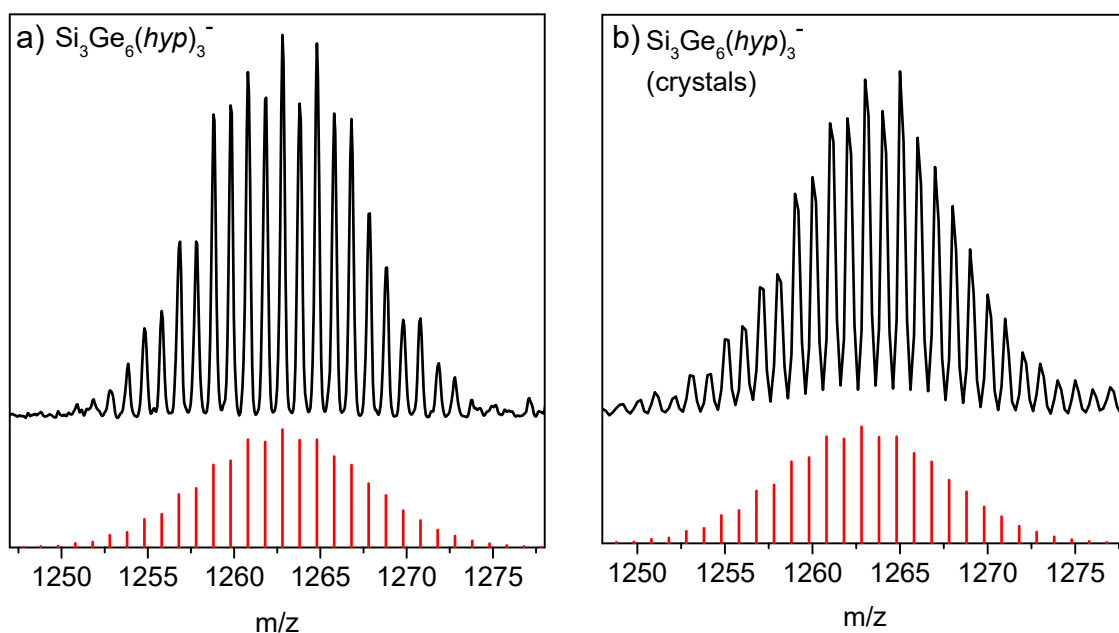


Figure 5.18. Selected high resolution areas of the ESI-MS spectrum of $[\text{E}_9(\text{hyp})_3]^-$ (E : Si, Ge) in negative ($-$) ion mode. a) Monitoring $[\text{Si}_3\text{Ge}_6(\text{hyp})_3]^-$ at 1262.8 m/z in an acetonitrile solution with a K^+ moiety cleaved, b) monitoring $[\text{Si}_3\text{Ge}_6(\text{hyp})_3]^-$ at 1262.8 m/z in a THF solution of dissolved crystals with a $[\text{K}(2.2.2\text{-crypt})]^+$ moiety cleaved. Simulated mass spectra with their isotopic distribution are shown below as red bars.

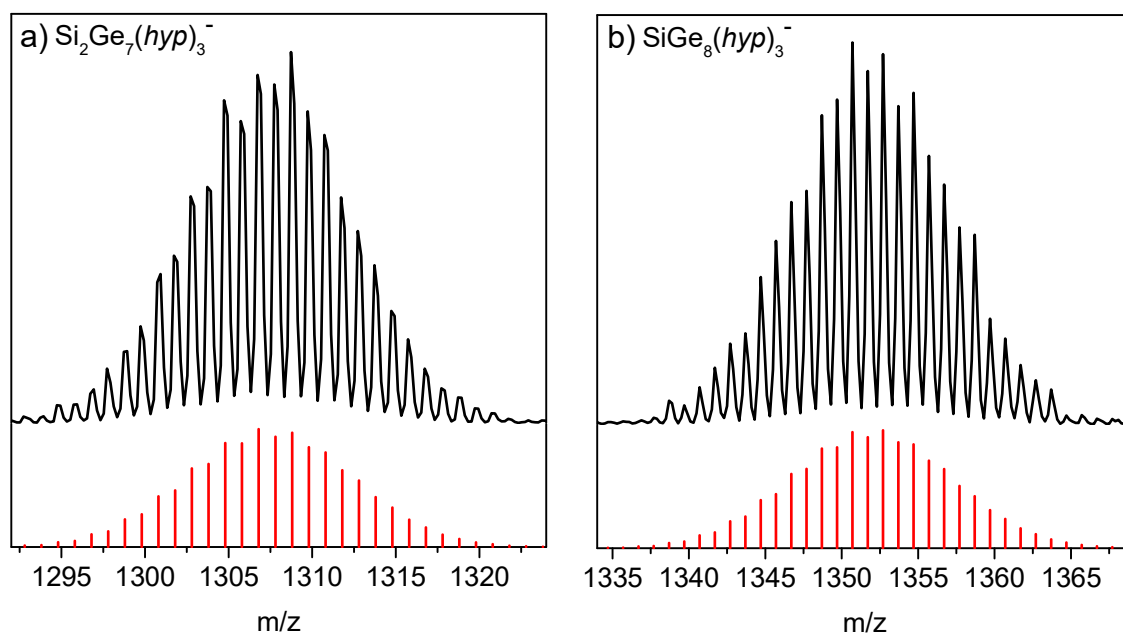


Figure 5.19. Selected high resolution areas of the ESI-MS spectrum of $[E_9(hyp)_3]^-$ (E : Si, Ge) in negative ($-$) ion mode. a) Monitoring $[Si_2Ge_7(hyp)_3]^-$ at 1307.8 m/z and b) monitoring $[SiGe_8(hyp)_3]^-$ at 1352.7 m/z in an acetonitrile solution with a K^+ moiety cleaved. Simulated mass spectra with their isotopic distribution are shown below as red bars.

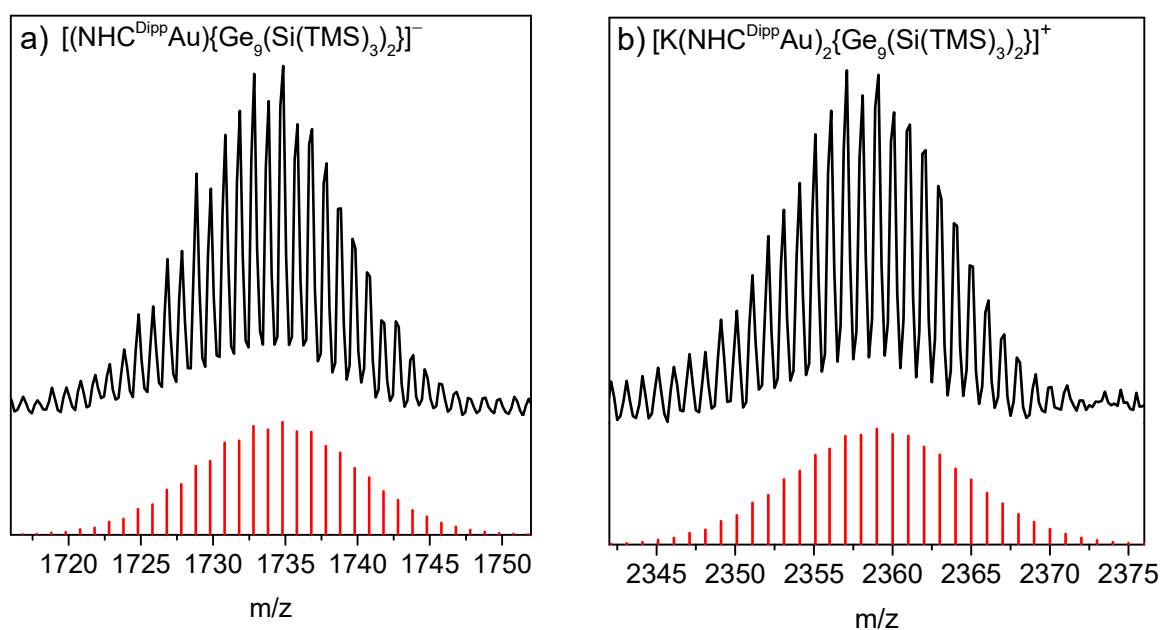


Figure 5.20. Selected high resolution areas of the ESI-MS spectrum of an acetonitrile solution of $[(NHC^{Dipp}Au)_2\{\eta^3,\eta^3-Ge_9(Si(TMS)_3)_2\}]^-$. a) Monitoring $[(NHC^{Dipp}Au)\{\eta^3,\eta^3-Ge_9(Si(TMS)_3)_2\}]^-$ at 1734.8 m/z in negative ($-$) ion mode with a $(NHC^{Dipp}Au)^+$ moiety cleaved, b) monitoring $[K(NHC^{Dipp}Au)_2\{\eta^3,\eta^3-Ge_9(Si(TMS)_3)_2\}]^+$ at 2359.0 m/z in positive ($+$) ion mode with a K^+ moiety attached. Simulated mass spectra with their isotopic distribution are shown below as red bars.

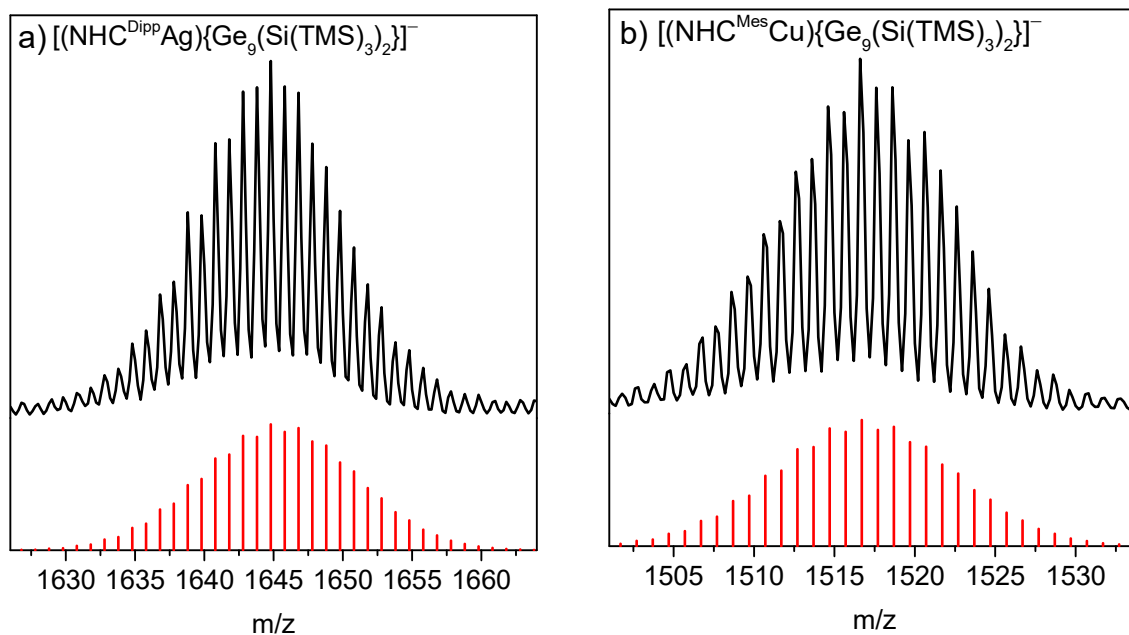


Figure 5.21. Selected high resolution areas of the ESI-MS spectrum of an acetonitrile solution of [(NHC^{Dipp}Ag)₂{η³,η³-Ge₉(Si(TMS)₃)₂}] and [(NHC^{Mes}Cu)₂{η³,η³-Ge₉(Si(TMS)₃)₂}] in negative (-) ion mode. a) Monitoring [(NHC^{Dipp}Ag){η³,η³-Ge₉(Si(TMS)₃)₂}]⁻ at 1644.8 m/z with a (NHC^{Dipp}Ag)⁺ moiety cleaved, b) monitoring [(NHC^{Mes}Cu){η³,η³-Ge₉(Si(TMS)₃)₂}]⁻ at 1516.6 m/z with a (NHC^{Mes}Cu)⁺ moiety cleaved. Simulated mass spectra with their isotopic distribution are shown below as red bars.

5.4 Crystals

Table 5.11. Fractional site occupation of cluster atoms in $K(2.2.2\text{-crypt})[\text{Si}_{1.68}\text{Ge}_{7.32}(\text{hyp})_3]$. Two E_9 -clusters are present in the cell.

Atom	Occupation	Atom	Occupation	Atom	Occupation	Atom	Occupation
Ge1	1.000	Si	–	Ge10	1.000	Si	–
Ge2	1.000	Si	–	Ge11	1.000	Si	–
Ge3	1.000	Si	–	Ge12	1.000	Si	–
Ge4	1.000	Si	–	Ge13	1.000	Si	–
Ge5	1.000	Si	–	Ge14	1.000	Si	–
Ge6	1.000	Si	–	Ge15	1.000	Si	–
Ge7	0.328(3)	Si29	0.672(3)	Ge16	0.452(3)	Si32	0.548(3)
Ge8	0.471(3)	Si30	0.529(3)	Ge17	0.405(3)	Si33	0.595(3)
Ge9	0.526(3)	Si31	0.474(3)	Ge18	0.459(3)	Si34	0.541(3)

Table 5.12. Selected bond lengths in $K(2.2.2\text{-crypt})[\text{Si}_{1.68}\text{Ge}_{7.32}(\text{hyp})_3]$.

Cluster 1		Cluster 2	
Atoms	Distance / Å	Atoms	Distance / Å
Ge1–Ge2	2.7092(8)	Ge10–Ge11	2.6566(7)
Ge1–Ge3	2.6401(6)	Ge10–Ge12	2.6554(6)
Ge1–Ge4	3.4223(8)	Ge10–Ge13	3.4802(9)
Ge1–Si29/Ge7	2.4662(9)	Ge10–Si32/Ge16	2.5023(9)
Ge1–Si31/Ge9	2.517(1)	Ge10–Si34/Ge18	2.512(1)
Ge2–Ge3	2.6815(7)	Ge11–Ge12	2.6910(9)
Ge2–Ge6	3.1470(8)	Ge11–Ge14	3.2688(8)
Ge2–Si29/Ge7	2.496(1)	Ge11–Si32/Ge16	2.5106(9)
Ge2–Si30/Ge8	2.5131(9)	Ge11–Si33/Ge17	2.517(1)
Ge3–Ge5	3.4906(8)	Ge12–Ge15	3.3046(9)

Ge3–Si30/Ge8	2.5012(9)	Ge12–Si33/Ge17	2.482(1)
Ge3–Si31/Ge9	2.522(1)	Ge12–Si34/Ge18	2.508(1)
Ge4–Ge5	2.6865(8)	Ge13–Ge14	2.6612(7)
Ge4–Ge6	2.6474(6)	Ge13–Ge15	2.6590(6)
Ge4–Si29/Ge7	2.486(1)	Ge13–Si32/Ge16	2.503(1)
Ge4–Si31/Ge9	2.5317(8)	Ge13–Si34/Ge18	2.5109(9)
Ge5–Ge6	2.6788(7)	Ge14–Ge15	2.7203(8)
Ge5–Si29/Ge7	2.5132(9)	Ge14–Si32/Ge16	2.5014(9)
Ge5–Si30/Ge8	2.5258(9)	Ge14–Si33/Ge17	2.498(1)
Ge6–Si30/Ge8	2.501(1)	Ge15–Si33/Ge16	2.479(1)
Ge6–Si31/Ge9	2.5207(9)	Ge15–Si34/Ge18	2.5112(9)
Si29/Ge7–Si1	2.338(1)	Si32/Ge16–Si13	2.342(2)
Si30/Ge8–Si5	2.355(2)	Si33/Ge17–Si17	2.339(1)
Si31/Ge9–Si9	2.349(2)	Si34/Ge18–Si22	2.337(2)

Table 5.13. Selected bond lengths and angles in $[(\text{NHC}^{\text{Dipp}}\text{Cu})_2\{\eta^3\text{-Ge}_9(\text{Si}(\text{TMS})_3)_2\}]$. ctf: center of the coordinating atoms of the triangular faces of the $[\text{Ge}_9]$ cluster.

Atoms	Distance / Å	Atoms	Distance / Å
Ge1–Ge2	2.5909(9)	Ge8–Ge9	2.505(1)
Ge1–Ge3	2.595(1)	Ge2–Ge3 (h_1)	2.900(1)
Ge1–Ge4	2.591(1)	Ge4–Ge5 (h_2)	2.906(1)
Ge1–Ge5	2.5781(9)	Ge7–Ge9 (h_3)	3.6969(4)
Ge2–Ge5	2.7804(9)	Ge6–Si1	2.388(2)
Ge2–Ge6	2.5774(9)	Ge8–Si5	2.43(1)
Ge2–Ge9	2.8269(9)	Cu1–Ge2	2.601(1)
Ge3–Ge4	2.805(1)	Cu1–Ge5	2.532(1)
Ge3–Ge6	2.5521(8)	Cu1–Ge9	2.405(1)

Appendix

Ge3–Ge7	2.8189(9)	Cu2–Ge3	2.532(1)
Ge4–Ge8	2.8333(9)	Cu2–Ge4	2.582(1)
Ge4–Ge8	2.5651(8)	Cu2–Ge7	2.413(1)
Ge5–Ge8	2.5638(9)	Cu1–C1	1.941(5)
Ge5–Ge9	2.8102(9)	Cu2–C4	1.913(5)
Ge6–Ge7	2.5132(8)	Atoms	Angle / °
Ge6–Ge9	2.5047(9)	C1-Cu1-ctf1	162.88(2)
Ge7–Ge8	2.5147(9)	C4-Cu2-ctf2	163.93(2)

5.5 Raman Measurements of Crystals

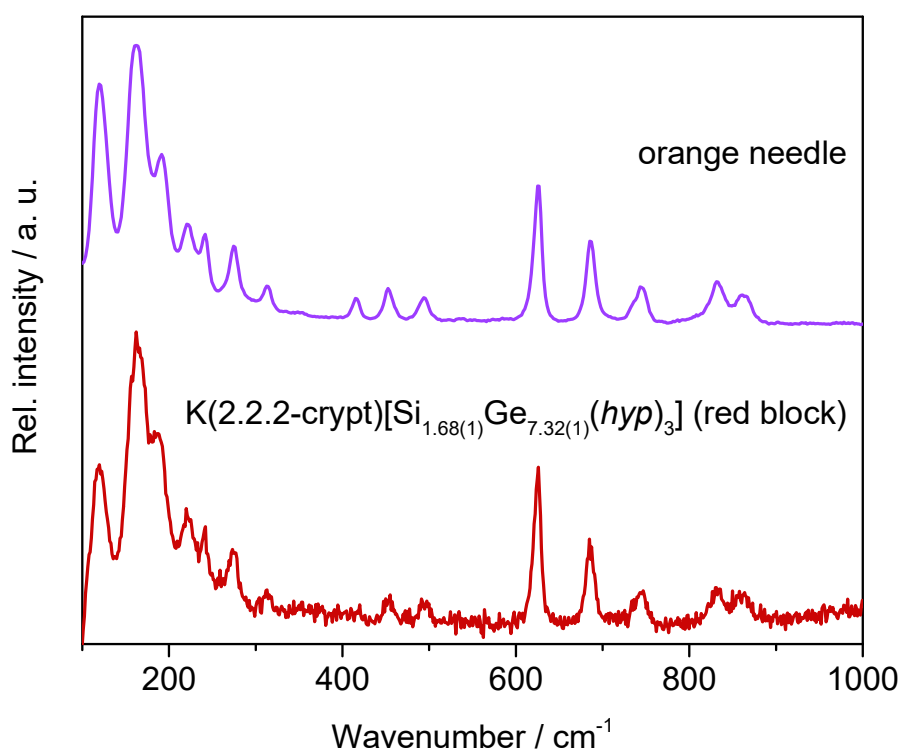


Figure 5.22. Raman spectra of $\text{K}(2.2.2\text{-crypt})[\text{Si}_{1.68(1)}\text{Ge}_{7.32(1)}(\text{hyp})_3]$ (red block) compared to orange needle from the same crystallization experiment. Spectra were measured at $\lambda = 532 \text{ nm}$.

Table 5.14. Originally obtained and shifted theoretical values for cluster exo bond vibrations in $[\text{Si}_2\text{Ge}_7\{\text{Si}(\text{SiH}_3)_3\}_3]^-$. Av: average value.

Vibration	Original value / cm^{-1}	Shifted value / cm^{-1}
Ge-Si stretching (ν_{exo})	399	414
E-Si bending (δ_{exo})	436-440	453-457
Si-Si stretching (ν_{exo})	467 and 484 (av: 475)	486 and 503 (av: 494)

5.6 NMR Measurements

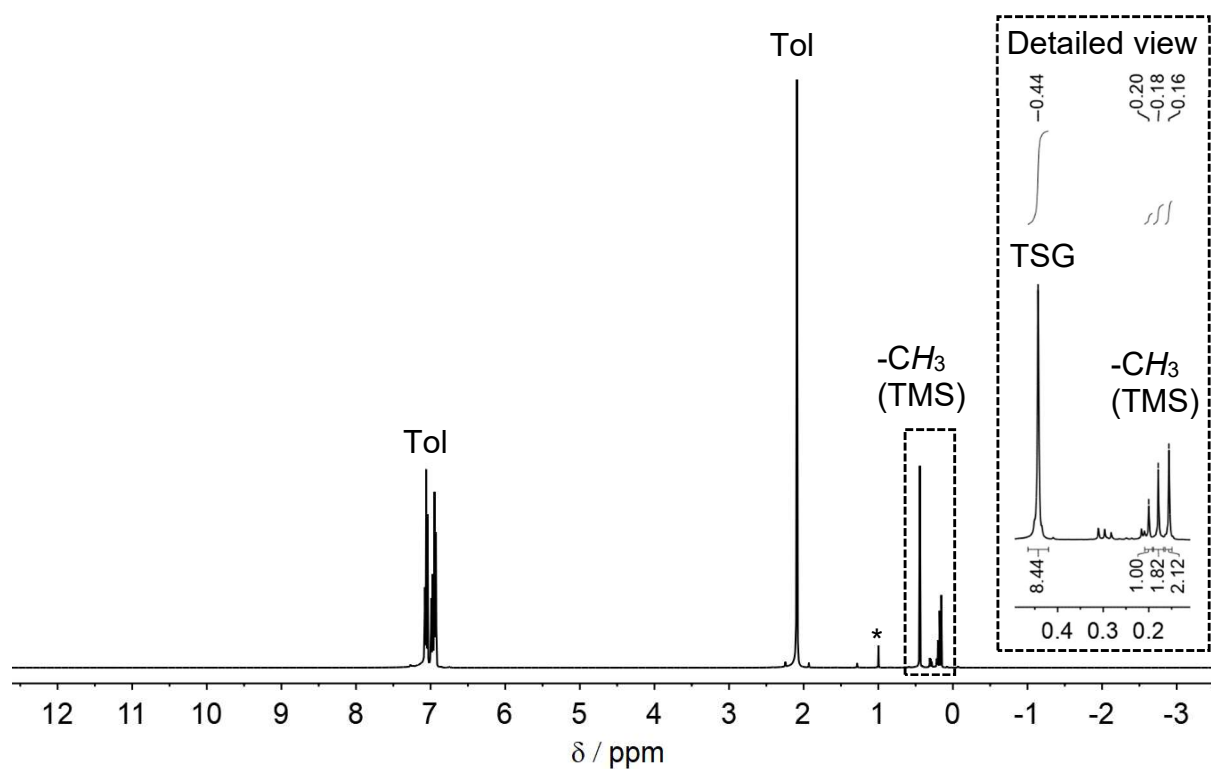


Figure 5.23. $^1\text{H-NMR}$ of $\text{K}[\text{Ge}_9(\text{hyp})_3]$ (TSG) starting from $\text{K}_{12}\text{Ge}_{17}$ as a precursor. *In situ* study in toluene. $\text{K}[\text{Ge}_9(\text{hyp})_3]$ (TSG) is the main reaction product. However, three additional distinct peaks are detected. A small byproduct (*) is present.

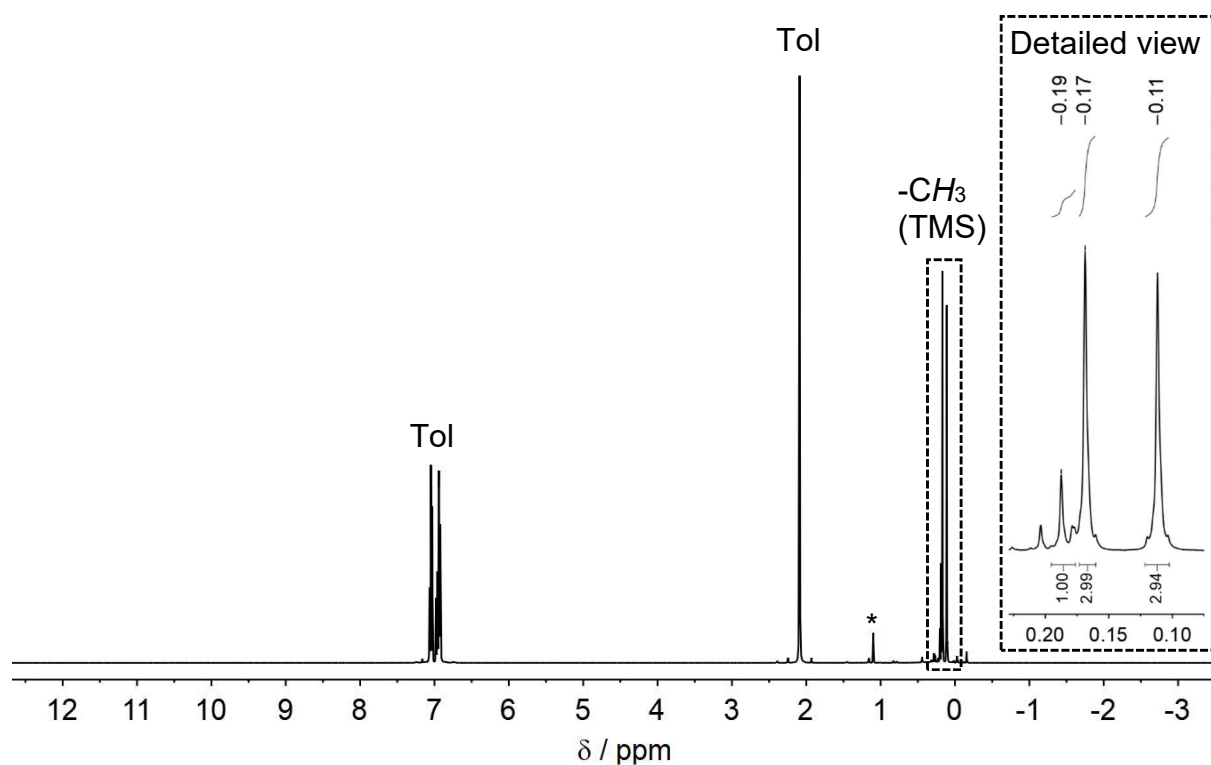


Figure 5.24. $^1\text{H-NMR}$ of $\text{K}[\text{E}_9(\text{hyp})_3]$ (E: Si, Ge) starting from $\text{K}_{12}\text{Si}_5\text{Ge}_{12}$ as a precursor. *In situ* study in toluene. Next to the solvent peaks, only a small byproduct (*) is present.

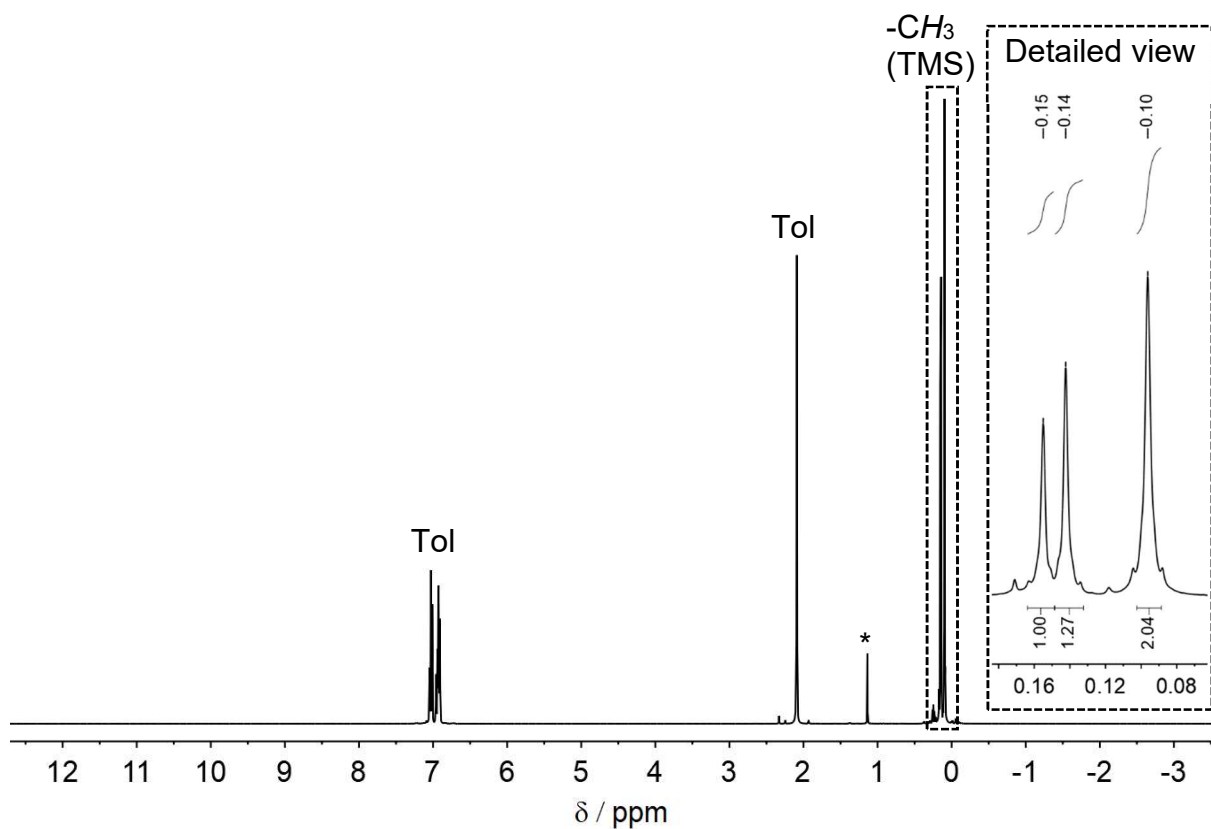


Figure 5.25. $^1\text{H-NMR}$ of $\text{K}[\text{E}_9(\text{hyp})_3]$ (E : Si, Ge) starting from $\text{K}_{12}\text{Si}_{12}\text{Ge}_5$ as a precursor. *In situ* study in toluene. Next to the solvent peaks, only a small byproduct (*) is present.

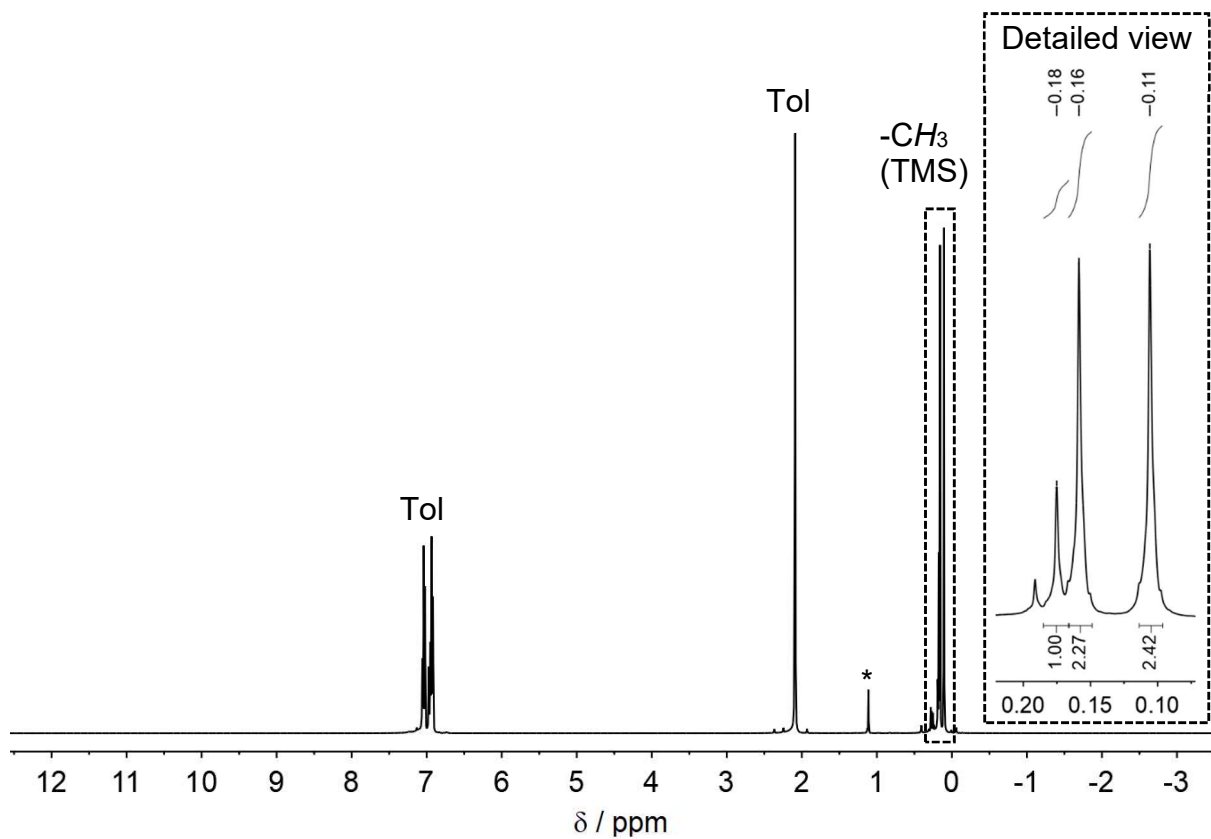


Figure 5.26. $^1\text{H-NMR}$ of $\text{K}[\text{Si}_9(\text{hyp})_3]$ starting from $\text{K}_{12}\text{Si}_{17}$ as a precursor. *In situ* study in toluene. A small byproduct (*) is present.

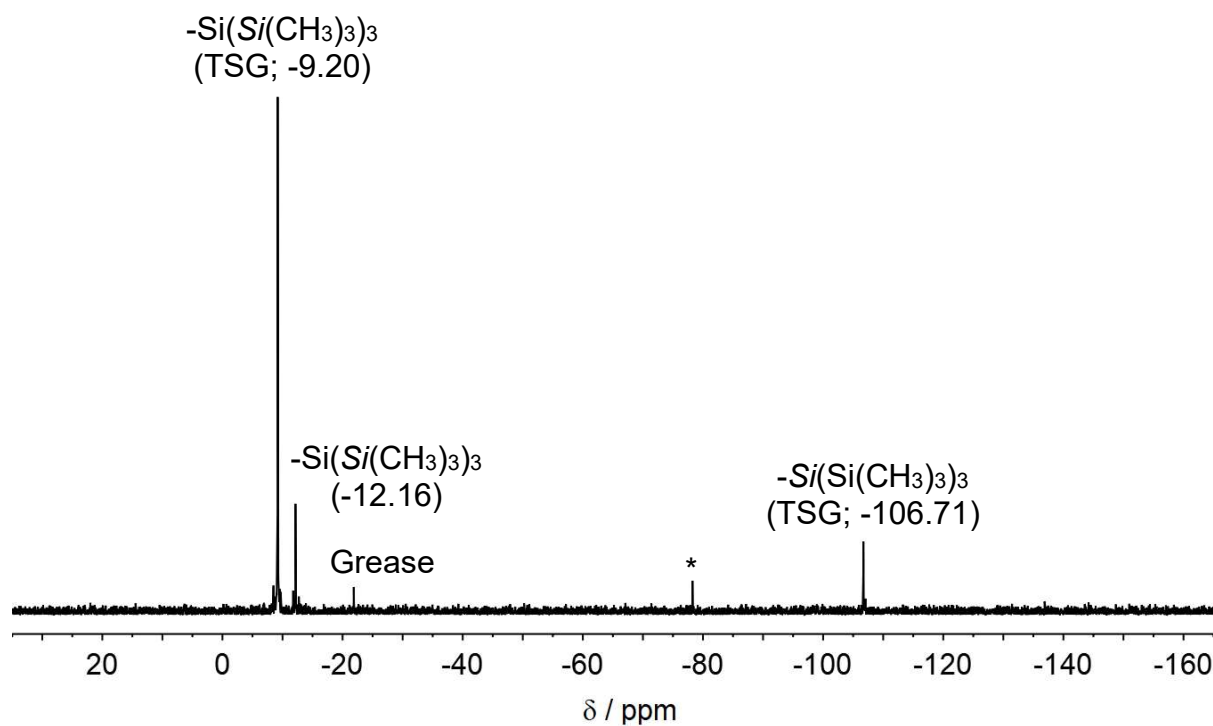


Figure 5.27. ^{29}Si -INEPT NMR of $\text{K}[\text{Ge}_9(\text{hyp})_3]$ (TSG) starting from $\text{K}_{12}\text{Ge}_{17}$ as a precursor. *In situ* study in toluene. A small byproduct (*) is present.

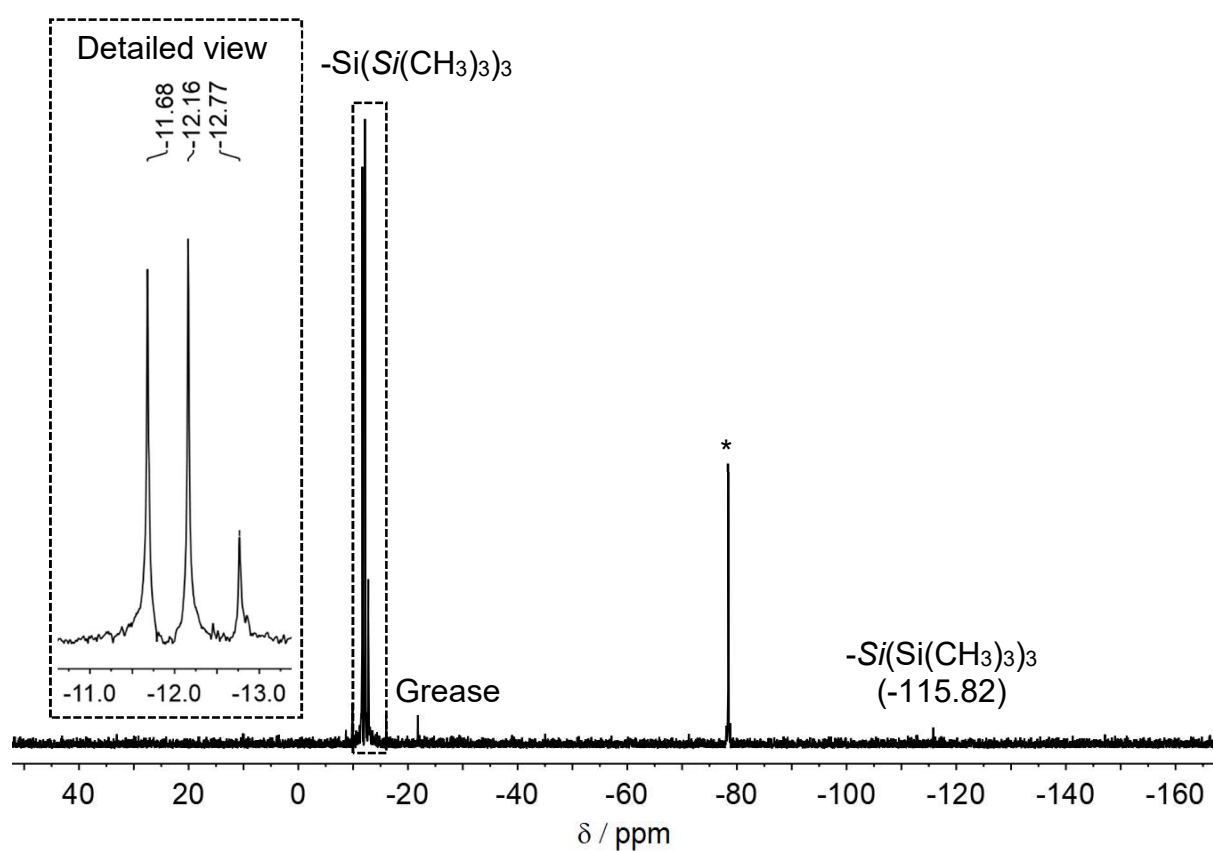


Figure 5.28. ^{29}Si -INEPT NMR of $\text{K}[\text{E}_9(\text{hyp})_3]$ (E: Si, Ge) starting from $\text{K}_{12}\text{Si}_5\text{Ge}_{12}$ as a precursor. *In situ* study in toluene. A byproduct (*) with boosted intensity.

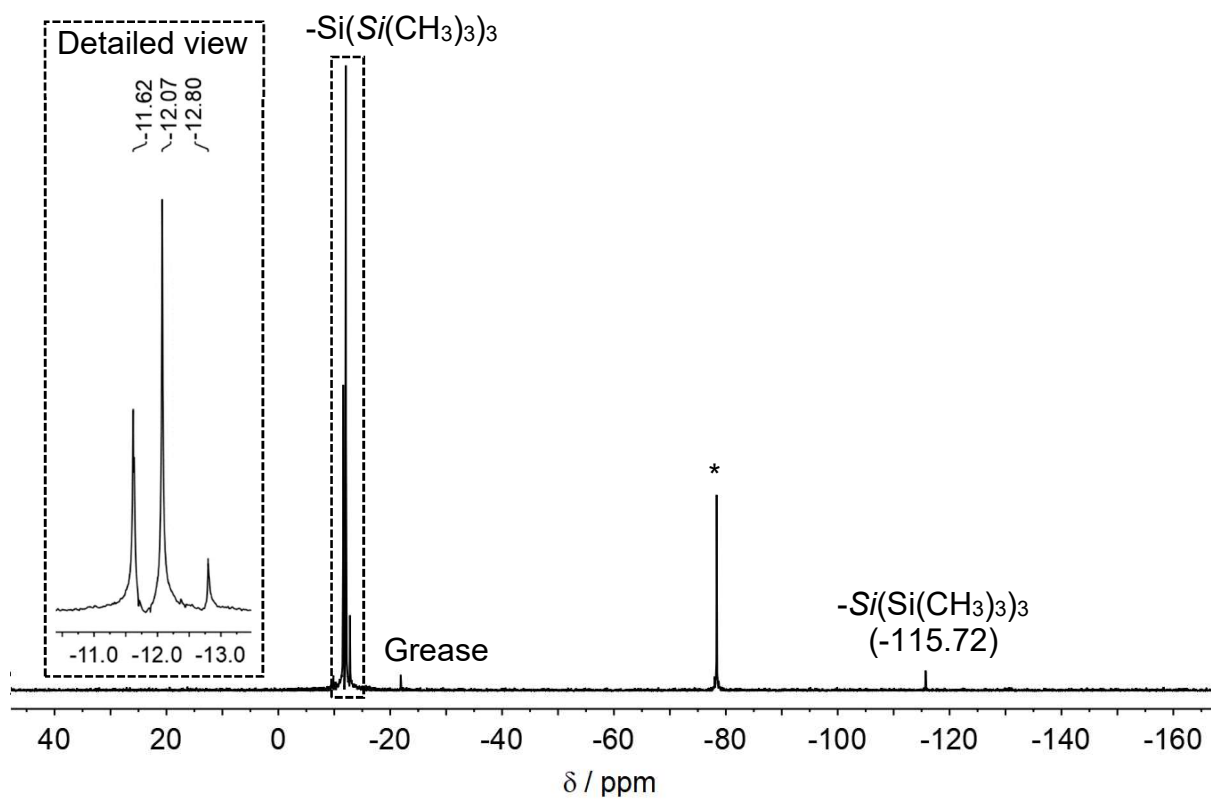


Figure 5.29. ^{29}Si -INEPT NMR of $\text{K}[\text{E}_9(\text{hyp})_3]$ (E : Si, Ge) starting from $\text{K}_{12}\text{Si}_{12}\text{Ge}_5$ as a precursor. *In situ* study in toluene. A byproduct (*) is detected with boosted intensity.

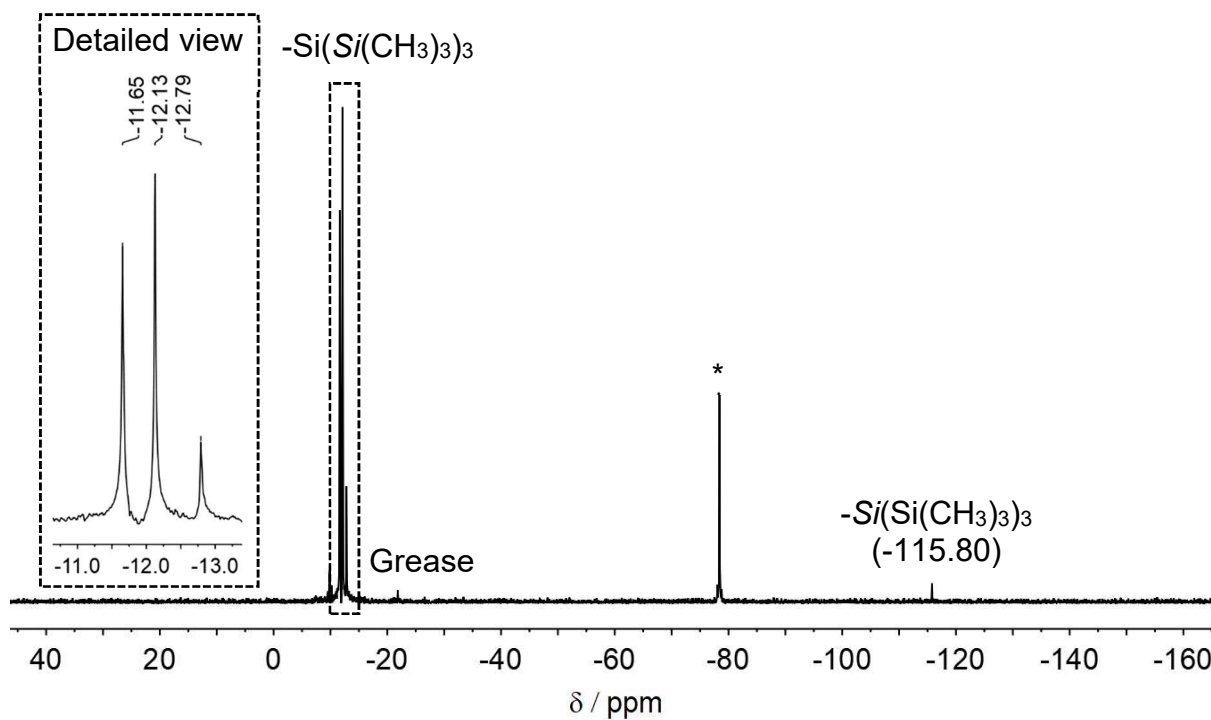


Figure 5.30. ^{29}Si -INEPT NMR of $\text{K}[\text{Si}_9(\text{hyp})_3]$ starting from $\text{K}_{12}\text{Si}_{17}$ as a precursor. *In situ* study in toluene. A byproduct (*) is detected with boosted intensity.

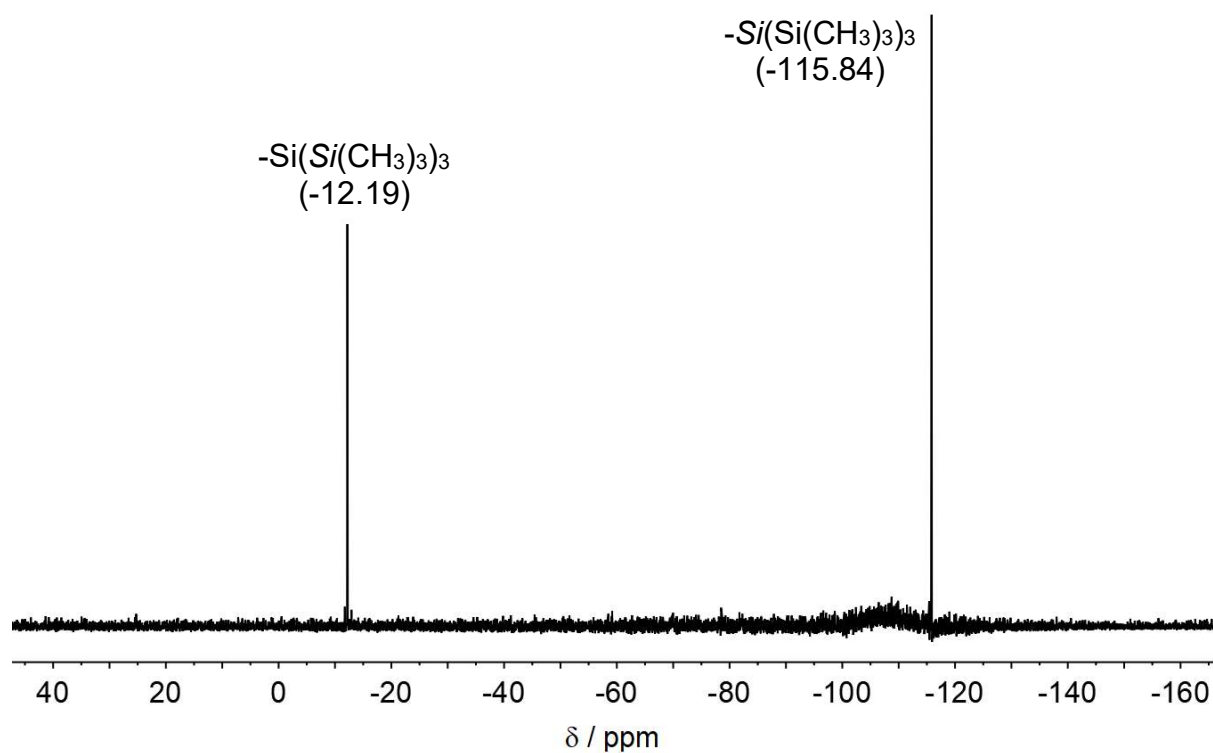


Figure 5.31. ^{29}Si -IG NMR of $\text{K}[\text{E}_9(\text{hyp})_3]$ (E : Si, Ge) starting from $\text{K}_{12}\text{Si}_{12}\text{Ge}_5$ as a precursor. *In situ* study in toluene. No byproducts are detected.

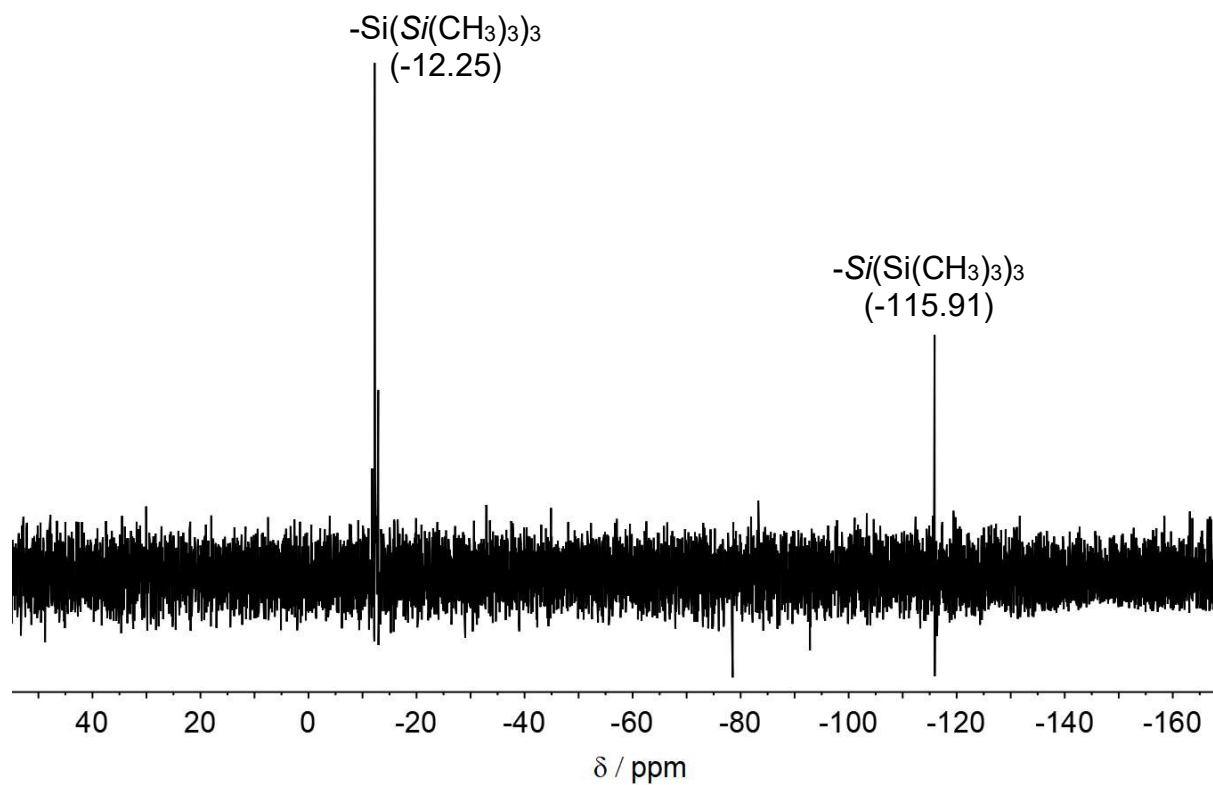


Figure 5.32. ^{29}Si -IG NMR of $\text{K}[\text{Si}_9(\text{hyp})_3]$ starting from $\text{K}_{12}\text{Si}_{17}$ as a precursor. *In situ* study in toluene. No byproducts are detected.

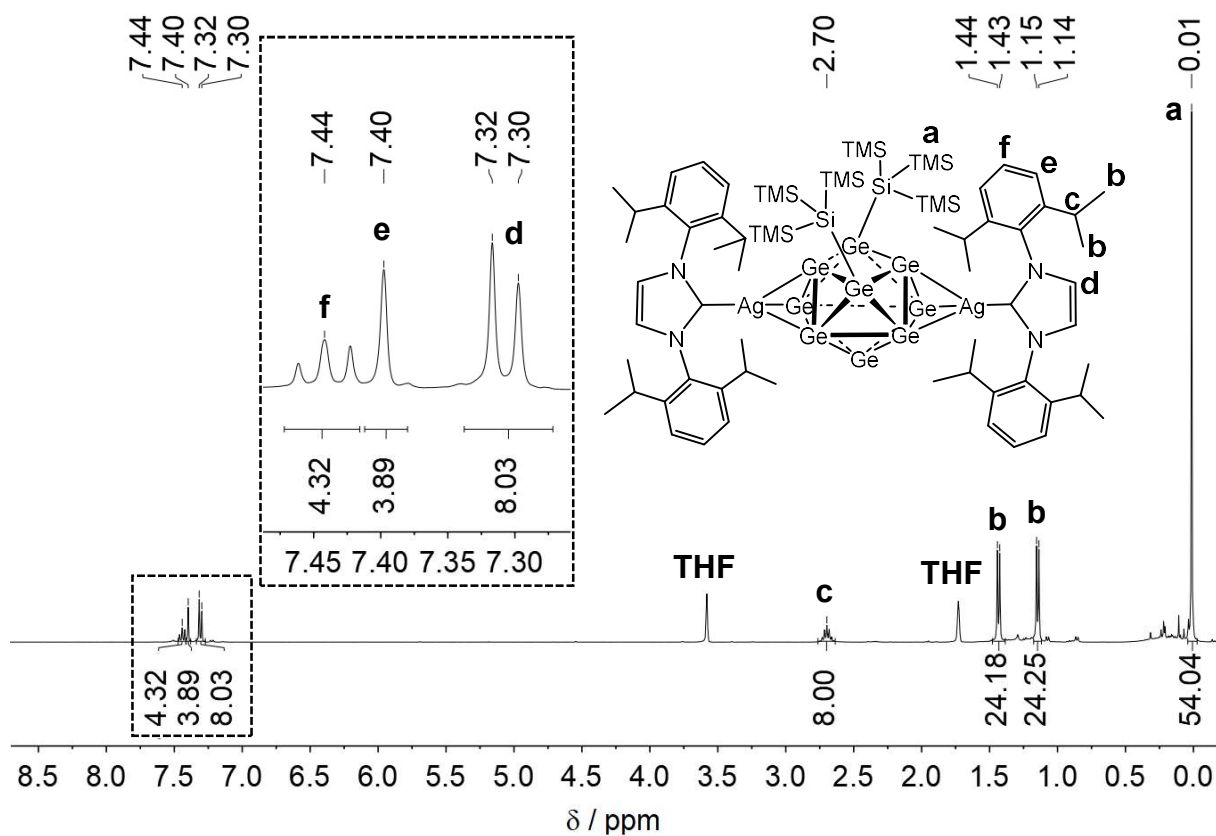


Figure 5.33. $^1\text{H-NMR}$ of $[(\text{NHC}^{\text{Dipp}}\text{Ag})_2\{\eta^3, \eta^3\text{-Ge}_9(\text{Si}(\text{TMS})_3)_2\}]$ in $\text{THF-}d_8$.

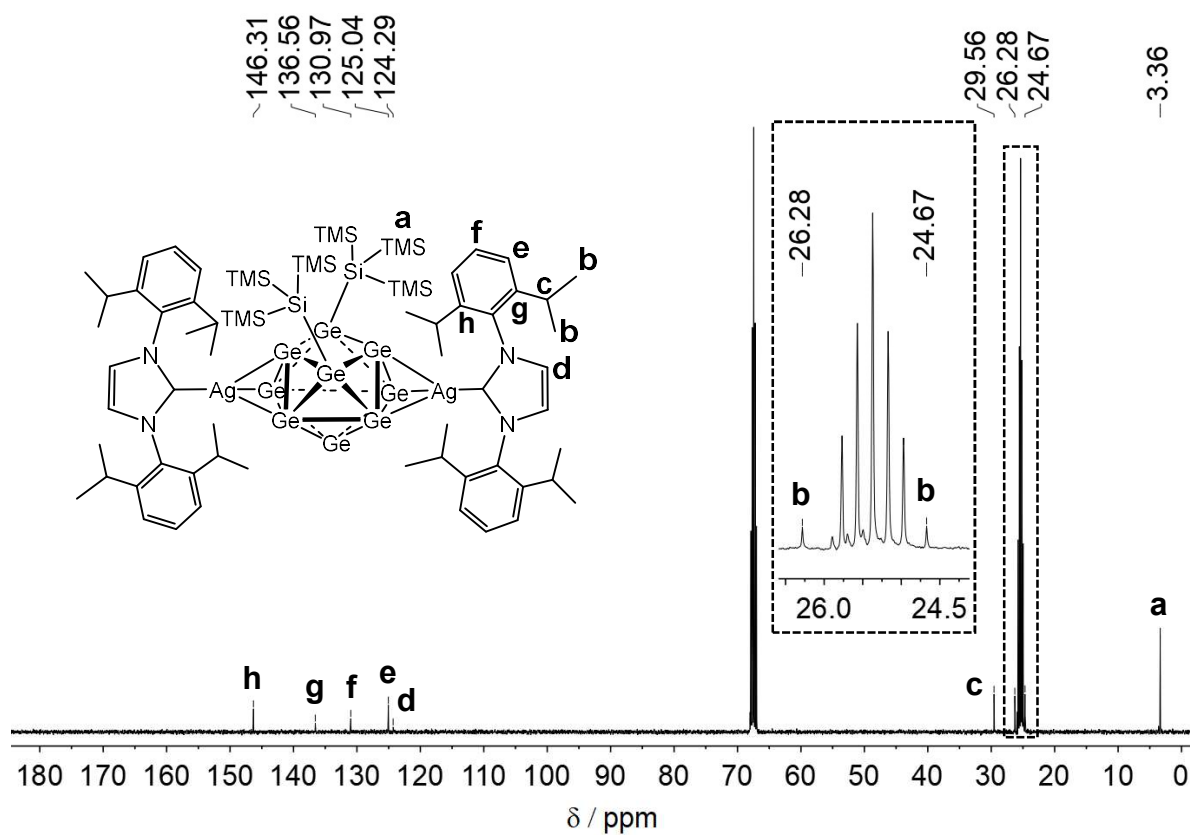


Figure 5.34. $^{13}\text{C-NMR}$ of $[(\text{NHC}^{\text{Dipp}}\text{Ag})_2\{\eta^3, \eta^3\text{-Ge}_9(\text{Si}(\text{TMS})_3)_2\}]$ in $\text{THF-}d_8$.

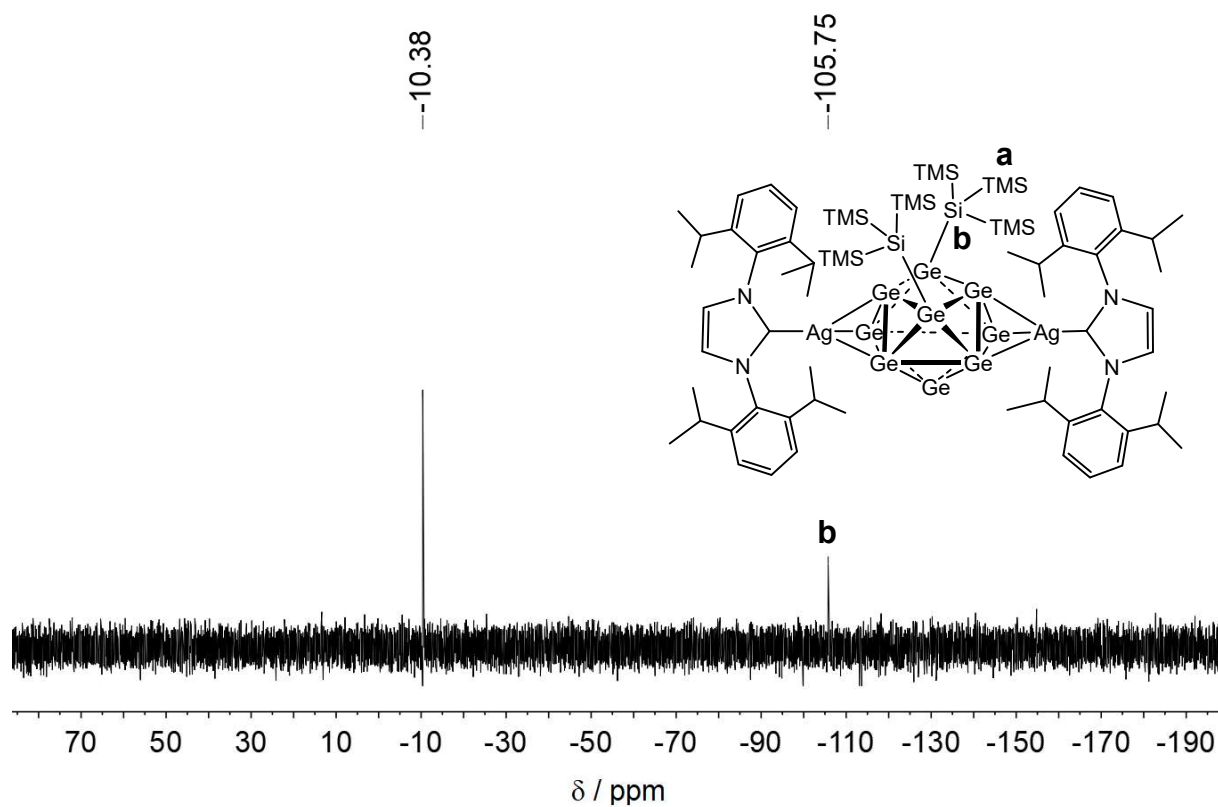


Figure 5.35. ^{29}Si -INEPT NMR of $[(\text{NHC}^{\text{Dipp}}\text{Ag})_2\{\eta^3, \eta^3\text{-Ge}_9(\text{Si}(\text{TMS})_3)_2\}]$ in $\text{THF-}d_8$.

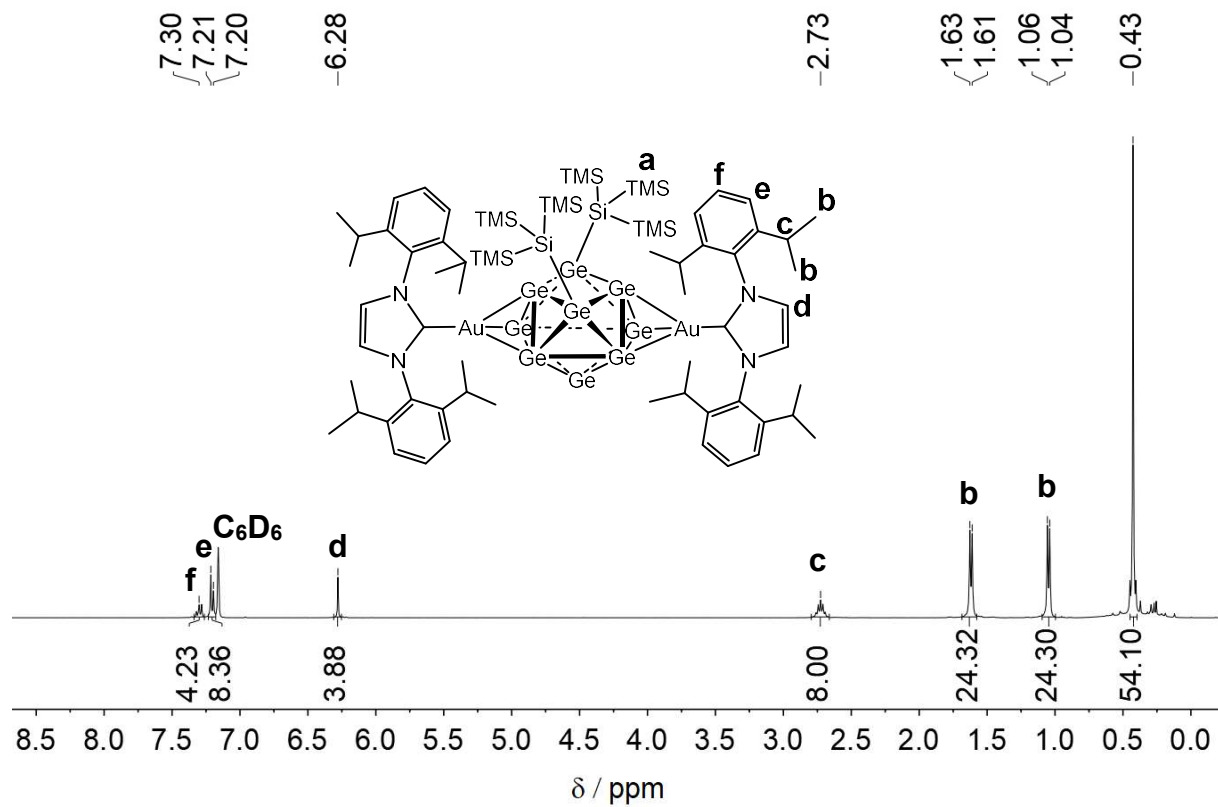


Figure 5.36. ^1H -NMR of $[(\text{NHC}^{\text{Dipp}}\text{Au})_2\{\eta^3, \eta^3\text{-Ge}_9(\text{Si}(\text{TMS})_3)_2\}]$ in C_6D_6 .

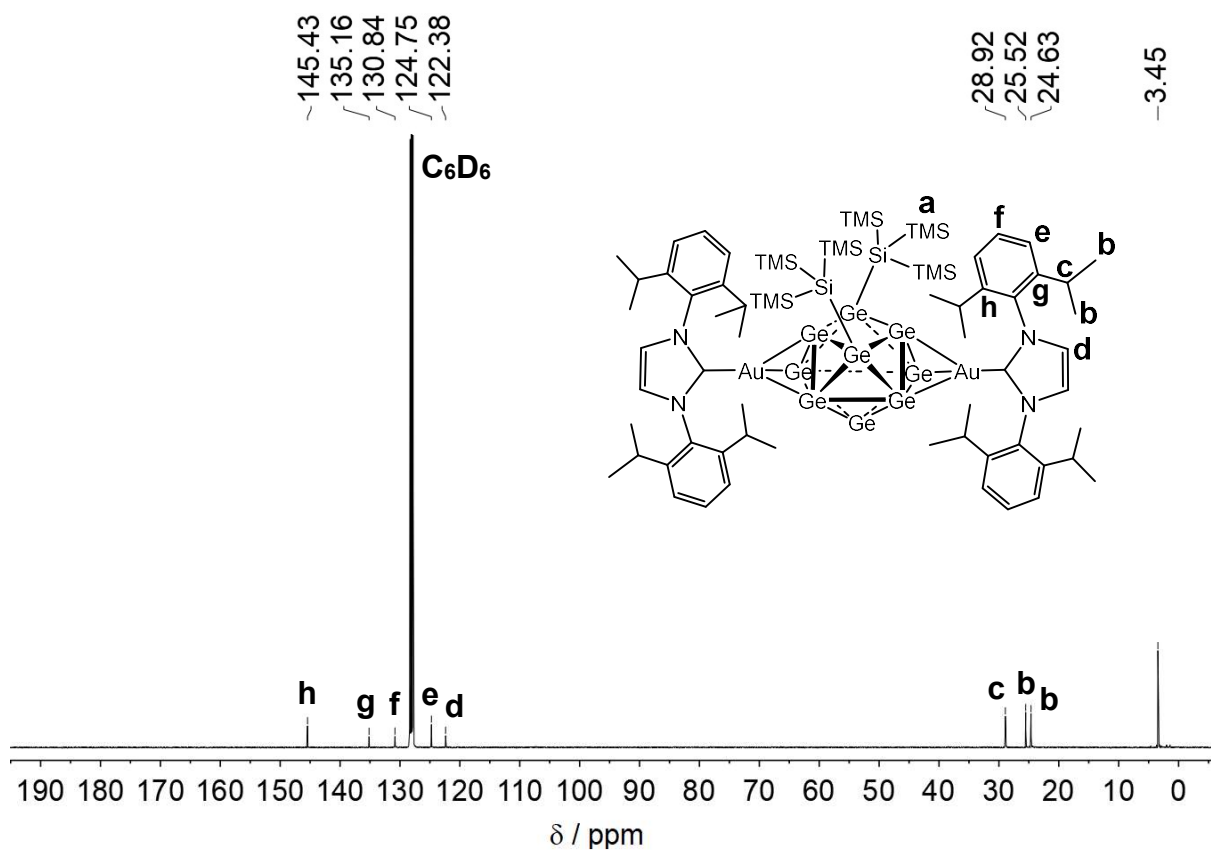


Figure 5.37. ^{13}C -NMR of $[(\text{NHC}^{\text{Dipp}}\text{Au})_2\{\eta^3, \eta^3\text{-Ge}_9(\text{Si}(\text{TMS})_3)_2\}]$ in C_6D_6 .

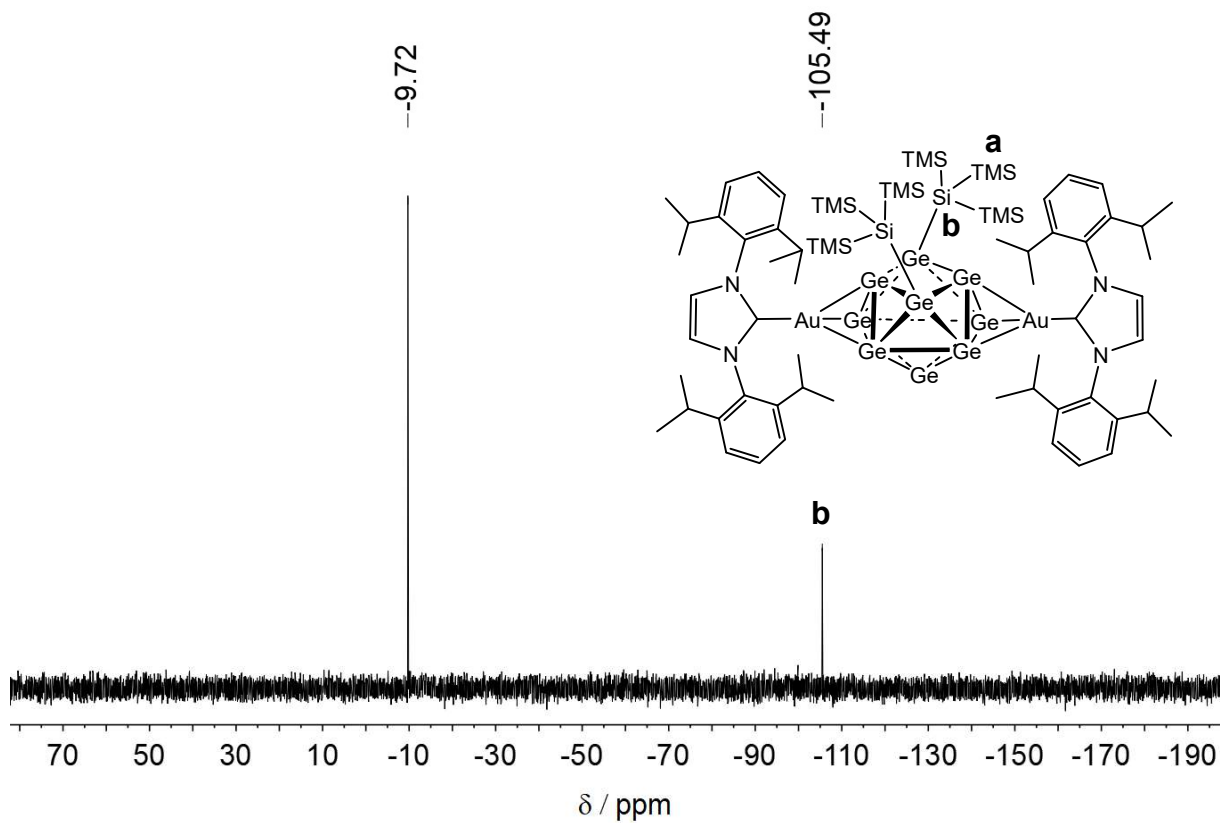


Figure 5.38. ^{29}Si -INEPT NMR of $[(\text{NHC}^{\text{Dipp}}\text{Au})_2\{\eta^3, \eta^3\text{-Ge}_9(\text{Si}(\text{TMS})_3)_2\}]$ in C_6D_6 .

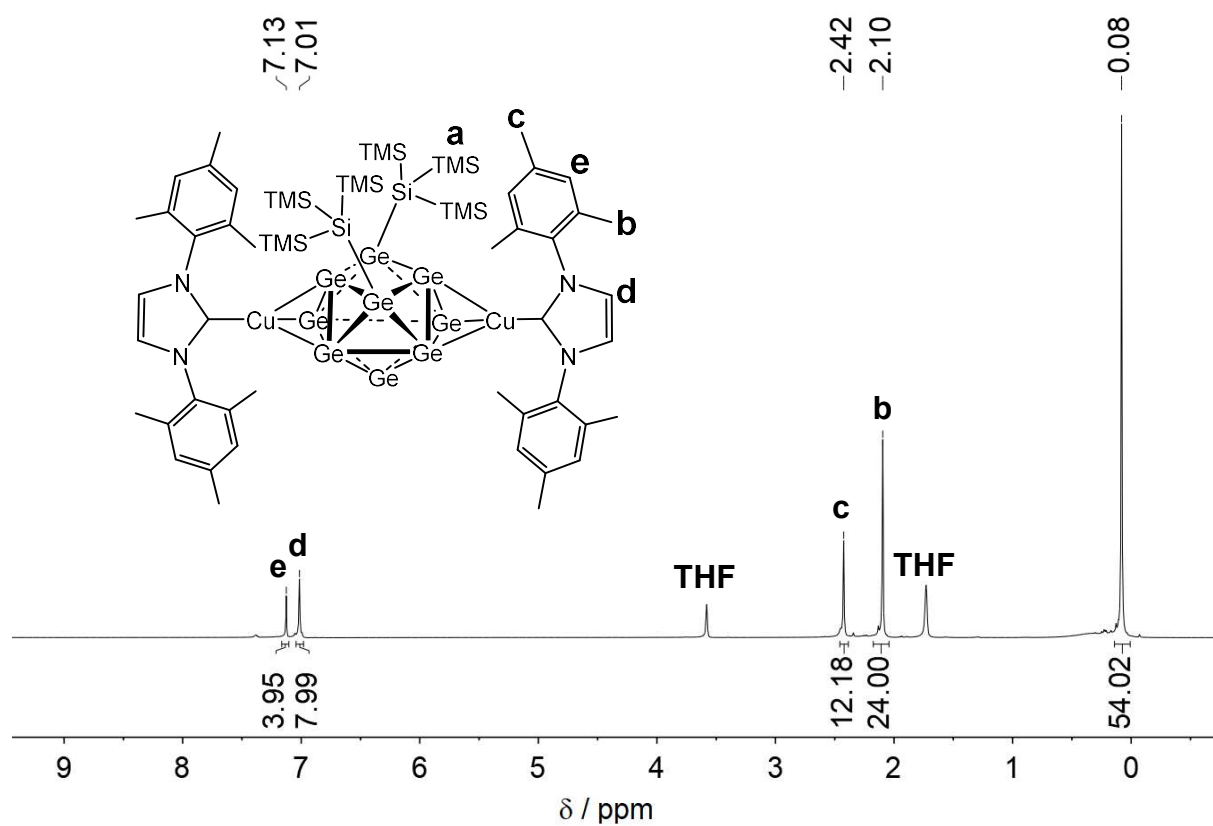


Figure 5.39. $^1\text{H-NMR}$ of $[(\text{NHC}^{\text{Mes}}\text{Cu})_2\{\eta^3, \eta^3\text{-Ge}_9(\text{Si}(\text{TMS})_3)_2\}]$ in $\text{THF-}d_8$.

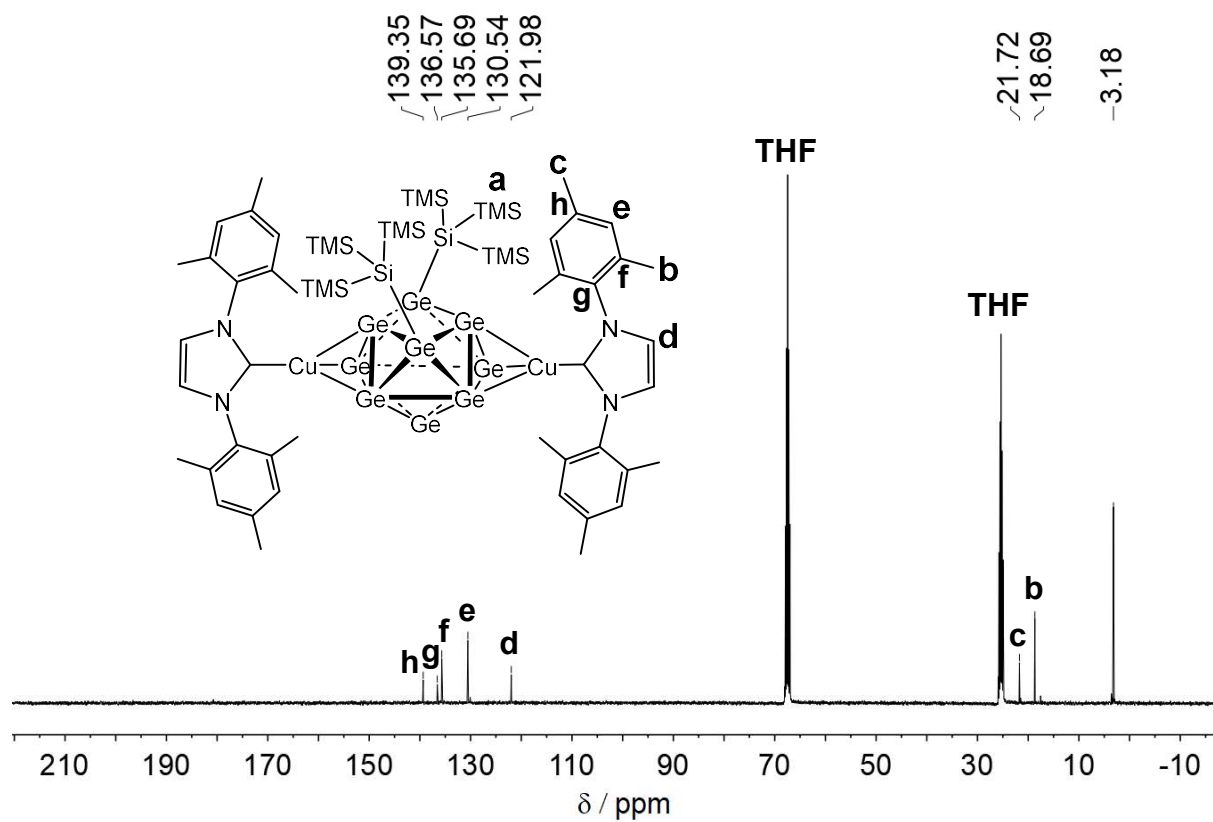


Figure 5.40. $^{13}\text{C-NMR}$ of $[(\text{NHC}^{\text{Mes}}\text{Cu})_2\{\eta^3, \eta^3\text{-Ge}_9(\text{Si}(\text{TMS})_3)_2\}]$ in $\text{THF-}d_8$.

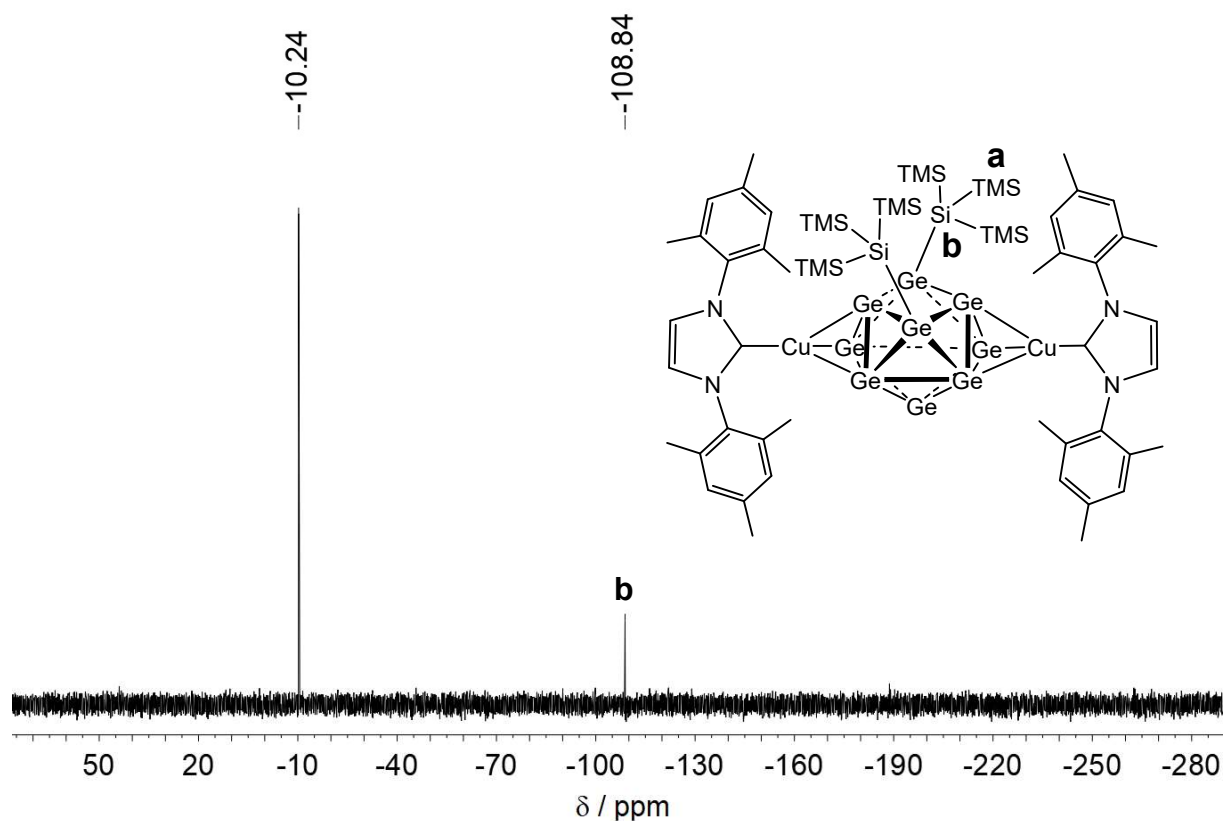


Figure 5.41. ^{29}Si -INEPT NMR of $[(\text{NHC}^{\text{Mes}}\text{Cu})_2\{\eta^3, \eta^3\text{-Ge}_9(\text{Si}(\text{TMS})_3)_2\}]$ in $\text{THF-}d_8$.

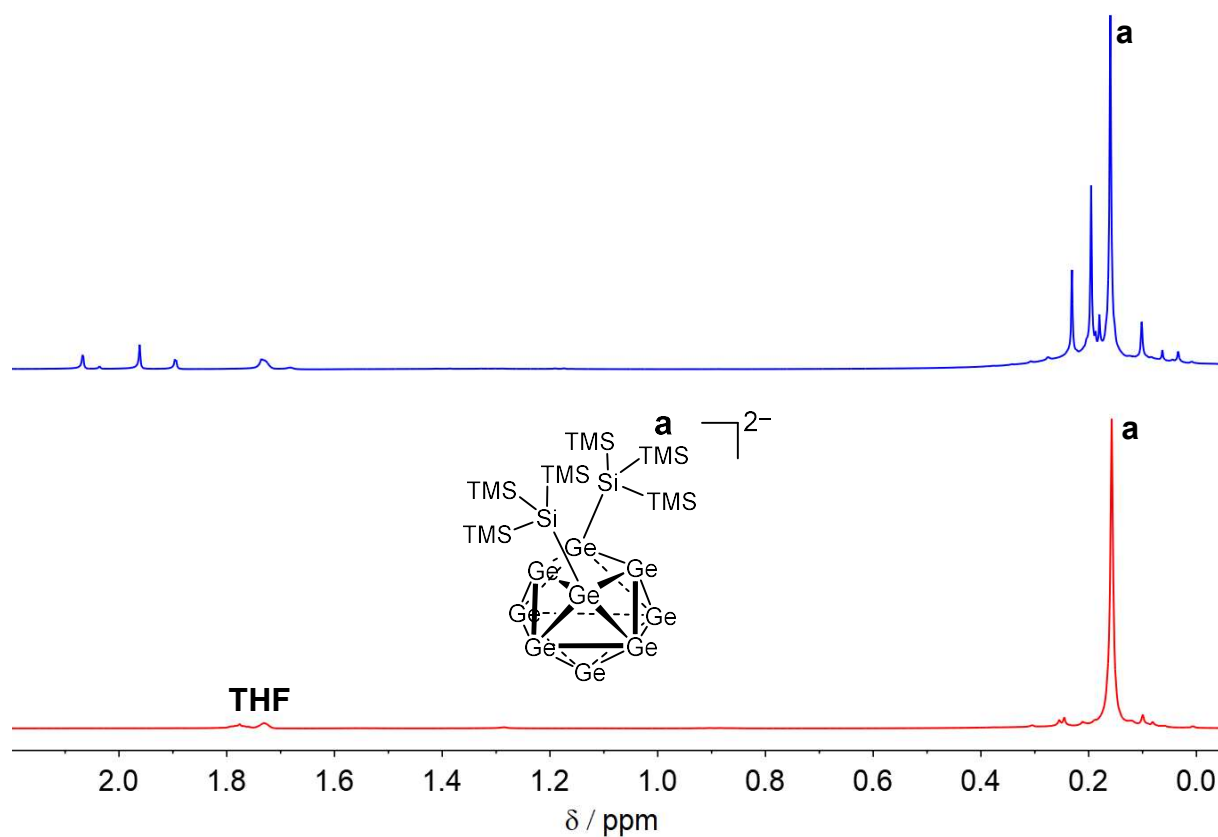


Figure 5.42. Comparison of ^1H -NMRs of silylation product of $\text{K}_{12}\text{Ge}_{17}$ with *hyp*-Cl (6 eq., blue line/top) and $[\text{Ge}_9\{\text{Si}(\text{TMS})_3\}_2]^{2-}$ (red line/bottom) in $\text{THF-}d_8$.

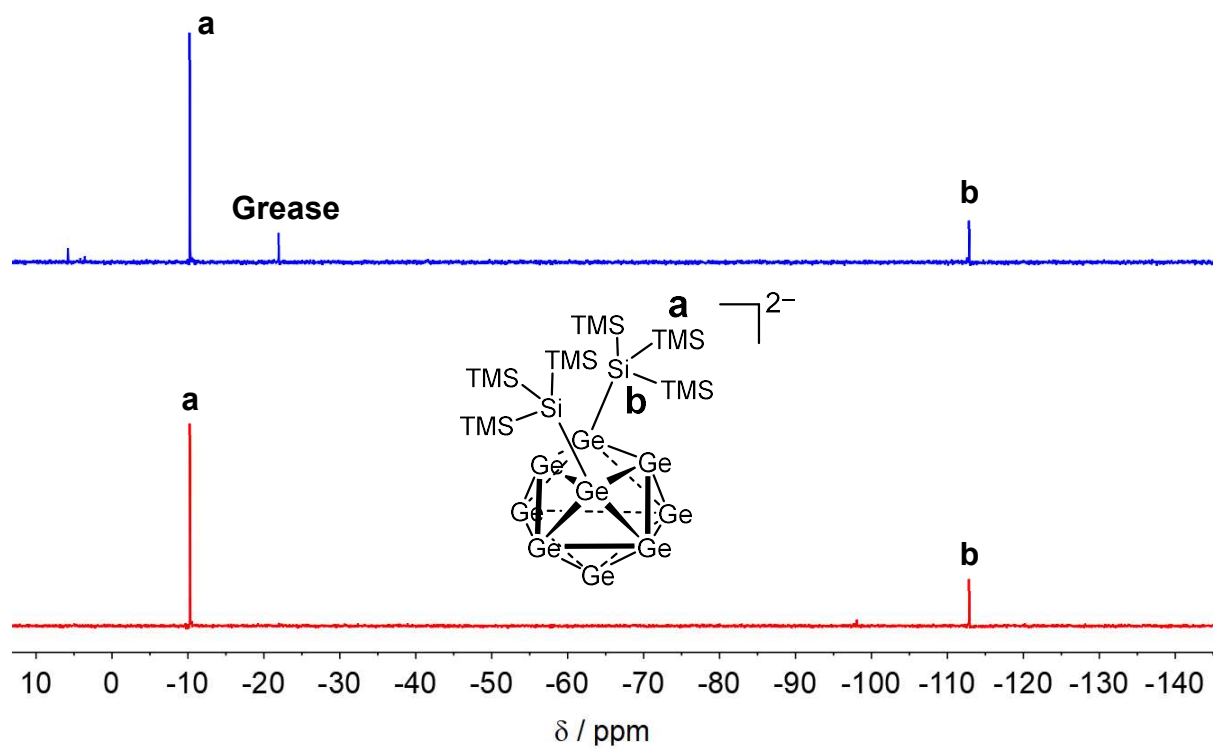


Figure 5.43. Comparison of ^{29}Si -INEPT NMRs of silylation product of $\text{K}_{12}\text{Ge}_{17}$ with *hyp*-Cl (6 eq., blue line/top) and $[\text{Ge}_9\{\text{Si}(\text{TMS})_3\}_2]^{2-}$ (red line/bottom) in $\text{THF}-d_8$.

5.7 XPS Investigations – Ge oxidation states

Table 5.15. Relative occupancy of Ge oxidation states on the surface of inverse opal structured thin films (without sputtering) for Ge 2p.

Precursor phase	Ge(0) / %	Ge(+II) / %	Ge(+IV) / %
$K_{12}Si_5Ge_{12}$	43.9	34.8	21.3
$K_{12}Si_8Ge_9$	3.1	9.6	87.3
$K_{12}Si_{12}Ge_5$	10.3	32.4	57.3

Table 5.16. Relative occupancy of Ge oxidation states in the inner structure of inverse opal structured thin films (after 40 min of Ar^+ sputtering) for Ge 2p.

Precursor phase	Ge(0) / %	Ge(+II) / %	Ge(+IV) / %
$K_{12}Si_5Ge_{12}$	69.0	20.0	11.0
$K_{12}Si_8Ge_9$	58.9	26.9	14.2
$K_{12}Si_{12}Ge_5$	56.4	24.1	19.5

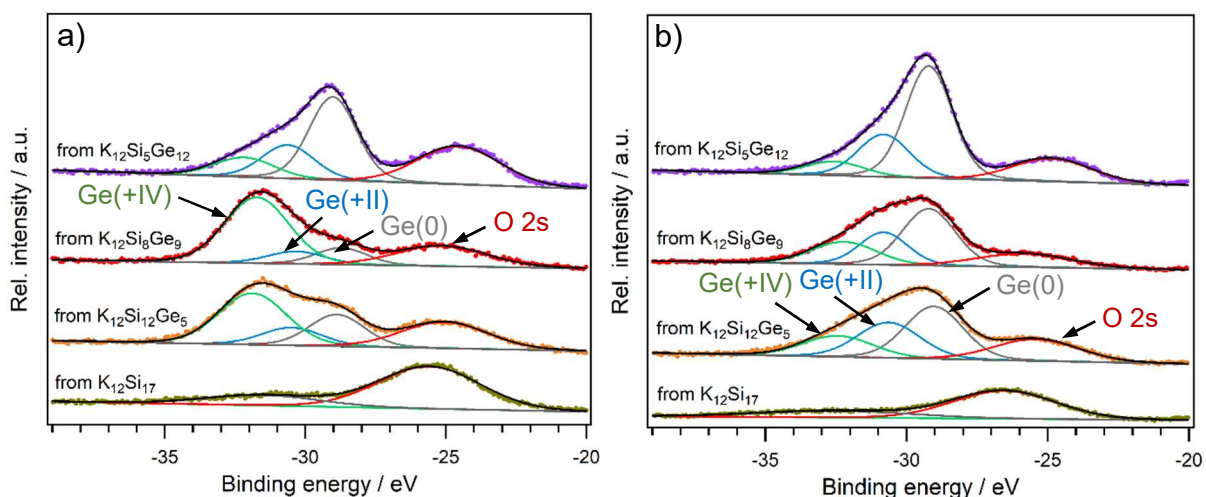


Figure 5.44. Ge 3d XPS spectra of inverse opal structured thin films from $K_{12}Si_5Ge_{12}$, $K_{12}Si_8Ge_9$, $K_{12}Si_{12}Ge_5$ and $K_{12}Si_{17}$ a) without and b) after 40 min of Ar^+ sputtering. Surface Ge is mostly oxidized to Ge(+IV), but sputtering reveals Ge(0) as the main component of the inner structure for all thin films containing Ge. The O 2s peak is mixing with the Ge 3d peak, resulting in a more accurate determination of Ge oxidation states through Ge 2p values.

Appendix

Table 5.17. Relative occupancy of Ge oxidation states on the surface of inverse opal structured thin films (without sputtering) for Ge 3d.

Precursor phase	Ge(0) / %	Ge(+II) / %	Ge(+IV) / %
$K_{12}Si_5Ge_{12}$	57.8	25.4	16.8
$K_{12}Si_8Ge_9$	15.1	12.3	72.6
$K_{12}Si_{12}Ge_5$	28.1	17.1	54.8

Table 5.18. Relative occupancy of Ge oxidation states in the inner structure of inverse opal structured thin films (after 40 min of Ar^+ sputtering) for Ge 3d.

Precursor phase	Ge(0) / %	Ge(+II) / %	Ge(+IV) / %
$K_{12}Si_5Ge_{12}$	63.7	26.5	9.8
$K_{12}Si_8Ge_9$	49.9	26.3	23.8
$K_{12}Si_{12}Ge_5$	45.3	33.0	21.7

5.8 References

- [1] L. Capuano, *International Energy Outlook 2018*, U.S. Energy Information Administration (EIA), obtained from <https://www.eia.gov/outlooks/ieol/>.
- [2] J. Flynn, R. Kasperson, H. Kunreuther, P. Slovic, *Issues Sci. Technol.* **1992**, *8*, 42-48.
- [3] A. Blowers, *Landscape Res.* **1999**, *24*, 241-264.
- [4] D. Easterling, H. Kunreuther, *The Dilemma of Siting a High-Level Nuclear Waste Repository*. Springer Science+Business Media, LLC: New York, 1995; p 285.
- [5] M. Höök, X.Tang, *Energ. Policy* **2013**, *52*, 797-809.
- [6] O. Edenhofer, R. Pichs-Madruga, Y. Sokona, K. Seyboth, et. al., IPCC Special Report on Renewable Energy Sources and Climate Change Mitigation, *Abu Dhabi 2011*, Working Group III of the IPCC, obtained from <https://www.unccllearn.org/sites/default/files/inventory/ipcc15.pdf>.
- [7] N. Oreskes, *Science* **2004**, *306*, 1686.
- [8] T. Jacob, J. Wahr, W. T. Pfeffer, S. Swenson, *Nature* **2012**, *482*, 514-518.
- [9] D. Qi, L. Chen, B. Chen, Z. Gao, W. Zhong, R. A. Feely, L. G. Anderson, H. Sun, J. Chen, M. Chen, L. Zhan, Y. Zhang, W.-J. Cai, *Nat. Clim. Change* **2017**, *7*, 195-199.
- [10] J. Cohen, J. A. Screen, J. C. Furtado, M. Barlow, D. Whittleston, D. Coumou, J. Francis, K. Dethloff, D. Entekhabi, J. Overland, J. Jones, *Nat. Geosci.* **2014**, *7*, 627-637.
- [11] C. B. Brown, *World energy consumption by fuel type and sector*, <https://grandsolarminimum.com/2018/11/19/world-energy-consumption/> (accessed: September 3rd, **2019**).
- [12] Federal Ministry for Economic Affairs and Energy (BMWi), *The Energy of the Future: Fourth "Energy Transition" Monitoring Report - Summary*, *Berlin, Germany: November 2015*.
- [13] Federal Ministry for Economic Affairs and Energy (BMWi), *Erneuerbare Energien*, <https://www.bmwi.de/Redaktion/DE/Dossier/erneuerbare-energien.html> (accessed: September 3rd, **2019**).
- [14] P. Brown, *Mitsubishi Installs 50MW Energy Storage System to Japanese Power Company*, <https://electronics360.globalspec.com/article/6402/mitsubishi-installs-50mw-energy-storage-system-to-japanese-power-company> (accessed: September 3rd, **2019**).

- [15] P. Crompton, *World's largest sodium-sulphur ESS deployed in Japan*, <http://www.bestmag.co.uk/content/world%E2%80%99s-largest-sodium-sulphur-ess-deployed-japan> (accessed: September 3rd, **2019**).
- [16] G. Bade, *Inside construction of the world's largest lithium ion battery storage facility*, <https://www.utilitydive.com/news/inside-construction-of-the-worlds-largest-lithium-ion-battery-storage-faci/431765/> (accessed: September 3rd, **2019**).
- [17] Q. Schiermeier, J. Tollefson, T. Scully, A. Witze, O. Morton, *Nature* **2008**, 454, 816-823.
- [18] L. R. Easton, M. J. Votaw, *Rev. Sci. Instrum.* **1959**, 30, 70-75.
- [19] D. R. Williams, *NASA Space Science Data Coordinated Archive - Vanguard 1*, <https://nssdc.gsfc.nasa.gov/nmc/spacecraft/display.action?id=1958-002B> (accessed: September 3rd, **2019**).
- [20] M. Fleischer, *Geol. Surv. Circular* **1953**, 285, 1-7.
- [21] A. Richter, M. Hermle, S. W. Glunz *IEEE J. Photovolt.* **2013**, 3, 1184-1191.
- [22] K. Yoshikawa, H. Kawasaki, W. Yoshida, T. Irie, K. Konishi, K. Nakano, T. Uto, D. Adachi, M. Kanematsu, H. Uzu, K. Yamamoto, *Nature Energy* **2017**, 2, 17032.
- [23] A. Bhambhani, *Fraunhofer ISE Achieves 34.1% Efficiency Level For Monolithic Triple-Junction & 24.3% Efficiency For III-V Semiconductor Layers Silicon Solar Cells*, <http://taiyangnews.info/technology/34-1-monolithic-triple-junction-solar-cell-efficiency/> (accessed: September 3rd, **2019**).
- [24] X. Li, T. Shi, G. Liu, L. Wen, B. Zhou, Y. Wang, *Opt. Express* **2015**, 23, 25316-25328.
- [25] T. Saga, *NPG Asia Mater.* **2010**, 2, 96-102.
- [26] R. R. Moskalyk, *Miner. Eng.* **2004**, 17, 393-402.
- [27] D. P. Nandedkar, *Phys. J.* **2016**, 2, 35-44.
- [28] R. Pillarisetty, *Nature* **2011**, 479, 324-328.
- [29] C. Claeys, E. Simoen, *Germanium-Based Technologies: from Materials to Devices*. Elsevier Science: Oxford, **2007**.
- [30] M. Scarselli, S. Masala, P. Castrucci, M. De Crescenzi, E. Gatto, M. Venanzi, A. Karmous, P. D. Szkutnik, A. Ronda, I. Berbezier, *Appl. Phys. Lett.* **2007**, 91, 141117.
- [31] M. G. Kanatzidis, *Adv. Mater.* **2007**, 19, 1165-1181.
- [32] P. D. Antunez, J. J. Buckley, R. L. Brutchey, *Nanoscale* **2011**, 3, 2399-2411.
- [33] A. D. Collord, H. W. Hillhouse, *Chem. Mater.* **2016**, 28, 2067-2073.

- [34] X. Li, Z. Yang, Y. Fu, L. Qiao, D. Li, H. Yue, D. He, *ACS Nano* **2015**, *9*, 1858-1867.
- [35] A. M. Chockla, K. C. Klavetter, C. B. Mullins, B. A. Korgel, *ACS Appl. Mater. Inter.* **2012**, *4*, 4658-4664.
- [36] S. Liua, J. Fenga, X. Biana, Y. Qianb, J. Liuc, H. Xu, *Nano Energy* **2015**, *13*, 651-657.
- [37] J. Liang, X. Li, Z. Hou, T. Zhang, Y. Zhu, X. Yan, Y. Qian, *Chem. Mater.* **2015**, *27*, 4156-4164.
- [38] S. A. Healy, M. A. Green, *Sol. Energ. Mat. Sol. C.* **1992**, *28*, 273-284.
- [39] T. Matsui, M. Kondo, K. Ogata, T. Ozawa, M. Isomura, *Appl. Phys. Lett.* **2006**, *89*, 142115.
- [40] X. Deng, X. Liao, S. Han, H. Povolny, P. Agarwal, *Sol. Energ. Mat. Sol. C.* **2000**, *62*, 89-95.
- [41] M. Isomura, K. Nakahata, M. Shima, S. Taira, K. Wakisaka, M. Tanaka, S. Kiyama, *Sol. Energ. Mat. Sol. C.* **2002**, *74*, 519-524.
- [42] N. Chandrasekharan, S. C. Sevov, *J. Electrochem. Soc.* **2010**, *157*, C140-C145.
- [43] M. M. Benthlohner, M. Waibel, P. Zeller, K. Sarkar, P. Müller-Buschbaum, D. Fattakhova-Rohlfing, T. F. Fässler, *Angew. Chem. Int. Ed.* **2016**, *55*, 2441-2445.
- [44] S. Geier, R. Jung, K. Peters, H. A. Gasteiger, D. Fattakhova-Rohlfing, T. F. Fässler, *Sustainable Energy Fuels* **2018**, *2*, 85-90.
- [45] M. Helgesen, M. Jorgensen, T. D. Nielsen, F. C. Krebs, *Printed Films: Materials Science and Applications in Sensors, Electronics and Photonics*. Woodhead Publishing: **2012**; Vol. 19, p 608.
- [46] J. A. Luceño-Sánchez, A. M. Díez-Pascual, R. P. Capilla, *Int. J. Mol. Sci.* **2019**, *20*, 976-1017.
- [47] C. J. Brabec, N. S. Sariciftci, J. C. Hummelen, *Adv. Funct. Mater.* **2001**, *11*, 15-26.
- [48] A. M. Bagher, *J. Renew. Sustain. Ener.* **2014**, *3*, 53-58.
- [49] T. F. O'Connor, A. V. Zaretski, S. Savagatrup, A. D. Printz, C. D. Wilkes, M. I. Diaz, E. J. Sawyer, D. J. Lipomi, *Sol. Energ. Mat. Sol. C.* **2016**, *144*, 438-444.
- [50] C.-C. Chen, L. Dou, R. Zhu, C.-H. Chung, T.-B. Song, Y. B. Zheng, S. Hawks, G. Li, P. S. Weiss, Y. Yang, *ACS Nano* **2012**, *6*, 7185-7190.
- [51] P. R. Berger, M. Kim, *J. Renew. Sustain. Ener.* **2018**, *10*, 013508.
- [52] G. P. Smestad, M. Grätzel, *J. Chem. Ed.* **1998**, *75*, 752-756.
- [53] M. Grätzel, *Nature* **2001**, *414*, 338-344.

Appendix

- [54] M. Ryan, *Platinum Metals Rev.* **2009**, *53*, 216-218.
- [55] J. Burschka, N. Pellet, S.-J. Moon, R. Humphry-Baker, P. Gao, M. K. Nazeeruddin, M. Grätzel, *Nature* **2013**, *499*, 316-320.
- [56] M. K. Nazeeruddin, F. De Angelis, S. Fantacci, A. Selloni, G. Viscardi, P. Liska, S. Ito, B. Takeru, M. Grätzel, *J. Am. Chem. Soc.* **2005**, *127*, 16835-16847.
- [57] A. Yella, H.-W. Lee, H. N. Tsao, C. Yi, A. K. Chandiran, Md. K. Nazeeruddin, E. W.-G. Diao, C.-Y. Yeh, S. M. Zakeeruddin, M. Grätzel, *Science* **2011**, *334*, 629-634.
- [58] H.-R. Wenk, A. Bulakh, *Minerals: Their Constitution and Origin*. Cambridge University Press.: New York, **2004**; p 640.
- [59] A. Kojima, K. Teshima, Y. Shirai, T. Miyasaka, *J. Am. Chem. Soc.* **2009**, *131*, 6050-6051.
- [60] G. Niu, X. Guo, L. Wang, *J. Mater. Chem. A* **2015**, *3*, 8970-8980.
- [61] M. M. Lee, J. Teuscher, T. Miyasaka, T. N. Murakami, H. J. Snaith, *Science* **2012**, *338*, 643-647.
- [62] A. Jaffe, Y. Lin, C. M. Beavers, J. Voss, W. L. Mao, H. I. Karunadasa, *ACS Cent. Sci.* **2016**, *24*, 201-209.
- [63] Y. Rong, Y. Hu, A. Mei, H. Tan, M. I. Saidaminov, S. I. Seok, M. D. McGehee, E. H. Sargent, H. Han, *Science* **2018**, *361*, eaat8235.
- [64] N. Marinova, S. Valero, J. L. Delgado *J. Colloid Interf. Sci.* **2017**, *488*, 373-389.
- [65] W. S. Yang, B.-W. Park, E. H. Jung, N. J. Jeon, Y. C. Kim, D. U. Lee, S. S. Shin, J. Seo, E. K. Kim, J. H. Noh, S. I. Seok, *Science* **2017**, *356*, 1376-1379.
- [66] C. Yi, J. Luo, S. Meloni, A. Boziki, N. Ashari-Astani, C. Grätzel, S. M. Zakeeruddin, U. Röthlisberger, M. Grätzel, *Energy Environ. Sci.* **2016**, *9*, 656-662.
- [67] The Perovskite Company Oxford PV, *Oxford PV sets world record for perovskite solar cell*, <https://www.oxfordpv.com/news/oxford-pv-sets-world-record-perovskite-solar-cell> (accessed: September 6th, **2019**).
- [68] J. Chun-Ren Ke, A. S. Walton, D. J. Lewis, A. Tedstone, P. O'Brien, W. R. Flavell, *Chem. Commun.* **2017**, *53*, 5231-5234.
- [69] D. Bryant, N. Aristidou, S. Pont, I. Sanchez-Molina, T. Chotchunangatchaval, S. Wheeler, J. R. Durrant, S. A. Haque, *Energy Environ. Sci.* **2016**, *9*, 1655-1660.
- [70] E. J. Juarez-Perez, L. K. Ono, M. Maeda, Y. Jiang, Z. Hawash, Y. Qi, *J. Mater. Chem. A* **2018**, *6*, 9604-9612.
- [71] E. J. Juarez-Perez, Z. Hawash, S. R. Raga, L. K. Ono, Y. Qi, *Energy Environ. Sci.* **2016**, *9*, 3406-3410.

- [72] F. Matteocchia, L. Cinàa, E. Lamannaa, S. Cacovichb, G. Divitinib, P. A. Midgleyb, C. Ducatib, A. Di Carlo, *Nano Energy* **2016**, *30*, 162-172.
- [73] S. N. Habisreutinger, T. Leijtens, G. E. Eperon, S. D. Stranks, R. J. Nicholas, H. J. Snaith, *Nano Lett.* **2014**, *14*, 5561-5568.
- [74] N. Rolston, B. L. Watson, C. D. Bailie, M. D. McGehee, J. Bastos, R. Gehlhaar, J.-E. Kim, D. Vak, A. Tej Mallajosyula, G. Gupta, A. D. Mohite, R. H. Dauskardt, *Extreme Mech. Lett.* **2016**, *9*, 353-358.
- [75] G. Grancini, C. Roldán-Carmona, I. Zimmermann, E. Mosconi, X. Lee, D. Martineau, S. Narbey, F. Oswald, F. De Angelis, M. Graetzel, M. K. Nazeeruddin, *Nature Comm.* **2017**, *8*, 15684.
- [76] H. Gaspar, F. Figueira, L. Pereira , A. Mendes , J. C. Viana, G. Bernardo, *Materials* **2018**, *11*, 2560-2595.
- [77] B. R. Weinberger, M. Akhtar, S. C. Gau, *Synthetic Met.* **1982**, *4*, 187-197.
- [78] G. Li, R. Zhu, Y. Yang, *Nature Photon.* **2012**, *6*, 153-161.
- [79] N. S. Sariciftci, L. Smilowitz, A. J. Heeger, F. Wudl, *Science* **1992**, *258*, 1474-1476.
- [80] J. C. Hummelen, B. W. Knight, F. LePeq, F. Wudl, J. Yaom, C. L. Wilkins, *J. Org. Chem.* **1995**, *60*, 532-538.
- [81] G. Yu, J. Gao, J. C. Hummelen, F. Wudl, A. J. Heeger, *Science* **1995**, *270*, 1789-1791.
- [82] M. M. Wienk, J. M. Kroon, W. J. H. Verhees, J. Knol, J. C. Hummelen, P. A. van Hal, R. A. J. Janssen, *Angew. Chem. Int. Ed.* **2003**, *42*, 3371-3375.
- [83] W. Lia, J. Caia, F. Caia, Y. Yana, H. Yic, R. S. Gurneya, D. Liua, A. Iraqic, T. Wanga, *Nano Energy* **2018**, *44*, 155-163.
- [84] X. Ma, W. Gao, J. Yu, Q. An, M. Zhang, Z. Hu, J. Wang, W. Tang, C. Yang, F. Zhang, *Energy Environ. Sci.* **2018**, *11*, 2134-2141.
- [85] B. Qi, Z.-G. Zhang, Z. Jin, D. Chi, Z. Qi, Y. Li, J. Wang, *Energy Environ. Sci.* **2014**, *7*, 1966-1973.
- [86] Y. Zhang, J. Yuan, L. Zhou, G. Zhang, H.-L. Yip, T.-K. Lau, X. Lu, C. Zhu, H. Peng, P. A. Johnson, M. Leclerc, Y. Cao, J. Ulanski, Y. Li, Y. Zou, *Joule* **2019**, *3*, 1140-1151.
- [87] L. Meng, Y. Zhang, X. Wan, C. Li, X. Zhang, Y. Wang, X. Ke, Z. Xiao, L. Ding, R. Xia, H.-L. Yip, Y. Cao, Y. Chen, *Science* **2018**, *361*, 1094-1098.
- [88] N. Asim, M. Mohammad, M. Badiei, *Nanomaterials for Green Energy*. Elsevier: **2018**; p 500.
- [89] A. Du Pasquier, D. D. T. Mastrogiovanni, L. A. Klein, T. Wang, E. Garfunkel, *Appl. Phys. Lett.* **2007**, *91*, 183501.

Appendix

- [90] D. J. Milliron, I. Gur, A. P. Alivisatos, *MRS Bull.* **2005**, *30*, 41-44.
- [91] B. R. Saunders, M. L. Turner, *Adv. Colloid Interfac.* **2008**, *138*, 1-23.
- [92] T. Wang, O. Sel, I. Djerdj, B. Smarsly, *Colloid Polym. Sci.* **2006**, *285*, 1-9.
- [93] B. Mandlmeier, J. M. Szeifert, D. Fatthakova-Rohlfing, H. Amenitsch, T. Bein, *J. Am. Chem. Soc.* **2011**, *133*, 17274-17282.
- [94] E. A. Gaulding, G. Liu, C. T. Chen, L. Löbbert, A. Li, G. Segev, J. Eichhorn, S. Aloni, A. M. Schwartzberg, I. D. Sharp, F. M. Toma, *J. Mater. Chem. A* **2017**, *5*, 11601-11614.
- [95] S. Geier. Alloy-Based Anodes with Inverse Opal Structure for Lithium Ion Batteries. TU Munich, **2018**.
- [96] H. Míguez, E. Chomski, F. García-Santamaría, M. Ibisate, S. John, C. López, F. Meseguer, J. P. Mondia, G. A. Ozin, O. Toader, H. M. van Driel, *Adv. Mater.* **2001**, *13*, 1634-1637.
- [97] X. Meng, R. Al-Salman, J. Zhao, N. Borissenko, Y. Li, F. Endres, *Angew. Chem. Int. Ed.* **2009**, *48*, 2703-2707.
- [98] W. Xin, J. Zhao, D. Ge, Y. Ding, Y. Li, F. Endres, *Phys. Chem. Chem. Phys.* **2013**, *15*, 2421-2426.
- [99] X. Liu, J. Zhao, Y. Zhang, X. An, Y. Ding, Y. Zhang, Y. Li, F. Endres, *Z. Phys. Chem.* **2013**, *227*, 1731-1739.
- [100] K. K. Rangan, P. N. Trikalitis, M. G. Kanatzidis, *J. Am. Chem. Soc.* **2000**, *122*, 10230-10231.
- [101] M. G. Kanatzidis, *Adv. Mater.* **2007**, *19*, 1165-1181.
- [102] P. N. Trikalitis, K. K. Rangan, T. Bakas, M. G. Kanatzidis, *Nature* **2001**, *410*, 671-675.
- [103] S. D. Korlann, A. E. Riley, B. L. Kirsch, B. S. Mun, S. H. Tolbert, *J. Am. Chem. Soc.* **2005**, *127*, 12516-12527.
- [104] A. E. Riley, S. D. Korlann, E. K. Richman, S. H. Tolbert, *Angew. Chem. Int. Ed.* **2006**, *45*, 235-241.
- [105] S. D. Korlann, A. E. Riley, B. S. Mun, S. H. Tolbert, *J. Phys. Chem. C* **2009**, *113*, 7697-7705.
- [106] A. Joannis, *C. R. Hebd. Seances Acad. Sci.* **1891**, *113*, 795.
- [107] S. Scharfe, T. F. Fässler, *Phil. Trans. R. Soc. A* **2010**, *368*, 1265-1284.
- [108] F. H. Smyth, J. Amer, *J. Am. Chem. Soc.* **1917**, *39*, 1299.
- [109] C. A. Kraus, *J. Am. Chem. Soc.* **1907**, *29*, 1571.
- [110] C. A. Kraus, *J. Am. Chem. Soc.* **1922**, *44*, 1216.

- [111] C. A. Kraus, *Trans. Am. Electrochem. Soc.* **1924**, *45*, 175.
- [112] C. A. Kraus, *J. Am. Chem. Soc.* **1925**, *47*, 43.
- [113] E. Zintl, J. Goubeau, W. Dullenkopf, *Z. Phys. Chem. A* **1931**, *154*, 1.
- [114] E. Zintl, A. Harder, *Z. Phys. Chem. A* **1931**, *154*, 47.
- [115] E. Zintl, W. Dullenkopf, *Z. Phys. Chem. B* **1932**, *16*, 183.
- [116] E. Zintl, H. Kaiser, *Z. Anorg. Allg. Chem.* **1933**, *211*, 113.
- [117] E. Zintl, A. Harder, S. Neumayr, *Z. phys. Chem. A* **1931**, *154*, 92.
- [118] F. Laves, *Die Naturwissenschaften*. Springer: Berlin, Heidelberg, **1941**.
- [119] D. Kummer, L. Diehl, *Angew. Chem. Int. Ed.* **1970**, *9*, 895.
- [120] L. Diehl, K. Khodadadeh, D. Kummer, J. Strahle, *Chem. Ber.* **1976**, *109*, 3404-3418.
- [121] T. F. Fässler, *Coord. Chem. Rev.* **2001**, *215*, 347-377.
- [122] J. D. Corbett, *Angew. Chem. Int. Ed.* **2000**, *39*, 670-690.
- [123] J. D. Corbett, *Chem. Rev.* **1985**, *85*, 383-397.
- [124] J. D. Corbett, D. G. Adolphson, D. J. Merryman, P. A. Edwards, F. J. Armatis, *J. Am. Chem. Soc.* **1975**, *97*, 6267-6268.
- [125] R. R. Marsh, J. P. Shoemaker, *Acta Cryst.* **1953**, *6*, 197-205.
- [126] E. Busmann, *Z. Anorg. Allg. Chem.* **1961**, *313*, 90-106.
- [127] H. G. von Schnering, J. Llanos, J.-H. Chang, K. Peters, E. M. Peters, R. Nesper, *Z. Kristallogr. NCS* **2005**, *220*, 324-326.
- [128] K. Wiesler, K. Brandl, A. Fleischmann, N. Korber, *Z. Anorg. Allg. Chem.* **2009**, *635*, 508-512.
- [129] P. A. Edwards, J. D. Corbett, *Inorg. Chem.* **1977**, *16*, 903-907.
- [130] J. Campbell, G. J. Schrobilgen, *Inorg. Chem.* **1997**, *36*, 4078-4081.
- [131] S. Joseph, C. Suchentrunk, N. Korber, *Z. Naturforsch.* **2010**, *65b*, 1059-1065.
- [132] C. Hoch, M. Wendorff, C. Röhr, *J. Alloy Compd.* **2003**, *361*, 206-221.
- [133] H. G. von Schnering, M. Baitinger, U. Bolle, W. Carrillo-Cabrera, J. Curda, Y. Grin, F. Heinemann, J. Llanos, K. Peters, A. Schmeding, M. Somer, *Z. Anorg. Allg. Chem.* **1997**, *623*, 1037-1039.
- [134] A. Spiekermann, S. D. Hoffmann, T. F. Fässler, *Angew. Chem. Int. Ed.* **2006**, *45*, 3459-3462.

Appendix

- [135] M. M. Bentlohner, C. Fischer, T. F. Fässler, *Chem. Commun.* **2016**, 52, 9841-9843.
- [136] K. Wade, *Inorg. Nucl. Chem. Lett.* **1972**, 8, 559-562.
- [137] K. Wade, *Advances in Inorganic Chemistry and Radiochemistry*. Elsevier: **1976**; Vol. 18.
- [138] C. Suchentrunk, N. Korber, *New J. Chem.* **2006**, 30, 1737-1739.
- [139] M. Waibel, C. B. Benda, B. Wahl, T. F. Fässler, *Chem. Eur. J.* **2011**, 17, 12928-12931.
- [140] M. Waibel, T. F. Fässler, *Inorg. Chem.* **2013**, 52, 5861-5866.
- [141] A. Nienhaus, S. D. Hoffmann, T. F. Fässler, *Z. Anorg. Allg. Chem.* **2006**, 632, 1752-1758.
- [142] L. J. Schiegerl, A. J. Karttunen, J. Tillmann, S. Geier, G. Raudaschl-Sieber, M. Waibel, T. F. Fässler, *Angew. Chem. Int. Ed.* **2018**, 57, 12950-12955.
- [143] S. Scharfe, F. Kraus, S. Stegmaier, A. Schier, T. F. Fässler, *Angew. Chem. Int. Ed.* **2011**, 50, 3630-3670.
- [144] M. W. Hull, S. C. Sevov, *J. Am. Chem. Soc.* **2009**, 131, 9026-9037.
- [145] C. B. Benda, J.-Q. Wang, B. Wahl, T. F. Fässler, *Eur. J. Inorg. Chem.* **2011**, 4262-4269.
- [146] D. J. Chapman, S. C. Sevov, *Inorg. Chem.* **2008**, 47, 6009-6013.
- [147] M. W. Hull, S. C. Sevov, *Inorg. Chem.* **2007**, 46, 10953-10955.
- [148] M. W. Hull, S. C. Sevov, *Chem. Commun.* **2012**, 48, 7720-7722.
- [149] C. B. Benda, H. He, W. Klein, M. Somer, T. F. Fässler, *Z. Anorg. Allg. Chem.* **2015**, 641, 1080-1086.
- [150] F. S. Kocak, P. Y. Zavalij, Y.-F. Lam, B. W. Eichhorn, *Chem. Commun.* **2009**, 4197-4199.
- [151] M. W. Hull, S. C. Sevov, *J. Organomet. Chem.* **2012**, 721-722, 85-91.
- [152] M. W. Hull, A. Ugrinov, I. Petrov, S. C. Sevov, *Inorg. Chem.* **2007**, 46, 2704-2708.
- [153] S. Frischhut, M. M. Bentlohner, W. Klein, T. F. Fässler, *Inorg. Chem.* **2017**, 56, 10691-10698.
- [154] M. M. Bentlohner, W. Klein, Z. H. Fard, L.-A. Jantke, T. F. Fässler, *Angew. Chem. Int. Ed.* **2015**, 54, 3748-3753.
- [155] M. M. Bentlohner, S. Frischhut, T. F. Fässler, *Chem. Eur. J.* **2017**, 23, 17089-17094.

- [156] D. F. Hansen, B. Zhou, J. M. Goicoechea, *J. Organomet. Chem.* **2012**, 721-722, 53-61.
- [157] A. Ugrinov, S. C. Sevov, *Chem. Eur. J.* **2004**, 10, 3727-3733.
- [158] M. M. Bentlohner, L.-A. Jantke, T. Henneberger, C. Fischer, K. Mayer, W. Klein, T. F. Fässler, *Chem. Eur. J.* **2016**, 22, 13946-13952.
- [159] A. Ugrinov, S. C. Sevov, *J. Am. Chem. Soc.* **2003**, 125, 14059-14064.
- [160] A. Ugrinov, S. C. Sevov, *J. Am. Chem. Soc.* **2002**, 124, 2442-2443.
- [161] A. Schnepf, *Angew. Chem. Int. Ed.* **2003**, 42, 2624-2625.
- [162] F. Li, S. C. Sevov, *Inorg. Chem.* **2012**, 51, 2706-2708.
- [163] L. J. Schiegerl, F. S. Geitner, C. Fischer, W. Klein, T. F. Fässler, *Z. Anorg. Allg. Chem.* **2016**, 642, 1419-1426.
- [164] K. Mayer, L. J. Schiegerl, T. F. Fässler, *Chem. Eur. J.* **2016**, 22, 18794-18800.
- [165] O. Kysliak, C. Schrenk, A. Schnepf, *Inorg. Chem.* **2015**, 54, 7083-7088.
- [166] O. Kysliak, T. Kunz, A. Schnepf, *Eur. J. Inorg. Chem.* **2017**, 805-810.
- [167] K. Mayer, L. J. Schiegerl, T. Kratky, S. Günther, T. F. Fässler, *Chem. Commun.* **2017**, 53, 11798-11801.
- [168] O. Kysliak, A. Schnepf, *Dalton Trans.* **2016**, 45, 2404-2408.
- [169] F. S. Geitner, C. Wallach, T. F. Fässler, *Chem. Eur. J.* **2018**, 24, 4103-4110.
- [170] F. S. Geitner, J. V. Dums, T. F. Fässler, *J. Am. Chem. Soc.* **2017**, 139, 11933-11940.
- [171] L. J. Schiegerl, A. J. Karttunen, W. Klein, T. F. Fässler, *Chem. Eur. J.* **2018**, 24.
- [172] L. J. Schiegerl, A. J. Karttunen, W. Klein, T. F. Fässler, *Chem. Sci.* **2019**, 10, 9130-9139.
- [173] F. Li, A. Muñoz-Castro, S. C. Sevov, *Angew. Chem. Int. Ed.* **2012**, 51, 8581-8584.
- [174] F. Li, S. C. Sevov, *J. Am. Chem. Soc.* **2014**, 136, 12056-12063.
- [175] F. Li, A. Muñoz-Castro, S. C. Sevov, *Angew. Chem. Int. Ed.* **2016**, 55, 8630-8633.
- [176] S. Frischhut, F. Kaiser, W. Klein, M. Drees, F. E. Kühn, T. F. Fässler, *Organometallics* **2018**, 37, 4560-4567.
- [177] S. Frischhut, W. Klein, T. F. Fässler, *C. R. Chim.* **2018**, 21, 932-937.
- [178] S. Frischhut, T. F. Fässler, *Dalton Trans.* **2018**, 47, 3223-3226.

Appendix

- [179] S. Frischhut, W. Klein, M. Drees, T. F. Fässler, *Chem. Eur. J.* **2018**, *24*, 9009-9014.
- [180] O. Kysliak, C. Schrenk, A. Schnepf, *Chem. Eur. J.* **2016**, *22*, 18787-18793.
- [181] F. Li, S. C. Sevov, *Inorg. Chem.* **2015**, *54*, 8121-8125.
- [182] C. Schenk, A. Schnepf, *Angew. Chem. Int. Ed.* **2007**, *46*, 5314-5316.
- [183] C. Schenk, F. Henke, G. Santiso-Quiñones, I. Krossing, A. Schnepf, *Dalton Trans.* **2008**, 4436-4441.
- [184] F. Henke, C. Schenk, A. Schnepf, *Dalton Trans.* **2009**, 9141-9145.
- [185] C. Schenk, A. Schnepf, *Chem. Commun.* **2009**, 3208-3210.
- [186] F. Henke, C. Schenk, A. Schnepf, *Dalton Trans.* **2011**, *40*, 6704-6710.
- [187] F. S. Geitner. Investigations on the Reactivity of Nine-Atomic Group 14 Element Zintl Anions in Solution. TU Munich, **2018**.
- [188] F. S. Geitner, M. A. Giebel, A. Pöthig, T. F. Fässler, *Molecules* **2017**, *22*, 1204-1217.
- [189] F. S. Geitner, T. F. Fässler, *Eur. J. Inorg. Chem.* **2016**, *17*, 2688-2691.
- [190] L. G. Perla, A. Muñoz-Castro, S. C. Sevov, *J. Am. Chem. Soc.* **2017**, *139*, 15176-15181.
- [191] *WinXPow*, STOE & Cie GmbH, **2011**.
- [192] *OriginPro*, OriginLab Corp., **2016**.
- [193] *X-Area*, STOE & Cie GmbH, **2015**.
- [194] *APEX Suite of Crystallographic Software*, Bruker AXS Inc., **2008**.
- [195] G. M. Sheldrick, *Acta Cryst. C* **2015**, *71*, 3-8.
- [196] A. L. Spek, *Acta Cryst. D* **2009**, *65*, 148-155.
- [197] A. L. Spek, *Acta Cryst. C* **2015**, *71*, 9-18.
- [198] G. R. Fulmer, A. J. M. Miller, N. H. Sherden, H. E. Gottlieb, A. Nudelman, B. M. Stoltz, J. E. Bercaw, K. I. Goldberg, *Organometallics* **2010**, *29*, 2176-2179.
- [199] *MestReNova*, Mestrelab Research S. L., **2015**.
- [200] F. A. Hegmann, R. R. Tykwinski, K. P. H. Lui, J. E. Bullock, J. E. Anthony, *Phys. Rev. Lett.* **2002**, *89*, 227403.
- [201] C. D. Wagner, *Faraday Discuss. Chem. Soc.* **1975**, *60*, 291-300.
- [202] *TURBOMOLE*, University of Karlsruhe and Forschungszentrum Karlsruhe GmbH, **2016**.

- [203] J. P. Perdew, M. Ernzerhof, *J. Chem. Phys.* **1996**, *105*, 9982-9985.
- [204] C. Adamo, V. Barone, *J. Chem. Phys.* **1999**, *110*, 6158-6170.
- [205] F. Weigend, R. Ahlrichs, *Phys. Chem. Chem. Phys.* **2005**, *7*, 3297-3305.
- [206] F. Weigend, M. Häser, H. Patzelt, R. Ahlrichs, *Chem. Phys. Lett.* **1998**, *294*, 143-152.
- [207] K. Eichkorn, O. Treutler, H. Öhm, M. Häser, R. Ahlrichs, *Chem. Phys. Lett.* **1995**, *240*, 283-290.
- [208] M. Sierka, A. Hogekamp, R. Ahlrichs, *J. Chem. Phys.* **2003**, *118*, 9136-9148.
- [209] F. Weigend, *Phys. Chem. Chem. Phys.* **2006**, *8*, 1057-1065.
- [210] A. Klamt, G. Schüürmann, *J. Chem. Soc. Perkin Trans.* **1993**, *2*, 799-805.
- [211] *Jmol - An Open-Source Java Viewer for Chemical Structures in 3D*, The Jmol Team, **2017**.
- [212] C. Steffen, K. Thomas, U. Huniar, A. Hellweg, O. Rubner, A. Schroer, *J. Comput. Chem.* **2010**, *31*, 2967-2970.
- [213] M. L. Laury, M. J. Carlson, A. K. Wilson, *J. Comput. Chem.* **2012**, *33*, 2380-2387.
- [214] M. Waibel, C. B. Benda, B. Wahl, T. F. Fässler, *Chem. Eur. J.* **2011**, *17*, 12928-12931.
- [215] M. Waibel, G. Raudaschl-Sieber, T. F. Fässler, *Chem. Eur. J.* **2011**, *17*, 13391-13394.
- [216] M. Asbrand, B. Eisenmann, *Z. Kristallogr.* **1992**, *198*, 283-284.
- [217] L. V. Titova, F. A. Hegmann, *Physics in Canada* **2009**, *65*, 101-104.
- [218] R. Ulbricht, E. Hendry, J. Shan, T. F. Heinz, M. Bonn, *Rev. Mod. Phys.* **2011**, *83*, 543-586.
- [219] N. F. Mott, E. A. Davis, R. A. Street *Phil. Mag.* **1975**, *32*, 961-996.
- [220] J. H. Strait, P. A. George, M. Levendorf, M. Blood-Forsythe, F. Rana, J. Park, *Nano Lett.* **2009**, *9*, 2967-2972.
- [221] M. C. Beard, G. M. Turner, C. A. Schmuttenmaer, *Phys. Rev. B* **2000**, *62*, 15764-15777.
- [222] T. Tiedje, J. M. Cebulka, D. L. Morel, B. Abeles, *Phys. Rev. Lett.* **1981**, *46*, 1425-1428.
- [223] D. G. Cooke, A. N. MacDonald, A. Hryciw, J. Wang, Q. Li, A. Meldrum, F. A. Hegmann, *Phys. Rev. B* **2006**, *73*, 193311.

Appendix

- [224] T. L. Cocker, D. Baillie, M. Buruma, L. V. Titova, R. D. Sydora, F. Marsiglio, F. A. Hegmann, *Phys. Rev. B* **2017**, *96*, 205439.
- [225] L. V. Titova, T. L. Cocker, S. Xu, J.-M. Baribeau, X. Wu, D. J. Lockwood, F. A. Hegmann, *Semicond. Sci. Technol.* **2016**, *31*, 105017.
- [226] J. M. Marshall, *Rep. Prog. Phys.* **1983**, *46*, 1235-1282.
- [227] H. Watakabe, T. Sameshima, H. Kanno, M. Miyao, *Thin Solid Films* **2006**, *508*, 315-317.
- [228] K. Moto, K. Yamamoto, T. Imajo, T. Suemasu, H. Nakashima, K. Toko, *Appl. Phys. Lett.* **2019**, *114*, 212107.
- [229] K. Toko, R. Yoshimine, K. Moto, T. Suemasu, *Sci. Rep.* **2017**, *7*, 16981.
- [230] M. Waibel, G. Raudaschl-Sieber, T. F. Fässler, *Chem. Eur. J.* **2011**, *17*, 13391-13394.
- [231] M. A. Giebel. Herstellung und Charakterisierung dünner Filme mit inverser Opalstruktur aus gemischten Polyanionen der Elemente Silizium und Germanium. TU Munich, **2015**.
- [232] T. Henneberger. Synthese und Reaktivität von Polyanionen der schweren Tetrelelemente. TU Munich, Munich, **2019**.
- [233] V. Queneau, E. Todorov, S. V. Sevov, *J. Am. Chem. Soc.* **1998**, *120*, 3263-3264.
- [234] M. Neumeier, F. Fendt, S. Gärtner, C. Koch, T. Gärtner, N. Korber, R. M. Gschwind, *Angew. Chem. Int. Ed.* **2013**, *52*, 4483-4486.
- [235] G. Kliche, M. Schwarz, H.-G. von Schnering, *Angew. Chem. Int. Ed.* **1987**, *26*, 349-351.
- [236] L. Vegard, *Z. Kristallogr.* **1928**, *67*, 239-259.
- [237] H. Míguez, E. Chomski, F. García-Santamaría, M. Ibisate, S. John, C. López, F. Meseguer, J. P. Mondia, G. A. Ozin, O. Toader, H. M. van Driel, *Adv. Mater.* **2001**, *13*, 1634-1637.
- [238] E. C. Honea, A. Ogura, C. A. Murray, K. Raghavachari, W. O. Sprenger, M. F. Jarrold, W. L. Brown, *Nature* **1993**, *366*, 42-44.
- [239] J. Gallmeier, H. Schaefer, A. Weiss, *Z. Naturforschg.* **1969**, *24 b*, 665-667.
- [240] D. L. Price, J. M. Rowe, J. J. Rush, E. Prince, D. G. Hinks, S. Susman, *J. Chem. Phys.* **1972**, *56*, 3697-3702.
- [241] A. S. Cooper, *Acta Cryst.* **1962**, *15*, 578-582.
- [242] F. Hastreiter, C. Lorenz, J. Hioe, S. Gärtner, N. Lokesh, N. Korber, R. M. Gschwind, *Angew. Chem. Int. Ed.* **2019**, <https://doi.org/10.1002/ange.201812955>.

- [243] C. Lorenz, F. Hastreiter, J. Hioe, L. Nanjundappa, S. Gärtner, N. Korber, R. M. Gschwind, *Angew. Chem. Int. Ed.* **2018**, *57*, 12956-12960.
- [244] Y. Kumai, S. Shirai, E. Sudo, J. Seki, H. Okamoto, Y. Sugiyama, H. Nakano, *J. Power Sources* **2011**, *196*, 1503-1507.
- [245] P. Musumeci, F. Roccaforte, R. Reitano, *Europhys. Lett.* **2001**, *55*, 674-678.
- [246] W. C. Ding, D. Hu, J. Zheng, P. Chen, B. W. Cheng, J. Z. Yu, Q. M. Wang, *J. Phys. D: Appl. Phys.* **2008**, *41*, 135101.
- [247] G. E. Jellison Jr., *Opt. Mater.* **1992**, *1*, 151-160.
- [248] G. E. Jellison Jr., *Opt. Mater.* **1992**, *1*, 41-47.
- [249] A. Esser, K. Seibert, H. Kurz, G. N. Parsons, C. Wang, B. N. Davidson, G. Lucovsky, R. J. Nemanich, *Phys. Rev. B* **1990**, *41*, 2879-2884.
- [250] K. E. Myers, Q. Wang, S. L. Dexheimer, *Phys. Rev. B* **2001**, *64*, 161309.
- [251] J. Lu, Y. Xie, F. Xu, L. Zhu, *J. Mater. Chem.* **2002**, *12*, 2755-2761.
- [252] S. C. Critchlow, J. D. Corbett, *Inorg. Chem.* **1982**, *21*, 3286-3290.
- [253] F. Lips, M. Raupach, W. Massa, S. Dehnen, *Z. Anorg. Allg. Chem.* **2011**, *637*, 859-863.
- [254] L. Kumari, J.-H. Lin, Y.-R. Ma, *J. Phys. D: Appl. Phys.* **2008**, *41*, 025405.
- [255] H. Olijnyk, *Phys. Rev. B* **1992**, *46*, 6589-6591.
- [256] T. F. Fässler, A. N. Kuznetsov, *Z. Anorg. Allg. Chem.* **2002**, *628*, 2537-2541.
- [257] E. Zintl, A. Harder, *Z. Phys. Chem. B - Chem. E* **1932**, *16*, 206-212.
- [258] C. R. Hubbard, H. E. Swanson, F. A. Mauer, *J. Appl. Cryst.* **1975**, *8*, 45-48.
- [259] W. Zhou, L. Liu, B. Li, P. Wu, Q. Song, *Comp. Mater. Sci.* **2009**, *46*, 921-931.
- [260] X. Cheng, R. Li, D. Li, Y. Li, X. Chen, *Phys. Chem. Chem. Phys.* **2015**, *17*, 6933-6947
- [261] O. Kysliak, D. D. Nguyen, A. Z. Clayborne, A. Schnepf, *Inorg. Chem.* **2018**, *57*, 12603-12609.
- [262] T. Henneberger, W. Klein, T. F. Fässler, *Z. Anorg. Allg. Chem.* **2018**, *644*, 1018-1027.
- [263] R. E. Wochele. Der Hypersilylrest, $-\text{Si}(\text{Si}(\text{CH}_3)_3)_3$, als Ligand in metallorganischen Verbindungen von Elementen der 13. und 14. Gruppe. University Stuttgart, **2001**.
- [264] W. Klein, C. Fischer, L.-A. Jantke, L. J. Schiegerl, T. F. Fässler, *Z. Anorg. Allg. Chem.* **2016**, *642*, 1314-1319.
- [265] J. M. Goicoechea, S. C. Sevov, *Organometallics* **2006**, *25*, 4530-4536.

Appendix

- [266] S. Scharfe, T. F. Fässler, *Eur. J. Inorg. Chem.* **2010**, 2010, 1207-1213.
- [267] S. Scharfe, T. F. Fässler, S. Stegmaier, S. D. Hoffmann, K. Ruhland, *Chem. Eur. J.* **2008**, 2008, 4479-4483.
- [268] K. Mayer, L.-A. Jantke, S. Schulz, T. F. Fässler, *Angew. Chem. Int. Ed.* **2017**, 56, 1-7.
- [269] T. F. Fässler F. S. Geitner, *Eur. J. Inorg. Chem.* **2016**, 2016, 2688-2691.
- [270] S. Ponou, T. F. Fässler, *ZAAC* **2007**, 633, 393-397.
- [271] B. Eisenmann, M. Somer, *Z. Naturforsch b* **1984**, 39, 736-738.